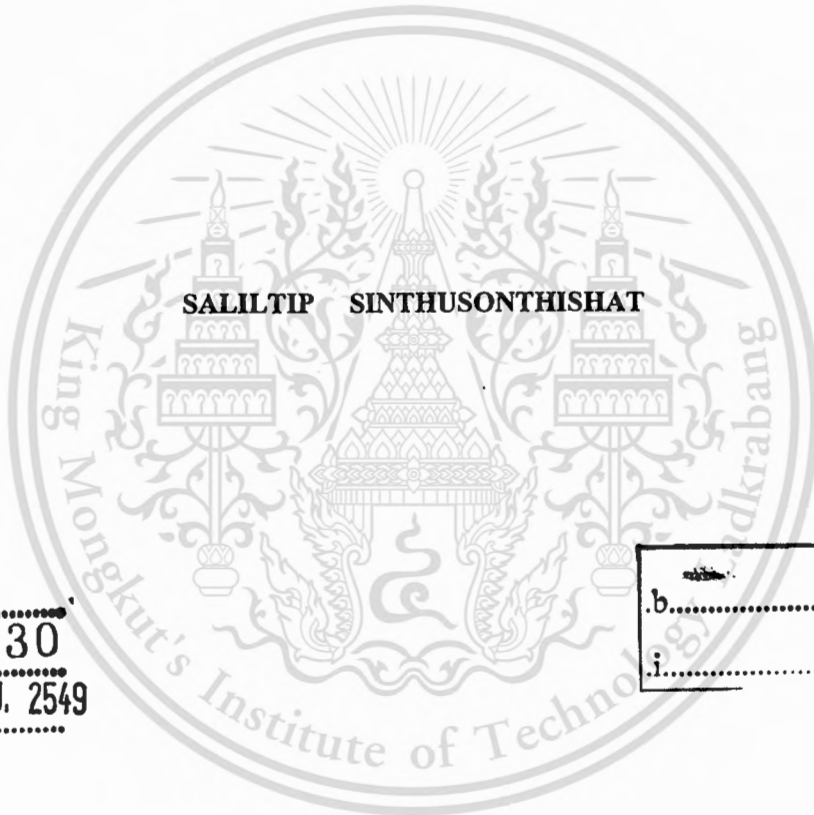


สำนักหอสมุดกลาง พระจอมเกล้าลาดกระบัง

**A NEW MODULATION STRATEGY FOR UNSYMMETRICAL PARAMETER
TYPE TWO-PHASE INDUCTION MOTOR DRIVES USING
A THREE-LEG VOLTAGE SOURCE INVERTER**



เลขหมู่.....
เลขทะเบียน..... 46630
วัน,เดือน,ปี..... 12 ก.ย. 2549

.b.....
.i.....

**A THESIS SUBMITTED IN PARTIAL FULFILLMENT
OF THE REQUIREMENT FOR THE DEGREE OF
DOCTOR OF ENGINEERING IN ELECTRICAL ENGINEERING
SCHOOL OF GRADUATE STUDIES
KING MONGKUT'S INSTITUTE OF TECHNOLOGY LADKRABANG**

2005

ISBN 974-15-1402-6

This material is reserved for educational use only, not allowed for commercial use.

Forbidden to modify the content, and cite the document when use.



COPYRIGHT 2005

SCHOOL OF GRADUATE STUDIES

KING MONGKUT'S INSTITUTE OF TECHNOLOGY LADKRABANG

This material is reserved for educational use only, not allowed for commercial use.

Forbidden to modify the content, and cite the document when use.

หัวข้อวิทยานิพนธ์	วิธีการมอดดูเลตแบบใหม่สำหรับขับเคลื่อนมอเตอร์เหนี่ยวนำสองเฟสที่มีพารามิเตอร์ไม่สมมาตร โดยใช้อินเวอร์เตอร์ชนิดจ่ายแรงดัน 3 กิ่ง
นักศึกษา	นางสลลทิพย์ สีนรุสนธิชาติ
รหัสนักศึกษา	42060022
ปริญญา	วิศวกรรมศาสตรดุษฎีบัณฑิต
สาขาวิชา	วิศวกรรมไฟฟ้า
พ.ศ.	2548
อาจารย์ผู้ควบคุมวิทยานิพนธ์	รศ. ดร. วิจิตร กิมเรศ

บทคัดย่อ

วิทยานิพนธ์นี้เป็นการนำเสนอวิธีการมอดดูเลตแบบใหม่ที่ให้แรงดันเฟสไม่สมดุลสำหรับขับเคลื่อนมอเตอร์เหนี่ยวนำสองเฟสที่มีพารามิเตอร์ไม่สมมาตร ซึ่งได้จากการดัดแปลงนำตัวเก็บประจุที่ต่ออนุกรมอยู่กับขดลวดช่วยของมอเตอร์เหนี่ยวนำหนึ่งเฟสที่มีใช้กันอยู่ ออกโดยใช้อินเวอร์เตอร์ชนิดจ่ายแรงดันไฟฟ้า 3 กิ่ง เทคนิคการมอดดูเลตนี้ได้จากการสร้างสัญญาณฟังก์ชันมอดดูเลตสามเฟสที่ทำให้แรงดันตกคร่อมขดลวดทั้งสองของมอเตอร์มีค่าไม่เท่ากัน ทำให้สามารถควบคุมแรงดันไฟฟ้าของขดลวดหลัก และขดลวดช่วยให้เป็นไปตามเทคนิคการควบคุม โดยแรงดันไฟฟ้าขดลวดหลักปรับตามหลักการคงที่อัตราส่วนแรงดันไฟฟ้าต่อความถี่ ส่วนขดลวดช่วยใช้การชดเชยแรงดันไฟฟ้าเพื่อชดเชยขนาดของกระแสไฟฟ้าเนื่องจากความไม่สมมาตรของค่าพารามิเตอร์ของขดลวดทั้งสอง เพื่อให้กระแสไฟฟ้าในแต่ละขดห่างกันเกือบ 90 องศาไฟฟ้าตลอดย่านกว้างความถี่รอบของการทำงาน ซึ่งเป็นการปรับปรุงแรงบิดแม่เหล็กของมอเตอร์ให้ดีขึ้น ในวิทยานิพนธ์ยังได้ใช้โมเดลคณิตศาสตร์มาวิเคราะห์พฤติกรรมของแรงดันฮาร์มอนิกส์ และวิเคราะห์คุณลักษณะต่าง ๆ ของมอเตอร์โดยใช้โมเดลมอเตอร์เหนี่ยวนำสองเฟสที่มีพารามิเตอร์ไม่เท่ากัน มีการทดสอบประเมินสมรรถนะในแง่ของผลกระทบของแรงดันฮาร์มอนิกส์ต่อคุณลักษณะต่าง ๆ ของมอเตอร์ คุณสมบัติของแรงบิดกับความถี่รอบ ประสิทธิภาพ การกระเพื่อมของแรงบิด เสียงที่ได้ยิน เป็นต้น หลังจากนั้นนำผลที่ได้ทั้งจากการคำนวณ และการวัดจริงเมื่อใช้แหล่งจ่ายแรงดันไฟฟ้าเป็นอินเวอร์เตอร์แบบ 2 กิ่ง และ 3 กิ่ง มาเปรียบเทียบกัน ผลการทดสอบในส่วนของความเครียดแรงดันฮาร์มอนิกส์ เสียงที่ได้ยิน ความคิดเพี้ยนของสัญญาณกระแสไฟฟ้า โลหะของกระแสไฟฟ้า คุณลักษณะต่าง ๆ ของกระแสไฟฟ้า และประสิทธิภาพของมอเตอร์ แสดงให้เห็นอย่างสอดคล้องกันว่าด้วยเทคนิคการมอดดูเลตที่ใช้กับอินเวอร์เตอร์ 3 กิ่งที่นำเสนอนี้เป็นผลให้สมรรถนะของมอเตอร์ดีกว่าการใช้อินเวอร์เตอร์แบบ 2 กิ่ง ซึ่งเป็นวิธีการควบคุมความเร็วรอบของมอเตอร์สองขดลวดแบบดั้งเดิมตลอดย่านกว้างความถี่รอบของการทำงาน

Thesis Title	A New Modulation Strategy for Unsymmetrical Parameter Type Two-Phase Induction Motor Drives Using A Three-Leg Voltage Source Inverter
Student	Mrs. Salitip Sinthusonthishat
Student ID.	42060022
Degree	Doctor of Engineering in Electrical
Programme	D. Eng. (Elec. Eng.)
Year	2005
Thesis Advisor	Assoc. Prof. Dr. Vijit Kinnares

ABSTRACT

This thesis proposes a new modulation scheme providing unbalanced output phase voltage of a standard three-leg voltage source inverter for unsymmetrical type two-phase induction motors adapted from existing single-phase permanent split capacitor induction motors by removing running capacitor in series with the auxiliary winding. This strategy allows unbalanced output phase voltage control with constant V/Hz for a main winding and voltage boost in order to compensate magnitude of current for an auxiliary winding. Consequently, electromagnetic torque is dramatically enhanced. Moreover, motor performance can be improved over a wide range of operating conditions, especially for a lower speed range. A Mathematical approach to analysis of PWM output voltages is fully given. The harmonic voltage characteristics are investigated and compared to that of a conventional two-leg half bridge topology. Practical verification under a wide range speed of realistic motor operation is presented to confirm correctness and performance of the proposed technique. An unsymmetrical two phase induction motor model and a control method are also described. The performance comparison such as the influence of harmonic voltage contents on motor characteristics, torque-speed profile, motor efficiency, torque pulsation and acoustic noise between a conventional two leg half-bridge and the proposed technique are investigated. The simulated and experimental results are in consistently good agreement. The results in terms of harmonic voltage stress, acoustic noise, harmonic current, total harmonic distortion of current, loci current, current characteristics, and motor efficiency, show that the performance of the proposed scheme is superior to that of the conventional technique.

This material is reserved for educational use only, not allowed for commercial use.

Forbidden to modify the content, and cite the document when use.

ACKNOWLEDGEMENTS

In the years during this research was undertaken, I have had the pleasure and privilege of working some wonderful people, each of whom deserves more thanks than this page allows.

Firstly, I would like to express my sincere appreciation to my supervisor, Associate Professor Dr. Vijit Kinnares for his guidance, encouragement and support throughout the course of this work. The results of his professional guidance were far beyond this thesis and will be beneficial to my future. I would principally like to thank Associate Professor Dr. Pichetjamroen Viriya, Dr. Nontawat Chuladaycha and Assistant Professor Dr. Anantawat Kunakorn, Department of Electrical Engineering, King Mongkut's Institute of Technology Ladkrabang for their extensively useful suggestions and insightful advices. Without their help, it would have been impossible for me to finish this doctoral work.

I am very grateful to the Director of Minburi Technical College, the staff of Elwe (Thailand) Co., Ltd., and Mr. Wattana Dewaje for providing all kinds of support and more importantly, allowing me to utilize all equipments and devices. I am profoundly indebted to Ajarn Santi Pookaiyaudom, Assistant President of Electrical Engineering Department at MUT, for his guidance and support.

Many thanks must be made to my colleagues and technician staffs, especially electrical machine staffs at Electrical Power Engineering Department of Mahanakorn University of Technology (MUT) for their assistance and collaboration. Special thanks to all members of Power Electronics and Machine Control Group of Electrical Power Engineering Department at King Mongkut's Institute of Technology Ladkrabang for their help and alliance. Also, I wish to extend my appreciation to Mr. Racha for all the helpfulness and the person who has shown me the true meaning of the word "friend".

I dramatically wish to express my deepest obligation to my parents, Pitak and Panida, my aunt, Benjawal, and my uncle, Rach-chapong, for their love, dream, and encouragement, particularly to my sons, Sopanut and Nutchapol, for their inspiration and patience.

Finally, I gratefully acknowledge the financial support for my doctoral degree registration from Mahanakorn University of Technology.

Saliltip Sinthusonthisat

TABLE OF CONTENTS

	PAGE
THAI ABSTRACT	I
ENGLISH ABSTRACT	II
ACKNOWLEDGEMENT	III
TABLE OF CONTENTS	IV
LIST OF TABLES	VI
LIST OF FIGURES	VII
CHAPTER 1. INTRODUCTION	1
1.1 Background	1
1.2 Objectives of The Research	5
1.3 Structure of The Thesis	6
1.4 Advantages	7
CHAPTER 2. TWO-PHASE INDUCTION MOTOR AND DRIVE TOPOLOGIES	8
2.1 Double Revolving Field Theory	8
2.2 Unsymmetrical Two-phase Induction Machines in D-Q Axis	18
2.3 Principle of Operation and Control Method	26
2.4 Motor Drive Systems	27
2.5 Noise Sources	37
CHAPTER 3. NOVEL MODULATING STRATEGY	40
3.1 Converter Modulation Strategy	40
3.2 Unbalanced Voltage for Improved Unsymmetrical Two-Phase Induction Motor Performance	46
3.3 Current Mode Analysis	47
3.4 Mathematical Analysis	67
3.5 Two-phase Inverter Modulation Control	84

This material is reserved for educational use only, not allowed for commercial use.

Forbidden to modify the content, and cite the document when use.

TABLE OF CONTENTS (Con.)

	PAGE
3.6 Control and Power Circuits	85
3.6.1 Power Circuit	85
3.6.2 Control Circuit	86
3.6.3 Blanking Time Circuit	89
3.6.4 Isolated Ground Circuit	89
3.6.5 Protection Circuit	90
3.7 Calculated and Measured Harmonic Voltage Spectra	92
CHAPTER 4. SIMULATION AND EXPERIMENTAL RESULTS	100
4.1 Unsymmetrical Two-phase Induction Motor Parameters	100
4.2 Composition of Two-phase Induction Motor Model	106
4.3 Experimental System	111
4.4 Results and Discussions	112
4.4.1 Harmonic Voltage Stress	112
4.4.2 Acoustic Noise	117
4.4.3 Harmonic Current and Total Harmonic Distortion of Current	120
4.4.4 Current Characteristics and Loci Current	128
4.4.5 Motor Efficiency and Output Torque	132
4.4.6 Speed and Torque Pulsations	136
4.5 Advantages and Disadvantages	139
CHAPTER 5. CONCLUSIONS AND FURTHER WORK	140
5.1 Conclusions	140
5.2 Further Work and Suggestion	142
REFERENCES	143

This material is reserved for educational use only, not allowed for commercial use.

Forbidden to modify the content, and cite the document when use.

TABLE OF CONTENTS (Con.)

	PAGE
APPENDIX A: JACOBI-ANGER AND BESSEL FUNCTION RELATIONSHIPS.....	152
APPENDIX B: UNSYMMETRICAL TWO-PHASE INDUCTION MOTOR TEST	157
APPENDIX C: SIMULATION PROGRAM	162
APPENDIX D: ACOUSTIC NOISE CALCULATION	164
APPENDIX E: IMPLEMENTED CIRCUITS AND TEST RIG.....	167
APPENDIX F: THE AUTHOR'S PUBLICATIONS	170
BIOGRAPHY	190



LIST OF TABLES

TABLE	PAGE
2.1 Comparison of various topologies	36
2.2 Induction motor noise sources, causes and treatments	39
3.1 Switch mode analysis	64
3.2 Setting up modulation index (M) for the two-leg VSI	84
3.3 Setting up modulation index (M) and (M_1) for the three-leg VSI	85
4.1 Generalized harmonics of SPWM signals for the auxiliary winding	116
4.2 Generalized harmonics of SPWM signals for the main winding	117
4.3 Comparison of the 2-leg and 3-leg inverter topologies in terms of THDi	128
4.4 Comparison of the 2-leg and 3-leg inverter topologies with different control method in terms of motor efficiency	136
4.5 The proposed 3-leg VSI evaluation	139
B.1 The impressed and induced voltages of each winding	158
B.2 The relationship of DC voltage and current of the main winding	158
B.3 The relationship of DC voltage and current of the auxiliary winding	158
B.4 Locked rotor test information	159
B.5 No load test information	159
B.6 Friction and windage losses test information	160

LIST OF FIGURES

FIGURE	PAGE
2.1 Single-phase motor equivalent circuit	10
2.2 Simplified single-phase motor equivalent circuit	11
2.3 Unsymmetrical two-phase motor equivalent circuit	12
2.4 Unsymmetrical two-phase induction machine	20
2.5 Idealized circuit model of unsymmetrical two-phase induction machine	20
2.6 Idealized circuit model of unsymmetrical two-phase induction machine	24
2.7 The relationship between fundamental inverter frequency and output voltage for each winding	27
2.8 Single-phase induction motor with auxiliary winding control	29
2.9 Single-phase voltage control with triacs	29
2.10 Single-phase ac-to-ac chopper	29
2.11 Single-phase higher power ac-to-ac chopper	30
2.12 Single-phase ac-to-ac cycloconverter	30
2.13 Single-phase full-bridge PWM inverter with a full-bridge rectifier	30
2.14 Single-phase full-bridge PWM inverter with a half-bridge rectifier	31
2.15 Single-phase full-bridge PWM inverter with a controlled rectifier	31
2.16 Single-phase half-bridge PWM inverter with half-bridge rectifier.....	31
2.17 Single-phase half-bridge PWM inverter with a controlled half-bridge rectifier	32
2.18 Two -phase full-bridge PWM inverter	32
2.19 Two-phase half-bridge PWM inverter	32
2.20 Two -phase half-bridge PWM inverter with a controlled rectifier	34
2.21 Two -phase semi full-bridge PWM inverter	34
2.22 The conventional two-leg half bridge inverter	35
2.23 The proposed three-leg semi-full bridge inverter	35
3.1 Main power circuit of the typical two-leg half bridge inverter	40
3.2 Principle of generating PWM patterns for the typical two-leg VSI	41
3.3 Main power circuit of the proposed three-leg semi-full bridge inverter	43

This material is reserved for educational use only, not allowed for commercial use.

Forbidden to modify the content, and cite the document when use.

LIST OF FIGURES (Con.)

FIGURE	PAGE
3.4 Phasor diagram of modulating functions for the two-phase drive system of the three-leg VSI	45
3.5 Principle of generating unbalanced PWM output voltages based on the proposed modulating functions for the three-leg VSI	46
3.6 Main power circuit for current mode analysis	47
3.7 Simulation of main power circuit for switch mode analysis	49
3.8 Simulation of control circuit for switch mode analysis	49
3.9 Simulated voltage and current waveforms for the proposed three-leg VSI with the analysis mode of current flow corresponding to v_D	50
3.10 Current flow in mode 1	51
3.11 Current flow in mode 2	53
3.12 Current flow in mode 3	55
3.13 Current flow in mode 4	56
3.14 Current flow in mode 5	58
3.15 Current flow in mode 6	59
3.16 Current flow in mode 7	61
3.17 Current flow in mode 8	63
3.18 Current flow analysis of the main winding	66
3.19 The unit cell for sine-triangular single phase modulation	73
3.20 Double-edge naturally sampled PWM of a bipolar half-bridge phase leg	74
3.21 Normalized harmonic voltages as a function of modulation index for both auxiliary and main winding voltages of the conventional technique	82
3.22 Normalized harmonic voltages as a function of modulation index of the proposed modulation technique	83
3.23 Circuit diagram of IGBTs Intelligent power module (IPM)	86
3.24 Block diagram for bipolar SPWM generation	87
3.25 Block diagram for unipolar SPWM generation	87
3.26 SPWM generator circuit	88

This material is reserved for educational use only, not allowed for commercial use.

Forbidden to modify the content, and cite the document when use.

LIST OF FIGURES (Con.)

FIGURE	PAGE
3.27 Blanking time circuit	90
3.28 Isolated ground circuit	91
3.29 Fault protection circuit	92
3.30 Reference sinusoidal signal phase C of the main winding voltage for the three-leg VSI	93
3.31 SPWM output voltages for the two-leg VSI	94
3.32 SPWM output voltages for the three-leg VSI	94
3.33 Calculated harmonic voltage spectra of the two-leg VSI at inverter frequency of 20 Hz	95
3.34 Calculated harmonic voltage spectra of the three-leg VSI at inverter frequency of 20 Hz	95
3.35 Measured harmonic voltage spectra of the two-leg VSI at inverter frequency of 20 Hz	96
3.36 Measured harmonic voltage spectra of the three-leg VSI at inverter frequency of 20 Hz	96
3.37 Calculated harmonic voltage spectra of the two-leg VSI at inverter frequency of 40 Hz	97
3.38 Calculated harmonic voltage spectra of the three-leg VSI at inverter frequency of 40 Hz	97
3.39 Measured harmonic voltage spectra of the two-leg VSI at inverter frequency of 40 Hz	98
3.40 Measured harmonic voltage spectra of the three-leg VSI at inverter frequency of 40 Hz	98
3.41 Calculated harmonic voltage spectra for both windings at inverter frequency of 50 Hz	99
3.42 Measured harmonic voltage spectra for both windings at inverter frequency of 50 Hz	99

This material is reserved for educational use only, not allowed for commercial use.

Forbidden to modify the content, and cite the document when use.

LIST OF FIGURES (Con.)

FIGURE	PAGE
4.1 Voltage and current relationship of the main winding	101
4.2 Voltage and current relationship of the auxiliary winding	101
4.3 Approximate equivalent circuit for locked rotor test	102
4.4 Approximate equivalent circuit for no load test	104
4.5 Friction and windage losses analysis	105
4.6 Main block diagram for an unsymmetrical two-phase motor fed by the two-leg VSI	107
4.7 Main block diagram for an unsymmetrical three-phase motor fed by the two-leg VSI	107
4.8 Two-phase voltage source diagram of the two-leg VSI	108
4.9 Two-phase voltage source diagram of the three-leg VSI	109
4.10 Details of <i>Extconn</i> block diagram	109
4.11 Details of <i>Qaxis</i> block diagram	110
4.12 Details of <i>Daxis</i> block diagram	110
4.13 Details of <i>Rotor</i> block diagram	110
4.14 Analysis diagram of voltage and current characteristics	111
4.15 Block diagram of experimental system	112
4.16 Measured results of voltage stress of the two-leg VSI at inverter frequency of 20 Hz	113
4.17 Measured results of voltage stress of the three-leg VSI at inverter frequency of 20 Hz	113
4.18 Measured results of voltage stress of the two-leg VSI at inverter frequency of 30 Hz	114
4.19 Measured results of voltage stress of the three-leg VSI at inverter frequency of 30 Hz	114
4.20 Measured results of voltage stress of the two-leg VSI at inverter frequency of 40 Hz	115
4.21 Measured results of voltage stress of the three-leg VSI at inverter frequency of 40 Hz	115
4.22 Measured results of both windings voltage stress at inverter frequency of 50 Hz	116
4.23 Measured spectra of acoustic noise with inverter fed induction motor at inverter frequency of 20 Hz	118
4.24 Measured spectra of acoustic noise with inverter fed induction motor at inverter frequency of 30 Hz	118
4.25 Measured spectra of acoustic noise with inverter fed induction motor at inverter frequency of 40 Hz	119

This material is reserved for educational use only; not allowed for commercial use.

Forbidden to modify the content, and cite the document when use.

LIST OF FIGURES (Con.)

FIGURE	PAGE
4.26 Measured spectra of acoustic noise with inverter fed induction motor at inverter frequency of 50 Hz	119
4.27 Simulated current waveform for two-leg VSI at inverter frequency of 20 Hz	120
4.28 Simulated current waveform for three-leg VSI at inverter frequency of 20 Hz	120
4.29 Simulated current waveform for two-leg VSI at inverter frequency of 30 Hz	121
4.30 Simulated current waveform for three-leg VSI at inverter frequency of 30 Hz	121
4.31 Simulated current waveform for two-leg VSI at inverter frequency of 40 Hz	122
4.32 Simulated current waveform for three-leg VSI at inverter frequency of 40 Hz	122
4.33 Simulated current waveform for two-leg VSI at inverter frequency of 50 Hz	123
4.34 Simulated current waveform for three-leg VSI at inverter frequency of 50 Hz	123
4.35 Measured current waveform for two-leg VSI at inverter frequency of 20 Hz	124
4.36 Measured current waveform for three-leg VSI at inverter frequency of 20 Hz	124
4.37 Measured current waveform for two-leg VSI at inverter frequency of 30 Hz	125
4.38 Measured current waveform for three-leg VSI at inverter frequency of 30 Hz	125
4.39 Measured current waveform for two-leg VSI at inverter frequency of 40 Hz	126
4.40 Measured current waveform for three-leg VSI at inverter frequency of 40 Hz	126
4.41 Measured current waveform for two-leg VSI at inverter frequency of 50 Hz	127
4.42 Measured current waveform for three-leg VSI at inverter frequency of 50 Hz	127
4.43 Experimental results of motor winding currents for the two-leg VSI	129
4.44 Experimental results of motor winding currents for the three-leg VSI	129
4.45 Experimental results of loci currents for the two-leg VSI	130
4.46 Experimental results of loci currents for the three-leg VSI	131
4.47 Experimental results of motor efficiency versus %load torque with reference frequency at 20 Hz	133
4.48 Experimental results of motor efficiency versus %load torque with reference frequency at 30 Hz	133
4.49 Experimental results of motor efficiency versus %load torque with reference frequency at 40 Hz	134

This material is reserved for educational use only, not allowed for commercial use.

LIST OF FIGURES (Con.)

FIGURE	PAGE
4.50 Experimental results of motor efficiency versus %load torque with reference frequency at 50 Hz	134
4.51 Torque as function of motor speed at various frequency for both simulation and experimental results with the unbalanced voltage control method	135
4.52 Torque as function of motor speed at various frequency for both simulation and experimental results with constant V/Hz control scheme for both windings	135
4.53 Speed pulsation of motor at the full load torque and the rated frequency	137
4.54 Torque pulsation of motor at the full load torque and the rated frequency	138
A.1 Bessel functions $J_n(\xi)$ for $n = 0, 1, 2, \dots, 6$	156
B.1 Circuit diagram for turn ratio test	157
B.2 Circuit diagram for DC test	159
B.3 Circuit diagram for locked rotor test	160
B.4 Circuit diagram for no load test	160
B.5 Unsymmetrical two-phase equivalent circuit of the tested motor	161
B.6 Relationship of each fundamental output voltage versus fundamental invert frequency ...	161
E.1 Overall experimental set up	167
E.2 Power circuit	167
E.3 Inverter configuration	167
E.4 Sinusoidal signal generator circuit	168
E.5 SPWM signal generator circuit	168
E.6 Isolated ground and protection circuits	168
E.7 Gate drive circuit	168
E.8 Overall test rig for normal operation	168
E.9 The tested motor with load coupling	169
E.10 Control unit	169
E.11 Overall test rig in case of acoustic noise test	169

This material is reserved for educational use only, not allowed for commercial use.

Forbidden to modify the content, and cite the document when use.

CHAPTER 1

INTRODUCTION

1.1 Background

Single-phase squirrel-cage induction motors are one of the most widely used types of low power ac motors in the world, especially for residential households or commercial applications where a three-phase power supply is not available. Recently, there has been a continuous debate concerning the motor of the future for low power applications. Specialists are focusing on superior motors [1], such as dc brushless, permanent magnet synchronous or electronically commutated type, because they have demonstrated improvements in efficiency, reliability, torque per volume/mass ratio, maintenance and service life. Nevertheless, the industry seems to respond with a manifested rigidity in changing the standard induction motor solutions since the most commonly installed motor is the typical standard single-phase induction motor. The investments in manufacturing, therefore, are mainly based on the easiness of transition from fixed speed to variable speed.

Although the ac drive technology for three-phase induction motors is mature today, single-phase motors still encounter difficulties when working at variable frequencies. The utilization of single-phase motors such as pumps, fans, blowers, compressor, tools, household appliances are predominantly fixed speed. When speed control is required, complicated mechanical techniques are traditionally used. Typical examples include gears, throttling valves, or electrical techniques, for instance: tapped winding and pole changing, which normally preclude continuous control of the rotational speed. For a motor's full speed operation under the utility's frequency with slip speed relying on load torque and the number of pole, the variable-frequency system with mechanical and/or electrical techniques has low efficiency. Furthermore, in the case of mechanical or electrical failure, the motors may not be allowed to operate as a bypassed process. Therefore, a great number of applications would profit from a single-phase motor driven from an adjustable speed controller. This is because the use of adjustable speed drives is an alternative to provide continuous-speed regulation, as well as saving both energy and consumer's costs [2]. In addition, the reduction in the cost of the power electronic circuitry yields economically justifiable applications for adjustable speed single-phase motor drives. An

This material is reserved for educational use only, not allowed for commercial use.

Forbidden to modify the content, and cite the document when use.

authentically variable speed operation from this motor with a wide range of speed and load would help applications designers to incorporate many new features into their products and have greater flexibility of control.

In recent years, several research groups have started to investigate different single-phase adjustable-speed motor drive systems. The main motivation behind this interest is the improvement of the performance of the existing single-phase standard solution. A few researchers tried to govern the capacitor run in series with the auxiliary winding electronically to be a continuously variable capacitance in accordance with the optimum capacitance value which strongly depends on the load, as well as on the amplitude and frequency of the supplying voltage [3-4]. However, the variable-frequency drive converters and controls are preferred as they are far more convenient to retrofit for previously installed motors. An ideal drive would also allow straight forward connection to the utility supply and the motor. Additionally, connection with the existing process control circuitry must be suitable. Some publications have discussed the performance of a standard motor fed from a single phase variable frequency supply with an unmodified capacitor run type motor [5-6]. The standard single phase motor has a quite limited characteristic when driven from a variable frequency source. Also, among the capacitor motor types, i.e. the motors which have capacitors in the auxiliary winding circuits for improving starting and/or running performances, the permanent split capacitor motors can work best with a variable frequency supply [7]. The permanent split capacitor motor has two windings which are spatially displaced at 90 electrical degrees in the stator, known as main and auxiliary winding. An ac capacitor is permanently connected in series with the auxiliary winding, called a running capacitor.

The adjustable speed single-phase cage motor controllers have been made in different types. Generally, there are two alternatives for implementing an adjustable-speed single-phase motor drive system [8]. The first one is a single-phase drive in which the single-phase motor is treated as a single-phase mode. The second one is a two-phase drive in which the single-phase motor is considered as a two-phase induction motor. There are many kinds of variable-voltage variable-frequency control techniques. Only a few alternative appearances have been reported to employ variable frequency converters to achieve continuous variable speed single-phase motor operation.

In case of single-phase controller, any single-phase motor variable speed controller would almost certainly be able to control the speed of a balanced two-phase motor. The single-

This material is reserved for educational use only, not allowed for commercial use.

phase motor drive topologies by a single-phase controller are mostly used the motor as a conventional standard type without modification. The first study of variable speed control using single phase ac-to-ac converter has been obtained through voltage control utilizing triacs or back to back thyristors. One of these approaches exploits a single phase converter to control the phase angle of the voltage only applied to the auxiliary winding, while the main winding remains connected to the ac supply [9]. This technique can achieve variable speed operation. However, it is at the expense of motor derating and torque ripple. Excessive heating of the motor also occurs during low speed operation. Ac-to-ac chopper inverters suffer large harmonic injections into the source and low input power factor. Additionally, this limits the speed range of the motor [10]. To minimize the harmonic injection, the topologies presented in [11-12] have been proposed. This technique is extended to a single-phase ac-to-ac cycloconverter [13-15]. In this case, the motor torque and current can be controlled in a much better manner, and also a wide range of speed variation can be obtained when compared to a conventional pole-changing, voltage-taps, and ac phase control techniques. At low speeds, however, the total harmonic distortion of current (THDi) is quite significant and the motor current has a considerable discontinuity. Next, single-phase both full-bridge and half-bridge PWM inverter drives are used. In these cases, it is possible to achieve reduced torque and speed pulsations, lower vibrations and less acoustic noise. After that, a controlled half-bridge rectifier with full-bridge PWM inverter which is a modified rectification of the previous topology is taken into account [16-17]. This technique yields the more advantages than the previous topologies because two extra IGBTs are used to control the current of utility supply as an active rectifier. The front-end controlled rectifier can be employed to limit the THDi, resulting in the increment of utility power factor. The drive system has a wide speed range in both directions, namely forward and reverse, and also has a very high input power factor for all operating conditions.

In the case of a two-phase drive system, variable speed operation of the two-phase motor can be divided into two conditions. Firstly, the instantaneous voltage across the main winding has to have the same phase as the instantaneous voltage across the auxiliary winding. The motor has to be started and run with the running capacitor in series with the auxiliary winding. The other condition employs the characteristics of two-phase voltage discrepancy to provide maneuverable control of the working motor. Twice winding voltages have to need the electrical degree phase shift. Practically, the voltage of the main wing may be in quadrature with that of the auxiliary winding. Both windings are supplied with separate voltages with different amplitudes. In this

This material is reserved for educational use only, not allowed for commercial use.

condition, there is no need for an ac running capacitor. A two-phase full-bridge PWM inverter, as demonstrated in [18] and [19], exploits a H-bridge to supply each winding voltage. Voltages and currents for both windings can be regulated independently. Consequently, two-phase independently controlled variable-frequency variable voltages to the windings of an induction motor can be accomplished. The conventional devices such as centrifugal switches and starting and running capacitors can all be eliminated. These enhance the advantages and reliability of the motor. Another benefit is the reduction of pulsating torque and audible noise effects. Therefore, the accurate control of torque and speed is possible. Field-oriented control has the potential to be implemented with this topology. Due to far more circuit elements, the half-bridge version of this technique as two-phase half-bridge PWM inverter is addressed. Only four power switching devices are utilized. Nevertheless, the voltage across the motor windings would be half of the dc bus voltage, meaning that not only the motor will be activated under half of the rated voltage, but also it is crucial to keep the voltage across the dc bus capacitor balanced. To avoid a voltage step-up transformer, the applied voltage has been attained by voltage-doublers circuit. Consequently, the input rectifying characteristics such as the total harmonic distortion (THD), the power factor (PF) and the ripple factor (RF) are substantially higher [20-21]. To improve the performance of a system, a two-phase PWM inverter with a switched mode rectifier for power factor correction is carried out by adding two anti-parallel power switching devices to the input rectifying diodes and exploiting an appropriate power factor correction circuit. The input rectifying functions, THD, PF and RF, can be improved significantly [16-17, 22]. In this case, it is possible to implement a space vector PWM technique for a two-phase inverter fed symmetrical two-phase induction motor. There are four voltage space vectors and no zero voltage vectors [23]. The two-phase symmetrical modulation to carry out the switching sequence in order to minimize the ripple content of the output current has been realized. Apart from an auxiliary winding of standard permanent split capacitor motors has a higher number of turns than main winding known as an unbalanced two-phase motor, this technique cannot be applied to the commonly existing motor. Thus, this controller would have applications in other areas. The latest topology, two-phase semi full-bridge PWM inverter, is a voltage source inverter with three-leg drive system. This structure is less expensive than the 4-leg VSI and provides better performance in terms of harmonic distortion when compared with that of the 2-leg VSI. Traditionally, the drive comprises a six pack IGBTs module or intelligent power module (IPM) to control a two-phase induction motor. A specially modulating PWM strategy to accomplish a wide range of variable speed operation of a balanced

or unbalanced two winding induction motor is needed [24]. To maximize the use of the dc bus voltage, and simultaneously to reduce the THD of the synthesized voltage, space vector PWM technique for unbalanced two-phase machine is developed [25]. The space vector PWM is made up of eight space voltage vectors, two of the voltage vectors are zero vectors, four voltage vectors are equal, and two of the vectors are unequal. Then, a current controlled hysteresis technique can also be used successfully. Among two-leg, three-leg, and four-leg topologies, the three-leg topology obtains almost the same overall performance like the four-leg topology, and is not costly. Besides, it exhibits lower harmonic distortion than the two-leg topology and avoids the flow of alternative current in the dc bus as well [26-27].

The current trend of an unsymmetrical single-phase induction motor seems to be toward a two-phase drive system. Therefore, when it is necessary to attain a two-phase drive system with enhanced motor performance, the three-leg system is a good trade-off between cost and performances. Nevertheless, because both winding voltages depend on a common inverter branch, the special modulating function of this system has to be produced [28].

1.2 Objectives of the Research

This research work is concerned with the principle of generating PWM patterns for driving inverter fed unsymmetrical type two-phase squirrel cage induction motors using a 3-leg inverter system. To maintain the 90 electrical degree difference of unbalanced type two-winding voltages with variable-voltage variable-frequency 3-leg VSI, the additional modulating function is summed with a balanced voltage function which is a part of the main winding voltage. The natural sampling PWM waveform with which the switching is taking place at the intersection of a sinusoidal target reference waveform and a high frequency carrier is known as sinusoidal pulse width modulation (SPWM). The mathematical solution to the harmonic contents of the proposed PWM strategy is obtained using Double Fourier Integral analysis with time-varying switching and is precisely expressed and interpreted. To achieve a wide range of operation, the fundamental amplitude of the main winding voltage is adjusted in relation with the frequency depending on a rated volt/hertz profile while that of the auxiliary winding voltage is proportional to inverter frequency with constant boost voltage at “ a ” (turns ratio) times. This means that the auxiliary voltage amplitude has to be higher than the main voltage amplitude by a factor equal to the turns ratio. The proposed PWM technique and the two-phase motor model are simulated to predict the

This material is reserved for educational use only, not allowed for commercial use.

Forbidden to modify the content, and cite the document when use.

harmonic voltage characteristics and the machine performance. To verify the validity of the proposed strategy, both simulation and experimental results of 3-leg VSI are compared with those of the conventional 2-leg VSI while the 4-leg VSI is not of interest here because of the increase in cost and switching devices. The results obviously show the improved performance of the proposed method. The proposed modulation technique is appropriate for the drive of the ordinarily asymmetrical two-phase induction machine.

1.3 Structure of the Thesis

This research is focused on the novel modulating strategy for unsymmetrical parameter two-phase induction motor drives using a three-leg voltage source inverter. The goal of this research is to create a new modulation technique for two-phase squirrel cage motors, to develop the motor performance over a wide range of operation, and to verify the validity of the proposed strategy by comparing the simulated results with the experimental results. The outline of this dissertation is as follows:

Chapter 2 describes a comprehensive model, theory, and control method of two-phase squirrel-cage induction motors. Both Double Revolving Field Theory and dynamic motor model with d-q axis analysis are expressed to forecast the steady state motor performance and effect of harmonic voltage contents in PWM signals of drive systems on the motor characteristics. In addition, an unsymmetrical two-phase machine model is demonstrated. To consider the benefit of each drive technique, various topologies are compared based on the number of devices, the size of DC link capacitor, input power factor, range of speed drive, motor performance, drive cost, control complexity, and motor efficiency. Also, switch modes of current flow using the proposed PWM inverter topology are analyzed.

Chapter 3 focuses on a new modulation strategy for an unsymmetrical type two-phase induction motor. A mathematical solution is expressed to the harmonic voltage contents of the proposed PWM strategy to precisely compare with the experimental results. Double Fourier Integral analysis of a two-level Pulse Width Modulating waveform with time-varying switching is also undertaken. This ensures that harmonic components caused by simulation round-off errors or practical implementation impacts such as blanking time, switch ON-state voltages, voltage ripple of dc link voltage, voltage drop in devices, etc., are not confused with intrinsic harmonic differences. The control and power circuit of the drive system are indicated. To prove the

This material is reserved for educational use only, not allowed for commercial use.

Forbidden to modify the content, and cite the document when use.

correctness and capabilities of the implemented circuits, the measured harmonic voltage spectra are compared with the calculated ones.

Chapter 4 deals with the structure of the unsymmetrical two-phase induction motor model. The model of double revolving field theory is used to predict the steady state motor performance, while that of two-phase induction motor analysis in d-q axis is exploited to predict the effect of harmonic voltage contents in PWM signals. All parameters in both models are derived from each type of test method rooted in the standard test method of single-phase induction motor. After that, an extensive investigation is conducted of the motor performance, such as torque-speed characteristics, speed pulsation, motor efficiency, harmonic voltage level, and acoustic noise. Additionally, to prove the accuracy and capabilities of the implemented circuit, the measured results are compared with simulated ones. The proposed 3-leg VSI results and the conventional 2-leg VSI at the same operating conditions are evaluated simultaneously to verify the benefit of the proposed technique.

Chapter 5 presents the conclusions of the work and identifies possibilities for further work.

1.4 Advantages

The new modulating function for an unsymmetrical two-phase induction motor drive proposed here can achieve an unbalanced two-phase voltage source inverter with 90 electrical degree differences under a wide range of operating conditions, especially at low speed. The voltages across the main and the auxiliary windings can be arbitrarily restrained following the control method. During the starting period, the starting torque can be the maximum possible starting torque of the motor, and can also generate good starting torque without excessive inrush current. With the proposed technique, the intrinsic harmonic voltage contents in PWM signals are dramatically decreased. The suggested mathematical equations can precisely interpret the breakdown of harmonic components in PWM voltage source. Therefore, the offered mathematical model can be the specific performance indicator of PWM waveform. The accurate machine equivalent circuit models give enhanced machine prediction and confirm the influence of harmonic voltage stress on motor. The proposed drive technique not only improves the motor performance but also develops the inverter characteristics. The proposed modulation technique can be properly applied to the drive of existing unsymmetrical two-phase induction machines.

This material is reserved for educational use only, not allowed for commercial use.

Forbidden to modify the content, and cite the document when use.

CHAPTER 2

TWO-PHASE INDUCTION MOTOR AND DRIVE TOPOLOGIES

Single-phase induction motors have been widely used in residential and industrial applications. The pure single-phase induction motor has no starting torque [29-34] and it must be started by means of an auxiliary winding which is displaced 90 electrical degrees in space from the main winding. Thus, almost all single-phase motor induction motors are actually two-phase motors. In the case of the capacitor-run motor, the so-called Permanent Split Capacitor Motor (PSCM), the main winding in the q-axis is adapted to carry most of the current in operation, while the auxiliary winding in the d-axis is modified to provide the required starting torque and higher motor performance.

2.1 Double Revolving Field Theory

In the revolving field theory of single-phase motors, the pulsating sinusoidal flux generated by a stator winding is resolved into two equal sinusoidal waves of flux gliding in opposite directions around the periphery of the air-gap at synchronous speed. The influence of these revolving fluxes, as well as the induced forward and backward revolving rotor fluxes, can be represented by a parallel circuit of two branches as indicated in Figure 2.1. One branch is the magnetizing reactance and the other is made up of the rotor leakage reactance in series with the rotor resistance divided by the slip.

Since the main and auxiliary windings are typically quite different, with a different number of turns, wire size and turns distribution, the turns ratio test should be made by Veinott technique [31]. This model assumes that the main and the auxiliary windings are in space quadrature. Then, the simplified equivalent circuit is demonstrated in Figure 2.2. The forward and backward impedances are defined as follows [32]:

Where

\hat{V}_m = main winding voltage

\hat{V}_a = auxiliary winding voltage

This material is reserved for educational use only, not allowed for commercial use.

Forbidden to modify the content, and cite the document when use.

- \hat{I}_m = main winding current
 \hat{I}_a = auxiliary winding current
 i_m = instantaneous current of main winding
 i_a = instantaneous current of auxiliary winding
 \hat{E}_{fm} = forward induced voltage of main winding
 \hat{E}_{fa} = forward induced voltage of auxiliary winding
 \hat{E}_{bm} = backward induced voltage of main winding
 \hat{E}_{ba} = backward induced voltage of auxiliary winding
 P_g = power across air gap
 P_{gf} = power across air gap produced by forward field
 P_{gb} = power across air gap produced by backward field
 a = turns ratio of auxiliary to main windings
 s = slip
 ω_s = synchronous angular frequency (rad/s)
 ϕ = phase angle between the main and the auxiliary winding currents
 ϕ_{fm} = total forward flux directly and indirectly produced by the main winding
 ϕ_{bm} = total backward flux directly and indirectly produced by the main winding
 ϕ_{fa} = total forward flux directly and indirectly produced by the auxiliary winding
 ϕ_{ba} = total backward flux directly and indirectly produced by the auxiliary winding
 T_e = average electromagnetic torque
 T_{pulse} = peak amplitude of pulsating torque
 R_{1m}, X_{1m} = main winding resistance and leakage reactance
 R_{1a}, X_{1a} = auxiliary winding resistance and leakage reactance
 X_m = main winding magnetizing reactance
 R_2, X_2 = rotor resistance and leakage reactance referred to main winding
 $a^2 R_2, a^2 X_2$ = rotor resistance and leakage reactance referred to auxiliary winding
 Z_f, Z_b = forward and backward impedance of main winding
 R_f, X_f = forward resistance and leakage reactance of main winding
 R_b, X_b = backward resistance and leakage reactance of main winding
 $a^2 R_f, a^2 X_f$ = forward resistance and leakage reactance referred to auxiliary winding
 $a^2 R_b, a^2 X_b$ = backward resistance and leakage reactance referred to auxiliary winding

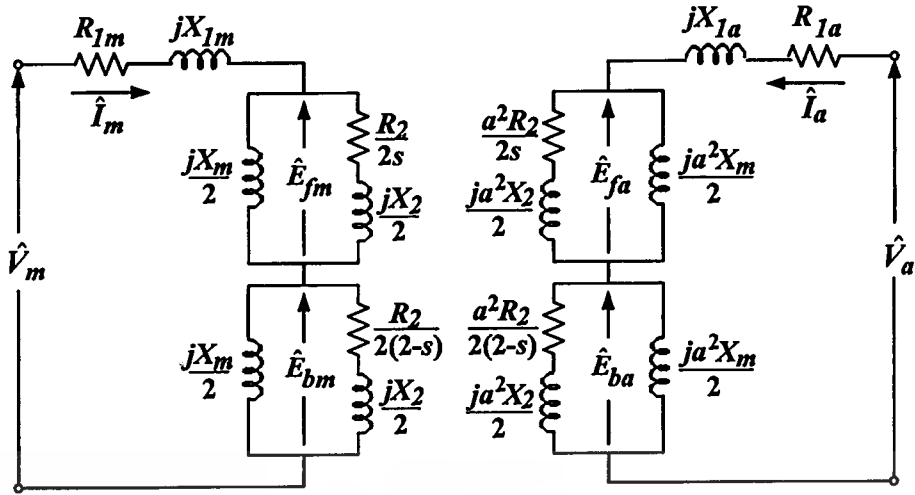


Figure 2.1 Single-phase motor equivalent circuit

$$\begin{aligned}
 Z_f &= R_f + jX_f = \frac{jX_m}{2} \parallel \left(\frac{R_2}{2s} + \frac{jX_2}{2} \right) \\
 &= \frac{\frac{jX_m}{2} \times \left(\frac{R_2}{2s} + \frac{jX_2}{2} \right)}{\frac{R_2}{2s} + j \left(\frac{X_m + X_2}{2} \right)} \\
 &= \frac{-X_2 X_m + \frac{jR_2 X_m}{4s}}{\frac{R_2}{2s} + j \left(\frac{X_m + X_2}{2} \right)} \\
 &= \frac{-X_2 X_m + \frac{jR_2 X_m}{4s}}{\frac{R_2}{2s} + j \left(\frac{X_m + X_2}{2} \right)} \cdot \frac{\frac{R_2}{2s} - j \left(\frac{X_m + X_2}{2} \right)}{\frac{R_2}{2s} - j \left(\frac{X_m + X_2}{2} \right)} \\
 &= \frac{\left[\frac{-R_2 X_2 X_m}{2s} \right] + \left[j \left(\frac{R_2}{s} \right)^2 \frac{X_m}{2} \right] + \left[\frac{jX_2 X_m (X_m + X_2)}{2} \right] + \left[\frac{R_2 X_m (X_m + X_2)}{2s} \right]}{\left(\frac{R_2}{s} \right)^2 - (X_m + X_2)^2} \\
 &= \frac{\left(\frac{R_2 X_m^2}{2s} \right) + j \left[\left(\left(\frac{R_2}{s} \right)^2 \frac{X_m}{2} \right) + \left[\frac{X_2 X_m (X_m + X_2)}{2} \right] \right]}{\left(\frac{R_2}{s} \right)^2 - (X_m + X_2)^2}
 \end{aligned} \tag{2.1}$$

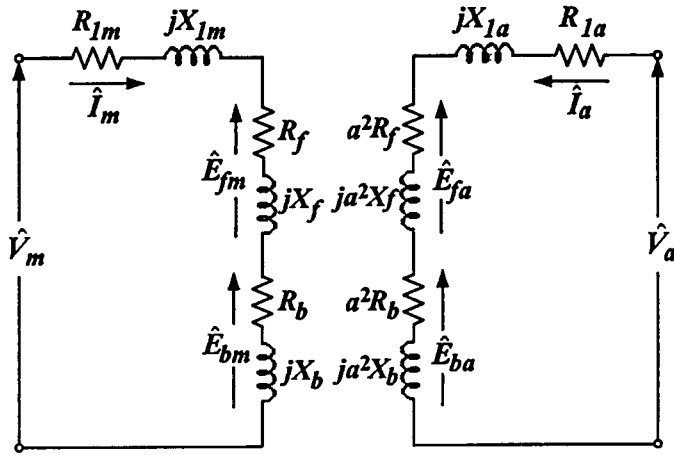


Figure 2.2 Simplified single-phase motor equivalent circuit

$$\begin{aligned}
 Z_b = R_b + jX_b &= \frac{jX_m}{2} \parallel \left(\frac{R_2}{2(2-s)} + \frac{jX_2}{2} \right) \\
 &= \frac{\frac{jX_m}{2} \times \left(\frac{R_2}{2(2-s)} + \frac{jX_2}{2} \right)}{\frac{R_2}{2(2-s)} + j \left(\frac{X_m + X_2}{2} \right)} = \frac{\frac{-X_2 X_m}{4} + \frac{jR_2 X_m}{4(2-s)}}{\frac{R_2}{2(2-s)} + j \left(\frac{X_m + X_2}{2} \right)} \\
 &= \frac{\frac{-X_2 X_m}{4} + \frac{jR_2 X_m}{4(2-s)}}{\frac{R_2}{2(2-s)} + j \left(\frac{X_m + X_2}{2} \right)} \cdot \frac{\frac{R_2}{2(2-s)} - j \left(\frac{X_m + X_2}{2} \right)}{\frac{R_2}{2(2-s)} - j \left(\frac{X_m + X_2}{2} \right)} \\
 &= \frac{\left[\frac{-R_2 X_2 X_m}{2(2-s)} \right] + \left[j \left(\frac{R_2}{(2-s)} \right)^2 \frac{X_m}{2} \right] + \left[\frac{jX_2 X_m (X_m + X_2)}{2} \right] + \left[\frac{R_2 X_m (X_m + X_2)}{2(2-s)} \right]}{\left(\frac{R_2}{(2-s)} \right)^2 - (X_m + X_2)^2} \\
 &= \frac{\left(\frac{R_2 X_m^2}{2(2-s)} \right) + j \left[\left(\frac{R_2}{(2-s)} \right)^2 \frac{X_m}{2} \right] + \left[\frac{X_2 X_m (X_m + X_2)}{2} \right]}{\left(\frac{R_2}{(2-s)} \right)^2 - (X_m + X_2)^2} \tag{2.2}
 \end{aligned}$$

Hence,

This material is reserved for educational use only, not allowed for commercial use.

Forbidden to modify the content, and cite the document when use.

$$R_f = \frac{R_2 X_m^2}{2s} \cdot \frac{1}{\left(\frac{R_2}{s}\right)^2 - (X_m + X_2)^2}, \quad X_f = \frac{X_m}{2} \cdot \frac{\left(\frac{R_2}{s}\right)^2 + X_2(X_m + X_2)}{\left(\frac{R_2}{s}\right)^2 - (X_m + X_2)^2}$$

$$R_b = \frac{R_2 X_m^2}{2(2-s)} \cdot \frac{1}{\left(\frac{R_2}{(2-s)}\right)^2 - (X_m + X_2)^2}, \quad X_b = \frac{X_m}{2} \cdot \frac{\left(\frac{R_2}{(2-s)}\right)^2 + X_2(X_m + X_2)}{\left(\frac{R_2}{(2-s)}\right)^2 - (X_m + X_2)^2}$$
(2.3)

Because both windings existing on the motor are excited simultaneously, their fluxes superimpose with each other without distortion. Since the main winding is displaced forward by 90 electrical degrees from the auxiliary winding, the voltage generated in the main winding by the forward flux of auxiliary winding must lag by 90 degrees the voltage which the same flux produces in the auxiliary winding. Additionally, the turns on the auxiliary winding are “ a ” times those of the main winding. The induced voltage magnitude of the auxiliary winding has to be “ a ” times that of the main winding. Under this condition, the equivalent circuit becomes as shown in Figure 2.3. This model is suggested by Morrill [32] known as the unsymmetrical two-phase motor equivalent circuit. Therefore,

$$\hat{V}_m = \hat{I}_m (R_{1m} + jX_{1m}) + \hat{E}_{fm} - \frac{j\hat{E}_{fa}}{a} + \hat{E}_{bm} + \frac{j\hat{E}_{ba}}{a}$$

$$\hat{V}_a = \hat{I}_a (R_{1a} + jX_{1a}) + \hat{E}_{fa} + ja\hat{E}_{fm} + \hat{E}_{ba} - ja\hat{E}_{bm}$$
(2.4)

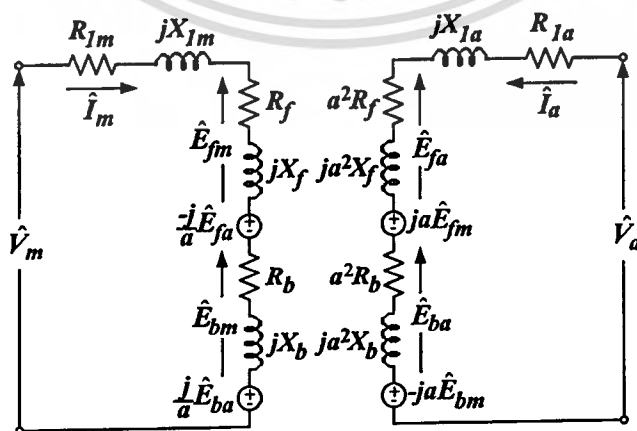


Figure 2.3 Unsymmetrical two-phase motor equivalent circuit

This material is reserved for educational use only, not allowed for commercial use.

Forbidden to modify the content, and cite the document when use.

when

$$\begin{aligned}
 \hat{E}_{fm} &= \hat{I}_m (R_f + jX_f) \\
 \hat{E}_{bm} &= \hat{I}_m (R_b + jX_b) \\
 \hat{E}_{fa} &= \hat{I}_a a^2 (R_f + jX_f) \\
 \hat{E}_{ba} &= \hat{I}_a a^2 (R_b + jX_b)
 \end{aligned} \tag{2.5}$$

Since, the single-phase induction motor composes of both forward and backward fields, motor performances can be reckoned by

$$\begin{aligned}
 P_g &= P_{gf} - P_{gb} = \text{Re} \left[(E_f - E_b) I_m^* + j (E_f - E_b) a I_a^* \right] \\
 &= \left[(R_f - R_b) (I_m^2 + (a I_a^2)) \right] + \left[\text{Re} \left\{ \left(-j \frac{E_{fa}}{a} - j \frac{E_{ba}}{a} \right) I_m^* \right\} \right] \\
 &\quad + \left[\text{Re} \left\{ (j a E_{fm} + j E_{bm}) I_a^* \right\} \right]
 \end{aligned} \tag{2.6}$$

where

$$\begin{aligned}
 \left(-j \frac{E_{fa}}{a} - j \frac{E_{ba}}{a} \right) I_m^* &= -j a \left\{ (R_f + R_b) + j (X_f + X_b) \right\} I_a^* I_m^* \\
 &= \left\{ (X_f + X_b) - j (R_f + R_b) \right\} a I_a^* I_m^*
 \end{aligned} \tag{2.7}$$

and

$$\begin{aligned}
 j a (E_{fm} + E_{bm}) I_a^* &= -j a \left\{ (R_f + R_b) + j (X_f + X_b) \right\} I_a^* I_m^* \\
 &= - \left\{ (X_f + X_b) - j (R_f + R_b) \right\} a I_a^* I_m^*
 \end{aligned} \tag{2.8}$$

The summation of Equations (2.7) and (2.8) is

$$\left(-j \frac{E_{fa}}{a} - j \frac{E_{ba}}{a} \right) I_m^* + j a (E_{fm} + E_{bm}) I_a^* = \left\{ (X_f + X_b) - j (R_f + R_b) \right\} a (I_a^* I_m^* - I_a^* I_m^*) \tag{2.9}$$

This material is reserved for educational use only, not allowed for commercial use.

Forbidden to modify the content, and cite the document when use.

If $I_a = I_a e^{j\theta_a}$ and $I_m = I_m e^{j\theta_m}$, thus

$$\begin{aligned} I_a I_m^* - I_a^* I_m &= I_a I_m \left(e^{j(\theta_a - \theta_m)} - e^{-j(\theta_a - \theta_m)} \right) \\ &= j2I_a I_m \sin(\theta_a - \theta_m) \end{aligned} \quad (2.10)$$

From Equation (2.10), the value of the second and the third terms of Equation (2.6) can be rewritten as follows:

$$\left[\operatorname{Re} \left\{ \left(-j \frac{E_{fa}}{a} - j \frac{E_{ba}}{a} \right) I_m^* \right\} \right] + \left[\operatorname{Re} \left\{ (jaE_{fm} + jE_{bm}) I_a^* \right\} \right] = 2I_a I_m (R_f + R_b) \sin(\theta_a - \theta_m) \quad (2.11)$$

Substituting Equation (2.11) into Equation (2.6), power across air gap can be defined by:

$$P_g = \left[(R_f - R_b) \left(I_m^2 + (aI_a^2) \right) \right] + 2I_a I_m (R_f + R_b) \sin(\theta_a - \theta_m) \quad (2.12)$$

The output power of the motor can be calculated by:

$$P_{out} = (1-s)P_g - \text{losses} \quad (2.13)$$

The “losses” in Equation (2.13) comprise core loss and rotational loss. The output torque of the motor is

$$T_{out} = \frac{P_{out}}{\omega_r} \quad (2.14)$$

Owing to the total flux is equal to the sum of the fluxes produced by both windings. The total stator current is identical to the addition of the input current of each phase. Torque of an unsymmetrical two-phase motor (T) can be expressed by:

$$T = (\phi_{fm} + \phi_{bm} + \phi_{fa} + \phi_{ba})(i_m + i_a) \quad (2.15)$$

In order to better understand and more easily analyze an unsymmetrical two-phase motor torque, Equation (2.15) is derived and is given by [8]:

$$T = \frac{1}{\omega_s} \left\{ \begin{aligned} & \left[I_m^2 \{ (R_f - R_b) + (R_f - R_b) \cos 2\omega t - (X_f - X_b) \sin 2\omega t \} \right] \\ & + \left[a^2 I_a^2 \{ (R_f - R_b) + (R_f - R_b) \cos 2(\phi + \omega t) - (X_f - X_b) \sin 2(\phi + \omega t) \} \right] \\ & + \left[2aI_m I_a (R_f + R_b) \sin \phi \right] \end{aligned} \right\} \quad (2.16)$$

Equation (2.16) is known as the “general equation for the torque of an unsymmetrical two-phase motor”. It will be noticed that some of the torque components are constant while others vary sinusoidally with the time at twice the supply frequency. Double-stator-frequency torque pulsations are produced by the interactions of the oppositely rotating flux and mmf waves which glide past each other at twice the synchronous speed. Over a period of time corresponding to any number of complete cycles of the line voltage, the alternating torque is integrated to zero and the average electromagnetic torque is:

$$T_e = \frac{1}{\omega_s} \left\{ \left[(I_m^2 + (aI_a)^2) \cdot (R_f - R_b) \right] + \left[2aI_m I_a (R_f + R_b) \sin \phi \right] \right\} \quad (2.17)$$

and the pulsating torque is:

$$T_{puls} = \frac{1}{\omega_s} \left\{ \left[I_m^4 + (aI_a)^4 + 2(aI_m I_a)^2 \cos 2\phi \right] \cdot \left[(R_f - R_b)^2 + (X_f - X_b)^2 \right] \right\}^{\frac{1}{2}} \quad (2.18)$$

From Equation (2.17), it can be seen that the maximum average torque will be present when $\phi = 90^\circ$. Simultaneously, the value of $\cos 2\phi$ in Equation (2.18) is -1. The undesirable pulsating torque as described in Equation (2.18) can also be eliminated at any motor slips at $\phi = 90^\circ$. If

$$I_m^4 + (aI_a)^4 - 2(aI_m I_a)^2 = 0 \quad (2.19)$$

thus,

$$\left(\frac{I_m}{aI_a} \right)^2 + \left(\frac{aI_a}{I_m} \right)^2 = 2 \quad (2.20)$$

giving

$$I_m = aI_a \quad (2.21)$$

This material is reserved for educational use only, not allowed for commercial use.

Forbidden to modify the content, and cite the document when use.

Equation (2.21) demonstrates that the relative amplitude of the winding currents should be the inverse of the winding turns ratio. In order to achieve the relationship between both currents, the voltage ratio is approximately equal to

$$V_a = a.V_m \quad (2.22)$$

From the equivalent circuit analysis, it is noticed that the total field is the resultant of the rotating field, while the resultant field is pulsating and the component fields are steady. This may affect the calculation of iron loss in the motor. Under these conditions, the voltage across the forward rotor is significantly higher than that across the backward rotor, and hence most of the iron loss takes place in the forward field. This causes the computed iron loss to be greater. Because the copper loss in the backward rotor is $I_{2b}^2 R_2$ and the input power is approximately $\frac{I_{2b}^2 R_2}{(2-s)}$, therefore, the power input to the backward rotor is less than its copper loss. The difference must be supplied mechanically through the shaft. Since the total field actually pulsates, the torque also pulsates. The pulsation increases with the slip. The rotating field and the maximum torque decrease with the slip.

To better understand the theory and operation of two-phase induction motor, it is necessary to study the nature of the magneto motive force (mmf) wave produced by a two-phase winding. As derived in [33], the mmf of any closed path in a magnetic circuit is defined by $\mathfrak{F} = Ni = \oint H \cdot dl$. The usefulness of the concept of mmf stems from the fact that, in well-defined magnetic circuits, mmf can be associated with various portions of a path in such a fashion that it is related by some simple geometric coefficient to the magnetic field intensity which exists over that portion of the path.

In the design of ac machines, serious efforts are made to distribute the winding so as to produce a close approximation to a sinusoidal space distribution of mmf. The fundamental component \mathfrak{F}_1 resolved by Fourier series [33] is

$$\mathfrak{F}_1 = \frac{4 Ni}{\pi} \cos \theta \quad (2.23)$$

where θ is measured from the magnetic axis of the stator coil. For a distributed P-pole winding having N_{ph} series turns per phase, the modified \mathfrak{F}_1 is given by:

$$\mathfrak{F}_1 = \frac{4}{\pi} k_w \frac{N_{ph}}{P} i_a \cos \theta \quad (2.24)$$

in which the factor $\frac{4}{\pi}$ arises from the Fourier-series analysis of the saw tooth mmf wave of a concentrated full-pitch coil, and the winding factor k_w takes into account the distribution factor (k_d) and pitch factor (k_p) of the winding ($k_w = k_d k_p$). The factor $k_w N_{ph}$ is the effective series turns per phase for the fundamental mmf. Accordingly, if the current $i_a = I_{\max} \cos \omega t$, the time maximum of the peak is expressed by:

$$F_{\max} = \frac{4}{\pi} k_w \frac{N_{ph}}{P} I_{\max} \quad (2.25)$$

Thus:

$$\mathfrak{F}_1 = F_{\max} \cos \theta \cos \omega t \quad (2.26)$$

For two-phase machines, both windings are displaced 90 electrical degrees in space. The main winding i_m is excited by a sinusoidally varying current in time and is $i_m = I_{\max} \cos \omega t$ while the auxiliary winding i_a is supplied by a sinusoidally varying current in time with 90 electrical degree phase shift. That is $i_a = I_{\max} \cos(\omega t - 90^\circ)$. Where the effective current of the main winding is the same as that of the auxiliary winding, the fundamental mmf of the main winding \mathfrak{F}_{main} is defined by:

$$\mathfrak{F}_{main} = F_{\max} \cos \theta \cos \omega t = \frac{1}{2} F_{\max} \cos(\theta - \omega t) + \frac{1}{2} F_{\max} \cos(\theta + \omega t) \quad (2.27)$$

and the fundamental mmf of the auxiliary winding \mathfrak{F}_{aux} is given by:

$$\begin{aligned} \mathfrak{F}_{aux} &= F_{\max} \cos(\theta - 90^\circ) \cos(\omega t - 90^\circ) \\ &= \frac{1}{2} F_{\max} \cos(\theta - \omega t) + \frac{1}{2} F_{\max} \cos(\theta + \omega t - 180^\circ) \\ &= \frac{1}{2} F_{\max} \cos(\theta - \omega t) - \frac{1}{2} F_{\max} \cos(\theta + \omega t) \end{aligned} \quad (2.28)$$

Therefore, the resultant mmf $\mathfrak{F}_{2\phi}$ can be computed as follows:

This material is reserved for educational use only, not allowed for commercial use.

Forbidden to modify the content, and cite the document when use.

$$\mathfrak{F}_{2\phi} = \mathfrak{F}_{main} + \mathfrak{F}_{aux} = F_{max} \cos(\theta - \omega t) \quad (2.29)$$

The result of displacing the two windings by 90° in space phase and displacing the winding currents by 90° in time phase with compensating current of the auxiliary winding by “ a ” times comprises only single positive-traveling wave. The wave has constant amplitude and space-phase angle ωt which is a linear function of time. These correspond to Equations (2.17) and (2.18) that when $I_m = I_a \angle 90^\circ$, there is either no backward field, resulting in no torque pulsation, or the constant peak magnitude of mmf wave, resulting in the maximum torque operating condition.

2.2 Unsymmetrical Two-phase Induction Machines in D-Q Axis

For a Permanent Split Capacitor Motor (PSCM) or single-phase capacitor run motor, the main and auxiliary stator windings are already aligned with the orthogonal axes. Twice stator windings are in the axes as indicated in Figure 2.4. If the coil sides of both main and auxiliary windings do not occupy the same slots, leakage fluxes coupling between them will be negligible. The cage rotor may be represented by a pair of equivalent qd symmetrical rotor windings [34].

Where

- v_{qs} = stator main winding instantaneous voltage
- v_{ds} = stator auxiliary winding instantaneous voltage
- v_{qr} = instantaneous voltage across rotor winding in q -axis
- v_{dr} = instantaneous voltage across rotor winding in d -axis
- i_{qs} = instantaneous current of stator main winding
- i_{ds} = instantaneous current of stator auxiliary winding
- i_{qr} = instantaneous current of rotor winding in q -axis
- i_{dr} = instantaneous current of rotor winding in d -axis
- λ_{qs} = flux linkage of stator main winding
- λ_{ds} = flux linkage of stator auxiliary winding
- λ_{qr} = flux linkage of rotor winding in q -axis
- λ_{dr} = flux linkage of rotor winding in d -axis
- ψ_{qs} = flux linkage per second with the units of volts of stator main winding
- ψ_{ds} = flux linkage per second with the units of volts of stator auxiliary winding

- Ψ_{qr} = flux linkage per second with the units of volts of rotor winding in q -axis
 Ψ_{dr} = flux linkage per second with the units of volts of rotor winding in d -axis
 Ψ_{mq} = flux linkage per second with the units of volts of magnetization in q -axis
 Ψ_{md} = flux linkage per second with the units of volts of magnetization in d -axis
 r_{qs} = resistance of stator main winding
 r_{ds} = resistance of stator auxiliary winding
 r_{qr} = resistance of rotor winding in q -axis
 r_{dr} = resistance of rotor winding in d -axis
 N_{qs} = stator main winding turns number
 N_{ds} = stator auxiliary winding turns number
 N_{qr} = rotor winding turns number in q -axis
 N_{dr} = rotor winding turns number in d -axis
 L_{qsqs} = self inductance of stator main winding
 L_{dsds} = self inductance of stator auxiliary winding
 L_{qrqr} = self inductance of rotor winding in q -axis
 L_{drdr} = self inductance of rotor winding in d -axis
 L_{mq} = magnetizing inductance for the main winding
 L_{md} = magnetizing inductance for the auxiliary winding
 X_{lqs} = leakage reactance of stator main winding
 X_{lds} = leakage reactance of stator auxiliary winding
 X_{lr} = leakage reactance of rotor winding
 X_{mq} = magnetizing reactance for the main winding
 X_{md} = magnetizing reactance for the auxiliary winding
 X_{Mq} = total reactance for the main winding
 X_{Md} = total reactance for the auxiliary winding
 \mathfrak{R}_g = reluctance of air gap
 T_{em} = electromagnetic torque
 T_{mech} = mechanical torque
 T_{damp} = damping torque

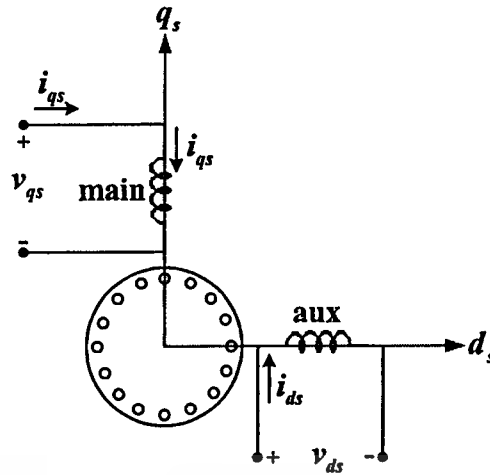


Figure 2.4 Unsymmetrical two-phase induction machine

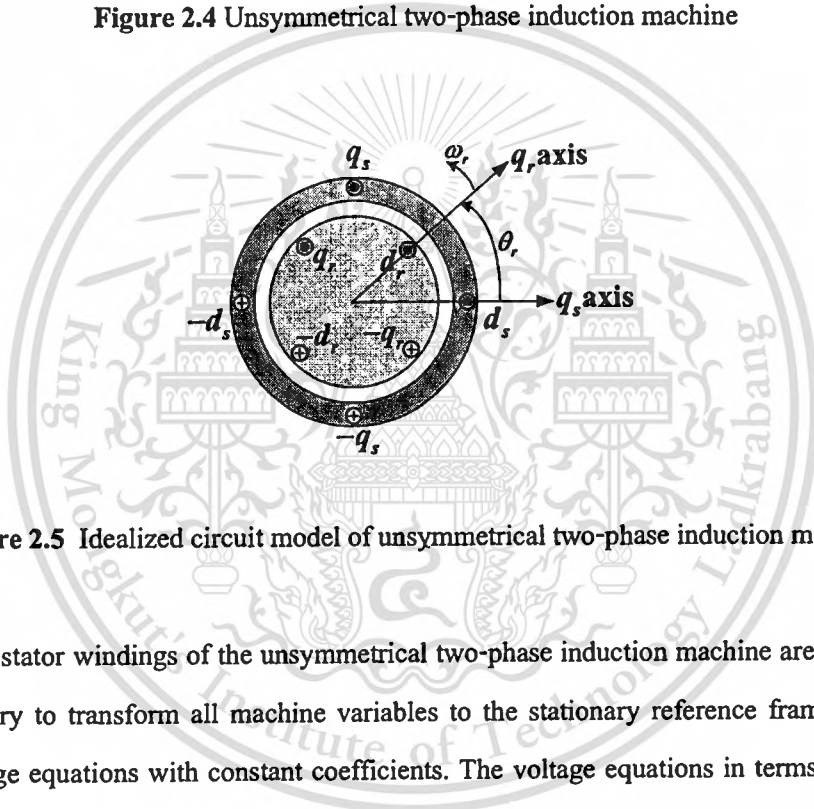


Figure 2.5 Idealized circuit model of unsymmetrical two-phase induction machine

Because the stator windings of the unsymmetrical two-phase induction machine are not identical, it is necessary to transform all machine variables to the stationary reference frame in order to obtain voltage equations with constant coefficients. The voltage equations in terms of stationary reference-frame variable (i.e. $\omega = 0$) of the magnetically coupled stator and rotor circuits shown in Figure 2.5 can be written as follows :

$$\begin{aligned}
 v_{qs} &= i_{qs} r_{qs} + \frac{d\lambda_{qs}}{dt}, & v_{ds} &= i_{ds} r_{ds} + \frac{d\lambda_{ds}}{dt} \\
 v_{qr} &= i_{qr} r_{qr} + \frac{d\lambda_{qr}}{dt}, & v_{dr} &= i_{dr} r_{dr} + \frac{d\lambda_{dr}}{dt}
 \end{aligned}
 \tag{2.30}$$

The flux linkages of the stator and rotor windings can be written compactly in terms of the winding inductances and currents as

This material is reserved for educational use only, not allowed for commercial use.

Forbidden to modify the content, and cite the document when use.

$$\begin{bmatrix} \lambda_{qs} \\ \lambda_{ds} \\ \lambda_{qr} \\ \lambda_{dr} \end{bmatrix} = \begin{bmatrix} L_{qsqs} & 0 & L_{qsqr} \cos \theta_r & L_{qsdr} \sin \theta_r \\ 0 & L_{dsds} & -L_{dsqr} \sin \theta_r & L_{dsdr} \cos \theta_r \\ L_{qrqs} \cos \theta_r & -L_{qrds} \sin \theta_r & L_{qrqr} & 0 \\ L_{drqs} \sin \theta_r & L_{drds} \cos \theta_r & 0 & L_{drdr} \end{bmatrix} \begin{bmatrix} i_{qs} \\ i_{ds} \\ i_{qr} \\ i_{dr} \end{bmatrix} \quad (2.31)$$

If the reluctance drops in iron are neglected and the reluctance of the uniform air-gap is \mathfrak{R}_g , the winding inductances may be expressed in terms of their effective turns, N_{qs} , N_{ds} , N_{qr} , and N_{dr} as

$$\begin{aligned} L_{qsqs} &= L_{lqs} + \frac{N_{qs}^2}{\mathfrak{R}_g} & L_{dsds} &= L_{lds} + \frac{N_{ds}^2}{\mathfrak{R}_g} \\ L_{qsqr} &= \frac{N_{qs} N_{qr}}{\mathfrak{R}_g} & L_{qsdr} &= \frac{N_{qs} N_{dr}}{\mathfrak{R}_g} \\ L_{dsqr} &= \frac{N_{ds} N_{qr}}{\mathfrak{R}_g} & L_{dsdr} &= \frac{N_{ds} N_{dr}}{\mathfrak{R}_g} \\ L_{qrqr} &= L_{lqr} + \frac{N_{qr}^2}{\mathfrak{R}_g} & L_{drdr} &= L_{ldr} + \frac{N_{dr}^2}{\mathfrak{R}_g} \end{aligned} \quad (2.32)$$

where L_{lqs} , L_{lds} , L_{lqr} , and L_{ldr} are the leakage inductances of the stator and rotor windings. For a symmetrical cage rotor $N_{qr} = N_{dr}$ and $L_{lqr} = L_{ldr}$; henceforward they will be denoted by N_r and L_{lr} , respectively.

Choosing the qd reference frame on the unsymmetrical stator, such that its q -axis is aligned with the axis of the qs winding and its d -axis with that of the ds winding, the rotor qd windings may be transformed to the chosen qd stationary reference using

$$\begin{bmatrix} f_{qr}^s \\ f_{dr}^s \end{bmatrix} = \underbrace{\begin{bmatrix} \cos \theta_r & \sin \theta_r \\ -\sin \theta_r & \cos \theta_r \end{bmatrix}}_{T_{qd}(\theta_r)} \begin{bmatrix} f_{qr}^r \\ f_{dr}^r \end{bmatrix} \quad (2.33)$$

where the variable f can be the phase voltages, currents, or flux linkages of the qr and dr windings, and θ_r is the angle between the axes of the qr and qs windings, measured from the stationary qs axis. The inverse of $[T_{qd}(\theta_r)]$ is

This material is reserved for educational use only, not allowed for commercial use.

Forbidden to modify the content, and cite the document when use.

$$[T_{qd}(\theta_r)]^{-1} = \begin{bmatrix} \cos \theta_r & -\sin \theta_r \\ \sin \theta_r & \cos \theta_r \end{bmatrix} \quad (2.34)$$

Besides the above rotational transformation to be applied to the variables of the rotating qr and dr windings,

$$\begin{aligned} \lambda_{qs} &= L_{lqs} i_{qs} + L_{mq} (i_{qs} + i_{qr}^{is}) \\ \lambda'_{ds} &= L'_{lds} i'_{ds} + L_{mq} (i'_{ds} + i_{dr}^{is}) \\ \lambda_{qr}^{is} &= L'_{lr} i_{qr}^{is} + L_{mq} (i_{qs} + i_{qr}^{is}) \\ \lambda_{dr}^{is} &= L'_{lr} i_{dr}^{is} + L_{mq} (i_{ds} + i_{dr}^{is}) \end{aligned} \quad (2.35)$$

The voltage equations of the qs and ds stator windings may be expressed in terms of the transformed and referred quantities as

$$\begin{aligned} v_{qs} &= i_{qs} r_{qs} + \frac{d\lambda_{qs}}{dt} \\ v'_{ds} &= i'_{ds} r'_{ds} + \frac{d\lambda'_{ds}}{dt} \end{aligned} \quad (2.36)$$

Applying the transformation, $[T_{qd}(\theta_r)]$, to the voltages, currents, and flux linkages of the qr and dr voltage equations, then

$$\begin{bmatrix} v_{qr}^s \\ v_{dr}^s \end{bmatrix} = [T_{qd}(\theta_r)] \begin{bmatrix} r_r & 0 \\ 0 & r_r \end{bmatrix} [T_{qd}(\theta_r)]^{-1} \begin{bmatrix} i_{qr}^s \\ i_{dr}^s \end{bmatrix} + [T_{qd}(\theta_r)] \frac{d[T_{qd}(\theta_r)]^{-1}}{dt} \begin{bmatrix} \lambda_{qr}^s \\ \lambda_{dr}^s \end{bmatrix} \quad (2.37)$$

It can be shown that

$$\frac{d[T_{qd}(\theta_r)]^{-1}}{dt} \begin{bmatrix} \lambda_{qr}^s \\ \lambda_{dr}^s \end{bmatrix} = \begin{bmatrix} -\sin \theta_r & \cos \theta_r \\ -\cos \theta_r & \sin \theta_r \end{bmatrix} \begin{bmatrix} \lambda_{qr}^s \frac{d\theta_r}{dt} \\ \lambda_{dr}^s \frac{d\theta_r}{dt} \end{bmatrix} + [T_{qd}(\theta_r)]^{-1} \begin{bmatrix} \frac{d\lambda_{qr}^s}{dt} \\ \frac{d\lambda_{dr}^s}{dt} \end{bmatrix} \quad (2.38)$$

Substituting Equation (2.38) in Equation (2.37), the simplified voltage equations of the qr and dr windings are expressed in terms of the transformed and referred quantities as

$$\begin{aligned} v_{qr}'s &= i_{qr}'s r_r' - \lambda_{dr}'s \frac{d\theta_r}{dt} + \frac{d\lambda_{qr}'s}{dt} \\ v_{dr}'s &= i_{dr}'s r_r' - \lambda_{qr}'s \frac{d\theta_r}{dt} + \frac{d\lambda_{dr}'s}{dt} \end{aligned} \quad (2.39)$$

$$\begin{aligned} v_{ds}' &= \frac{N_{qs}}{N_{ds}} v_{ds} & i_{ds}' &= \frac{N_{ds}}{N_{qs}} i_{ds} \\ L_{mq}' &= \frac{N_{qs}^2}{\mathfrak{R}_g} & L_{md}' &= \left(\frac{N_{qs}}{N_{ds}} \right)^2 \frac{N_{ds}^2}{\mathfrak{R}_g} \\ L_{lds}' &= \left(\frac{N_{qs}}{N_{ds}} \right)^2 L_{lds} & r_{ds}' &= \left(\frac{N_{qs}}{N_{ds}} \right)^2 r_{ds} \\ L_{lr}' &= \left(\frac{N_{qs}}{N_r} \right)^2 L_{lr} & r_r' &= \left(\frac{N_{qs}}{N_r} \right)^2 r_r \\ v_{qr}'s &= \frac{N_{qs}}{N_r} v_{qr}^s & v_{dr}'s &= \frac{N_{qs}}{N_r} v_{dr}^s \\ i_{qr}'s &= \frac{N_r}{N_{qs}} i_{qr}^s & i_{dr}'s &= \frac{N_r}{N_{qs}} i_{dr}^s \\ \lambda_{qr}'s &= \frac{N_{qs}}{N_r} \lambda_{qr}^s & \lambda_{dr}'s &= \frac{N_{qs}}{N_r} \lambda_{dr}^s \end{aligned} \quad (2.40)$$

The equivalent circuit of the unsymmetrical two-phase machine in qd reference frame is demonstrated in Figure 2.6 [37]. Variables and parameters in the figure are referred to the main qs winding following Equation (2.40). The sum of instantaneous input power to all four windings of stator and rotor may be expressed as

$$P_{in} = v_{qs} i_{qs} + v_{ds}' i_{ds}' + v_{qr}'s i_{qr}'s + v_{dr}'s i_{dr}'s \quad (2.41)$$

Substituting Equations (2.36) and (2.39) in Equation (2.41), as well as eliminating terms associated with copper losses and the rate of change of magnetic field energy, the instantaneous electromagnetic torque may be indicated as

This material is reserved for educational use only, not allowed for commercial use.

Forbidden to modify the content, and cite the document when use.

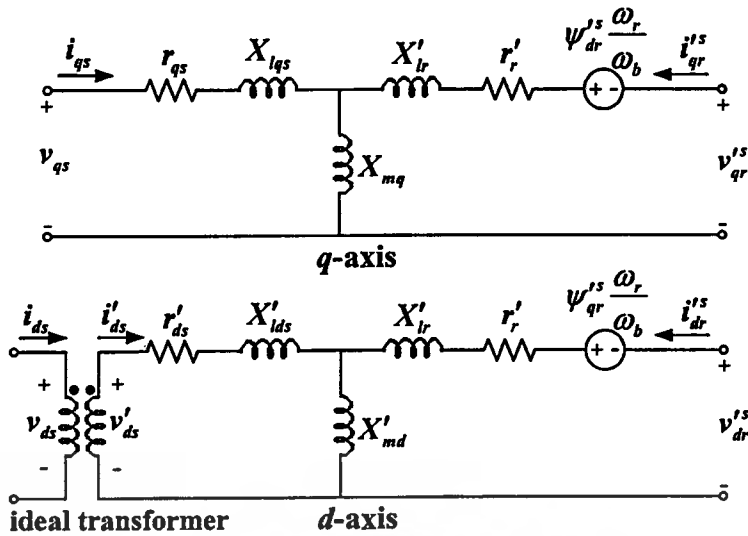


Figure 2.6 Equivalent circuit of an unsymmetrical two-phase induction machine

$$T_{em} \frac{d\theta_{rm}}{dt} = (\lambda_{qr}^{is;is} - \lambda_{dr}^{is;is}) \frac{d\theta_r}{dt} \quad (2.42)$$

Since $\frac{d\theta_{rm}}{dt} = \frac{2}{P} \frac{d\theta_r}{dt}$, the developed torque becomes

$$\begin{aligned} T_{em} &= \frac{P}{2} (\lambda_{qr}^{is;is} - \lambda_{dr}^{is;is}) \\ &= \frac{P}{2} L_{mq} (i_{dr}^{is} i_{qs} - i_{qr}^{is} i_{ds}) \end{aligned} \quad (2.43)$$

Using flux linkage per second (ψ) for $\omega_b \lambda$ and also reactance X for $\omega_b L$, when $\omega_b = 2\pi f_{rated}$ and $\omega_{bm} = \frac{2\omega_b}{P}$, the equations of two-phase motor in the simulation are rearranged as Equations (2.44)-(2.50) for voltage and flux equations, and Equations (2.51)-(2.53) for electromagnetic torque and rotor motion equations.

$$\begin{aligned} \psi_{qs} &= \omega_b \int \left\{ v_{qs} + \frac{r_{qs}}{X_{lqs}} (\psi_{mq} - \psi_{qs}) \right\} dt \quad (2.44) \\ \psi'_{ds} &= \omega_b \int \left\{ v'_{ds} + \frac{r'_{ds}}{X'_{lds}} (\psi'_{md} - \psi'_{ds}) \right\} dt \end{aligned}$$

$$\psi_{qr}^{is} = \omega_b \int \left\{ v_{qr}^{is} + \frac{\omega_r}{\omega_b} \psi_{dr}^{is} + \frac{r_r'}{X_{lr}'} (\psi_{mq} - \psi_{qr}^{is}) \right\} dt \quad (2.45)$$

$$\psi_{dr}^{is} = \omega_b \int \left\{ v_{dr}^{is} + \frac{\omega_r}{\omega_b} \psi_{qr}^{is} + \frac{r_r'}{X_{lr}'} (\psi_{md}' - \psi_{dr}^{is}) \right\} dt$$

$$\psi_{mq} = X_{mq} (i_{qs} + i_{qr}^{is}) \quad (2.46)$$

$$\psi_{md}' = X_{mq} (i_{ds}' + i_{dr}^{is})$$

$$\psi_{qs} = X_{lqs} i_{qs} + \psi_{mq}$$

$$\psi_{ds}' = X_{lds}' i_{ds}' + \psi_{md}' \quad (2.47)$$

$$\psi_{qr}^{is} = X_{lr}' i_{qr}^{is} + \psi_{mq}$$

$$\psi_{dr}^{is} = X_{lr}' i_{dr}^{is} + \psi_{md}'$$

$$i_{qs} = \frac{\psi_{qs} - \psi_{mq}}{X_{lqs}}$$

$$i_{ds}' = \frac{\psi_{ds}' - \psi_{md}'}{X_{lds}'}$$

$$i_{qr}^{is} = \frac{\psi_{qr}^{is} - \psi_{mq}}{X_{lr}'}$$

$$i_{dr}^{is} = \frac{\psi_{dr}^{is} - \psi_{md}'}{X_{lr}'}$$

(2.48)

where

$$\frac{1}{X_{Mq}} = \frac{1}{X_{mq}} + \frac{1}{X_{lqs}} + \frac{1}{X_{lr}'} \quad (2.49)$$

$$\frac{1}{X_{Md}} = \frac{1}{X_{md}} + \frac{1}{X_{lds}'} + \frac{1}{X_{lr}'}$$

and

$$\psi_{mq} = X_{Mq} \left(\frac{\psi_{qs}}{X_{lqs}} + \frac{\psi_{qr}^{is}}{X_{lr}'} \right) \quad (2.50)$$

$$\psi_{md}' = X_{Md} \left(\frac{\psi_{ds}'}{X_{lds}'} + \frac{\psi_{dr}^{is}}{X_{lr}'} \right)$$

$$T_{em} = \frac{P}{2\omega_b} (\psi'_{ds} i'_{qs} - \psi_{qs} i'_{ds}) \quad N-m \quad (2.51)$$

$$J \frac{d\omega_{rm}}{dt} = T_{em} + T_{mech} - T_{damp} \quad N-m \quad (2.52)$$

$$2H \frac{d(\omega_r/\omega_b)}{dt} = T_{em} + T_{mech} - T_{damp} \quad \text{in per unit} \quad (2.53)$$

Let the variable $H = \frac{J\omega_{bm}^2}{2S_b}$ and S_b is base apparent power.

2.3 Principle of Operation and Control Method

From Equations (2.17)-(2.29), the optimum control method to operate an unsymmetrical two-phase motor under variable frequency control is a hold of both winding voltages in quadrature with a ratio “ a ” of the main winding to the auxiliary winding voltages. This methodology limits the backward field as low as possible. Many papers [7, 18-19, 24, 35-36] have proved better performance of this method. To more easily understand the control method, the inverter frequencies are plotted against the fundamental output voltage of the auxiliary winding V_{D1} and of the main winding V_{Q1} , represented in Figure 2.7 as solid and dashed lines, respectively. While the fundamental frequency (f) varies up to the rated value, volt/hertz of the main winding, which can be calculated by Faraday’s law, is kept constant at a nominal value (i.e. $\frac{V}{f} = 4.44N\phi$). The fundamental amplitude of the auxiliary winding voltage is proportional to inverter frequencies with a boost voltage level at “ a ” times V/Hz of the main winding in the frequency range of $0 < f < \frac{f_{rated}}{a}$. When the inverter frequency reaches $\frac{f_{rated}}{a}$, the auxiliary winding voltage will be maintained constant at a rated value for the reason of preventing machine saturation in the frequency range of $\frac{f_{rated}}{a} \leq f \leq f_{rated}$. This makes the motor under constant torque control mode. Also, the resultant air-gap flux is nearly circular.

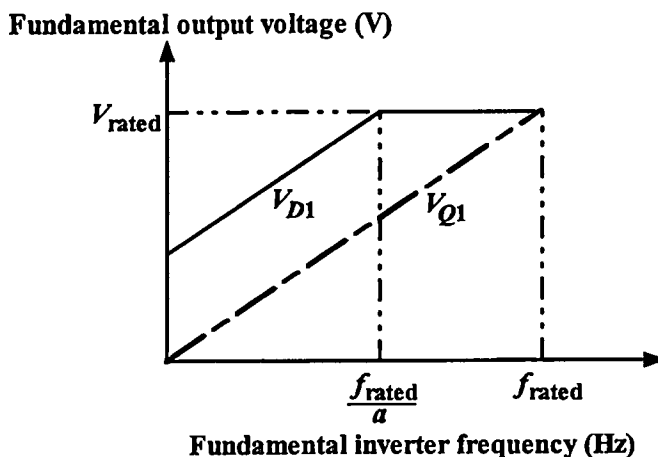


Figure 2.7 The relationship between fundamental inverter frequency and output voltage for each winding

2.4 Motor Drive Systems

The adjustable speed single-phase cage motor controllers have been made in different types [1-19, 22-27, 29-30, 35-36, 39-62]. Generally, there are two different alternatives to implement an adjustable-speed single-phase motor drive system. The first one is a single-phase drive in which the single-phase motor is treated as a single-phase mode. The second one is a two-phase drive in which the single-phase motor is considered as a two-phase induction motor. There are many kinds of variable-voltage variable-frequency control techniques [38]. Only the main alternatives appear to have been reported to employ variable frequency converters to achieve continuous variable speed single-phase motor operation.

The first approach of the single-phase drive is a single-phase converter. Output voltage of the drive is only applied to the auxiliary winding, while the main winding remains connected to the ac supply [9]. This drive configuration is indicated in Figure 2.8. This technique can achieve variable speed operation although it is at the expense of motor derating and torque ripple. In addition, excessive heating of the motor occurs during low speed operation. Variable speed control, using single phase ac-to-ac chopper, has been obtained through voltage control utilizing triacs or back to back thyristors as illustrated in Figure 2.9 [10]. However, harmonic distortion in the line current is significant when this control is implemented. The technique provides low input power factor. This also suffers significantly from large harmonic injection into the source. To minimize the harmonic injection, ac-to-ac chopper with four switching devices as shown in Figure 2.10 and 2.11 have been proposed [11-12]. In these drive topologies; there is no need for

This material is reserved for educational use only, not allowed for commercial use.

Forbidden to modify the content, and cite the document when use.

costly dc bus capacitors. Harmonic distortion can be reduced by the bridge circuit with controlled turn-off capability in Figure 2.11. The motor performance and input power factor can be enhanced by implementing various PWM strategies. Nevertheless, the speed variation will be over a limited range. This technique is extended to be single-phase ac-to-ac cycloconverter as demonstrated in Figure 2.12 [13-15]. In this case, the motor torque and current can be controlled in a much better manner. This scheme also allows a medium speed range that would not be otherwise practical. Moreover, the total harmonic distortion is quite significant and the motor current has a considerable discontinuity. The configuration presented in Figure 2.13 is a single-phase full-bridge PWM inverter drive which comprises a full bridge diode rectifier plus a full bridge IGBTs base. A dc link capacitor is required to supply the reactive power needed by the motor. The circuit topology in Figure 2.14 seems similar to that given in Figure 2.13. Nevertheless, a half-bridge rectifier is used. By this case, it is possible to achieve reduced torque and speed pulsations, lower vibrations and less acoustic noise. Then, the controlled rectifier with full-bridge PWM inverter is taken into account. The inverter topology is demonstrated in Figure 2.15 [7]. This technique yields more advantages than the previous topologies because two extra IGBTs are used to control the current of utility supply as an active rectifier. The front-end controlled rectifier can be employed to limit the total harmonic distortion, resulting in the increment of utility power factor. The drive system has a wide speed range in both directions, specifically forward and reverse, and also has very high input power factor for all operating conditions. The most compromised cost of single-phase drive system is a half-bridge rectifier with a half-bridge PWM inverter as shown in Figure 2.16 [53]. This inverter is made up of only two power switching devices and two diodes. The last type of single-phase drive topology is single-phase half-bridge PWM inverter with a controlled half-bridge rectifier. This drive system is an extension of the previous case as illustrated in Figure 2.17. The half-bridge controlled rectifier (Q_1 and Q_2) is needed to regulate the voltage across the motor terminals. By single-phase PWM inverter with either a half-bridge rectifier or controlled half-bridge rectifier topologies, the motor has to overcome the problem of maintaining the dc bus mid-point balanced.

In case of two-phase drive system, if the voltage across the main winding is in quadrature with that across the auxiliary winding, an ac running capacitor in series with the auxiliary winding is not needed. The first topology of two-phase drive system is two-phase full-bridge PWM inverter as indicated in Figure 2.18. A H-bridge is exploited to supply each winding. Voltage or current for both windings can be governed independently. As a result, the accurate control of

This material is reserved for educational use only, not allowed for commercial use.

Forbidden to modify the content, and cite the document when use.

torque and speed is possible. This topology has the potential to be implemented with the field-oriented control.

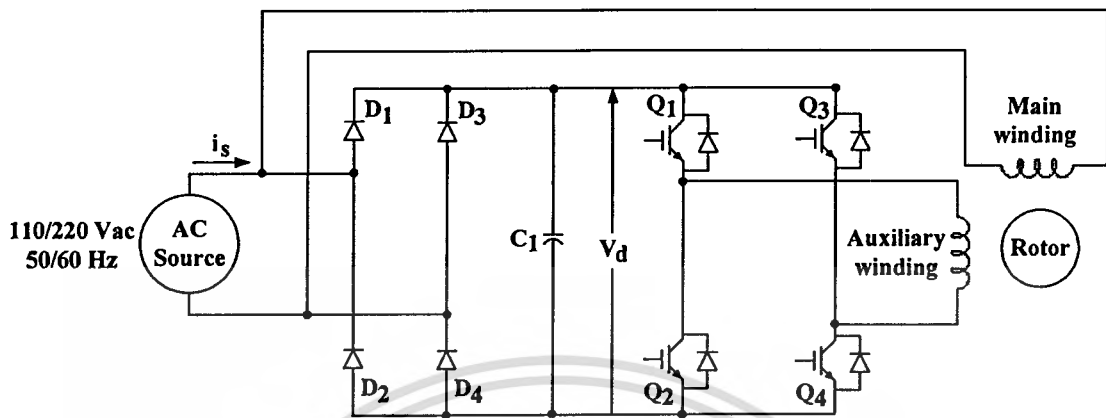


Figure 2.8 Single-phase induction motor with auxiliary winding control

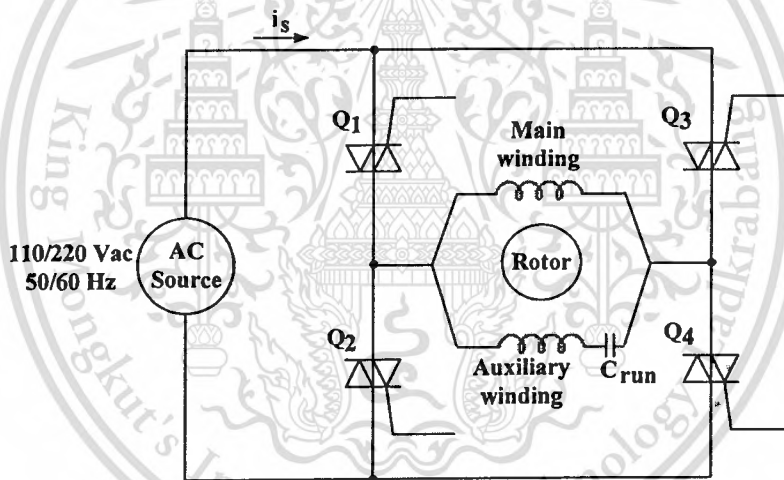


Figure 2.9 Single-phase voltage control with triacs

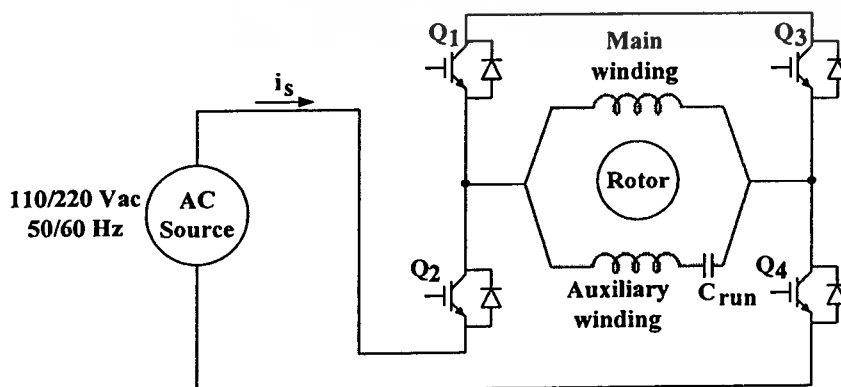


Figure 2.10 Single-phase ac-to-ac chopper

This material is reserved for educational use only, not allowed for commercial use.

Forbidden to modify the content, and cite the document when use.

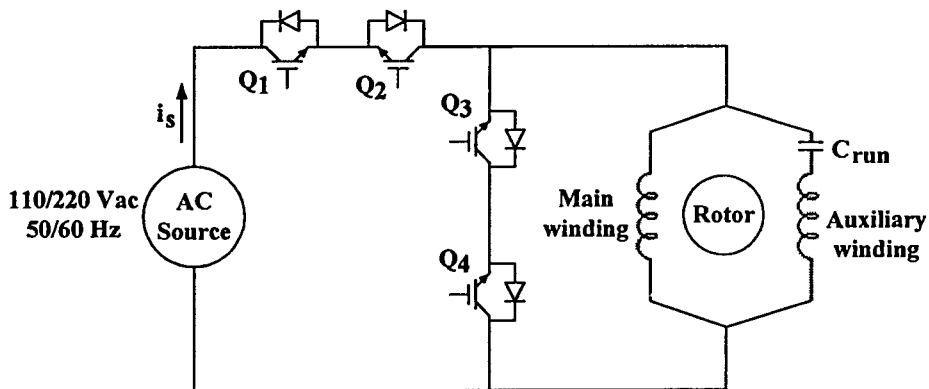


Figure 2.11 Single-phase higher power ac-to-ac chopper

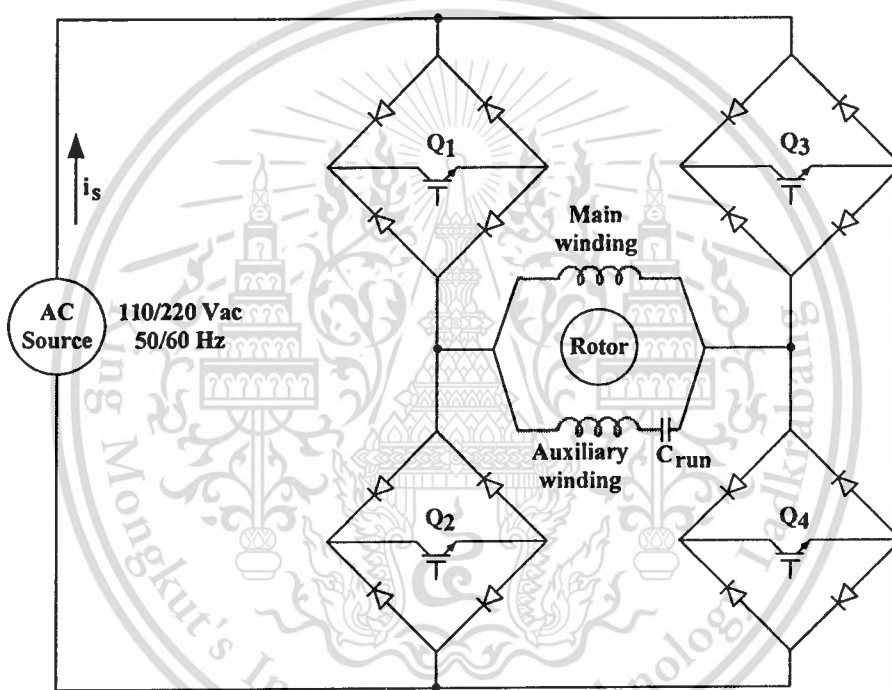


Figure 2.12 Single-phase ac-to-ac cycloconverter

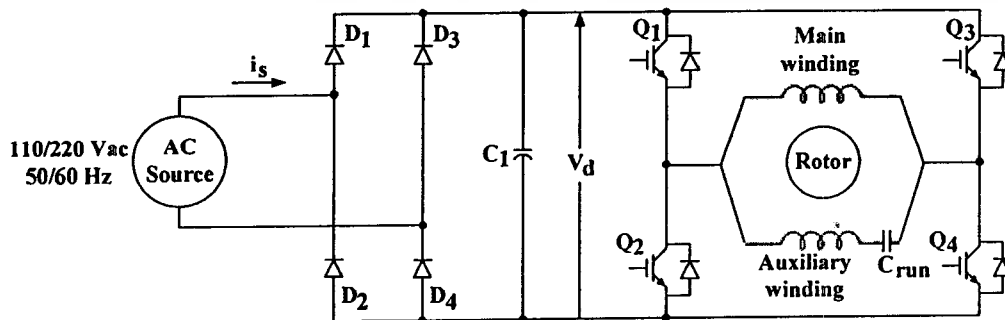


Figure 2.13 Single-phase full-bridge PWM inverter with a full-bridge rectifier

This material is reserved for educational use only, not allowed for commercial use.

Forbidden to modify the content, and cite the document when use.

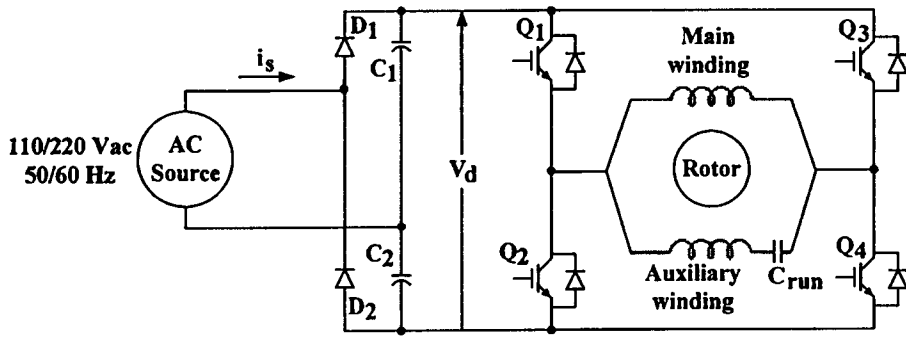


Figure 2.14 Single-phase full-bridge PWM inverter with a half-bridge rectifier

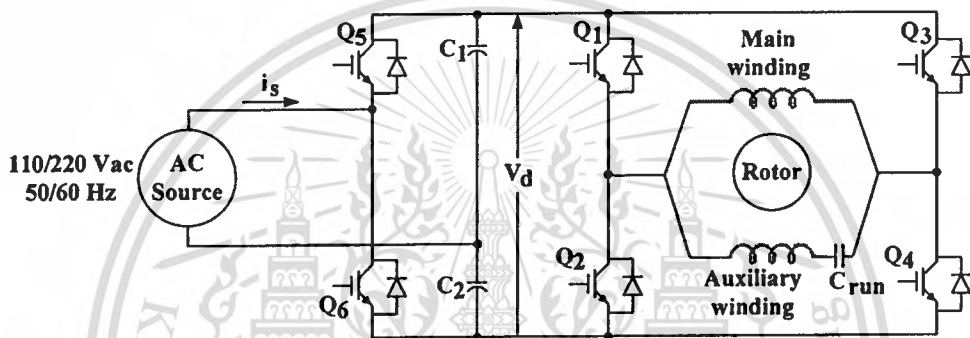


Figure 2.15 Single-phase full-bridge PWM inverter with a controlled rectifier

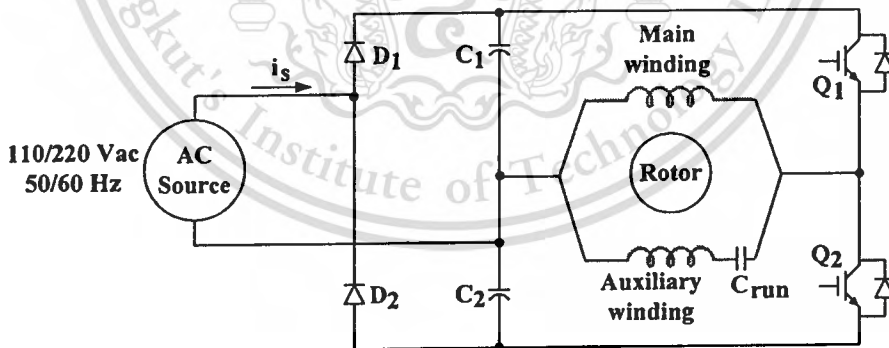


Figure 2.16 Single-phase half-bridge PWM inverter with half-bridge rectifier

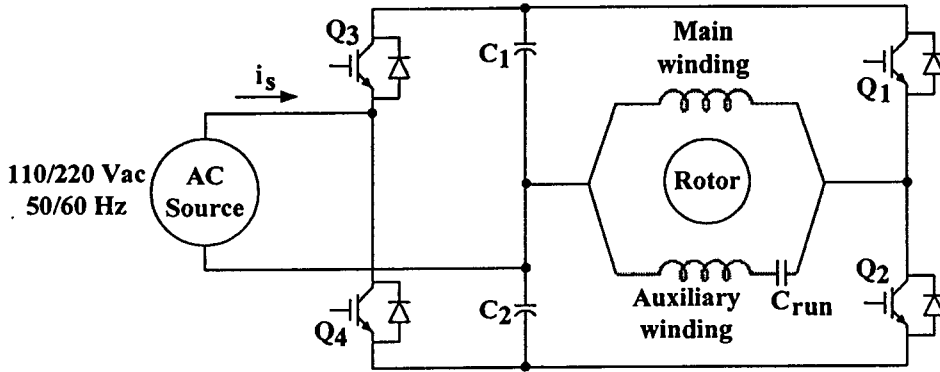


Figure 2.17 Single-phase half-bridge PWM inverter with a controlled half-bridge rectifier

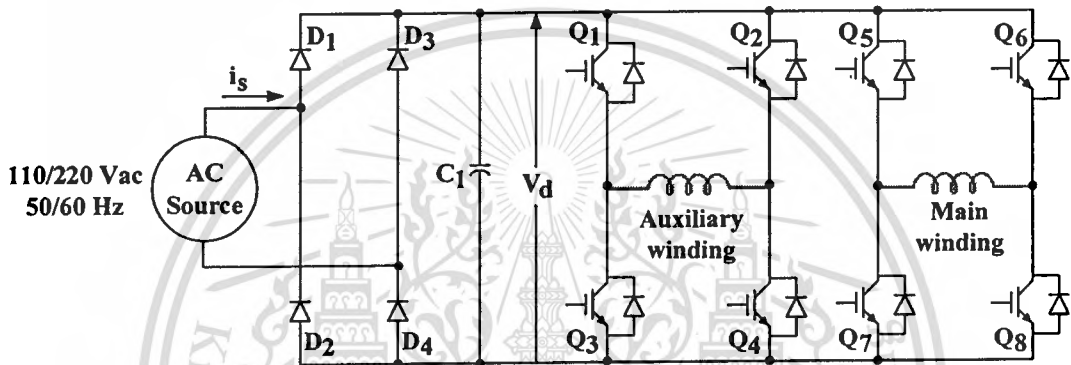


Figure 2.18 Two-phase full-bridge PWM inverter

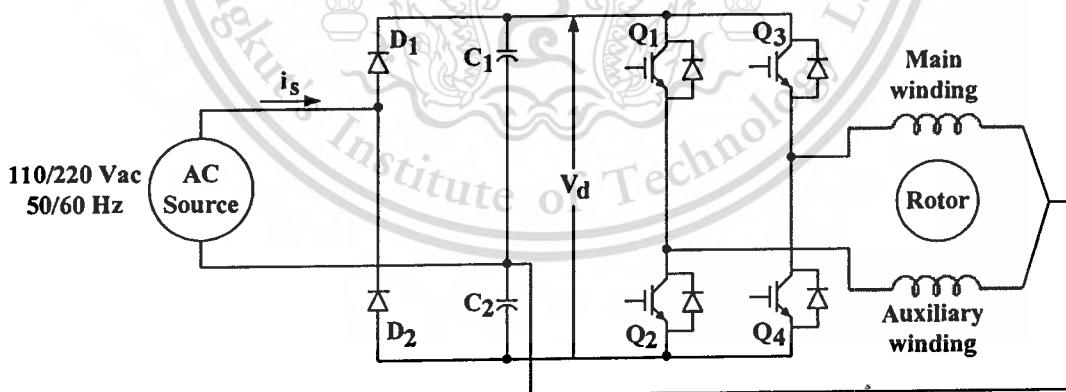


Figure 2.19 Two-phase half-bridge PWM inverter

It is noted that this topology is composed of eight power switches and four diodes. Due to the additional circuit elements, the half-bridge version of this technique as two-phase half-bridge PWM inverter is addressed. Figure 2.19 shows that this inverter utilizes only four power

This material is reserved for educational use only, not allowed for commercial use.

Forbidden to modify the content, and cite the document when use.

switching devices and two diodes [18, 43-44]. Nevertheless, the voltage across the motor windings would be half of the dc bus voltage. This means that not only the motor will be activated under half of the rated voltage, but it is also crucial to keep the voltage across the dc bus capacitor balanced. To avoid a voltage step-up transformer, the applied voltage has been attained by voltage-doublers circuit. By this rectifier, the input rectifying characteristics such as the harmonic distortion, the power factor and the ripple factor are considerably high [20]. To improve the performance of the inverter, a two-phase PWM inverter with controlled rectifier, which employed the power factor correction technique by replacing the two input rectifying diodes by two power switching devices and exploiting an appropriate power factor correction circuit, is carried out as illustrated in Figure 2.20. The input rectifying functions, the harmonic distortion, the power factor and the ripple factor can be significantly better [16-17, 22]. It is possible to implement a space vector PWM technique for a two-phase inverter fed symmetrical two-phase induction motor. There are four voltage space vectors and no zero voltage vectors [23]. The two-phase symmetrical modulation capable of performing the switching sequence in order to minimize the ripple content of the output current has been realized. Apart from an auxiliary winding of standard permanent split capacitor motors that has a higher number of turns than main winding, known as unbalanced two-phase motor, this technique cannot be applied to the commonly existing motor. Thus, this controller would have application in other areas. The latest topology, two-phase semi full-bridge PWM inverter, is a voltage source inverter with three-leg drive system as demonstrated in Figure 2.21. This structure is less expensive than the 4-leg VSI and provides better performance in terms of harmonic distortion when compared with that of the 2-leg VSI. Traditionally, the drive comprises a six pack IGBTs module or intelligent power module (IPM) to control a two-phase induction motor. A specially modulating PWM strategy to accomplish wide range variable speed operation of a balanced or unbalanced two winding induction motor is needed [18, 39]. To maximize the use of the dc bus voltage, and simultaneously to reduce the THD of the synthesized voltage, space vector PWM technique for unbalanced two-phase machine is developed [25]. The space vector PWM is made up of eight space voltage vectors, two of the voltage vectors are zero vectors, four voltage vectors are equal, and two of the vectors are unequal. Then, a current controlled hysteresis technique can also be used successfully. Among two-leg, three-leg, and four-leg topologies, the three-leg topology obtains almost the same overall performance as the four-leg topology, and is not expensive. Also, it exhibits lower harmonic distortion than the two-leg topology and avoids the flow of alternative

This material is reserved for educational use only, not allowed for commercial use.

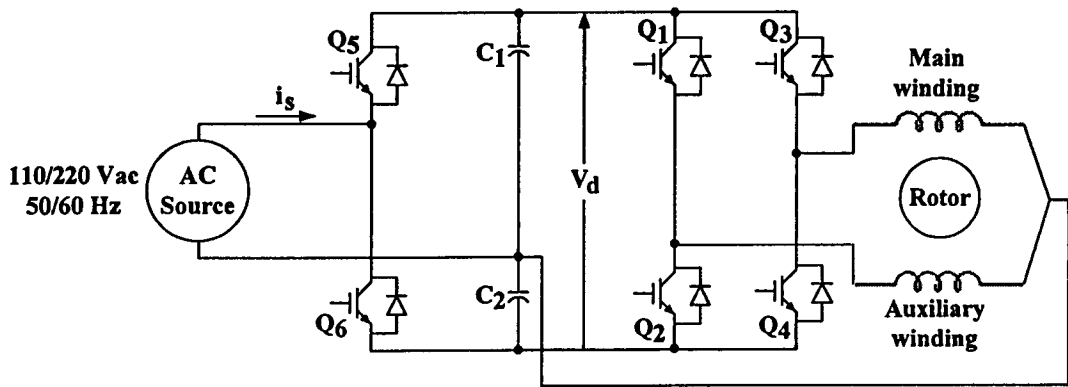


Figure 2.20 Two -phase half-bridge PWM inverter with a controlled rectifier

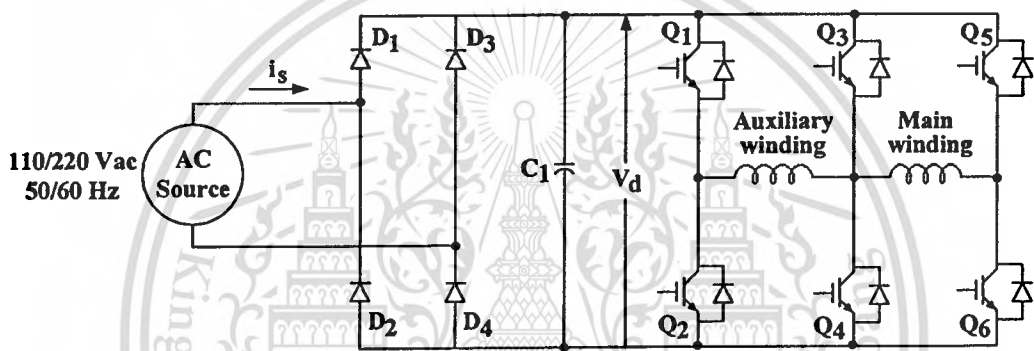


Figure 2.21 Two -phase semi full-bridge PWM inverter

current in the dc bus as well [27, 26]. Therefore, when it is necessary to attain a two-phase drive system with enhanced motor performance, the three-leg system is a good trade-off between cost and performance. Nevertheless, because both winding voltages depend on a common inverter branch, the special modulating function of this system has to be produced. To consider the benefit of each drive technique, various topologies based on the number of devices, the size of DC link capacitor, input power factor, range of speed drive, motor performance, drive cost, control complexity, and motor efficiency are compared as shown in Table 2.1. It can be seen that the topology in which the two currents are independently controlled is the best in terms of performance whilst it requires the largest number of components.

This research is based on unsymmetrical type two-phase induction motor fed by the three-leg VSI so-called semi-full bridge PWM inverter. The two existing standard single-phase induction motor windings are used without rewind, Two-phase voltages which are in quadrature

are applied to the motor windings. According to the supplied voltage characteristic, a running capacitor in series with the auxiliary winding is removed. To represent the advantages of the recommended three-leg drive with the proposed modulation strategy, the conventional two-leg half bridge inverter is compared at the same conditions. The conventional two-leg half bridge inverter supplying a two-phase induction motor as shown in Figure 2.22 consists of a single phase voltage doublers rectifier, two filter capacitors in series, and two legs of an IGBT pair. One end of the main and auxiliary windings are connected to the two-leg inverter. The other ends are connected together with the center-tap of the filter capacitors. Figure 2.23 indicates the proposed three-leg VSI for an unsymmetrical type two-phase motor drive system. When compared to the two-leg half bridge inverter, the terminal voltages across each winding are based on its phase voltage and the connected voltage. Therefore, to generate the unbalanced two-phase voltage supply, the special modulating function for the third leg is needed. The modulating function and generating pattern strategies will be proposed in Chapter 3.

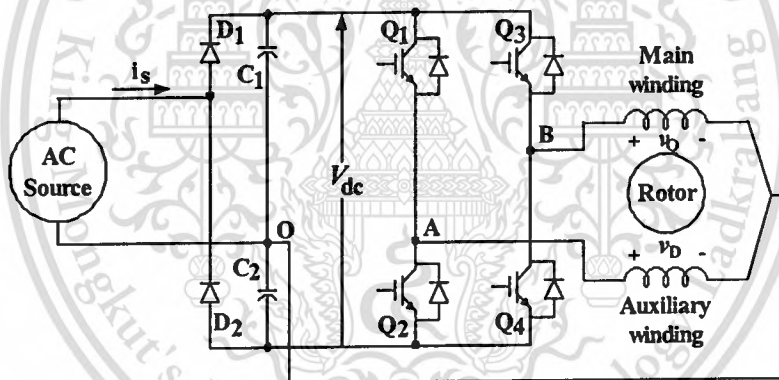


Figure 2.22 The conventional two-leg half bridge inverter

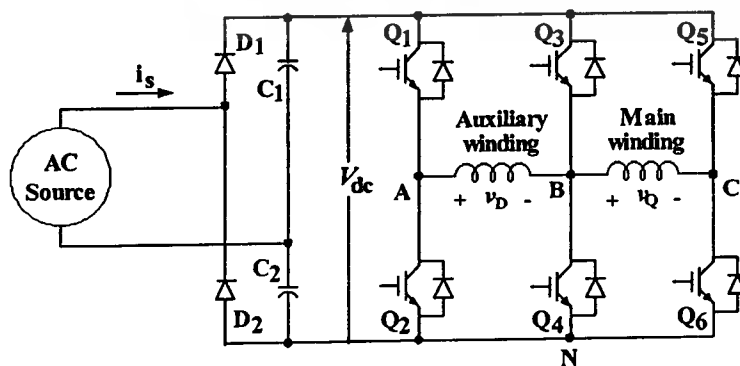


Figure 2.23 The proposed three-leg semi-full bridge inverter

Table 2.1 Comparison of various topologies

Characteristics	AC-AC Chopper	Cycloconverter		Single-phase PWM Inverter				Two-phase PWM Inverter					
		Conventional	Non-conventional	Half-bridge		Full-bridge Inverter		Balanced		Unbalanced			
				Inverter		Rated DC Voltage							
				2S+4D	4S+4D	4S+6D	6S+6D	4S+8D	6S+8D	6S+10D	8S+10D	4S+8D	6S+8D
Number of Devices	4S+4D	4S+16D	1S+4D	2S+4D	4S+4D	4S+6D	6S+6D	4S+8D	6S+8D	6S+10D	8S+10D	4S+8D	6S+8D
DC Link Capacitor	Not used	Not used	Not used	Very large	Very large	Very large	Very large	Large	Large	Large	Large	Very large	Very large
Input Power Factor	Good	Good	Good	Good	Best	Good	Best	Good	Best	Good	Best	Good	Best
Range of Speed Drive	Narrow	Medium	Medium	Wide	Wide	Wide	Wide	Wide	Wide	Wide	Wide	Wide	Wide
Motor Performance	Good	Good	Poor	Better	Better	Better	Better	Better	Better	Best	Best	Best	Best
Drive Cost	Low	Low	Lowest	Medium	High	Medium	High	Medium	High	High	Highest	High	Highest
Control Complexity	Simple	Medium	Simplest	Medium	Complex	Medium	Complex	Medium	Complex	Complex	More complex	Complex	More complex
Motor Efficiency	-	High	Low	High	High	High	High	High	High	Highest	Highest	Highest	Highest

2.5 Noise Sources

Airborne induction motor noise can be categorized according to its source as magnetic noise, windage noise, and mechanical noise [63-65].

Magnetic noise of induction motors has two predominant sources. The first source is due to the radial force waves created by the air-gap flux density. This portion is caused by periodic forces which exist primarily in the air gap between stator and rotor. These forces produce radial components appearing at harmonics of the line frequency and at frequencies related to the slip and line frequency. Furthermore, the forces are proportional to the square of the flux density. As a result, flux densities should be kept low to minimize these double-line-frequency noises. The second part of the magnetic noise is the magnetostrictive expansion of the core steel. Since the induction motor hum is from the basic slot harmonic force field, the appropriate skewing of either the rotor or the stator slots will decrease the magnitude of these slot harmonics. During acceleration, when the rotor reaches the speed at which the force frequency coincides with shaft resonance, the amplitude of shaft bending will increase. The magnetic noise may be loud. An oversized shaft is, therefore, helpful in ensuring quiet operation.

The pulsating torque due to two separate fields is also a source of noise. This type of noise is especially prominent in motors having unbalanced currents and in single-phase motors. One remedy is an elastic mounting such as a rubber ring around the bearing housing, providing torsion elasticity with a maximum of radial stiffness.

Variable frequency drives will cause an increase in magnetic noise. This increase is a result of the additional magnetic forces which are generated in the motor by the higher frequency voltage harmonics coming from the driver [66-70]. The presence of electrical, electromagnetic, and mechanical asymmetries (separately or in combination) produces a new set of magnetic force waves. If these waves are of appropriate nodal pattern and frequency, they will excite resonances of either the rotor or the stator. In order to avoid excessive noise produced by the voltage harmonics, the additional magnetic noise created in the motor can be minimized as follows:

- 1) Filtering the output voltage of the drivers.
- 2) Increasing the core length and/or frame size and diameter to decrease the magnetic field in the motor's air gap.
- 3) Avoiding a core resonance at the commutation frequency by especially determining the PWM strategies.

Windage noise is generated by the interaction of both the moving parts of the rotor with the cooling air passing through the motor and the moving air with stationary parts of the motor. The primary source of windage noise in an induction motor is not only the fans but also the rotor bars in the vent areas and at the rotor ends [66]. The frequency of windage noise equals the passing frequency of the fan blades or rotor bars. Frequencies may vary with manufacturers and machine size. However, the passing frequency and noise for the rotor bars are at a higher and more irritating frequency than that of the fans. To minimize the noise levels, installing sound insulation in the top covers, where space allows, will reduce windage noise significantly. For new designs, the utilization of enclosures with increasing weather protection can dramatically decrease noise levels. Noise reductions will be accomplished by a frame-size increase and/or isolation-type enclosure built around the motor.

Many mechanical noises are associated with the bearing assembly and can be appreciable. Some of the noise sources in induction motors as well as possible noise control and reduction are indicated in Table 2.2 [64]. No general rules can be given for induction motors as to relative importance of these three types of noise.

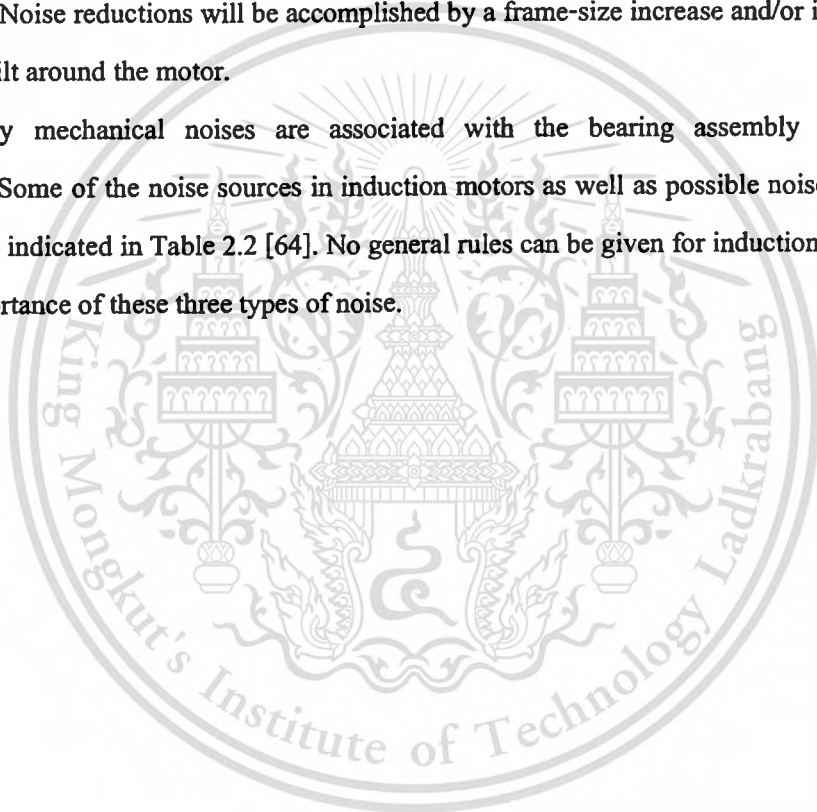


Table 2.2 Induction motor noise sources, causes and treatments

Noise source	Cause	Component causing noise	Noise control and reduction
Magnetic	Radial	Air gap	Correct eccentricity of rotor and stator by machining and adjustment
	Variable force field radial in direction	Slotting of rotor and stator punching	Skew stator or rotor slots, use closed rotor and semi closed stator slots
		Dissymmetry harmonics due to higher harmonics in stator current	Reduce dissymmetry by improved magnetic circuit design; avoid resonance of rotor frame, particularly at lower modes which are more effective sound radiators
Windage	Modulation	Siren effect	Displace rotor ducts axially or acoustically treat interior surfaces
		Fan blades	Change number of fan blades, remove stationary obstacles from air stream, or use aerodynamic directional fan
	Turbulence	Fan	Redesign fan and air stream path, add acoustic filters or acoustically treat the ventilating passages
Mechanical	Impact	Sleeve bearing	Correct end play of shaft, decrease clearance between shaft and sleeve, modify oil grooves
		Ball bearing	Reduce radial play by preloading, decrease shaft or housing tolerances
		Loose laminations	Improve clamping of laminations
	Friction	Sleeve bearing	Increase clearance and oil viscosity, scrape sleeve surface
		Ball bearing	Increase preload pressure, change type of grease
	Unbalance	Rotor	Mechanical balance required
	Instability	Bearing	Change oil viscosity and oil grooves in bearings

CHAPTER 3

NOVEL MODULATING STRATEGY

3.1 Converter Modulation Strategy

The conventional two-leg half bridge inverter supplying a two-phase induction motor as shown in Figure 3.1 consists of a single-phase voltage doublers rectifier, two filter capacitors in series, and two legs of an IGBT pair. One end of the main and auxiliary windings are connected to the two-leg inverter. The other ends are connected together with the center-tap of the filter capacitors. Their fundamental components of output voltage are shifted by 90 electrical degree differences. The principle of generating balanced two-phase PWM output voltages is based on a comparison between balanced two-phase modulating sinusoidal signals with 90 electrical degree phase shift compared to a common triangular wave, known as a sinusoidal pulse width modulation (SPWM) and is illustrated in Figure 3.2. The obtained PWM output voltages are classified as bipolar PWM.

To generate output voltages for both windings of an unsymmetrical two-phase induction motor using the typical two-leg half bridge voltage source inverter, the two modulating function signals with balanced output voltages for a two-leg system are:

$$\begin{aligned} v_a &= V_m \sin(\omega_r t) \\ v_b &= V_m \sin(\omega_r t - 90^\circ) \end{aligned} \tag{3.1}$$

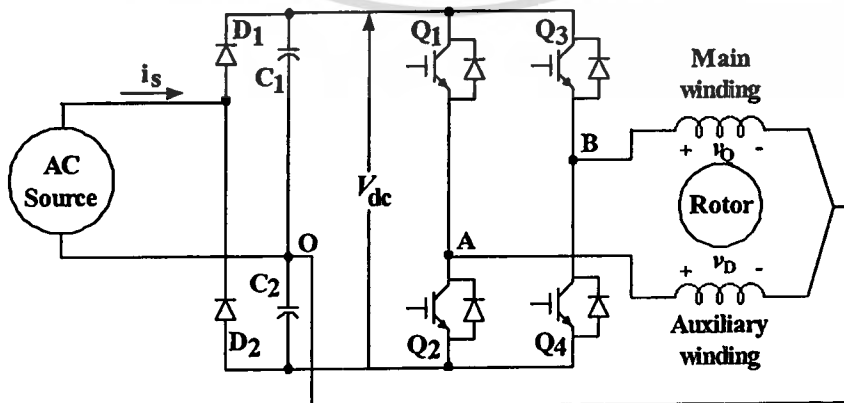


Figure 3.1 Main power circuit of the typical two-leg half bridge inverter

This material is reserved for educational use only, not allowed for commercial use.

Forbidden to modify the content, and cite the document when use.

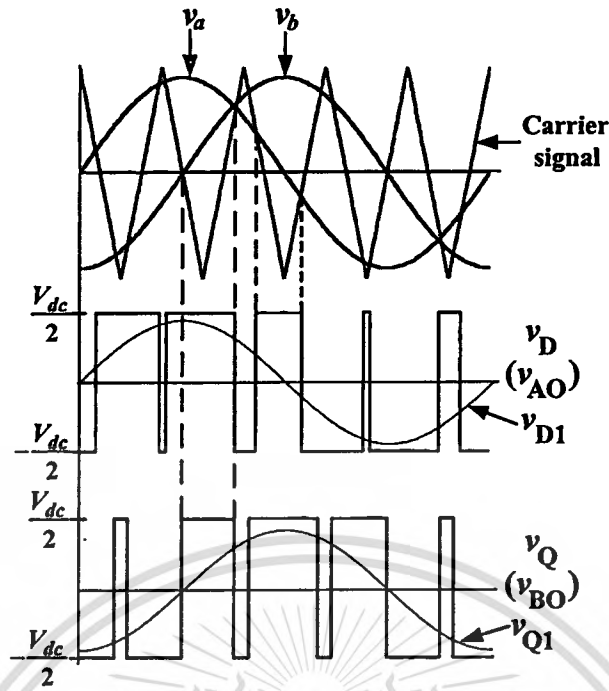


Figure 3.2 Principle of generating PWM patterns for the typical two-leg VSI

The amplitude and frequency of the output phase voltages can be independently controlled by varying a sinusoidal reference amplitude and a frequency of each modulating signal whilst the carrier signal is fixed with a constant frequency and amplitude. More details of PWM parameters such as modulation index, modulation frequency ratio can be found in [20, 71-73]. It is noticed that an unbalanced case in accordance with the control method previously illustrated in Figure 2.7 can also be easily obtained due to independent control for each modulating signal. The fundamental output voltage of the auxiliary winding can be expressed as

$$v_{D1} = \frac{MV_{dc}}{2} \sin(\omega_r t) \quad (3.2)$$

Also, the fundamental output voltage of the main winding can be expressed as

$$v_{Q1} = \frac{MV_{dc}}{2} \sin(\omega_r t - 90^\circ) \quad (3.3)$$

Where

v_a = reference modulating function of control signal phase a

v_b = reference modulating function of control signal phase b

This material is reserved for educational use only, not allowed for commercial use.

Forbidden to modify the content, and cite the document when use.

- v_c = reference modulating function of control signal phase c
 v_{Q1} = fundamental main winding voltage
 v_{D1} = fundamental auxiliary winding voltage
 v_{AN} = PWM voltage of phase A
 v_{BN} = PWM voltage of phase B
 v_{CN} = PWM voltage of phase C
 v_{AB} = PWM auxiliary winding terminal voltage
 v_{BC} = PWM main winding terminal voltage
 V_m = amplitude of modulating function
 V_d = dc link voltage
 V_x = amplitude of additional modulating function
 V_i = amplitude of carrier signal
 $M_1 = \frac{V_x}{V_i}$ = modulation index of additional modulating function
 $M = \frac{V_m}{V_i}$ = modulation index
 $m_f = \frac{f_{carrier}}{f_{reference}}$ = modulation frequency ratio
 ω_r = reference angular frequency (rad/s)
 ω_c = carrier angular frequency (rad/s)

Figure 3.3 indicates the proposed three-leg VSI for an unsymmetrical type two-phase motor drive system. The main and the auxiliary windings are connected across the bridge as an unbalanced three phase load. When compared to the two-leg half bridge inverter, the terminal voltages across each winding are based on its phase voltage and the connected voltage. Therefore, to generate the unbalanced two-phase voltage supply which achieves the maximum possible converter utilization, the special modulating function is necessarily required.

For the proposed three-leg semi full bridge PWM inverter, the third modulating function for the third leg is given in Equation (3.4). With these modulating functions for balanced output voltages, both winding voltages are always in quadrature.

$$\begin{aligned}
 v_a &= V_m \sin (\omega_r t) \\
 v_b &= V_m \sin (\omega_r t - 90^\circ) \\
 v_c &= V_m \sin (\omega_r t - 180^\circ)
 \end{aligned} \tag{3.4}$$

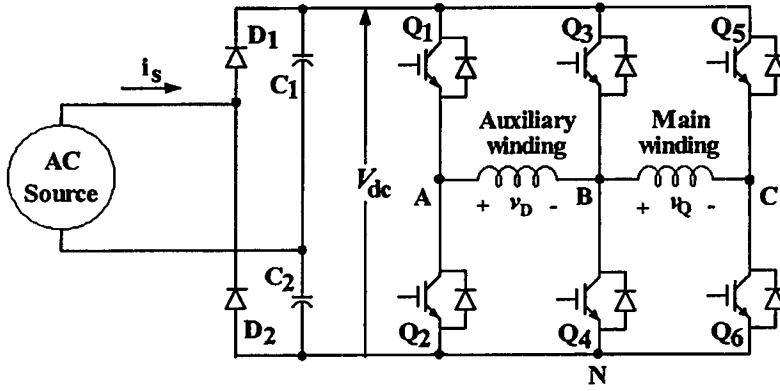


Figure 3.3 Main power circuit of the proposed three-leg semi-full bridge inverter

The reference modulating functions of the first leg (terminal A), the second leg (terminal B), and the third leg (terminal C) of the proposed inverter are v_a , v_b and v_c , respectively. Unfortunately, unbalanced output voltages having 90 electrical degree phase differences cannot occur with independent control of those modulating function signals. In order to overcome this problem, an additional modulating function is required. The proposed modulating function is a modified modulating function of the third inverter's leg, obtained by adding a new function (v_{c2}) to the previous modulating function (v_c) in Equation (3.4). As the reference modulating functions of the third leg at terminal C should be v_c , with the proposed scheme the instantaneous voltage of v_c is rewritten as follows:

Let

$$v_{c1} = V_m \sin (\omega, t - 180^\circ) \quad (3.5)$$

and additional modulating function

$$v_{c2} = V_x \sin (\omega, t - 45^\circ) \quad (3.6)$$

and let

$$v_c = v_{c1} + v_{c2} \quad (3.7)$$

The modulating function for the third leg v_c in Equation (3.4) can be rewritten as:

This material is reserved for educational use only, not allowed for commercial use.

Forbidden to modify the content, and cite the document when use.

$$v_c = V_m \sin(\omega_r t - 180^\circ) + V_x \sin(\omega_r t - 45^\circ) \quad (3.8)$$

Thus

$$\begin{aligned} v_{ab} &= v_a - v_b \\ &= V_m \sin(\omega_r t) - V_m \sin(\omega_r t - 90^\circ) \\ &= V_m \sin(\omega_r t) + V_m \cos(\omega_r t) \\ &= V_m [\sin(\omega_r t) + \cos(\omega_r t)] \\ &= \sqrt{2} V_m \sin(\omega_r t + 45^\circ) \end{aligned} \quad (3.9)$$

and

$$\begin{aligned} v_{bc} &= v_b - v_c \\ &= V_m \sin(\omega_r t - 90^\circ) - [V_m \sin(\omega_r t - 180^\circ) + V_x \sin(\omega_r t - 45^\circ)] \\ &= V_m [\sin(\omega_r t) - \cos(\omega_r t)] - V_x \sin(\omega_r t - 45^\circ) \\ &= \sqrt{2} V_m \sin(\omega_r t - 45^\circ) - V_x \sin(\omega_r t - 45^\circ) \\ &= (\sqrt{2} V_m - V_x) \sin(\omega_r t - 45^\circ) \end{aligned} \quad (3.10)$$

It can be seen in Equations (3.9) and (3.10) that the two voltages, v_{ab} and v_{bc} are equivalent to the fundamental auxiliary and main winding voltages, respectively, and they are in quadrature. The amplitude of both voltages is 1.414 times the amplitude of each modulating function. The implication is that this technique gives an advantage in terms of dc voltage utilization over the two-leg half bridge VSI.

In order to better understand the principle of the proposed modulating functions, the phasor diagrams in Figure 3.4 (a) for the balanced two-phase terminal voltage and 3.4 (b) for the unbalanced two-phase terminal voltage are illustrated. It is clear from Figure 3.4 that, with the additional modulating function, v_{c2} , the output terminal voltage with different magnitude and fixed 90° phase shift is unbalanced under any operating conditions. The principle of generating unbalanced PWM output voltages based on the proposed modulation scheme for the three-leg

VSI is described in Figure 3.5. The given PWM output voltages are classified as unipolar PWM. The fundamental output voltage of the auxiliary winding can be expressed as

$$\begin{aligned}
 v_{D1} &= v_{AB} = v_A - v_B \\
 &= \frac{MV_{dc}}{2} \sin(\omega_r t) - \frac{MV_{dc}}{2} \sin(\omega_r t - 90^\circ) \\
 &= \frac{\sqrt{2}MV_{dc}}{2} \sin(\omega_r t + 45^\circ)
 \end{aligned} \tag{3.12}$$

Also, the fundamental output voltage of the main winding can be expressed as

$$\begin{aligned}
 v_{Q1} &= v_{BC} = v_B - v_C \\
 &= \frac{MV_{dc}}{2} \sin(\omega_r t - 90^\circ) - \left[\frac{MV_{dc}}{2} \sin(\omega_r t - 180^\circ) + \frac{M_1 V_{dc}}{2} \sin(\omega_r t - 45^\circ) \right] \\
 &= \frac{\sqrt{2}MV_{dc}}{2} \sin(\omega_r t - 45^\circ) - \frac{M_1 V_{dc}}{2} \sin(\omega_r t - 45^\circ) \\
 &= \frac{(\sqrt{2}M - M_1)V_{dc}}{2} \sin(\omega_r t - 45^\circ)
 \end{aligned} \tag{3.13}$$

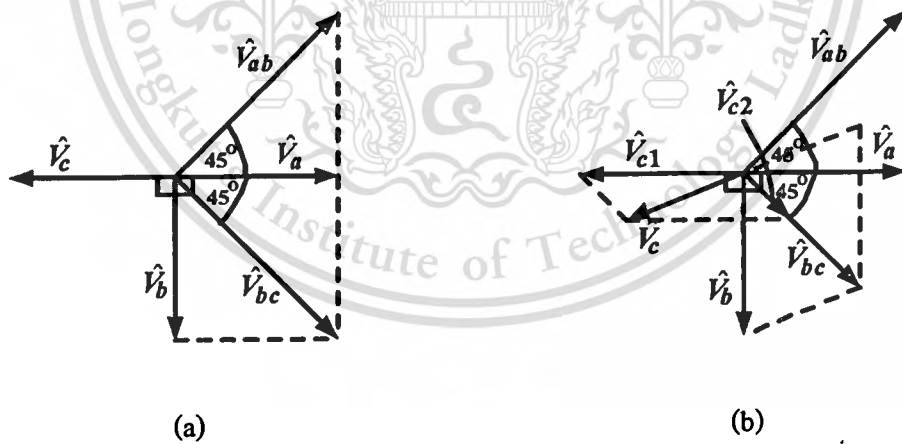


Figure 3.4 Phasor diagram of modulating functions for the two-phase drive system of the three-leg VSI

- (a) balanced output voltage case
- (b) unbalanced output voltage case

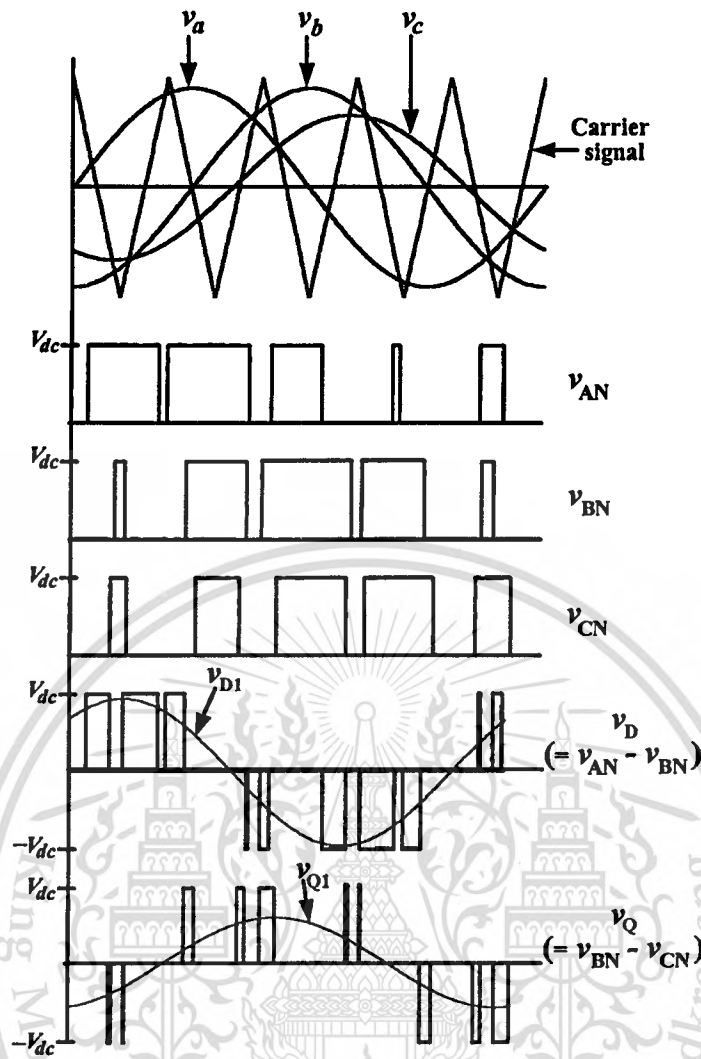


Figure 3.5 Principle of generating unbalanced PWM output voltages based on the proposed modulating functions for the three-leg VSI

It can be seen in Equations (3.10) and (3.11) that the fundamental PWM output voltages for both windings are in quadrature and can be set by M and M_1 corresponding to the control method previously shown in Figure 2.7.

3.2 Unbalanced Voltage for Improved Unsymmetrical Two-Phase Induction Motor Performance

As described in the previous section, the unbalanced two-phase voltage source with the three-leg semi-full bridge SPWM inverter can be achieved with the proposed converter modulation control scheme. To eliminate the backward field from occurring in the motor's air

This material is reserved for educational use only, not allowed for commercial use.

Forbidden to modify the content, and cite the document when use.

gap, the auxiliary winding voltage is boosted using a turns ratio of the auxiliary winding to that of the main winding of “a”. This allows a wide range of operation, especially at low speed which is the main problem for variable speed drives of single-phase induction motors in the past. The amplitude of both winding voltages can be arbitrarily controlled by modulating factors M and M_1 . Both voltages can be fixed at 90 electrical degree phase difference in a range of operating conditions. Over a period of time corresponding to any number of complete cycles of the terminal, the dc voltage component integrates to zero. This is because positive and negative parts in each voltage cycle are in symmetry and means that no dc voltage component is included in the SPWM voltage source of the two-phase motor. For this reason, neither higher current coming from magnetic circuit saturation nor parasitic torques is added in the motor.

The proposed inverter provides less harmonic voltage components than other techniques, especially the conventional two-phase driver. As a result, the voltage stress on the motor, principally one of magnetic and acoustic noise generation, can be significantly reduced. Moreover, the current flow in the motor may have a more sinusoidal wave shape than other drive topologies thereby enhancing the motor’s efficiency.

3.3 Current Mode Analysis

As discussed in the previous section, the proposed three-leg VSI for generating unbalanced PWM output voltages to supply an unsymmetrical two-phase induction motor is made up of six power switching devices and six diodes. In order to more simply analyze the current flow via each winding; the VSI circuit is redrawn as shown in Figure 3.6.

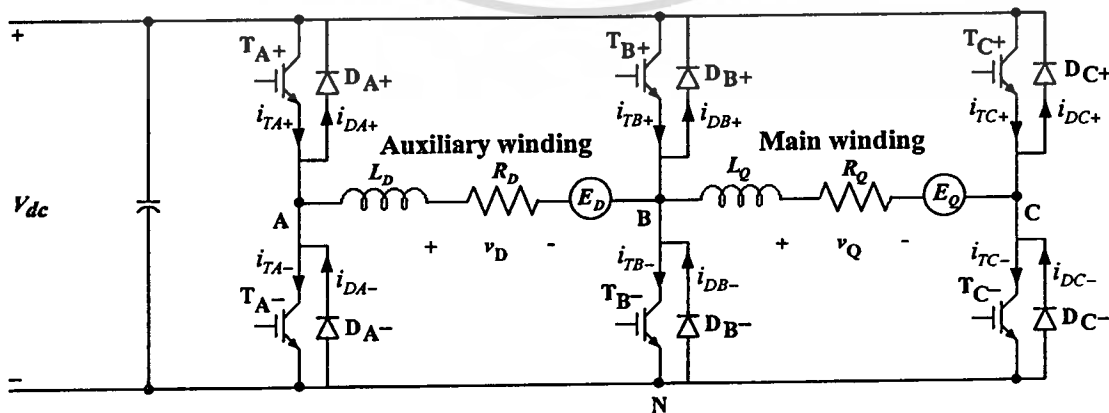


Figure 3.6 Main power circuit for current mode analysis

Each winding is connected with the middle point of two branches; that is, nodes A and B for the auxiliary winding and nodes B and C for the main winding. R_D, L_D , and E_D are the resistance, inductance and induced voltage of the auxiliary winding, respectively. R_Q, L_Q , and E_Q are the resistance, inductance and induced voltage of the main winding, respectively.

To illustrate steady-state operation of the converter, several assumptions are made:

- The components are ideal;
- The winding impedances are constant;
- The induced voltages of the windings are sinusoidally identical.

To better ensure the switch mode characteristics, the main power circuit in Figure 3.6 is simulated using the program OrCAD 9.1, as shown in Figure 3.7. Q1-Q6 represent the IGBTs switching devices. R1 and L1 are a resistance and an inductance of the auxiliary winding, while R2 and L2 are those of the main winding. E1 and E2 represent the average induced voltages of the auxiliary and the main windings. Figure 3.8 displays the gate-drive circuits which generate SPWM output voltages to control each power switching device. In the simulation, sinusoidal waveforms of 30 Hz are generated from four sinusoidal voltage sources V2, V3, V4, and V5 which are displaced by 0, 90, 45, and 180 electrical degrees, respectively. Only V4 and V5 are summed together. The amplitude of these reference signals are governed in accordance with Table 3.2. Three sinusoidal voltage signals are modulated with the same triangular wave of 360 Hz (for convenient wave shape consideration) while the actual frequency of the implemented triangular wave is 5 kHz. The integrated circuit LF351 is used as a comparator. The output signals from the comparator U1 is the gate driver of the top first branch of the inverter, Q1. Simultaneously, the signal is converted by not-gate and triggers the power switching device Q2. An output signal from the comparator U2 (s3) and its inverted signal (s4) are utilized to regulate the second-leg of switching devices, Q3-Q4. The power devices Q5-Q6 are turned on/off by the control signals from s5-s6 generated by the comparator U3. Using the generated PWM pattern, the typical behavior with time variance of the auxiliary and the main winding currents can be analyzed in i_D and i_Q waveforms, sequentially; as demonstrated in Figure 3.9. Unipolar PWM voltages of those windings are represented as v_D and v_Q while the induced voltages are represented by E_D and E_Q . With the proposed strategy, the output current of the three-leg voltage source converter can be divided into eight identical modes. It is assumed that the load current of mode A1 is i_{D1} . The load current of mode A2 is i_{D2} and those of mode A3, A4, A5, A6, A7, and A8 are $i_{D3}, i_{D4}, i_{D5}, i_{D6}, i_{D7}$, and i_{D8} , respectively.

This material is reserved for educational use only, not allowed for commercial use.

Forbidden to modify the content, and cite the document when use.

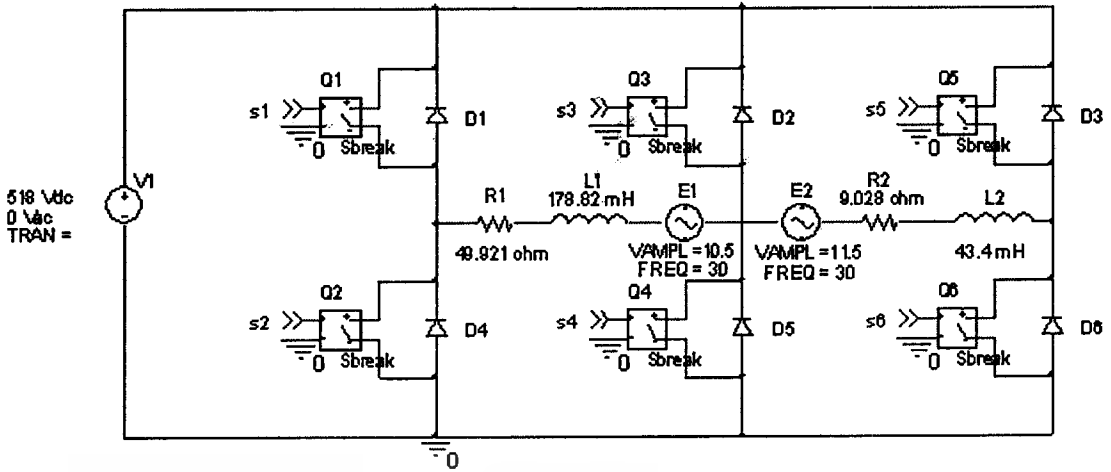


Figure 3.7 Simulation of main power circuit for switch mode analysis

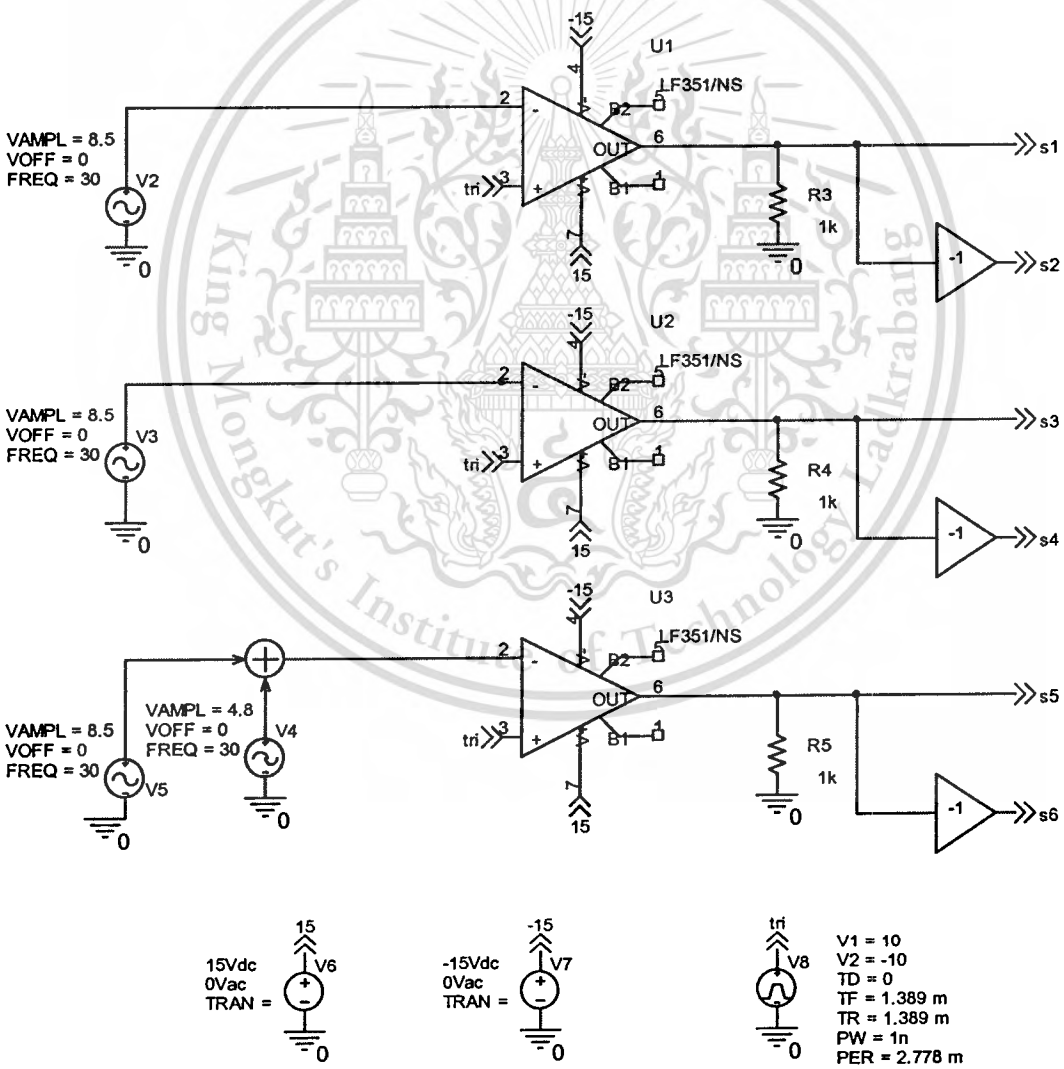


Figure 3.8 Simulation of control circuit for switch mode analysis

This material is reserved for educational use only, not allowed for commercial use.

Forbidden to modify the content, and cite the document when use.

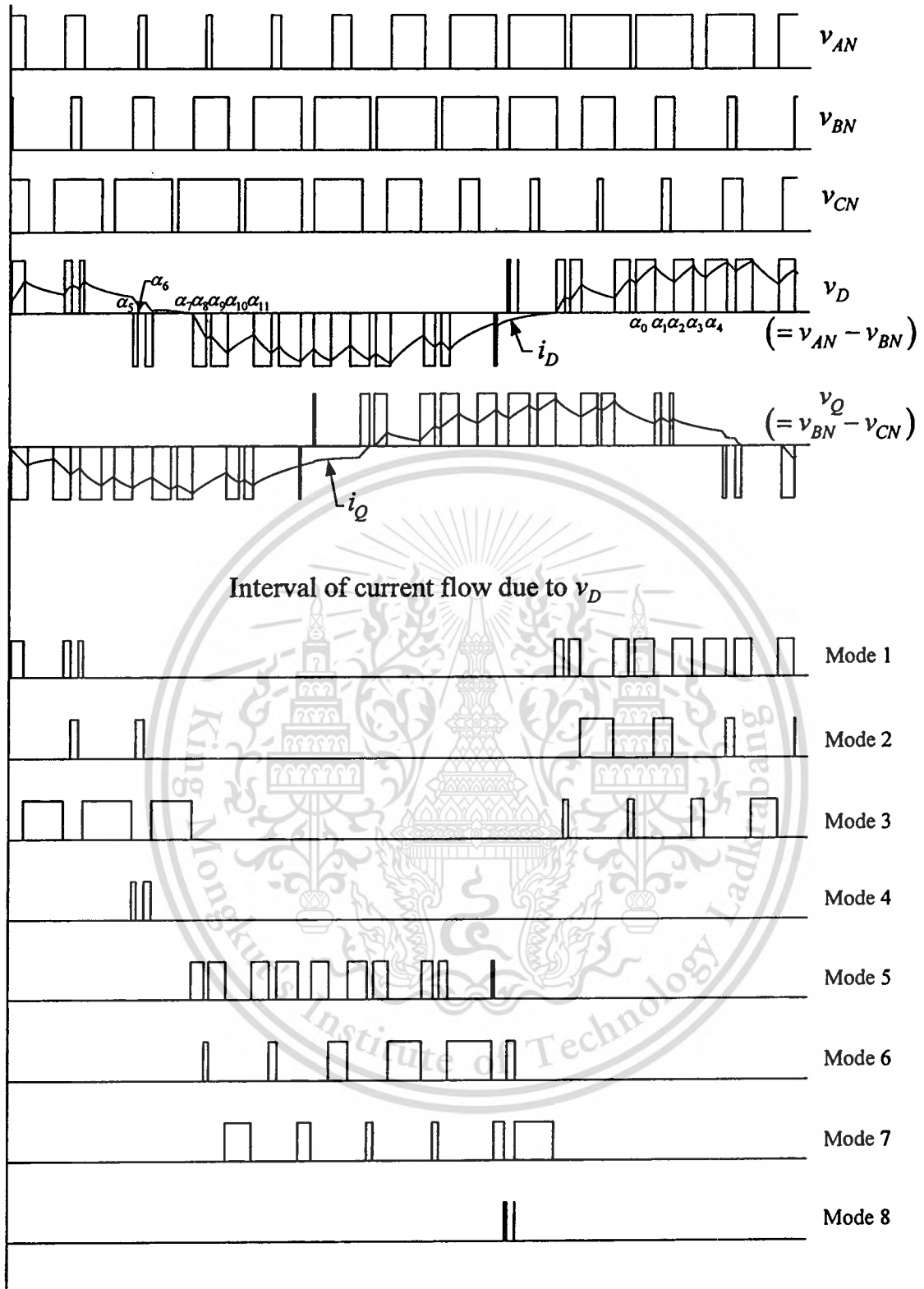


Figure 3.9 Simulated voltage and current waveforms for the proposed three-leg VSI with the analysis mode of current flow corresponding to v_D

The induced voltage of mode A1 is E_{D1} while those of mode A2 to mode A8 are $E_{D2}, E_{D3}, E_{D4}, \dots, E_{D8}$, respectively. Due to the high carrier frequency (5 kHz) of the implemented inverter, the instantaneous induced voltage value can be determined as a sinusoidal voltage function.

A description of the different modes of current flow corresponding to the auxiliary winding voltage v_D can be considered as follows:

Mode A1: At α_0 , switches T_{A+} and T_{B-} are conducting and the current flows from source to load. The active components under this mode are illustrated in Figure 3.10. The input voltage is V_{dc} and the load current i_{D1} of this mode can be derived by Equation (3.14).

$$L_D \frac{di_{D1}}{dt} + R_D i_{D1} + E_{D1} = V_{dc} \quad (3.14)$$

Equation 3.14 is in the form of a linear first-order differential equation which can be rewritten in the standard form of a linear equation:

$$\frac{di_{D1}}{dt} + \frac{R_D}{L_D} i_{D1} = \frac{V_{dc} - E_{D1}}{L_D} \quad (3.15)$$

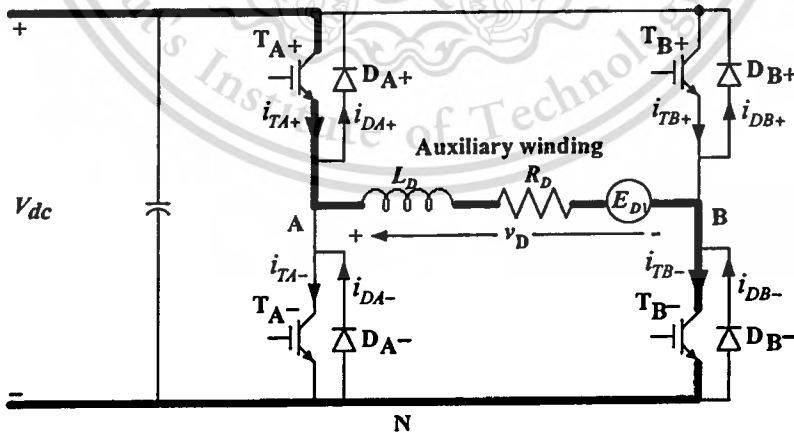


Figure 3.10 Current flow in mode A1

As the general standard form of a linear equation is $\frac{dy}{dx} + P(x)y = f(x)$, then $P(x)$ is equivalent to $\frac{R_D}{L_D}$. A common integrating factor can be solved as $e^{\int P(x)dx}$ and therefore the

integrating factor of Equation (3.15) is $e^{\int \frac{R_D}{L_D} dt} = e^{\frac{R_D t}{L_D}}$. Multiplying Equation (3.15) by the integrating factor:

$$e^{\frac{R_D t}{L_D}} \left(\frac{di_{D1}}{dt} + \frac{R_D}{L_D} i_{D1} \right) = e^{\frac{R_D t}{L_D}} \left(\frac{V_{dc} - E_{D1}}{L_D} \right)$$

$$\frac{d \left(e^{\frac{R_D t}{L_D}} i_{D1} \right)}{dt} = \left(\frac{V_{dc} - E_{D1}}{L_D} \right) e^{\frac{R_D t}{L_D}} \quad (3.16)$$

Integrating both sides of Equation (3.16):

$$e^{\frac{R_D t}{L_D}} i_{D1} = \frac{L_D}{R_D} \left(\frac{V_{dc} - E_{D1}}{L_D} \right) e^{\frac{R_D t}{L_D}} + C_1$$

$$e^{\frac{R_D t}{L_D}} i_{D1} = \left(\frac{V_{dc} - E_{D1}}{R_D} \right) e^{\frac{R_D t}{L_D}} + C_1 \quad (3.17)$$

Dividing Equation (3.17) by $e^{\frac{R_D t}{L_D}}$. Thus,

$$i_{D1} = \left(\frac{V_{dc} - E_{D1}}{R_D} \right) + C_1 e^{-\frac{R_D t}{L_D}} \quad (3.18)$$

The constant C_1 can be determined from the initial condition, for example when the mode A1 occurs at $\alpha_0 \leq \omega t \leq \alpha_1$. Consequently, when $\omega t = \alpha_0$, $i_{D1} = I_{D0}$

$$I_{D0} = \left(\frac{V_{dc} - E_{D1}}{R_D} \right) + C_1$$

$$C_1 = I_{D0} - \left(\frac{V_{dc} - E_{D1}}{R_D} \right) \quad (3.19)$$

Substituting C_1 yields

This material is reserved for educational use only, not allowed for commercial use.

Forbidden to modify the content, and cite the document when use.

$$\begin{aligned}
 i_{D1} &= \left(\frac{V_{dc} - E_{D1}}{R_D} \right) + \left\{ I_{D0} - \left(\frac{V_{dc} - E_{D1}}{R_D} \right) \right\} e^{-\frac{R_D t}{L_D}} \\
 &= I_{D0} e^{-\frac{R_D t}{L_D}} + \left(\frac{V_{dc} - E_{D1}}{R_D} \right) \left(1 - e^{-\frac{R_D t}{L_D}} \right) \quad \text{for } i_{D1} \geq 0,
 \end{aligned} \tag{3.20}$$

At the end of this mode at $\omega t = \alpha_1$, the load current becomes I_{D1} . That is

$$I_{D1} = I_{D0} e^{-\frac{R_D t}{L_D}} + \left(\frac{V_{dc} - E_{D1}}{R_D} \right) \left(1 - e^{-\frac{R_D t}{L_D}} \right) \quad \text{for } i_{D1} \geq 0 \tag{3.21}$$

Mode A2: For this mode, T_{A+} and T_{B+} are turned on. The power switching device T_{A+} and the freewheeling diode D_{B+} both conduct and the load current continues to flow through D_{B+} as depicted in Figure 3.11. The freewheeling diode provides a path for the continuity of the load current. The load current during mode A2, i_{D2} , can be expressed by:

$$\begin{aligned}
 L_D \frac{di_{D2}}{dt} + R_D i_{D2} + E_{D2} &= 0 \\
 \frac{di_{D2}}{dt} + \frac{R_D}{L_D} i_{D2} &= -\frac{E_{D2}}{L_D}
 \end{aligned} \tag{3.22}$$

Equation (3.22) can be solved by the linear first-order differential equation solution method. As described for mode A1, the solution of Equation (3.22) can be recognized firstly by calculation of the integrating factor, which equals $e^{\int \frac{R_D}{L_D} dt} = e^{\frac{R_D t}{L_D}}$. Hence, i_{D2} can be defined by:

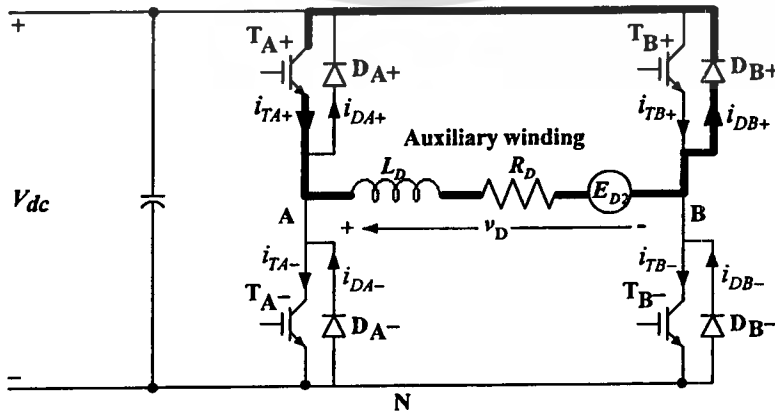


Figure 3.11 Current flow in mode A2

$$e^{\frac{R_D t}{L_D}} \left(\frac{di_{D2}}{dt} + \frac{R_D}{L_D} i_{D2} \right) = e^{\frac{R_D t}{L_D}} \left(\frac{-E_{D2}}{L_D} \right)$$

$$\frac{d \left(e^{\frac{R_D t}{L_D}} i_{D2} \right)}{dt} = \left(\frac{-E_{D2}}{L_D} \right) e^{\frac{R_D t}{L_D}} \quad (3.23)$$

Integrating both sides of Equation (3.23):

$$e^{\frac{R_D t}{L_D}} i_{D2} = \frac{L_D}{R_D} \left(\frac{-E_{D2}}{L_D} \right) e^{\frac{R_D t}{L_D}} + C_2$$

$$e^{\frac{R_D t}{L_D}} i_{D2} = \left(\frac{-E_{D2}}{R_D} \right) e^{\frac{R_D t}{L_D}} + C_2 \quad (3.24)$$

Dividing Equation (3.24) by $e^{\frac{R_D t}{L_D}}$, therefore,

$$i_{D2} = \left(\frac{-E_{D2}}{R_D} \right) + C_2 e^{-\frac{R_D t}{L_D}} \quad (3.25)$$

The constant C_2 can be determined from the initial condition, such as when $\alpha_1 \leq \omega t \leq \alpha_2$ the initial condition is $\omega t = \alpha_1$, and $i_{D2} = I_{D1}$. This is given by:

$$I_{D1} = \left(\frac{-E_{D2}}{R_D} \right) + C_2$$

$$C_2 = I_{D1} + \left(\frac{E_{D2}}{R_D} \right) \quad (3.26)$$

Substituting Equation (3.26) into Equation (3.25), the load current i_{D2} is

$$i_{D2} = \left(\frac{-E_{D2}}{R_D} \right) + \left\{ I_{D1} + \left(\frac{E_{D2}}{R_D} \right) \right\} e^{-\frac{R_D t}{L_D}}$$

$$= I_{D1} e^{-\frac{R_D t}{L_D}} - \left(\frac{E_{D2}}{R_D} \right) \left(1 - e^{-\frac{R_D t}{L_D}} \right) \quad \text{for } i_{D2} \geq 0 \quad (3.27)$$

This material is reserved for educational use only, not allowed for commercial use.

Forbidden to modify the content, and cite the document when use.

At the end of this mode at $\omega t = \alpha_2$, the load current becomes I_{D2} , where

$$I_{D2} = I_{D1} e^{\frac{-R_D t}{L_D}} - \left(\frac{E_{D2}}{R_D} \right) \left(1 - e^{\frac{-R_D t}{L_D}} \right) \quad \text{for } i_{D2} \geq 0 \quad (3.28)$$

Mode A3: The active components are shown in Figure 3.12. The switch T_{B-} and the anti-parallel diode D_{A-} of T_{A-} are conducting. The anti-parallel diode D_{A-} provides a path for the continuity of the load current. The load current during mode A3, i_{D3} , can be given by:

$$L_D \frac{di_{D3}}{dt} + R_D i_{D3} + E_{D3} = 0 \quad (3.29)$$

$$\frac{di_{D3}}{dt} + \frac{R_D}{L_D} i_{D3} = -\frac{E_{D3}}{L_D}$$

Equation (3.29) is similar to Equation (3.22) except for the current amplitude because of the initial condition value and time. The solution methodology of this mode is the same as for mode A2 and is expressed by:

$$i_{D3} = \left(\frac{-E_{D3}}{R_D} \right) + C_3 e^{\frac{-R_D t}{L_D}} \quad (3.30)$$

If the initial condition i_{D3} is I_{D2} at $\omega t = \alpha_3$ (for instance where $\alpha_3 \leq \omega t \leq \alpha_4$), the constant value C_3 can be determined from

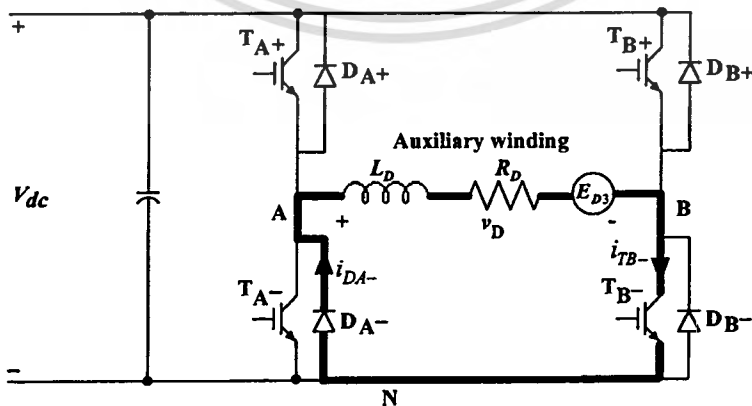


Figure 3.12 Current flow in mode A3

$$I_{D2} = \left(\frac{-E_{D3}}{R_D} \right) + C_3 \quad (3.31)$$

$$C_3 = I_{D2} + \left(\frac{E_{D3}}{R_D} \right)$$

The constant C_3 is superseded in Equation (3.30). As a result, the load current i_{D3} is given by:

$$i_{D3} = \left(\frac{-E_{D3}}{R_D} \right) + \left\{ I_{D2} + \left(\frac{E_{D3}}{R_D} \right) \right\} e^{\frac{-R_D t}{L_D}} \quad (3.32)$$

$$= I_{D2} e^{\frac{-R_D t}{L_D}} - \left(\frac{E_{D3}}{R_D} \right) \left(1 - e^{\frac{-R_D t}{L_D}} \right) \quad \text{for } i_{D3} \geq 0$$

At the end of this mode, the load current at $\omega t = \alpha_4$ becomes I_{D3} . That is defined by:

$$I_{D3} = I_{D2} e^{\frac{-R_D t}{L_D}} - \left(\frac{E_{D3}}{R_D} \right) \left(1 - e^{\frac{-R_D t}{L_D}} \right) \quad \text{for } i_{D3} \geq 0 \quad (3.33)$$

Mode A4: This mode is valid when the switching devices T_{A-} and T_{B+} turn on. The freewheeling diode D_{A-} and D_{B+} are conducting. The twice freewheeling diodes are used as a path for the continuity of the load current as drawn in Figure 3.13.

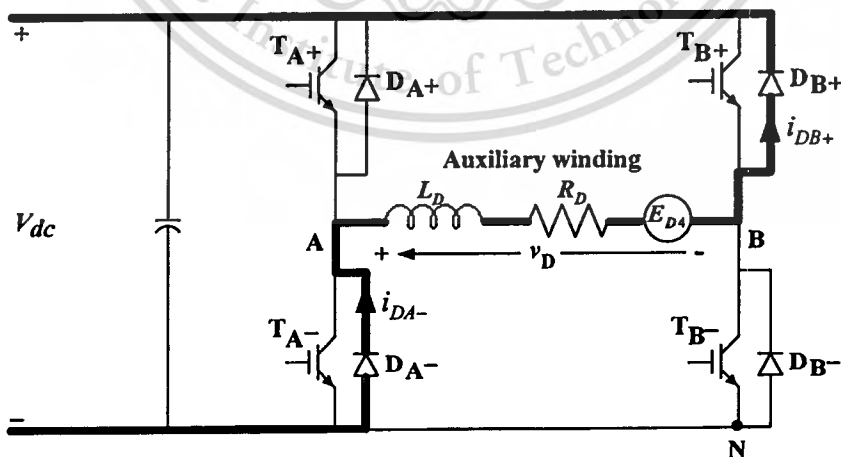


Figure 3.13 Current flow in mode A4

Although the reverse voltage is supplied across the winding, the current also continuously flows in the same direction similar to the previous mode. Because the average induced voltage is higher than the dc input voltage or $L_D \frac{di_{D4}}{dt} + R_D i_{D4} \geq V_{dc} - E_{D4}$, the current stabilizes the flow from load to supply. This mode occurs within a few pulses of the first negative half cycle. The current can be computed by Equation (3.34).

$$\begin{aligned}
 L_D \frac{di_{D4}}{dt} + R_D i_{D4} + E_{D4} &= V_{dc} \\
 \frac{di_{D4}}{dt} + \frac{R_D}{L_D} i_{D4} &= \frac{V_{dc} - E_{D4}}{L_D} \\
 i_{D4} &= \left(\frac{V_{dc} - E_{D4}}{R_D} \right) + C_4 e^{\frac{-R_D t}{L_D}}
 \end{aligned} \tag{3.34}$$

The constant C_4 can be determined from the initial condition. For example, when $\alpha_5 \leq \omega t \leq \alpha_6$, this mode starts at $\omega t = \alpha_5$ which provides $i_{D4} = I_{D3}$. This is expressed by:

$$\begin{aligned}
 I_{D3} &= \left(\frac{V_{dc} - E_D}{R_D} \right) + C_4 \\
 C_4 &= I_{D3} - \left(\frac{V_{dc} - E_D}{R_D} \right)
 \end{aligned} \tag{3.35}$$

Replacing C_4 gives

$$\begin{aligned}
 i_{D4} &= \left(\frac{V_{dc} - E_D}{R_D} \right) + \left\{ I_{D3} - \left(\frac{V_{dc} - E_D}{R_D} \right) \right\} e^{\frac{-R_D t}{L_D}} \\
 &= I_{D3} e^{\frac{-R_D t}{L_D}} + \left(\frac{V_{dc} - E_D}{R_D} \right) \left(1 - e^{\frac{-R_D t}{L_D}} \right) \quad \text{for } i_{D4} \geq 0
 \end{aligned} \tag{3.36}$$

At the end of this mode at $\omega t = \alpha_6$, the load current turns becomes I_{D4} and is given by:

$$I_{D4} = I_{D3} e^{\frac{-R_D t}{L_D}} + \left(\frac{V_{dc} - E_D}{R_D} \right) \left(1 - e^{\frac{-R_D t}{L_D}} \right) \quad \text{for } i_{D4} \geq 0 \tag{3.37}$$

Mode A5: This mode is valid when the switching devices T_{A-} and T_{B+} conduct. The input voltage V_{dc} is across the winding. Due to the fact that dc voltage source supplies more voltage than average induced voltage E_{D5} , the current flows from a source to load as shown in Figure 3.14. The load current i_{D5} can be analyzed as follows:

$$L_D \frac{di_{D5}}{dt} + R_D i_{D5} + E_{D5} = V_{dc}$$

$$\frac{di_{D5}}{dt} + \frac{R_D}{L_D} i_{D5} = \frac{V_{dc} - E_{D5}}{L_D} \quad (3.38)$$

$$i_{D5} = \left(\frac{V_{dc} - E_{D5}}{R_D} \right) + C_5 e^{\frac{-R_D t}{L_D}}$$

The constant C_5 can be resolved by the initial condition such as when $\alpha_7 \leq \omega t \leq \alpha_8$, and the mode begins at $\omega t = \alpha_7$. Hence, $i_{D4} = I_{D3}$, and C_5 is

$$I_{D4} = \left(\frac{V_{dc} - E_{D5}}{R_D} \right) + C_5$$

$$C_5 = I_{D4} - \left(\frac{V_{dc} - E_{D5}}{R_D} \right) \quad (3.39)$$

Substitution of C_5 gives

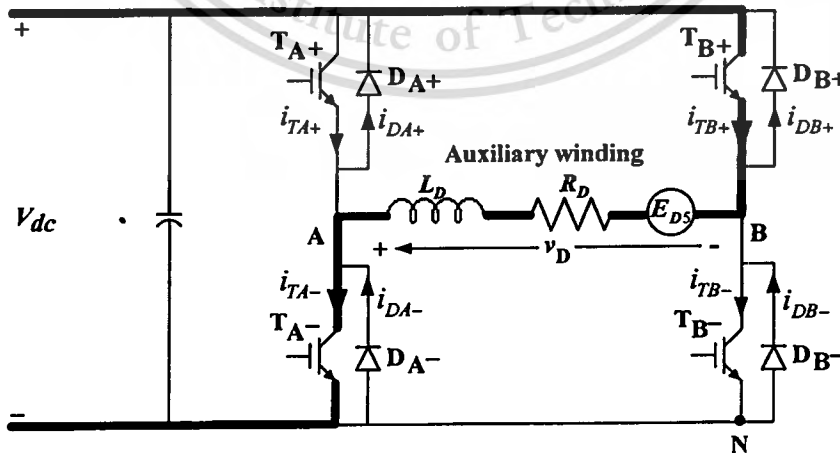


Figure 3.14 Current flow in mode A5

$$\begin{aligned}
 i_{D5} &= \left(\frac{V_{dc} - E_{D5}}{R_D} \right) + \left\{ I_{D4} - \left(\frac{V_{dc} - E_{D5}}{R_D} \right) \right\} e^{-\frac{R_D t}{L_D}} \\
 &= I_{D4} e^{-\frac{R_D t}{L_D}} + \left(\frac{V_{dc} - E_{D5}}{R_D} \right) \left(1 - e^{-\frac{R_D t}{L_D}} \right) \quad \text{for } i_{D5} \leq 0
 \end{aligned} \tag{3.40}$$

At the end of this mode at $\omega t = \alpha_3$, the load current becomes I_{D5} and is written as:

$$I_{D5} = I_{D4} e^{-\frac{R_D t}{L_D}} + \left(\frac{V_{dc} - E_{D5}}{R_D} \right) \left(1 - e^{-\frac{R_D t}{L_D}} \right) \quad \text{for } i_{D5} \leq 0 \tag{3.41}$$

Mode A6: At this mode, T_{A+} and T_{B+} are on. The output current circulates in a loop through the power switching device T_{B+} and the freewheeling diode D_{B+} as shown in Figure 3.15. Similarly to mode A2, the freewheeling diode contributes a path for the continuity of the load current. The load current i_{D6} can be expressed as:

$$\begin{aligned}
 L_D \frac{di_{D6}}{dt} + R_D i_{D6} + E_{D6} &= 0 \\
 \frac{di_{D6}}{dt} + \frac{R_D}{L_D} i_{D6} &= -\frac{E_{D6}}{L_D} \\
 e^{\frac{R_D t}{L_D}} i_{D6} &= \left(\frac{-E_{D6}}{R_D} \right) e^{\frac{R_D t}{L_D}} + C_6
 \end{aligned} \tag{3.42}$$

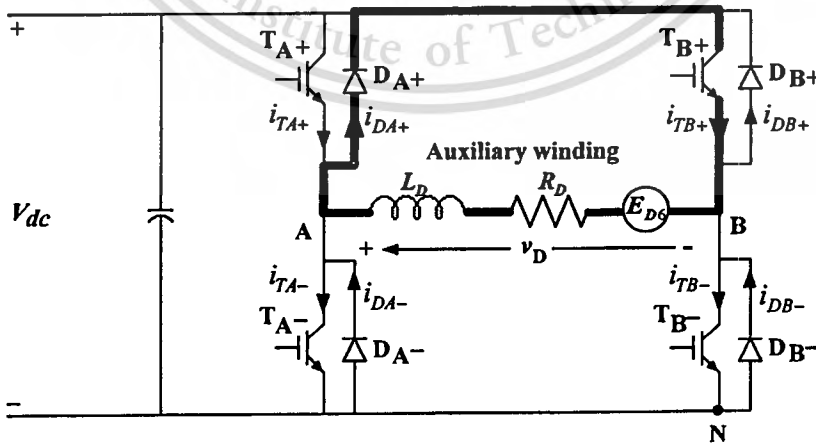


Figure 3.15 Current flow in mode A6

Dividing Equation (3.42) by $e^{\frac{R_D t}{L_D}}$ gives,

$$i_{D6} = \left(\frac{-E_{D6}}{R_D} \right) + C_6 e^{\frac{-R_D t}{L_D}} \quad (3.43)$$

The constant C_6 can be calculated from the initial condition such as when $\alpha_8 \leq \omega t \leq \alpha_9$ at $\omega t = \alpha_8, i_{D6} = I_{D5}$. This is given by:

$$I_{D5} = \left(\frac{-E_{D6}}{R_D} \right) + C_6 \quad (3.44)$$

$$C_6 = I_{D5} + \left(\frac{E_{D6}}{R_D} \right)$$

Substituting C_6 in Equation (3.43), the load current i_{D6} is:

$$\begin{aligned} i_{D6} &= \left(\frac{-E_{D6}}{R_D} \right) + \left\{ I_{D5} + \left(\frac{E_{D6}}{R_D} \right) \right\} e^{\frac{-R_D t}{L_D}} \\ &= I_{D5} e^{\frac{-R_D t}{L_D}} - \left(\frac{E_{D6}}{R_D} \right) \left(1 - e^{\frac{-R_D t}{L_D}} \right) \quad \text{for } i_{D6} \leq 0 \end{aligned} \quad (3.45)$$

At the end of this mode at $\omega t = \alpha_9$, the load current becomes I_{D6} . That is

$$I_{D6} = I_{D5} e^{\frac{-R_D t}{L_D}} - \left(\frac{E_{D6}}{R_D} \right) \left(1 - e^{\frac{-R_D t}{L_D}} \right) \quad \text{for } i_{D6} \leq 0 \quad (3.46)$$

Mode A7: The active components are shown in Figure 3.16. Switches T_{A-} and T_{B-} are on state. The switching device T_{A-} and the freewheeling diode D_{B-} are conducting. The load current i_{D7} flows continuously from T_{A-} through D_{B-} . The load current i_{D7} can be defined as follows:

$$I_{D7} = I_{D6} e^{\frac{-R_D t}{L_D}} - \left(\frac{E_{D7}}{R_D} \right) \left(1 - e^{\frac{-R_D t}{L_D}} \right) \quad \text{for } i_{D7} \leq 0 \quad (3.50)$$

Mode A8: This mode is available when the switches T_{A+} and T_{B-} conduct. The current in this mode flow from load to source as illustrated in Figure 3.17. The load current i_{D8} can be derived from Equation (3.51).

$$\begin{aligned} L_D \frac{di_{D8}}{dt} + R_D i_{D8} + E_{D8} &= V_{dc} \\ \frac{di_{D8}}{dt} + \frac{R_D}{L_D} i_{D8} &= \frac{V_{dc} - E_{D8}}{L_D} \\ \frac{d \left(e^{\frac{R_D t}{L_D}} i_{D8} \right)}{dt} &= \left(\frac{V_{dc} - E_{D8}}{L_D} \right) e^{\frac{R_D t}{L_D}} \\ i_{D8} &= \left(\frac{V_{dc} - E_{D8}}{R_D} \right) + C_8 e^{\frac{-R_D t}{L_D}} \end{aligned} \quad (3.51)$$

The constant C_8 can be determined from the initial condition. If $\alpha_{12} \leq \omega t \leq \alpha_{13}$, for example, an initial-state current at $\omega t = \alpha_{12}$ results in $i_{D8} = I_{D7}$.

$$\begin{aligned} I_{D7} &= \left(\frac{V_{dc} - E_{D8}}{R_D} \right) + C_8 \\ C_8 &= I_{D7} - \left(\frac{V_{dc} - E_{D8}}{R_D} \right) \end{aligned} \quad (3.52)$$

Substituting C_8 into Equation (3.52) gives

$$\begin{aligned} i_{D8} &= \left(\frac{V_{dc} - E_{D8}}{R_D} \right) + \left\{ I_{D7} - \left(\frac{V_{dc} - E_{D8}}{R_D} \right) \right\} e^{\frac{-R_D t}{L_D}} \\ &= I_{D7} e^{\frac{-R_D t}{L_D}} + \left(\frac{V_{dc} - E_{D8}}{R_D} \right) \left(1 - e^{\frac{-R_D t}{L_D}} \right) \quad \text{for } i_{D8} \leq 0 \end{aligned} \quad (3.53)$$

At the end of this mode at $\omega t = \alpha_{13}$, the load current changes to I_{D8} . That is

$$I_{D8} = I_{D7} e^{\frac{-R_D t}{L_D}} + \left(\frac{V_{dc} - E_{D8}}{R_D} \right) \left(1 - e^{\frac{-R_D t}{L_D}} \right) \quad \text{for } i_{D8} \leq 0 \quad (3.54)$$

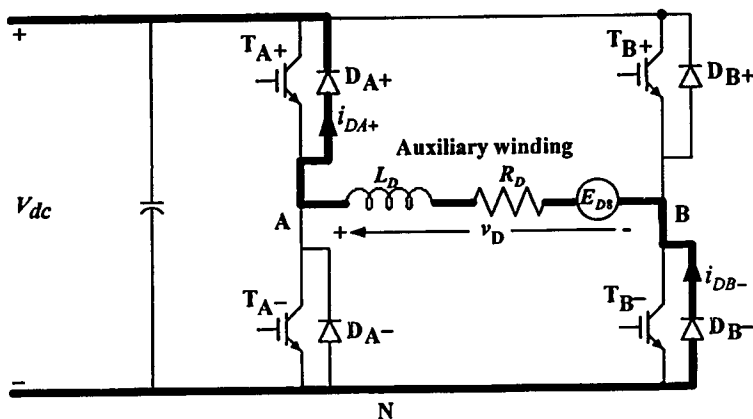


Figure 3.17 Current flow in mode A8

It is observed from the results that the final load current of the previous mode has to be the initial load current of the next step. At all regions of positive voltage level, switching devices (i.e. IGBTs in this research) toggle from modes A1 to A2. Then, turn to mode A1 and go to mode A3. After that, the modes in a loop sequence from A1-A2-A1-A3 until the voltage across the winding is changed from positive to negative. During this process, the load current can be separated step by step with modes A4-A2-A4-A3.

When the dc voltage level is more than the average induced voltage, the switching devices turn on/off from mode A5 to mode A6. After that, the devices switch to mode A5 and go to mode A7. In this stage, IGBTs operate following modes A5-A6-A5-A7. When the voltage across the winding is changed to the positive level, the maintained average induced voltage of the winding is still higher than the supply voltage. Consequently, the load current circulates from load to the supply. In this time, the current mode can be computed by modes A8-A6-A8-A7.

When the average induced voltage equals to dc voltage source, the instantaneous current is zero. After that, the current will flow in opposite direction and can be calculated by the next switching mode. That is, the devices are again driven according to modes A1-A2-A1-A3. It is noticed that modes A1-A4 contribute the positive voltage level (V_{dc} , 0) while modes A5-A8 provide the negative voltage level (0, $-V_{dc}$) across the auxiliary winding. Because the inductive parameter in the motor windings causes the current to lag, the instantaneous current position may lag the voltage stage. The relationship between voltage current and the step of switching device operations is summarized in Table 3.1.

The terminal voltage across the main winding is v_{BC} or v_Q which is in quadrature with v_D . As for the auxiliary winding current, the instantaneous load current of the main winding

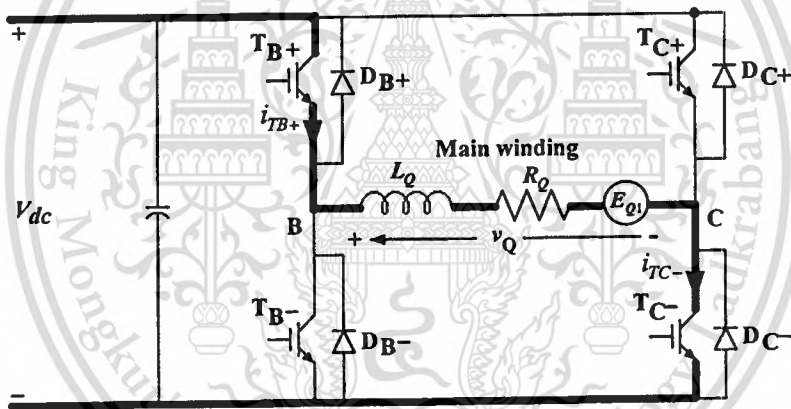
This material is reserved for educational use only, not allowed for commercial use.

Forbidden to modify the content, and cite the document when use.

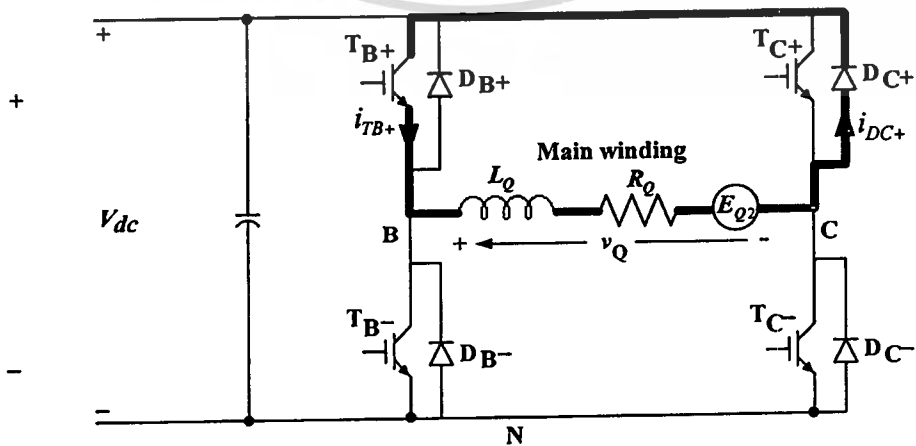
i_Q can be analyzed into eight modes. Current characteristics of each modes can be calculated using the same method as for the switching mode investigation of the auxiliary winding. Due to the discrepancy of both winding's impedance, the current amplitude and phase are not the same and are shifted in phase by nearly 90 electrical degrees. Eight mode current characteristics of the main winding (M1-M8) are illustrated in Figure 3.18 (a)-(h).

Table 3.1 Switch mode analysis

Description	Switching mode
$v \Rightarrow +, i \Rightarrow +$	A1-A2-A1-A3
$v \Rightarrow -, i \Rightarrow +$	A4-A2-A4-A3
$v \Rightarrow -, i \Rightarrow -$	A5-A6-A5-A7
$v \Rightarrow +, i \Rightarrow -$	A8-A6-A8-A7



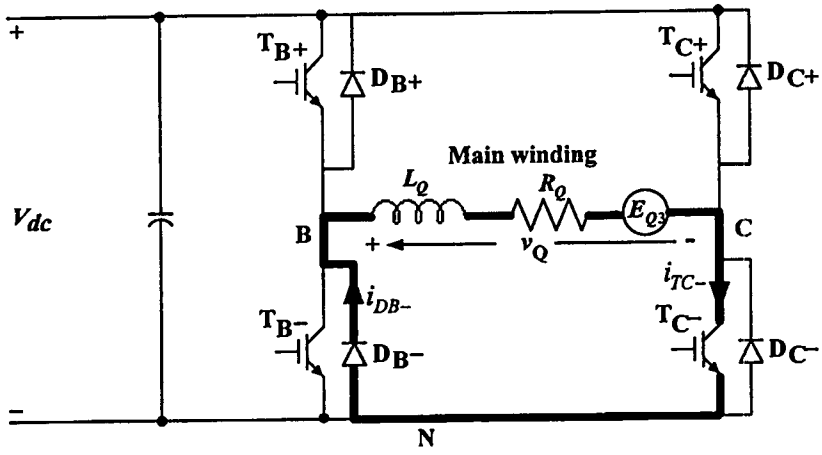
(a) mode M1



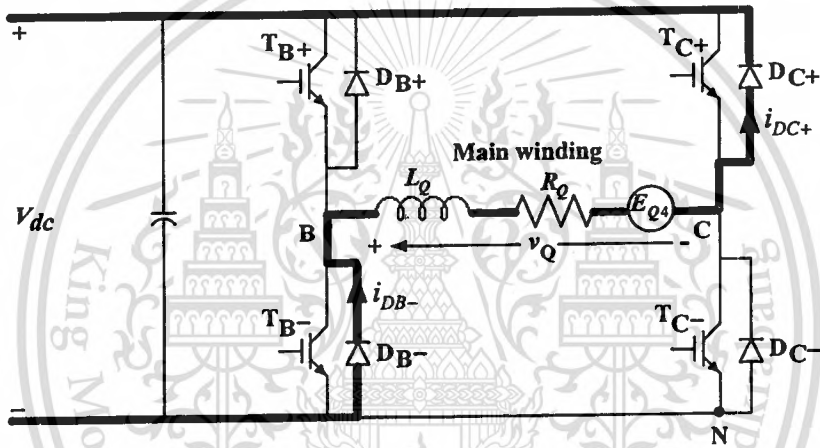
(b) mode M2

This material is reserved for educational use only, not allowed for commercial use.

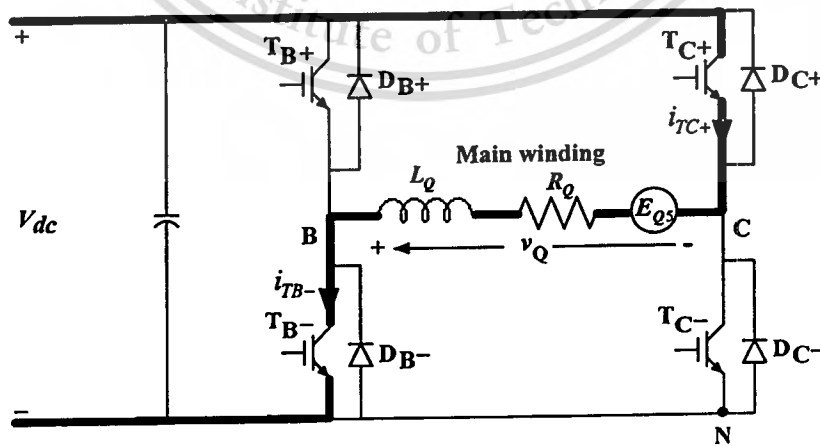
Forbidden to modify the content, and cite the document when use.



(c) mode M3



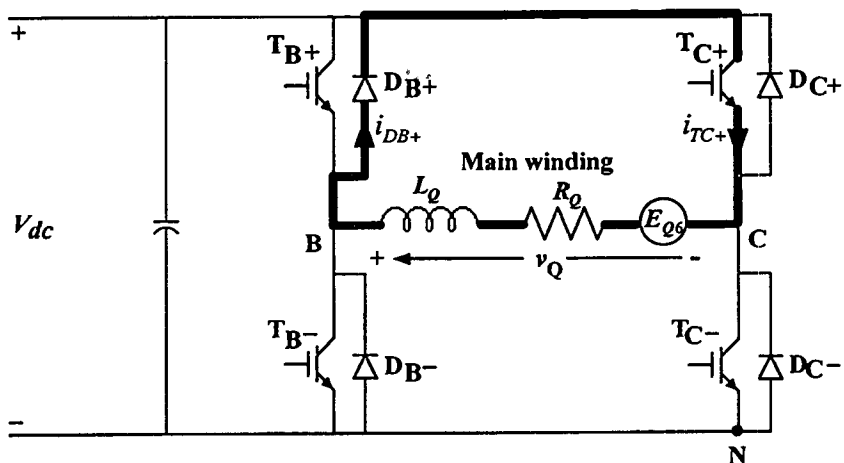
(d) mode M4



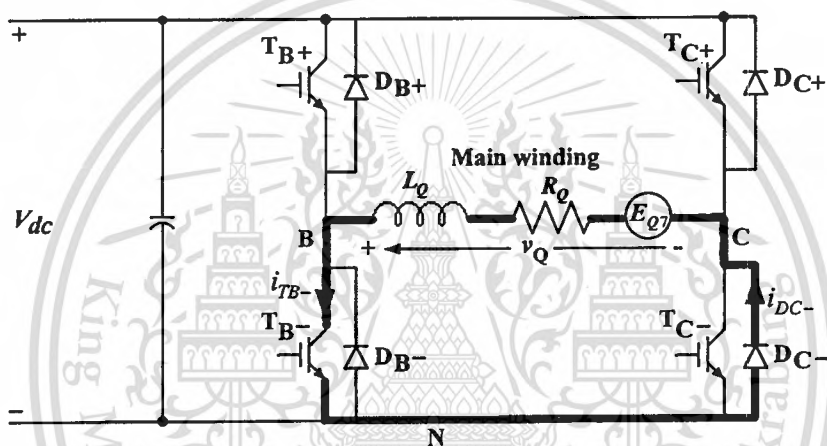
(e) mode M5

This material is reserved for educational use only, not allowed for commercial use.

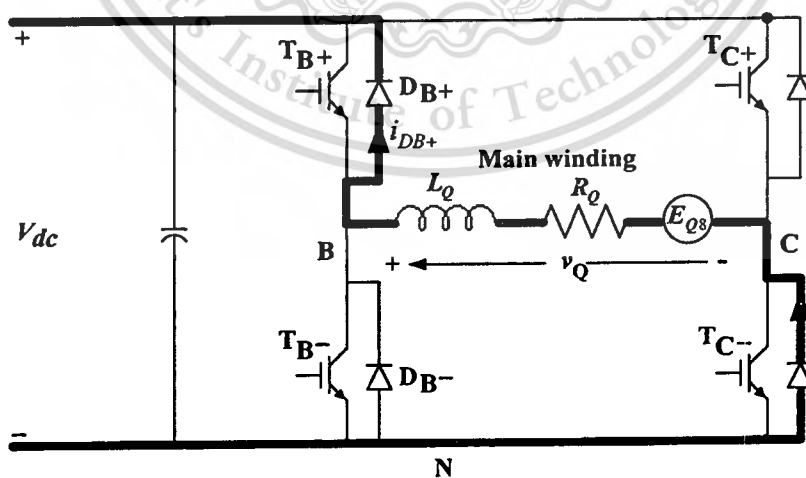
Forbidden to modify the content, and cite the document when use.



(f) mode M6



(g) mode M7



(h) mode M8

Figure 3.18 Current flow analysis of the main winding

This material is reserved for educational use only, not allowed for commercial use.

Forbidden to modify the content, and cite the document when use.

3.4 Mathematical Analysis

Determination of the harmonic frequency components of a PWM waveform is quite complex and is often done by using a Fast Fourier Transform analysis of a simulated time-varying switched waveform. Since the PWM waveform is not a periodic function, and no rational relationship exists between the modulating and the carrier frequencies, a Single Fourier Series approach is inapplicable. The best known analytical method of determining the harmonic components of a PWM switching was first developed by Bowes and Bird [74]. This analysis approach, with reference to pulse-duration modulation, was originally developed for communication systems by Bennet [75] and Black [76].

The analysis process assumes that the reference modulating wave is a single sinusoid with frequency ω_r radians per second. The carrier angular frequency is ω_c radians per second. The pulse train is non-periodic. Also both ω_r and ω_c are not commensurable. From the principle of Fourier transform theory [78], any regular time-varying waveform $f(t)$ can be expressed as a summation of its harmonic components

$$f(t) = \frac{a_0}{2} + \sum_{m=1}^{\infty} (a_m \cos m\omega t + b_m \sin m\omega t) \quad (3.55)$$

where

$$a_m = \frac{1}{\pi} \int_{-\pi}^{\pi} f(t) \cos m\omega t d(\omega t) \quad m = 0, 1, 2, \dots, \infty \quad (3.56)$$

$$b_m = \frac{1}{\pi} \int_{-\pi}^{\pi} f(t) \sin m\omega t d(\omega t) \quad m = 1, 2, 3, \dots, \infty \quad (3.57)$$

A waveform $f(x, y)$ varies as a function of two independent time variables

$$x(t) = \omega_c t + \theta_c \quad (3.58)$$

$$y(t) = \omega_r t + \theta_r \quad (3.59)$$

A simple Fourier series at a special value of $y = y_1$ can be written as

This material is reserved for educational use only, not allowed for commercial use.

Forbidden to modify the content, and cite the document when use.

$$f(x, y_1) = \frac{a_0(y_1)}{2} + \sum_{m=1}^{\infty} (a_m(y_1) \cos mx + b_m(y_1) \sin mx) \quad (3.60)$$

where

$$a_m(y_1) = \frac{1}{\pi} \int_{-\pi}^{\pi} f(x, y_1) \cos mx \, dx \quad m = 0, 1, 2, \dots, \infty \quad (3.61)$$

$$b_m(y_1) = \frac{1}{\pi} \int_{-\pi}^{\pi} f(x, y_1) \sin mx \, dx \quad m = 1, 2, 3, \dots, \infty \quad (3.62)$$

The coefficients $a_m(y_1)$ and $b_m(y_1)$ are clearly just particular values of two functions $a_m(y)$ and $b_m(y)$ which vary cyclically over the entire range of y . Consequently, the values of these coefficients are periodic with respect to y in an interval of 2π . These may be rewritten as follows for all possible values of y :

$$a_m(y) = \frac{c_{m0}}{2} + \sum_{n=1}^{\infty} [c_{mn} \cos ny + d_{mn} \sin ny] \, dx \quad m = 0, 1, 2, \dots, \infty \quad (3.63)$$

$$b_m(y) = \frac{e_{m0}}{2} + \sum_{n=1}^{\infty} [e_{mn} \cos ny + f_{mn} \sin ny] \, dx \quad m = 1, 2, 3, \dots, \infty \quad (3.64)$$

where

$$c_{mn} = \frac{1}{\pi} \int_{-\pi}^{\pi} a_m(y) \cos ny \, dy = \frac{1}{\pi^2} \int_{-\pi}^{\pi} \int_{-\pi}^{\pi} f(x, y) \cos mx \cos ny \, dx \, dy \quad (3.65)$$

$m = 0, 1, 2, \dots, \infty \quad n = 0, 1, 2, \dots, \infty$

$$d_{mn} = \frac{1}{\pi} \int_{-\pi}^{\pi} a_m(y) \sin ny \, dy = \frac{1}{\pi^2} \int_{-\pi}^{\pi} \int_{-\pi}^{\pi} f(x, y) \cos mx \sin ny \, dx \, dy \quad (3.66)$$

$m = 0, 1, 2, \dots, \infty \quad n = 1, 2, 3, \dots, \infty$

$$e_{mn} = \frac{1}{\pi} \int_{-\pi}^{\pi} b_m(y) \cos ny \, dy = \frac{1}{\pi^2} \int_{-\pi}^{\pi} \int_{-\pi}^{\pi} f(x, y) \sin mx \cos ny \, dx \, dy \quad (3.67)$$

$m = 1, 2, 3, \dots, \infty \quad n = 0, 1, 2, \dots, \infty$

$$f_{mn} = \frac{1}{\pi} \int_{-\pi}^{\pi} b_m(y) \sin ny \, dy = \frac{1}{\pi^2} \int_{-\pi}^{\pi} \int_{-\pi}^{\pi} f(x, y) \sin mx \sin ny \, dx \, dy \quad (3.68)$$

$$m = 1, 2, 3, \dots, \infty \quad n = 1, 2, 3, \dots, \infty$$

It is seen that the obtained solution is general for any time t since the x and y values are periodic. The second step is to expand these functions using trigonometric identities. Thus,

$$c_{mn} = \frac{1}{2\pi^2} \int_{-\pi}^{\pi} \int_{-\pi}^{\pi} f(x, y) \cos(mx + ny) \, dx \, dy$$

$$+ \frac{1}{2\pi^2} \int_{-\pi}^{\pi} \int_{-\pi}^{\pi} f(x, y) \cos(mx - ny) \, dx \, dy \quad (3.69)$$

$$m = 0, 1, 2, \dots, \infty \quad n = 0, 1, 2, \dots, \infty$$

$$d_{mn} = \frac{1}{2\pi^2} \int_{-\pi}^{\pi} \int_{-\pi}^{\pi} f(x, y) \sin(mx + ny) \, dx \, dy$$

$$- \frac{1}{2\pi^2} \int_{-\pi}^{\pi} \int_{-\pi}^{\pi} f(x, y) \sin(mx - ny) \, dx \, dy \quad (3.70)$$

$$m = 0, 1, 2, \dots, \infty \quad n = 1, 2, 3, \dots, \infty$$

$$e_{mn} = \frac{1}{2\pi^2} \int_{-\pi}^{\pi} \int_{-\pi}^{\pi} f(x, y) \sin(mx + ny) \, dx \, dy$$

$$+ \frac{1}{2\pi^2} \int_{-\pi}^{\pi} \int_{-\pi}^{\pi} f(x, y) \sin(mx - ny) \, dx \, dy \quad (3.71)$$

$$m = 1, 2, 3, \dots, \infty \quad n = 0, 1, 2, \dots, \infty$$

$$f_{mn} = \frac{1}{2\pi^2} \int_{-\pi}^{\pi} \int_{-\pi}^{\pi} f(x, y) \cos(mx - ny) \, dx \, dy$$

$$- \frac{1}{2\pi^2} \int_{-\pi}^{\pi} \int_{-\pi}^{\pi} f(x, y) \cos(mx + ny) \, dx \, dy \quad (3.72)$$

$$m = 1, 2, 3, \dots, \infty \quad n = 1, 2, 3, \dots, \infty$$

The general Fourier component form for $f(x, y)$ can now be expressed as

$$\begin{aligned}
 f(x, y) = & \frac{c_{00}}{2} + \frac{1}{2} \sum_{n=1}^{\infty} [c_{0n} \cos ny + d_{0n} \sin ny] + \frac{1}{2} \sum_{m=1}^{\infty} [c_{m0} \cos mx + d_{m0} \sin mx] \\
 & + \sum_{m=1}^{\infty} \sum_{n=1}^{\infty} \left[\begin{aligned} & (c_{mn} \cos ny + d_{mn} \sin ny) \cos mx \\ & + (e_{mn} \cos ny + f_{mn} \sin ny) \sin mx \end{aligned} \right]
 \end{aligned} \tag{3.73}$$

Using the trigonometric identities, Equation (3.30) can be rearranged to

$$\begin{aligned}
 f(x, y) = & \frac{c_{00}}{4} + \frac{1}{2} \sum_{n=1}^{\infty} [c_{0n} \cos ny + d_{0n} \sin ny] + \frac{1}{2} \sum_{m=1}^{\infty} [c_{m0} \cos mx + d_{m0} \sin mx] \\
 & + \sum_{m=1}^{\infty} \sum_{n=1}^{\infty} \left[\begin{aligned} & \frac{1}{2} [c_{mn} \cos(mx+ny) + c_{mn} \cos(mx-ny)] \\ & + \frac{1}{2} [d_{mn} \sin(mx+ny) - d_{mn} \sin(mx-ny)] \\ & + \frac{1}{2} [e_{mn} \sin(mx+ny) + e_{mn} \sin(mx-ny)] \\ & + \frac{1}{2} [f_{mn} \cos(mx-ny) - f_{mn} \cos(mx+ny)] \end{aligned} \right]
 \end{aligned} \tag{3.74}$$

which can be rewritten as

$$\begin{aligned}
 f(x, y) = & \frac{c_{00}}{4} + \frac{1}{2} \sum_{n=1}^{\infty} [c_{0n} \cos ny + d_{0n} \sin ny] + \frac{1}{2} \sum_{m=1}^{\infty} [c_{m0} \cos mx + d_{m0} \sin mx] \\
 & + \frac{1}{2} \sum_{m=1}^{\infty} \sum_{n=1}^{\infty} \left[\begin{aligned} & [(c_{mn} - f_{mn}) \cos(mx+ny)] + [(e_{mn} + d_{mn}) \sin(mx+ny)] \\ & + [(c_{mn} + f_{mn}) \cos(mx-ny)] + [(e_{mn} - d_{mn}) \sin(mx-ny)] \end{aligned} \right]
 \end{aligned} \tag{3.75}$$

For $m = 1, 2, 3, \dots, \infty$, $n = 1, 2, 3, \dots, \infty$ are

$$\frac{1}{2}(c_{mn} - f_{mn}) = \frac{1}{2\pi^2} \int_{-\pi}^{\pi} \int_{-\pi}^{\pi} f(x, y) \cos(mx+ny) dx dy \tag{3.76}$$

$$\frac{1}{2}(c_{mn} + f_{mn}) = \frac{1}{2\pi^2} \int_{-\pi}^{\pi} \int_{-\pi}^{\pi} f(x, y) \cos(mx-ny) dx dy \tag{3.77}$$

$$\frac{1}{2}(e_{mn} + d_{mn}) = \frac{1}{2\pi^2} \int_{-\pi}^{\pi} \int_{-\pi}^{\pi} f(x, y) \sin(mx+ny) dx dy \tag{3.78}$$

This material is reserved for educational use only, not allowed for commercial use.

Forbidden to modify the content, and cite the document when use.

$$\frac{1}{2}(e_{mn} - d_{mn}) = \frac{1}{2\pi^2} \int_{-\pi}^{\pi} \int_{-\pi}^{\pi} f(x, y) \sin(mx - ny) dx dy \quad (3.79)$$

Finally, it can be seen from Equations (3.66) and (3.68) that for any given value of n , $d_{mn} = -d_{m(-n)}$ and $f_{mn} = -f_{m(-n)}$ the $(mx - ny)$ terms in Equation (3.75) can be attained alternatively by summing the $(mx + ny)$ terms over negative n . Hence, the complete solution for $f(x, y)$, becomes

$$\begin{aligned} f(x, y) = & \frac{c_{00}}{4} + \frac{1}{2} \sum_{n=1}^{\infty} [c_{0n} \cos ny + d_{0n} \sin ny] + \frac{1}{2} \sum_{m=1}^{\infty} [c_{m0} \cos mx + d_{m0} \sin mx] \\ & + \frac{1}{2} \sum_{m=1}^{\infty} \sum_{\substack{n=-\infty \\ (n \neq 0)}}^{\infty} [(c_{mn} - f_{mn}) \cos(mx + ny) + (e_{mn} + d_{mn}) \sin(mx + ny)] \end{aligned} \quad (3.80)$$

To define the resultant coefficients into complex form, Equation (3.78) is multiplied by j , and added to Equation (3.76). The coefficients then become

$$\bar{C}_{mn} = A_{mn} + jB_{mn} = \frac{(c_{mn} - f_{mn})}{2} + j \frac{(e_{mn} + d_{mn})}{2} \quad (3.81)$$

where

$$\begin{aligned} A_{mn} + jB_{mn} = & \frac{1}{2\pi^2} \int_{-\pi}^{\pi} \int_{-\pi}^{\pi} f(x, y) [\cos(mx + ny) + j \sin(mx + ny)] dx dy \\ = & \frac{1}{2\pi^2} \int_{-\pi}^{\pi} \int_{-\pi}^{\pi} f(x, y) e^{j(mx+ny)} dx dy \end{aligned} \quad (3.82)$$

Equation (3.80) can now be expressed in terms of these alternative coefficients as

$$\begin{aligned} f(x, y) = & \frac{A_{00}}{2} + \sum_{n=1}^{\infty} [A_{0n} \cos ny + B_{0n} \sin ny] + \sum_{m=1}^{\infty} [A_{m0} \cos mx + B_{m0} \sin mx] \\ & + \sum_{m=1}^{\infty} \sum_{\substack{n=-\infty \\ (n \neq 0)}}^{\infty} [A_{mn} \cos(mx + ny) + B_{mn} \sin(mx + ny)] \end{aligned} \quad (3.83)$$

Equation (3.83) can be expressed in terms of time by substituting x and y from Equations (3.58) and (3.59), respectively. As a result,

$$\begin{aligned}
 f(t) = & \frac{A_{00}}{2} + \sum_{n=1}^{\infty} \left[A_{0n} \cos(n[\omega_r t + \theta_r]) + B_{0n} \sin(n[\omega_r t + \theta_r]) \right] \\
 & + \sum_{m=1}^{\infty} \left[A_{m0} \cos(m[\omega_c t + \theta_c]) + B_{m0} \sin(m[\omega_c t + \theta_c]) \right] \\
 & + \sum_{m=1}^{\infty} \sum_{\substack{n=-\infty \\ (n \neq 0)}}^{\infty} \left[A_{mn} \cos(m[\omega_c t + \theta_c] + n[\omega_r t + \theta_r]) \right. \\
 & \left. + B_{mn} \sin(m[\omega_c t + \theta_c] + n[\omega_r t + \theta_r]) \right]
 \end{aligned} \tag{3.84}$$

This $f(t)$ form is commonly used in the literature [74]. The carrier index variable m and the reference index variable n define the frequency of each harmonic component of the phase output voltage.

The first term of Equation (3.41), $\frac{A_{00}}{2}$ where $m = n = 0$, corresponds to the DC offset component of the pulse width-modulated waveform.

The second term, $\sum_{n=1}^{\infty} A_{0n} \cos(n[\omega_r t + \theta_r]) + B_{0n} \sin(n[\omega_r t + \theta_r])$ where $m = 0$, defines the desired fundamental output waveform for $n=1$ and includes undesirable low-order harmonics around the fundamental output for $1 < n \leq \infty$ which should be minimized or eliminated by the modulation process.

The third term, $\sum_{m=1}^{\infty} A_{m0} \cos(m[\omega_c t + \theta_c]) + B_{m0} \sin(m[\omega_c t + \theta_c])$ where $n = 0$, corresponds to the carrier wave harmonics. The lowest frequency term is the modulating carrier frequency, $m = 1$. For $1 < m \leq \infty$, the relatively high frequency components are generated.

Finally, the last term of the equation, $\sum_{m=1}^{\infty} \sum_{\substack{n=-\infty \\ (n \neq 0)}}^{\infty} A_{mn} \cos(m[\omega_c t + \theta_c] + n[\omega_r t + \theta_r])$ $+ B_{mn} \sin(m[\omega_c t + \theta_c] + n[\omega_r t + \theta_r])$ where $m \neq n \neq 0$, is related to the sideband harmonics which generally exist as groups around the carrier harmonic frequencies.

For this research, naturally sine-triangular modulation is preferred because it comprises lower harmonics than naturally sine-sawtooth modulation [77]. This type of modulation is a double-edge naturally sampled modulation [76]. The phase leg of VSI is switched to the upper DC rail when the sinusoidal reference waveform is greater than the triangular carrier waveform

This material is reserved for educational use only, not allowed for commercial use.

Forbidden to modify the content, and cite the document when use.

(i.e. $v_{reference} > v_{carrier}$, $v_{AN} = \frac{V_{dc}}{2}$), and to the lower DC rail when the carrier waveform is greater than the reference waveform (i.e. $v_{reference} < v_{carrier}$, $v_{AN} = \frac{-V_{dc}}{2}$) [71]. To obtain a sinusoidal output using this harmonic components approach, the sinusoidal reference waveform has the form

$$v_{an} = M \sin(\omega_r t + \theta_r) = M \sin y \quad (3.85)$$

where

M = modulation index or modulation depth

ω_r = reference output or baseband frequency

θ_r = arbitrary output phase

V_{dc} = DC voltage

The unit cell for sine-triangle single phase modulation is shown in Figure 3.19. The unit cell is defined over the interval $-\pi < \omega_c t < \pi$ rather than from 0 to 2π for simplicity of result. Over multiple carrier and fundamental cycles, the sinusoidal waveform replicates over the x, y plane. The slope of line A in Figure 3.20 (a) is a sinusoidal waveform against the carrier waveform, that is $\frac{y}{x} = \frac{\omega_r}{\omega_c}$ or the so-called carrier ratio. If p is the number of the cell along the x axis, counted from the origin, the sinusoidal reference waveform for double-edge naturally sampled modulation can be expressed as:

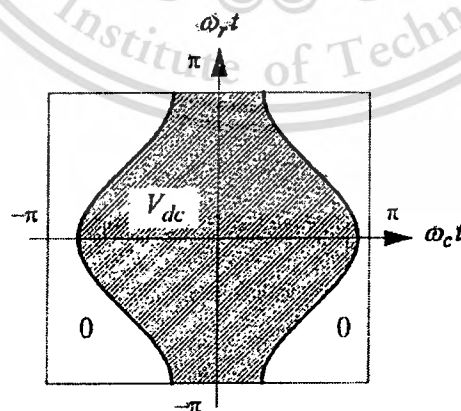


Figure 3.19 The unit cell for sine-triangular single phase modulation

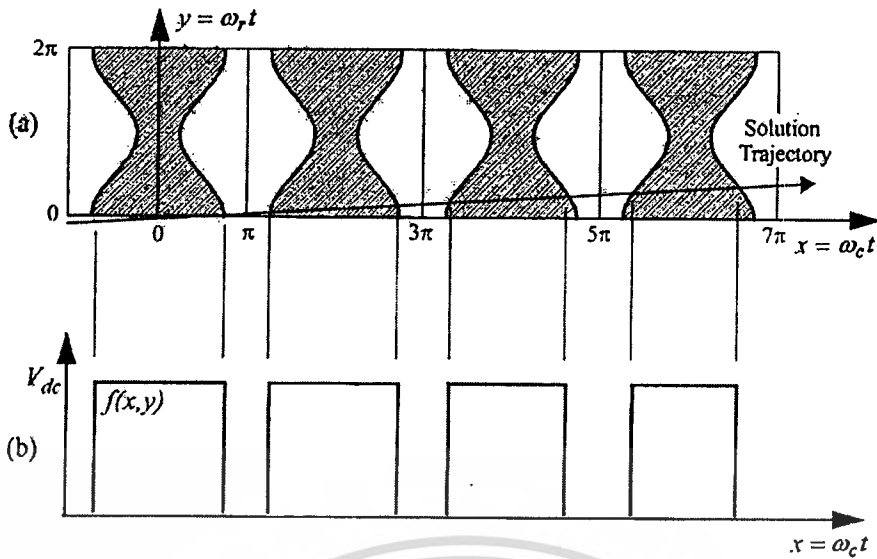


Figure 3.20 Double-edge naturally sampled PWM of a bipolar half-bridge phase leg

(a) x, y plane showing intersection of reference with unit cells

(b) x, y plane showing resulting PWM voltage

For $f(x, y)$ changing from 0 to V_{dc}

$$x = 2\pi p - \frac{\pi}{2}(1 + M \sin \omega_r t) \quad p = 0, 1, 2, \dots, \infty \quad (3.86)$$

and for $f(x, y)$ changing from V_{dc} to 0

$$x = 2\pi p + \frac{\pi}{2}(1 + M \sin \omega_r t) \quad p = 0, 1, 2, \dots, \infty \quad (3.87)$$

The switched voltage $v_{AN}(t)$ measured from the phase output voltage then becomes the waveform indicated in Figure 3.20 (b). Under the integration limits defined by Equations (3.86) and (3.87), Equation (3.81) becomes

$$\bar{C}_{mn} = A_{mn} + jB_{mn} = \frac{1}{2\pi^2} \int_{-\pi}^{\pi} \int_{-\frac{\pi}{2}(1+M \sin y)}^{\frac{\pi}{2}(1+M \sin y)} V_{dc} e^{j(mx+ny)} dx dy \quad (3.88)$$

For $m = n = 0$,

This material is reserved for educational use only, not allowed for commercial use.

Forbidden to modify the content, and cite the document when use.

$$\begin{aligned}
 A_{00} + jB_{00} &= \frac{V_{dc}}{2\pi^2} \int_{-\pi}^{\pi} \int_{-\frac{\pi}{2}(1+M \sin y)}^{\frac{\pi}{2}(1+M \sin y)} dx dy \\
 &= \frac{V_{dc}}{2\pi^2} \int_{-\pi}^{\pi} \pi(1 + M \sin y) dy \\
 &= V_{dc}
 \end{aligned} \tag{3.89}$$

Therefore, $A_{00} = V_{dc}$, $B_{00} = 0$.

For $m = 0$, $n > 0$, thus

$$\begin{aligned}
 A_{0n} + jB_{0n} &= \frac{V_{dc}}{2\pi^2} \int_{-\pi}^{\pi} \int_{-\frac{\pi}{2}(1+M \sin y)}^{\frac{\pi}{2}(1+M \sin y)} e^{jny} dx dy \\
 &= \frac{V_{dc}}{2\pi^2} \int_{-\pi}^{\pi} \pi(1 + M \sin y) e^{jny} dy
 \end{aligned} \tag{3.90}$$

From $\sin y = \frac{e^{jy} - e^{-jy}}{2j}$, Equation (3.90) becomes

$$\begin{aligned}
 A_{0n} + jB_{0n} &= \frac{V_{dc}}{2\pi} \int_{-\pi}^{\pi} e^{jny} + Me^{jny} \sin y dy \\
 &= \frac{V_{dc}}{2\pi} \int_{-\pi}^{\pi} e^{jny} + \frac{Me^{jny}}{2j} (e^{jy} - e^{-jy}) dy \\
 &= \frac{V_{dc}}{2\pi} \int_{-\pi}^{\pi} e^{jny} + \frac{Me^{jny}}{2j} (e^{j(n+1)y} - e^{j(n-1)y}) dy
 \end{aligned} \tag{3.91}$$

Since for any nonzero value of n ,

$$\begin{aligned}
 \int_{-\pi}^{\pi} e^{jny} dy &= \frac{e^{jny}}{jn} \Big|_{-\pi}^{\pi} = \frac{1}{jn} [e^{jn\pi} - e^{-jn\pi}] \\
 &= \frac{2e^n}{n} \left[\frac{e^{j\pi} - e^{-j\pi}}{2j} \right] = \frac{2e^n}{n} \sin \pi = 0
 \end{aligned} \tag{3.92}$$

Therefore, Equation (3.90) should be rewritten as

$$A_{0n} + jB_{0n} = \begin{cases} \frac{V_{dc}}{2\pi} \int_{-\pi}^{\pi} \frac{M}{2j} dy & \text{for } n=1 \\ 0 & \text{for } n \neq 1 \end{cases} \quad (3.93)$$

Equation (3.93) can be simplified to

$$\begin{aligned} A_{01} + jB_{01} &= \frac{V_{dc}}{2\pi} \int_{-\pi}^{\pi} \frac{M}{2j} dy \\ &= j \frac{MV_{dc}}{2} \end{aligned} \quad (3.94)$$

For $m > 0, n = 0$,

$$\begin{aligned} A_{m0} + jB_{m0} &= \frac{V_{dc}}{2\pi^2} \int_{-\pi}^{\pi} \int_{-\frac{\pi}{2}(1+M \sin y)}^{\frac{\pi}{2}(1+M \sin y)} e^{jmx} dx dy \\ &= \frac{V_{dc}}{j2m\pi^2} \int_{-\pi}^{\pi} e^{jm\frac{\pi}{2}(1+M \sin y)} - e^{-jm\frac{\pi}{2}(1+M \sin y)} dy \end{aligned} \quad (3.95)$$

From the Bessel function integral expression $\int_{-\pi}^{\pi} e^{j\xi \sin \theta - n\theta} d\theta = 2\pi J_n(\xi)$ [79], Equation (3.95)

becomes

$$A_{m0} + jB_{m0} = \frac{V_{dc}}{jm\pi} \left[e^{jm\frac{\pi}{2}} J_0\left(m\frac{\pi}{2}M\right) - e^{-jm\frac{\pi}{2}} J_0\left(-m\frac{\pi}{2}M\right) \right] \quad (3.96)$$

and from $J_0(-\xi) = J_0(\xi)$,

$$A_{m0} + jB_{m0} = \frac{2V_{dc}}{m\pi} J_0\left(mM\frac{\pi}{2}\right) \sin\left(m\frac{\pi}{2}\right) \quad (3.97)$$

For $m > 0, n \neq 0$, Equation (3.88) can be written as follows

$$\begin{aligned}
A_{mn} + jB_{mn} &= \frac{V_{dc}}{j2m\pi^2} \int_{-\pi}^{\pi} e^{jny} \left[e^{jm\frac{\pi}{2}(1+M\sin y)} - e^{-jm\frac{\pi}{2}(1+M\sin y)} \right] dy \\
&= \frac{V_{dc}}{j2m\pi^2} \int_{-\pi}^{\pi} \left[e^{jny} e^{jm\frac{\pi}{2}} e^{jm\frac{\pi}{2}M\sin y} - e^{jny} e^{-jm\frac{\pi}{2}} e^{-jm\frac{\pi}{2}M\sin y} \right] dy
\end{aligned} \tag{3.98}$$

Using the Bessel function integral expression, Equation (3.98) then becomes

$$\begin{aligned}
A_{mn} + jB_{mn} &= \frac{V_{dc}}{jm\pi} \left[e^{jm\frac{\pi}{2}} j^n J_n \left(mM \frac{\pi}{2} \right) - e^{-jm\frac{\pi}{2}} j^{-n} J_n \left(mM \frac{\pi}{2} \right) \right] \\
&= \frac{V_{dc}}{jm\pi} J_n \left(mM \frac{\pi}{2} \right) \left[e^{jm\frac{\pi}{2}} e^{jn\frac{\pi}{2}} - e^{-jm\frac{\pi}{2}} e^{-jn\frac{\pi}{2}} \right] \\
&= \frac{2V_{dc}}{m\pi} J_n \left(mM \frac{\pi}{2} \right) \sin \left[(m+n) \frac{\pi}{2} \right]
\end{aligned} \tag{3.99}$$

The complete solution for sine-triangle double-edge naturally sampled modulation of a bipolar half-bridge phase leg can now be formed by substituting the results of Equations (3.89), (3.94), (3.97) and (3.99) back into Equation (3.84). The time-varying phase output voltage $v_{AN}(t)$ can be expressed in terms of harmonic voltage components as

$$\begin{aligned}
v_{AN}(t) &= \frac{V_{dc}}{2} + \frac{MV_{dc}}{2} \sin(\omega_r t + \theta_r) + \frac{2V_{dc}}{\pi} \sum_{m=1}^{\infty} \frac{J_0(mM\frac{\pi}{2})}{m} \sin(m\frac{\pi}{2}) \cos(m\omega_c t + \theta_c) \\
&\quad + \frac{2V_{dc}}{\pi} \sum_{m=1}^{\infty} \sum_{n=\pm 1}^{\pm \infty} \frac{J_n(mM\frac{\pi}{2})}{m} \sin \left[(m+n) \frac{\pi}{2} \right] \cos \left[m(\omega_c t + \theta_c) + n(\omega_r t + \theta_r) \right]
\end{aligned} \tag{3.100}$$

For two-level natural sampled PWM with a triangular carrier signal, the phase voltage across terminals A , B and C to node N along with the control signals of v_{an} , v_{bn} and v_{cn} , respectively (see Figures 2.7 and 3.5) can be described as follows:

$$\begin{aligned}
v_{AN}(t) = & \frac{V_{dc}}{2} + \frac{MV_{dc}}{2} \sin(\omega_r t) + \frac{2V_{dc}}{\pi} \sum_{m=1}^{\infty} \frac{J_o(mM \frac{\pi}{2})}{m} \sin(m \frac{\pi}{2}) \cos(m\omega_c t) \\
& + \frac{2V_{dc}}{\pi} \sum_{m=1}^{\infty} \sum_{n=\pm 1}^{\pm \infty} \frac{J_n(mM \frac{\pi}{2})}{m} \sin \left[(m+n) \frac{\pi}{2} \right] \cos(m\omega_c t + n\omega_r t)
\end{aligned} \tag{3.101}$$

$$\begin{aligned}
v_{BN}(t) = & \frac{V_{dc}}{2} + \frac{MV_{dc}}{2} \sin(\omega_r t - \frac{\pi}{2}) + \frac{2V_{dc}}{\pi} \sum_{m=1}^{\infty} \frac{J_o(mM \frac{\pi}{2})}{m} \sin(m \frac{\pi}{2}) \cos(m\omega_c t) \\
& + \frac{2V_{dc}}{\pi} \sum_{m=1}^{\infty} \sum_{n=\pm 1}^{\pm \infty} \frac{J_n(mM \frac{\pi}{2})}{m} \sin \left[(m+n) \frac{\pi}{2} \right] \cos \left[m\omega_c t + n \left(\omega_r t - \frac{\pi}{2} \right) \right]
\end{aligned} \tag{3.102}$$

$$\begin{aligned}
v_{CN}(t) = & \frac{V_{dc}}{2} + \frac{MV_{dc}}{2} \sin(\omega_r t - \pi) + \frac{M_1 V_{dc}}{2} \sin(\omega_r t - \frac{\pi}{4}) \\
& + \frac{2V_{dc}}{\pi} \sum_{m=1}^{\infty} \frac{J_o(mM \frac{\pi}{2})}{m} \sin(m \frac{\pi}{2}) \cos(m\omega_c t) \\
& + \frac{2V_{dc}}{\pi} \sum_{m=1}^{\infty} \frac{J_o(mM_1 \frac{\pi}{2})}{m} \sin(m \frac{\pi}{2}) \cos(m\omega_c t) \\
& + \frac{2V_{dc}}{\pi} \sum_{m=1}^{\infty} \sum_{n=\pm 1}^{\pm \infty} \frac{J_n(mM \frac{\pi}{2})}{m} \sin \left[(m+n) \frac{\pi}{2} \right] \cos \left[m\omega_c t + n(\omega_r t - \pi) \right] \\
& + \frac{2V_{dc}}{\pi} \sum_{m=1}^{\infty} \sum_{n=\pm 1}^{\pm \infty} \frac{J_n(mM_1 \frac{\pi}{2})}{m} \sin \left[(m+n) \frac{\pi}{2} \right] \cos \left[m\omega_c t + n \left(\omega_r t - \frac{\pi}{4} \right) \right]
\end{aligned} \tag{3.103}$$

Hence, the instantaneous PWM output voltage across the auxiliary winding $v_{AB}(t)$ is

$$\begin{aligned}
v_{AB}(t) &= v_{AN}(t) - v_{BN}(t) \\
&= \frac{MV_{dc}}{2} \sin(\omega_r t) - \frac{MV_{dc}}{2} \sin(\omega_r t - \frac{\pi}{2}) \\
&\quad + \frac{2V_{dc}}{\pi} \sum_{m=1}^{\infty} \frac{J_0(mM \frac{\pi}{2})}{m} \sin(m \frac{\pi}{2}) \cos(m\omega_c t) \\
&\quad - \frac{2V_{dc}}{\pi} \sum_{m=1}^{\infty} \frac{J_0(mM \frac{\pi}{2})}{m} \sin(m \frac{\pi}{2}) \cos(m\omega_c t) \\
&\quad + \frac{2V_{dc}}{\pi} \sum_{m=1}^{\infty} \sum_{n=-\infty}^{\infty} \frac{J_n(mM \frac{\pi}{2})}{m} \sin\left[(m+n) \frac{\pi}{2}\right] \cos[m\omega_c t + n(\omega_r t)] \\
&\quad - \frac{2V_{dc}}{\pi} \sum_{m=1}^{\infty} \sum_{n=-\infty}^{\infty} \frac{J_n(mM \frac{\pi}{2})}{m} \sin\left[(m+n) \frac{\pi}{2}\right] \cos\left[m\omega_c t + n(\omega_r t - \frac{\pi}{2})\right]
\end{aligned} \tag{3.104}$$

The PWM output voltage for the auxiliary winding given by an instantaneous terminal voltage $v_{AB}(t)$ consists of six terms:

- a) Terms 1 and 2 generate the fundamental amplitude voltages for each phase. After rearrangement, the fundamental voltage across the auxiliary winding is

$$\begin{aligned}
v_{D1} &= \frac{MV_{dc}}{2} \sin(\omega_r t) - \frac{MV_{dc}}{2} \sin(\omega_r t - \frac{\pi}{2}) \\
&= \frac{MV_{dc}}{2} \left[\sin(\omega_r t) - \sin(\omega_r t - \frac{\pi}{2}) \right] \\
&= \frac{\sqrt{2}}{2} MV_{dc} \sin(\omega_r t + \frac{\pi}{4})
\end{aligned} \tag{3.105}$$

The fundamental voltage is directly proportional to the modulation index M . It is noticed that, when compared to the conventional half bridge VSI, the proposed technique offers increased dc voltage utilization by a factor of 1.414.

- b) Terms 3 and 4 represent the amplitude of the harmonics at the carrier frequency and multiples of carrier frequency for each phase which are equal, resulting in cancellation in Equation (3.18). This means that harmonics at the carrier frequency and multiples of the carrier frequency are absent i.e. harmonics of the order of $m_f, 2m_f, 3m_f, \dots$, where the modulation frequency ratio or modulation index $m_f = \frac{\omega_c}{\omega_r}$.

This material is reserved for educational use only, not allowed for commercial use.

Forbidden to modify the content, and cite the document when use.

c) Terms 5 and 6 provide the amplitudes of the harmonics in the sidebands around each multiple of the carrier frequency. According to the $\sin\left[(m+n)\frac{\pi}{2}\right]$ part,

i) only even-order sidebands exist for odd harmonics of the carrier i.e. harmonics of the order of $m_f \pm 2, m_f \pm 4, 3m_f \pm 2, 3m_f \pm 4, \dots$,

ii) only odd-order sidebands exist for even harmonics of the carrier i.e. harmonics of the order of $2m_f \pm 1, 2m_f \pm 3, 4m_f \pm 1, 4m_f \pm 3, \dots$,

It is noticed that these harmonic characteristics are similar to a single phase unipolar PWM [21, 71-72].

The PWM output voltage for the main winding is an instantaneous voltage $v_{BC}(t)$.

$$\begin{aligned}
 v_{BC}(t) &= v_{BN}(t) - v_{CN}(t) \\
 &= \frac{MV_{dc}}{2} \sin(\omega_r t - \frac{\pi}{2}) - \frac{MV_{dc}}{2} \sin(\omega_r t - \pi) - \frac{M_1 V_{dc}}{2} \sin(\omega_r t - \frac{\pi}{4}) \\
 &\quad + \frac{2V_{dc}}{\pi} \sum_{m=1}^{\infty} \frac{J_o(mM\frac{\pi}{2})}{m} \sin(m\frac{\pi}{2}) \cos(m\omega_c t) \\
 &\quad - \frac{2V_{dc}}{\pi} \sum_{m=1}^{\infty} \frac{J_o(mM\frac{\pi}{2})}{m} \sin(m\frac{\pi}{2}) \cos(m\omega_c t) \\
 &\quad - \frac{2V_{dc}}{\pi} \sum_{m=1}^{\infty} \frac{J_o(mM_1\frac{\pi}{2})}{m} \sin(m\frac{\pi}{2}) \cos(m\omega_c t) \\
 &\quad + \frac{2V_{dc}}{\pi} \sum_{m=1}^{\infty} \sum_{n=\pm 1}^{\pm \infty} \frac{J_n(mM\frac{\pi}{2})}{m} \sin\left[(m+n)\frac{\pi}{2}\right] \cos\left[m\omega_c t + n(\omega_r t - \frac{\pi}{2})\right] \\
 &\quad - \frac{2V_{dc}}{\pi} \sum_{m=1}^{\infty} \sum_{n=\pm 1}^{\pm \infty} \frac{J_n(mM\frac{\pi}{2})}{m} \sin\left[(m+n)\frac{\pi}{2}\right] \cos\left[m\omega_c t + n(\omega_r t - \pi)\right] \\
 &\quad - \frac{2V_{dc}}{\pi} \sum_{m=1}^{\infty} \sum_{n=\pm 1}^{\pm \infty} \frac{J_n(mM_1\frac{\pi}{2})}{m} \sin\left[(m+n)\frac{\pi}{2}\right] \cos\left[m\omega_c t + n(\omega_r t - \frac{\pi}{4})\right]
 \end{aligned} \tag{3.106}$$

The instantaneous PWM output voltage $v_{BC}(t)$ comprises nine terms:

- a) Terms 1, 2 and 3 give the fundamental amplitude voltage. The fundamental voltage across the main winding can be rearranged as

This material is reserved for educational use only, not allowed for commercial use.

Forbidden to modify the content, and cite the document when use.

$$\begin{aligned}
v_{Q1} &= \frac{MV_{dc}}{2} \sin(\omega_r t - \frac{\pi}{2}) + \frac{MV_{dc}}{2} \sin(\omega_r t) - \frac{M_1 V_{dc}}{2} \sin(\omega_r t - \frac{\pi}{4}) \\
&= \frac{MV_{dc}}{2} [\sin(\omega_r t) - \cos(\omega_r t)] - \frac{M_1 V_{dc}}{2} \left[\cos(\omega_r t) \cos\left(\frac{\pi}{4}\right) - \sin(\omega_r t) \sin\left(\frac{\pi}{4}\right) \right] \\
&= \frac{MV_{dc}}{2} [\sin(\omega_r t) - \cos(\omega_r t)] - \frac{M_1 V_{dc}}{2\sqrt{2}} [\sin \omega_r t - \cos \omega_r t] \\
&= \left(\frac{\sqrt{2}MV_{dc}}{2} - \frac{M_1 V_{dc}}{2} \right) \sin(\omega_r t - \frac{\pi}{4})
\end{aligned} \tag{3.107}$$

When comparing the voltage v_{D1} with v_{Q1} , it is clearly shown that the phase shifting between the main and the auxiliary winding voltage is in quadrature. Moreover, the fundamental amplitude of the main winding voltage can be arbitrarily controlled by M_1 .

- b) Terms 4, 5 and 6 provide the amplitude of harmonics at the carrier frequency and multiples of the carrier frequency. Since terms 4 and 5 are cancelled, and the magnitude of M_1 in term 6 is less than M , the harmonics magnitude at the carrier frequency and multiples of carrier frequency generated from M_1 in part of the proposed modulation scheme is lower than those harmonics produced from M in the portion of the two-leg inverter. Due to the $\sin\left(\frac{m\pi}{2}\right)$ part with $m=2, 4, 6, \dots$, there are no harmonics at even multiples of the carrier frequency.
- c) Terms 7, 8 and 9 generate the amplitude of the harmonics in the sidebands around each multiple of the carrier frequency. As for terms 5 and 6 of $v_{AB}(t)$, only even-order sidebands exist for odd harmonics of the carrier, and only odd-order sidebands are maintained for even harmonics of the carrier. Where u , w and s are variables, let

$$\begin{aligned}
u &= \frac{2V_{dc}}{\pi} \sum_{m=1}^{\infty} \sum_{n=\pm 1}^{\pm \infty} \frac{J_n(mM \frac{\pi}{2})}{m} \sin\left[(m+n)\frac{\pi}{2}\right] \cos\left[m\omega_c t + n(\omega_r t - \frac{\pi}{2})\right] \\
w &= \frac{2V_{dc}}{\pi} \sum_{m=1}^{\infty} \sum_{n=\pm 1}^{\pm \infty} \frac{J_n(mM \frac{\pi}{2})}{m} \sin\left[(m+n)\frac{\pi}{2}\right] \cos\left[m\omega_c t + n(\omega_r t - \pi)\right] \\
s &= \frac{2V_{dc}}{\pi} \sum_{m=1}^{\infty} \sum_{n=\pm 1}^{\pm \infty} \frac{J_n(mM_1 \frac{\pi}{2})}{m} \sin\left[(m+n)\frac{\pi}{2}\right] \cos\left[m\omega_c t + n(\omega_r t - \frac{\pi}{4})\right]
\end{aligned} \tag{3.108}$$

Owing to $M > M_1$, and with the property of the Bessel function, it can be

This material is reserved for educational use only, not allowed for commercial use.

Forbidden to modify the content, and cite the document when use.

determined that, under the same conditions, the values of u and w have to be more than that of s . Because the harmonic sidebands of 3-leg VSI with the proposed modulation technique are made up of $u + w - s$ whilst those of 2-leg VSI are composed of u , the harmonic sidebands around each multiple of the carrier frequency of the proposed technique yield a slightly higher amplitude than those of the conventional technique.

The amplitude of the fundamental output voltage of the auxiliary voltage is only proportional to the modulation index M , while that of the main winding is directly governed by both M and M_1 . In order to control the magnitude of each output phase voltage in accordance with the control methodology in Figure 2.7 in Chapter 2, the appropriate M and M_1 can be set. However, overmodulating operation for a beyond base speed region is not considered. In order to examine harmonic contents, the dominant harmonic voltages normalized by the fundamental components as a function of modulation index are computed as shown in Figures 3.21 and 3.22 for 2-leg VSI and 3-leg VSI, respectively. Only the harmonics with significant amplitude are plotted. From these two figures, it can be seen that, due to the additional modulating function for the desired main windings voltage control methodology, the unipolar PWM scheme of the 3-leg VSI comprises lower harmonic voltages than the bipolar PWM pattern of 2-leg VSI, especially at m_f . This implies that total harmonic distortion of current (THD_i) for the proposed technique is substantially less than for the conventional method.

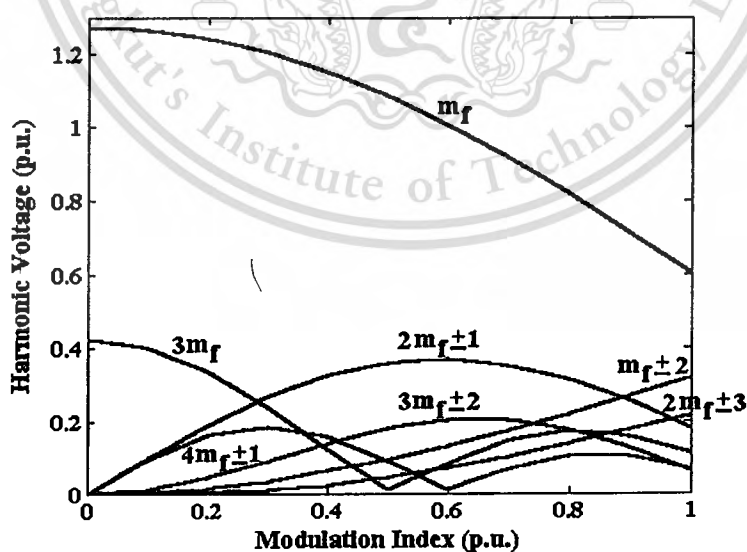


Figure 3.21 Normalized harmonic voltages as a function of modulation index for both auxiliary and main winding voltages of the conventional technique

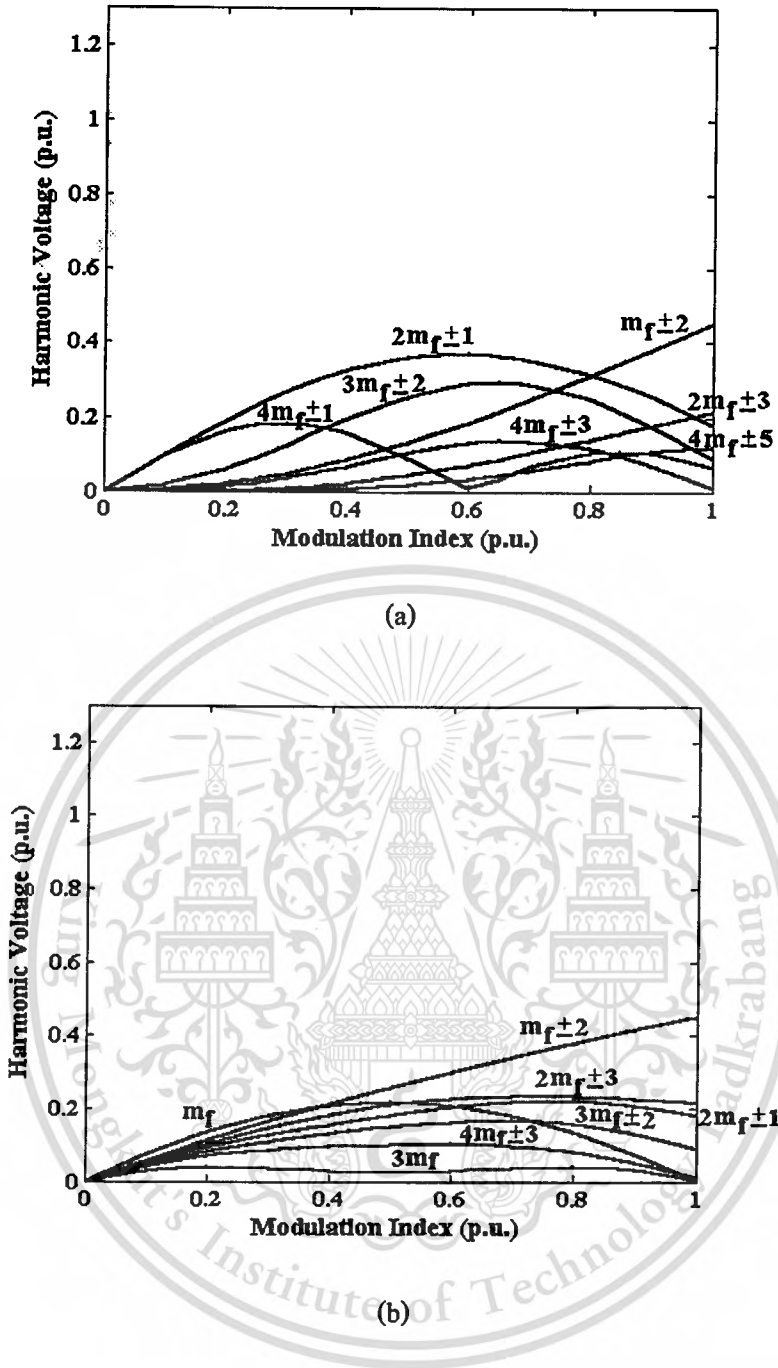


Figure 3.22 Normalized harmonic voltages as a function of modulation index
of the proposed modulation technique

(a) auxiliary winding

(b) main winding

3.5 Two-phase Inverter Modulation Control

In this research, the effectiveness of PWM patterns for improving the quality of motor performance is demonstrated theoretically and experimentally. Several publications [80-83] have shown that the iron loss increase is strongly dependent on either modulation index or switching frequency. As a consequence, it is mandatory to maintain these two parameters in the same manner. In order to study the influence of inverter strategies on the motor performance and to inspect the harmonic voltage contents, the tested motor was supplied by both two-leg and three-leg VSI at the same conditions. The sinusoidal reference frequencies of 20, 30, 40 and 50 Hz, as well as the triangular carrier frequency of 5 kHz were selected. The reason was that the motor was driven under constant torque region, and the switching frequency was in the range of commercial drives available. DC link voltage of the two-leg and three-leg VSI were kept constant at 732 V and 518 V, consecutively. Conducting the converter modulation strategy as mentioned in Section 3.1, the modulation index used to control the output voltage across both windings are shown in Table 3.2 and 3.3.

Table 3.2 Setting up modulation index (M) for the two-leg VSI

inverter frequency (Hz)	Main winding			Auxiliary winding		
	rms voltage (V)	peak voltage (V)	modulation Index	rms voltage (V)	peak voltage (V)	modulation Index
50	220	311.13	0.85	220	311.13	0.85
45	198	280.01	0.77	220	311.13	0.85
40	176	248.90	0.68	220	311.13	0.85
35	154	217.79	0.60	220	311.13	0.85
30	132	186.68	0.51	220	311.13	0.85
25	110	155.56	0.43	187	263.46	0.72
20	88	123.45	0.34	149.6	211.57	0.58
15	66	93.34	0.26	112.2	158.67	0.43
10	44	62.23	0.17	73.8	105.78	0.29
5	22	31.11	0.09	37.4	52.89	0.14

Table 3.3 Setting up modulation index (M) and (M_1) for the three-leg VSI

inverter frequency (Hz)	Main winding		Auxiliary winding		modulation index (M)	modulation index (M_1)
	rms voltage (V)	peak voltage (V)	rms voltage (V)	peak voltage (V)		
50	220	311.13	220	311.13	0.85	0.00
45	198	280.01	220	311.13	0.85	0.12
40	176	248.90	220	311.13	0.85	0.24
35	154	217.79	220	311.13	0.85	0.36
30	132	186.68	220	311.13	0.85	0.48
25	110	155.56	187	263.46	0.72	0.42
20	88	123.45	149.6	211.57	0.58	0.34
15	66	93.34	112.2	158.67	0.43	0.25
10	44	62.23	73.8	105.78	0.29	0.17
5	22	31.11	37.4	52.89	0.14	0.08

3.6 Control and Power Circuits

3.6.1 Power Circuit

The selected power switching is an IGBTs Intelligent Power Module (IPM) Mitsubishi PM25RSB120. The PM25RSB120 is a 1200 V, 25 A, flat-base type IPM with insulated package. The IPM is the isolated base modules designed for power switching applications operating at frequencies to 20 kHz. Built in control circuits provide optimum gate drive and protection for the IGBT and free-wheel diode power devices. Its structure and circuit diagram are shown in Figure 3.23. Its applications are based on inverter, uninterruptible power supply (UPS), motion/servo control, and power supplies. The IPM features comprise complete output circuit, gate drive circuit, and protection logic such as short circuit, over current, over temperature, as well as under voltage. At the top of the figure, the UP, VP, and WP pins are the gate drive terminal of three upper IGBT branches, while the UN, VN, and WN pins are three lower ones. U_{Fo}, V_{Fo}, and W_{Fo} pins are reference fault signals. In case of any faults, reference faults voltage is approximately 0 V. In normal condition, that voltage should be nearly 15 V.

ICL8038 precision waveform generator. The frequency of all sinusoidal waves can be controlled by the button switch which is a software regulation, while that of the triangle can be governed by a 50 kΩ variable resistor. The compromised carrier frequency of triangular wave was 5 kHz. Output signals from Figure 3.26 were three SPWM signals in quadrature, SPWM1, SPWM2, and SPWM3.

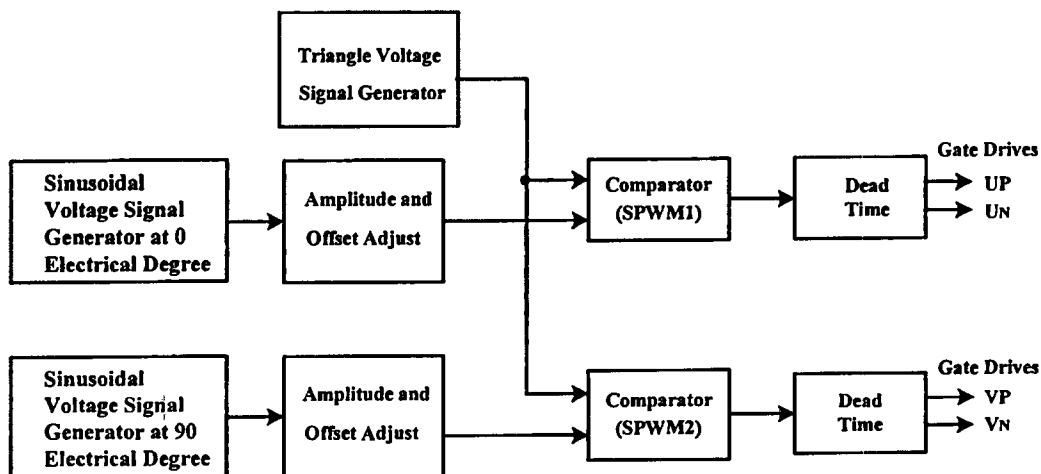


Figure 3.24 Block diagram for bipolar SPWM generation

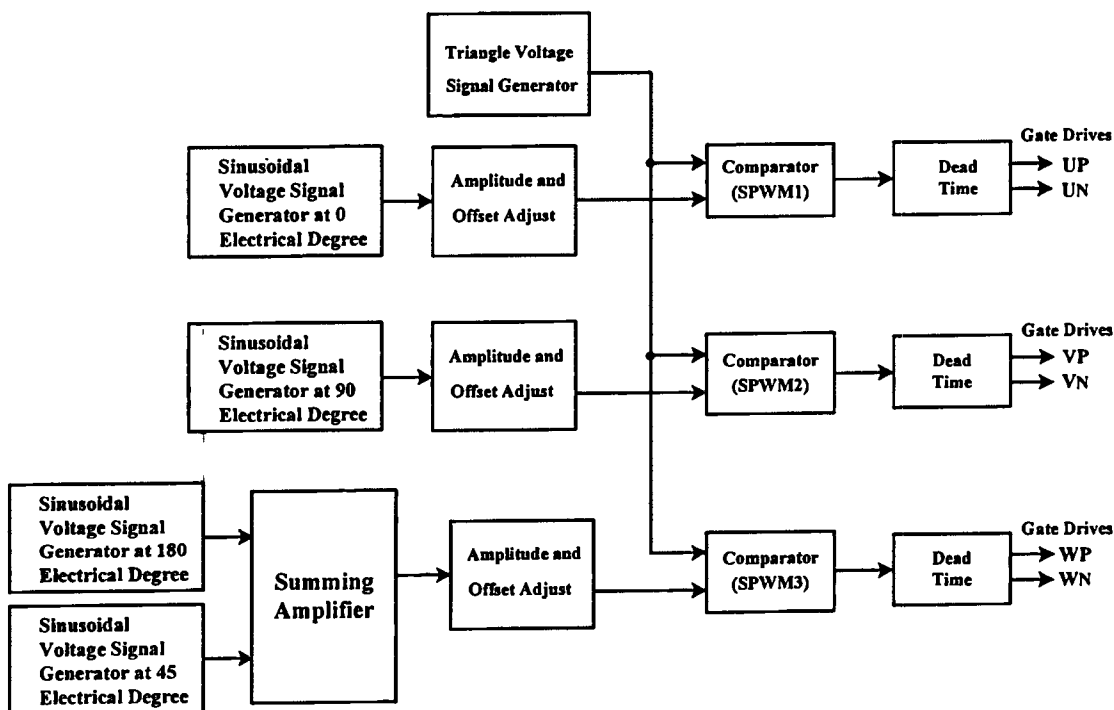


Figure 3.25 Block diagram for unipolar SPWM generation

3.6.3 Blanking Time Circuit

To prevent the short branch state from damaging the power switching devices in the same leg, blanking time or delay time circuits was utilized. Each leg of the switching devices is composed of two IGBT devices, for upper and lower switches. These IGBTs must be turned on/off with little delay time. To achieve this, the MC14557, a static clocked serial shift register whose length can be programmed to any number of bits between 1 and 64 was used in the system. The blanking time circuit is illustrated in Figure 3.27. The serial data from the previous circuit, SPWM1, SPWM2, and/or SPWM3, were submitted to the data input B-pin by connecting the A/B-pin selected input to ground. Output clock coming from an oscillator 1 MHz was connected to CLK position (pin-4). The delay time was set by the control inputs (L1, L2, L4, L8, L16, and L30). The chosen number of bits is equal to the sum of the subscripts of the enabled length control inputs plus one. According to the IPM type, the compromised delay time of the upper and the lower IGBT was 4 μ s. As a result, the control input pin-15 (L4) was applied with 5 V of dc supply, while the others (L1, L2, L8, L16, and L30) were connected to ground line.

3.6.4 Isolated Ground Circuit

The short circuit fault between control and power circuits can be overcome by using an isolated ground circuit as indicated in Figure 3.28. HCPL4504 is a high speed transistor optocoupler with shorter propagation delays and higher current transfer ration for TTL and IPM applications. These features make HCPL4504 an excellent solution to IPM inverter dead time and other switching problems. The optocoupler is made up of an insulating layer between a LED and an integrated photo detector providing electrical insulation between input and output. Separation of connections for the photo-diode bias and output-transistor collector increased the speed up to a hundred times that of a conventional phototransistor coupler by reducing the base collector capacitance. Six optocoupler of HCPL4504 were used in the circuits. These optocoupler can be divided into two parts, three for the upper and three for the lower gate drives. IGBT will be turned on if the input signals (U, V, W, U', V' and W') were zero voltage, and vice versa.

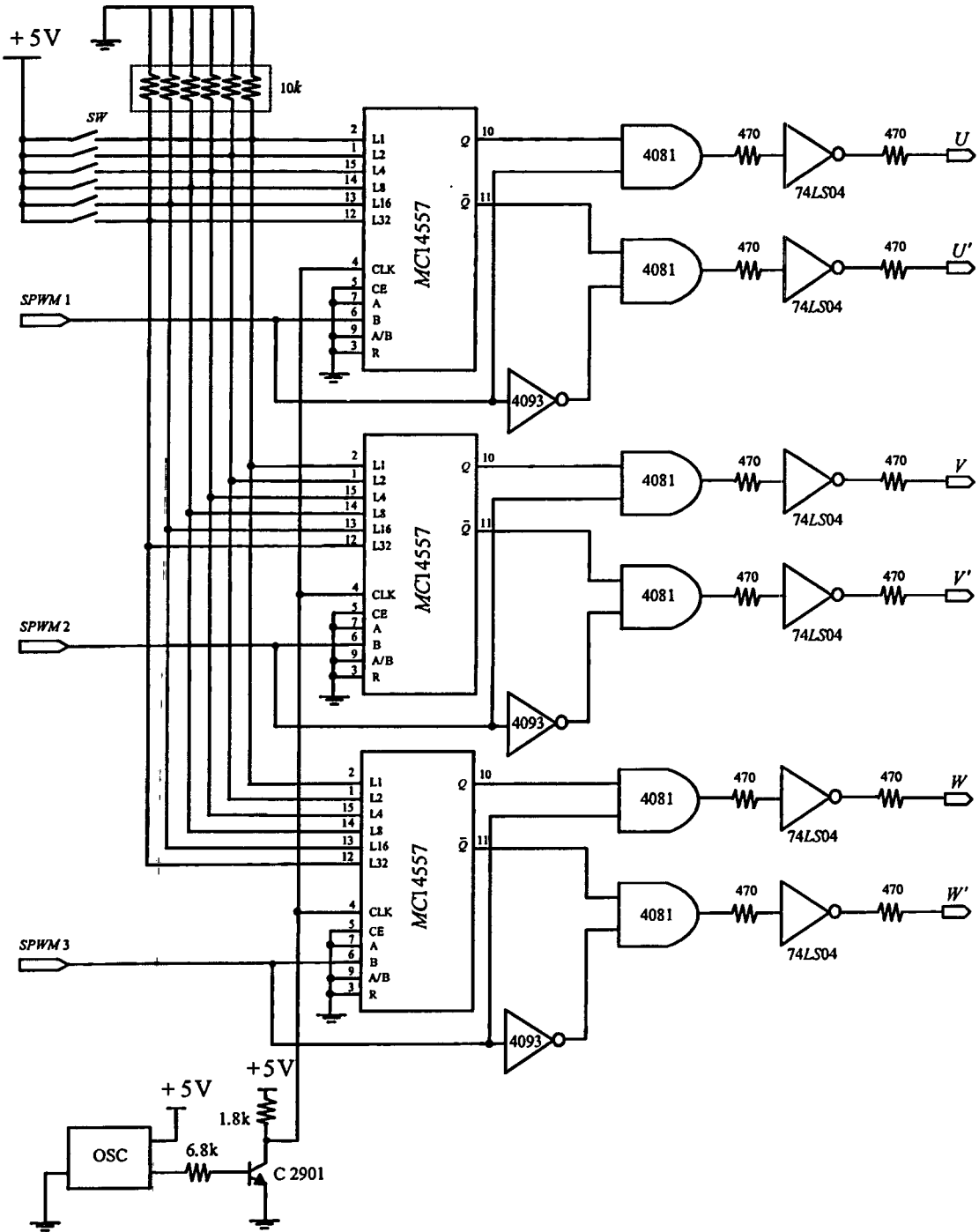


Figure 3.27 Blanking time circuit

3.6.5 Protection Circuit

In order to prevent any cases of faults, all signals from fault detector of the IPM (UFo, VFo, WFo, and Fo) were sent to opto isolator TLP521 which is a high density mounting phototransistor optically coupled isolator. The diagram of the protection circuit is shown in Figure

This material is reserved for educational use only, not allowed for commercial use.

Forbidden to modify the content, and cite the document when use.

3.29. The U_{Fo}, V_{Fo}, and W_{Fo} signals could be detected from the three upper IGBT gate drive, while the F_o signal was received from the lower one. At normal operating condition, the input signals of TLP521 were approximately 15 V. The output signal of 5 V from TLP521 was transferred to pin-4 or pin-set of 74HC74, D-flip flopto receive no output signal from pin-6, \bar{Q} . A transistor PNP-type, BC327, would then be turned on, as well as drive optocoupler HCPL4504 with 5 V dc supply. As a result, the gate drive signal remained continuous.

In case of faults, the input voltage will be approximately zero which triggers the zero voltage at the set-pin of D-flip flop, leading to no output voltage of the flip flop. At this state, BC327 will be turned off. The optocoupler HCPL4504 then receives no input signal, resulting in no gate drive signal of the IPM.

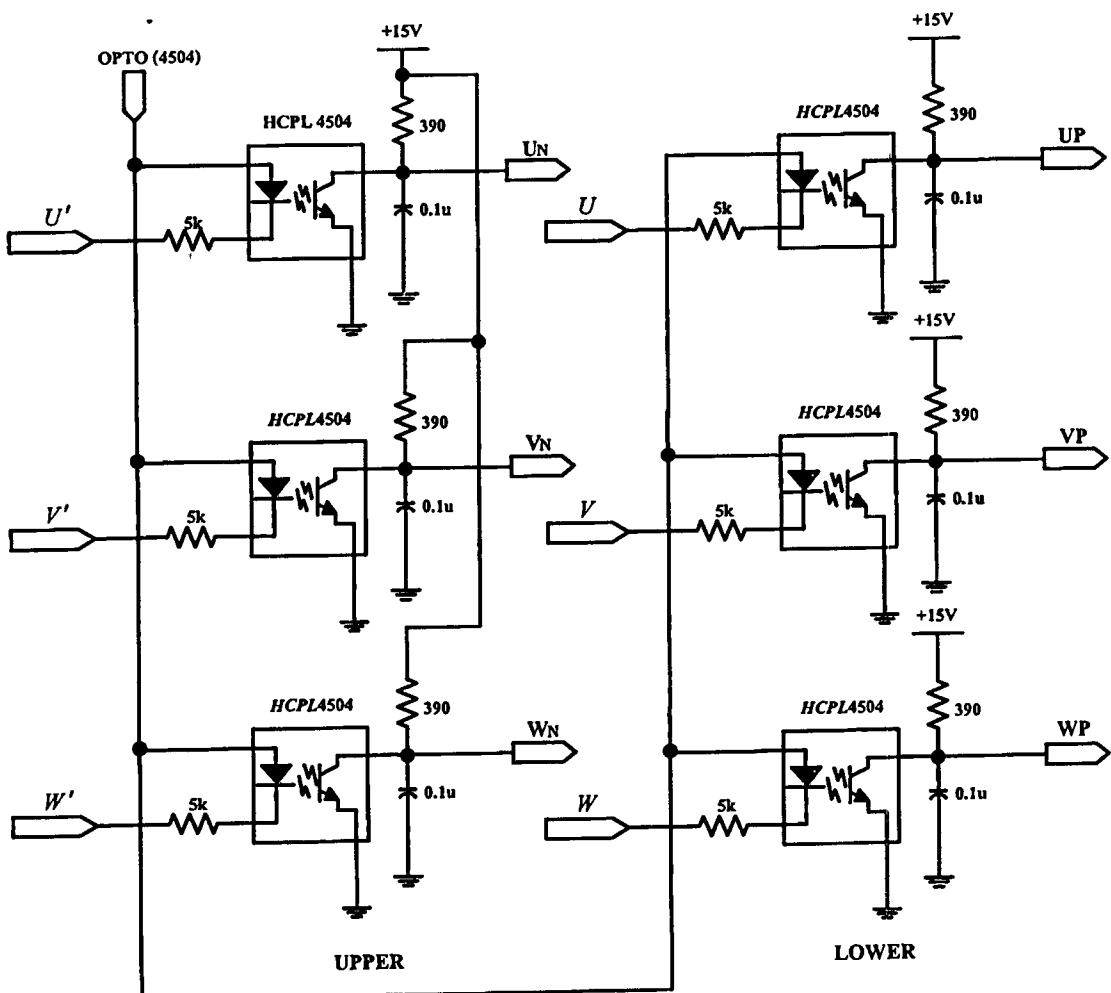


Figure 3.28 Isolated ground circuit

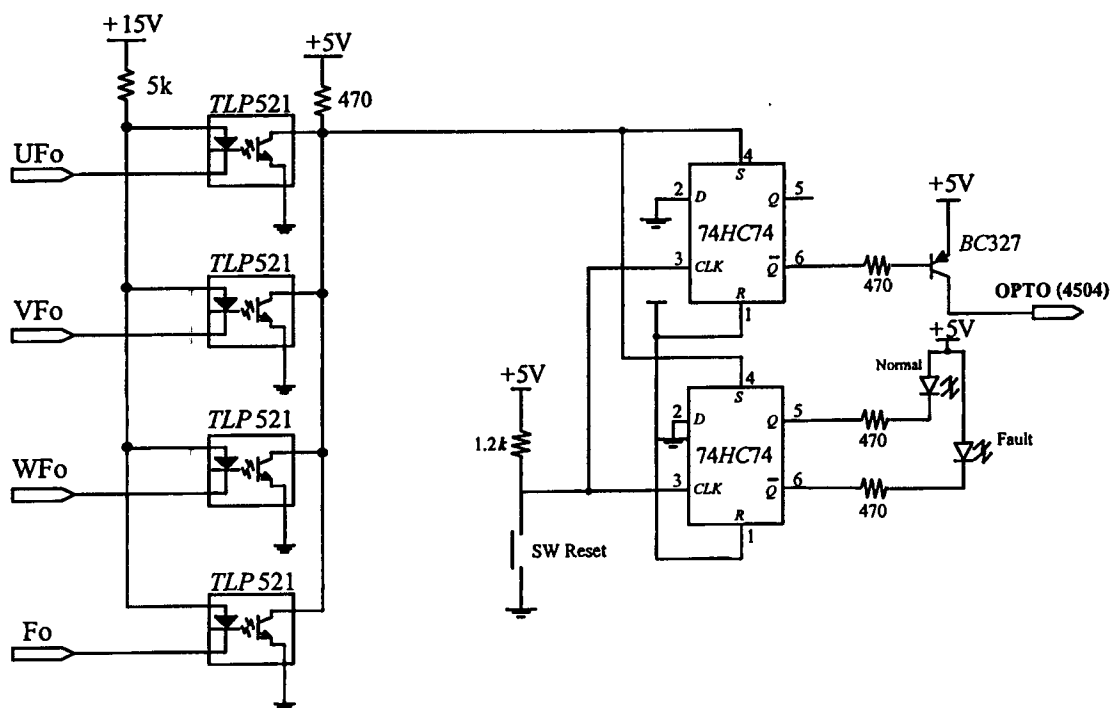


Figure 3.29 Fault protection circuit

3.7 Calculated and Measured Harmonic Voltage Spectra

In order to verify accuracy and features of the proposed modulation strategy, the drive system was setup as described in the previous Section. Again, asynchronously natural-sampled PWM signals were generated by comparing a triangular carrier with a sinusoidal reference modulating function generated from a microcontroller. 25 A, 1200 V IGBT IPM was used for the main power circuit. Experimental data of voltage were recorded using a Power Harmonics Analyzer, Yokogawa Model PZ4000. Practical verification of the theoretical predictions derived from mathematical terms was corroborated.

Prior to conduct the harmonic voltage spectra analysis, the simulated signals should be compared with the measured signals. Figure 3.30 shows the comparison of reference sinusoidal signals of the third branch (phase C) of inverter at frequency of 40 Hz. V_{c1} was 8.5 V, and V_{c2} was 2.4 V. The summation of V_{c1} and V_{c2} was 6.8 V. The tested reference waveforms of the third inverter's leg given from $v_{c1} + v_{c2}$ or $V_m \sin(\omega t - 180^\circ) + V_x \sin(\omega t - 45^\circ)$ were in accordance with the calculated ones. The simulated results in terms of PWM output voltage configurations of the auxiliary and the main windings were investigated and compared to the measured ones, as illustrated in Figure 3.31 and Figure 3.32 for the two-leg and the three-leg

inverters, respectively. At inverter frequency of 20 Hz, for example, the fundamental peak voltage of the main winding was approximately 123.5 V, and that of the auxiliary winding was nearly 211.6 V.

The calculated and measured rms output voltages versus frequency are illustrated in Figures 3.33-3.42 for the frequency ranges of 20-50 Hz, respectively. To obtain the fundamental output voltages across each winding for the proposed control technique, both modulation indexes M and M_1 were regulated as indicated in Tables 3.1 and 3.2, for the two-leg and the three-leg inverters, consecutively.

The calculated amplitudes of each harmonic voltage from the fundamental up to 25 kHz harmonic frequency showed significant harmonic contents. The prominent harmonic voltages took place at the same frequency domain in accordance with the mathematical analysis previously mentioned in Section 3.2. Comparison of the calculated harmonic voltages to the results from the equivalent circuit in Chapter 2 was conducted. The calculated results were almost identical to the experimental results. It was confirmed that validation of numerical analysis and the drive implementation were attained. In Figure 3.42 although the sidebands voltage of the two-leg VSI were slightly less than those of the three-leg VSI, the harmonic magnitude at carrier frequency of the two-leg VSI was remarkably higher than those of the three-leg one, thus resulting in higher motor losses.

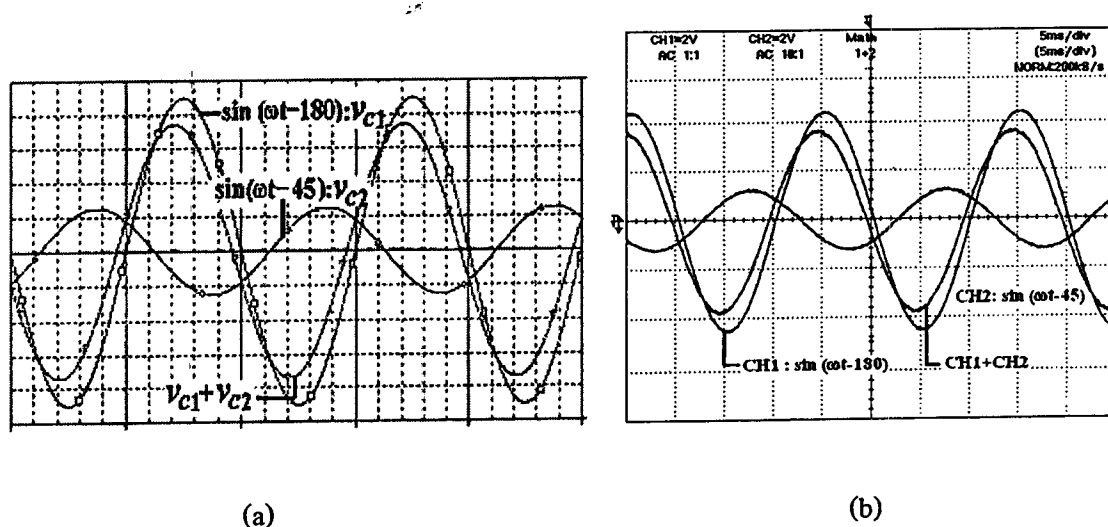


Figure 3.30 Reference sinusoidal signal phase C of the main winding voltage

(a) simulated results

(b) measured results

CH1: rms voltage 8.5 V, CH2: rms voltage 2.4 V, CH1+CH2: rms voltage 6.8 V

This material is reserved for educational use only, not allowed for commercial use.

Forbidden to modify the content, and cite the document when use.

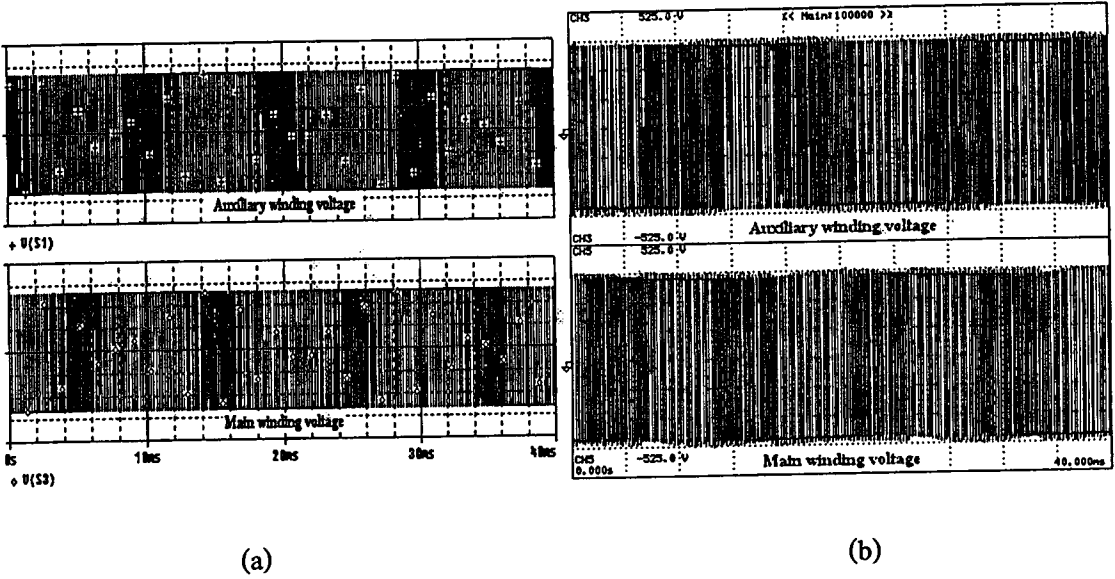


Figure 3.31 SPWM output voltages for the two-leg VSI

- (a) simulated results
- (b) measured results

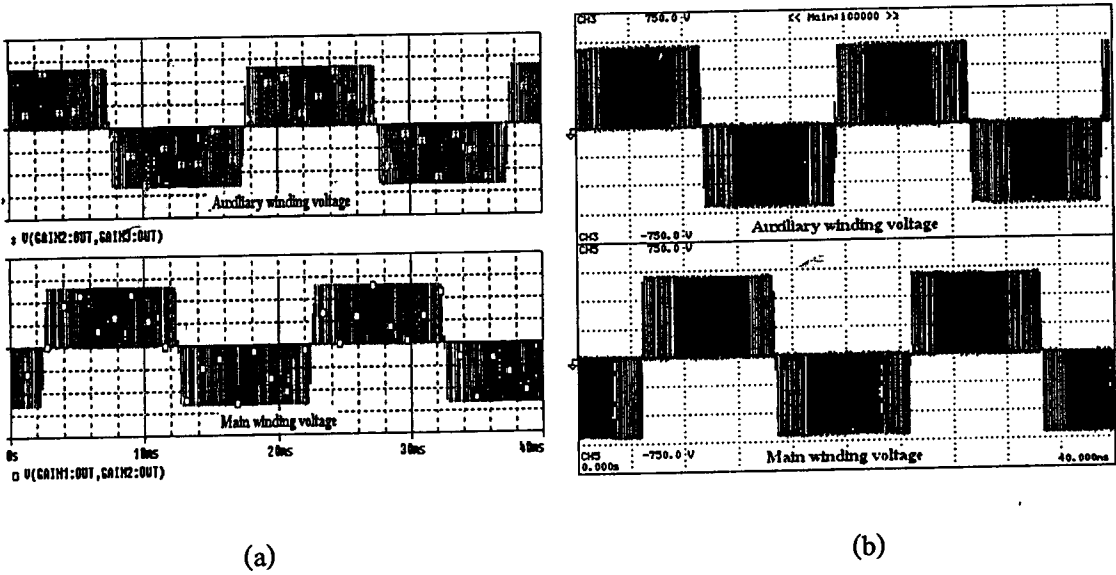


Figure 3.32 SPWM output voltages for the three-leg VSI

- (a) simulated results
- (b) measured results

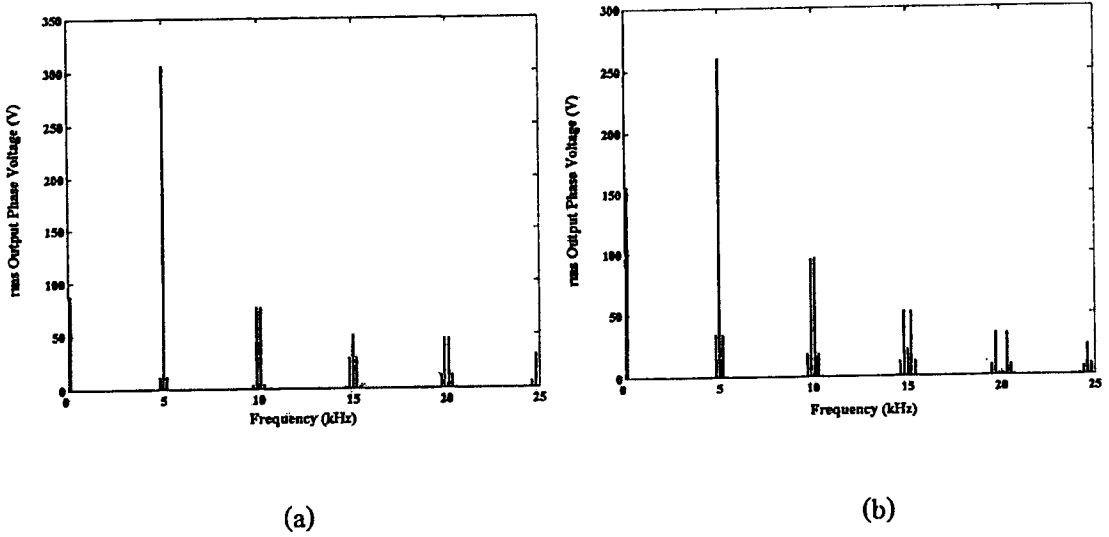


Figure 3.33 Calculated harmonic voltage spectra of the two-leg VSI at inverter frequency of 20 Hz

- (a) main winding
- (b) auxiliary winding

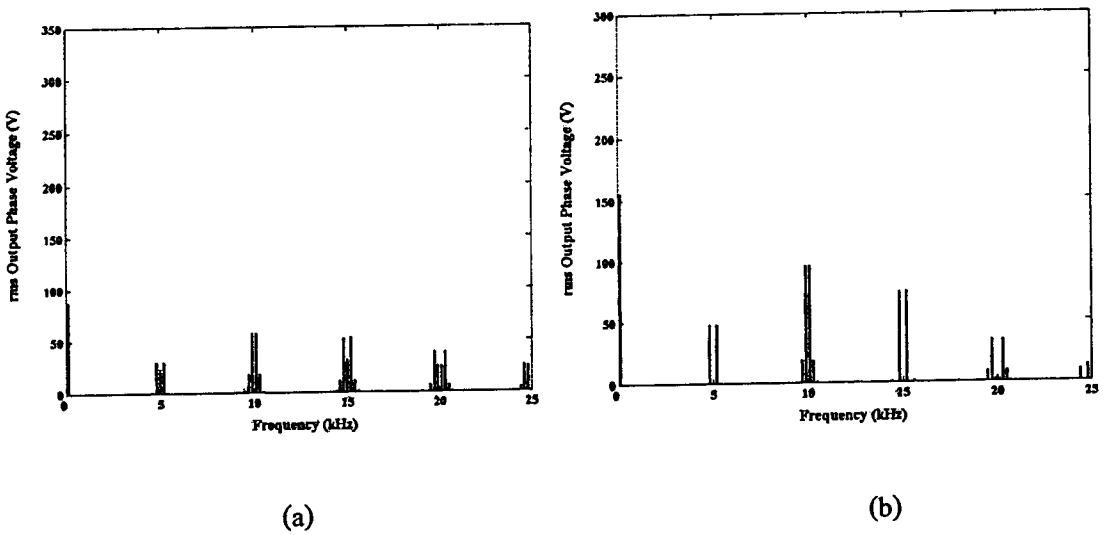
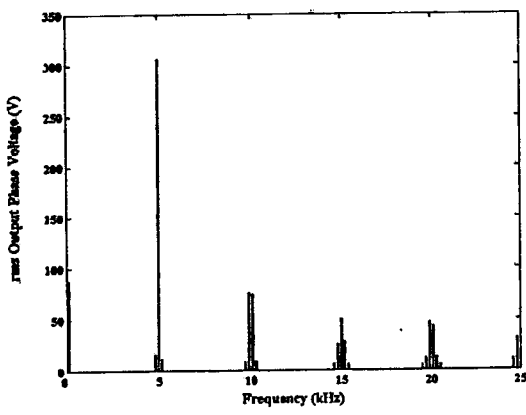
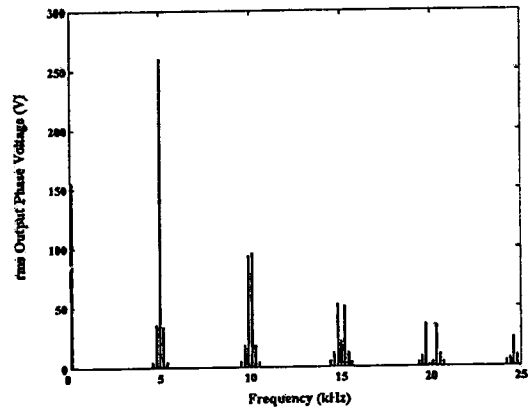


Figure 3.34 Calculated harmonic voltage spectra of the three-leg VSI at inverter frequency of 20 Hz

- (a) main winding
- (b) auxiliary winding



(a)

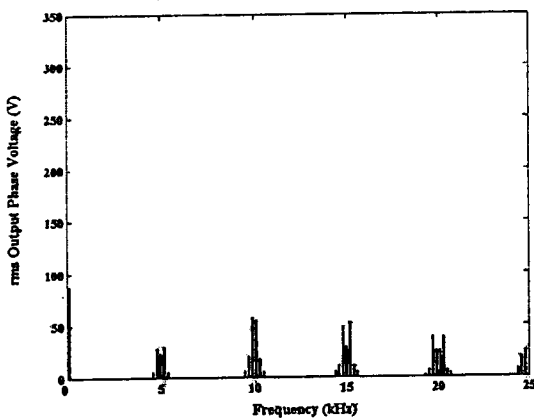


(b)

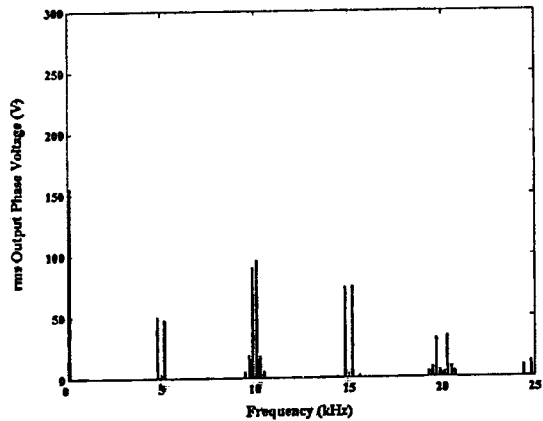
Figure 3.35 Measured harmonic voltage spectra of the two-leg VSI
at inverter frequency of 20 Hz

(a) main winding

(b) auxiliary winding



(a)



(b)

Figure 3.36 Measured harmonic voltage spectra of the three-leg VSI
at inverter frequency of 20 Hz

(a) main winding

(b) auxiliary winding

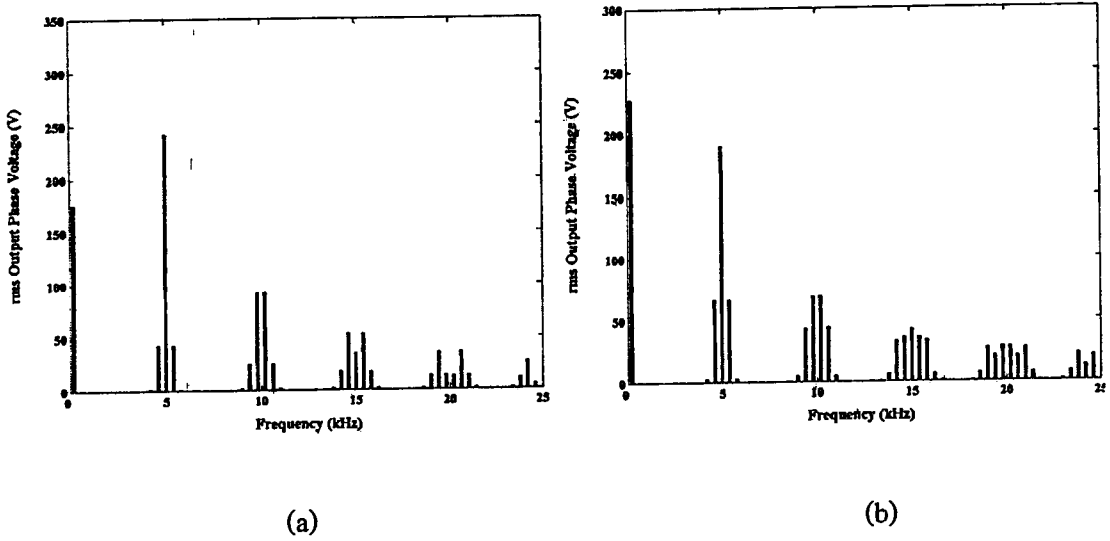


Figure 3.37 Calculated harmonic voltage spectra of the two-leg VSI
at inverter frequency of 40 Hz

- (a) main winding
- (b) auxiliary winding

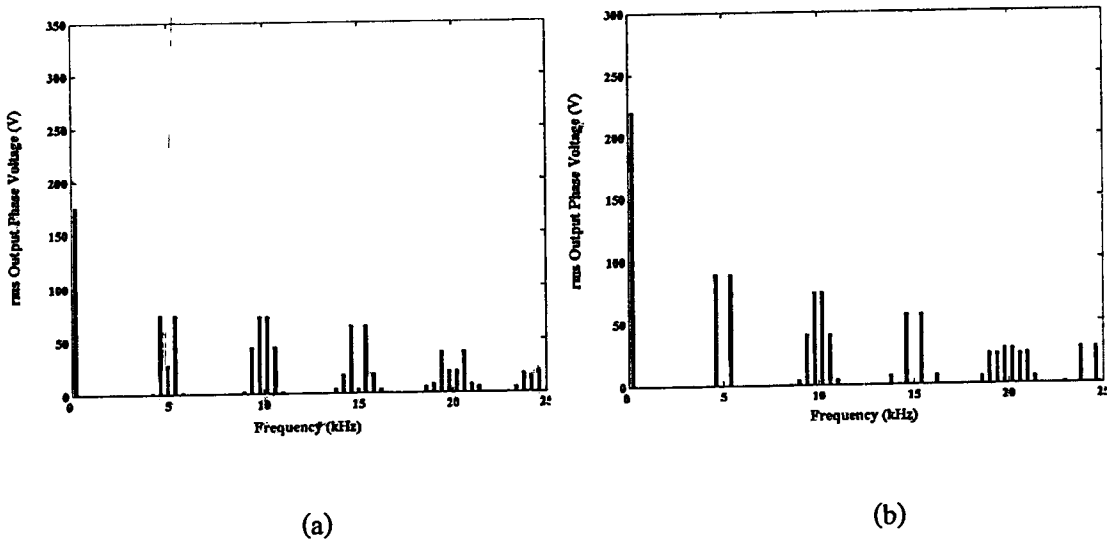


Figure 3.38 Calculated harmonic voltage spectra of the three-leg VSI
at inverter frequency of 40 Hz

- (a) main winding
- (b) auxiliary winding

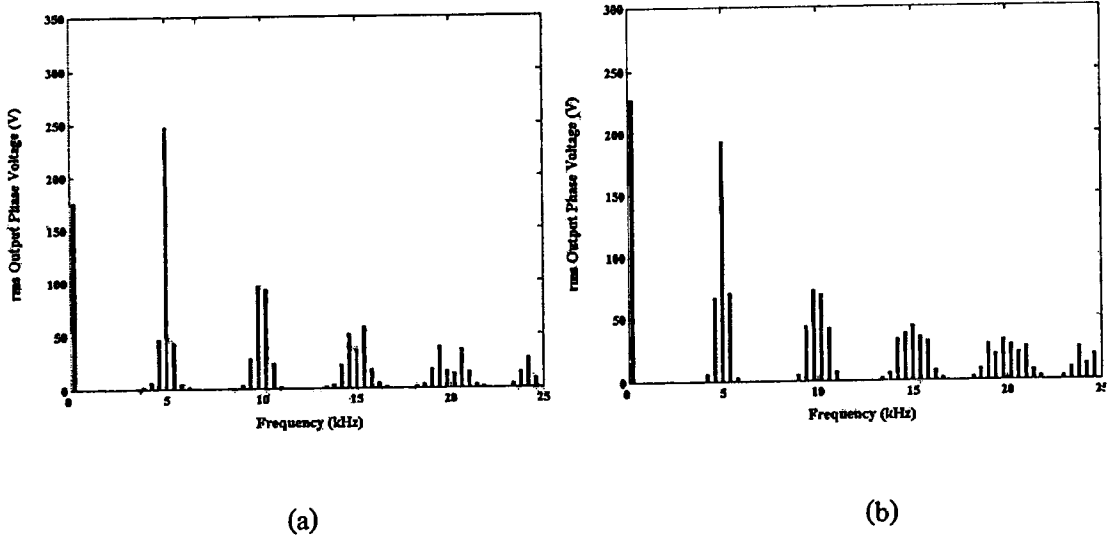


Figure 3.39 Measured harmonic voltage spectra of the two-leg VSI
at inverter frequency of 40 Hz

(a) main winding

(b) auxiliary winding

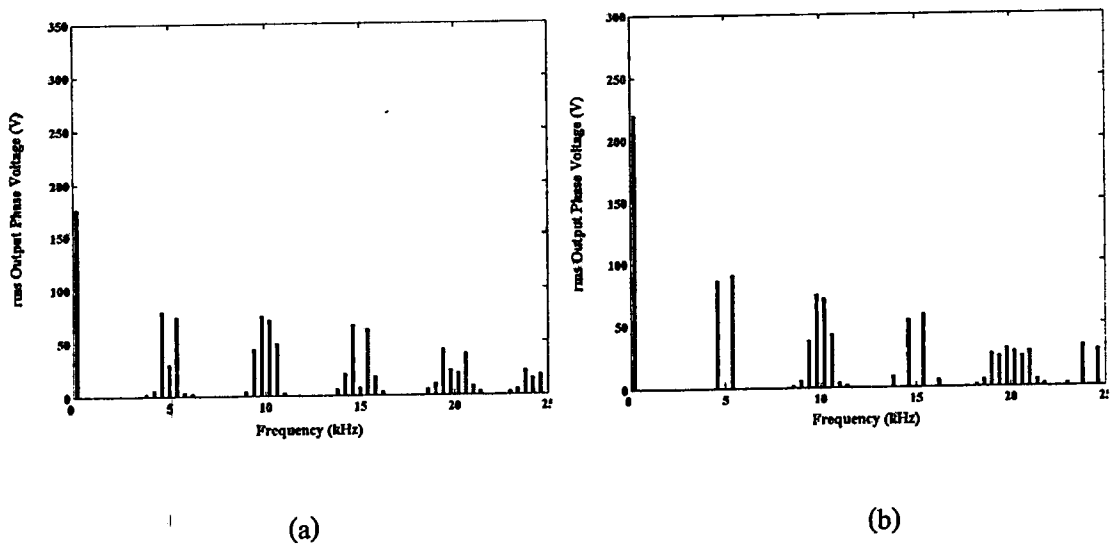


Figure 3.40 Measured harmonic voltage spectra of the three-leg VSI
at inverter frequency of 40 Hz

(a) main winding

(b) auxiliary winding

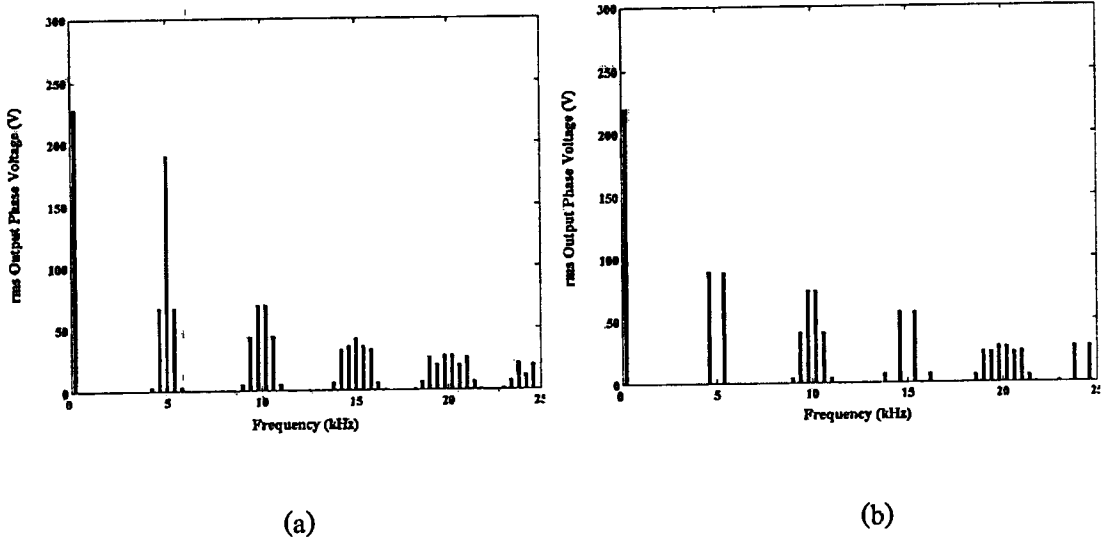


Figure 3.41 Calculated harmonic voltage spectra for both windings
at inverter frequency of 50 Hz

- (a) the two-leg VSI
- (b) the three-leg VSI

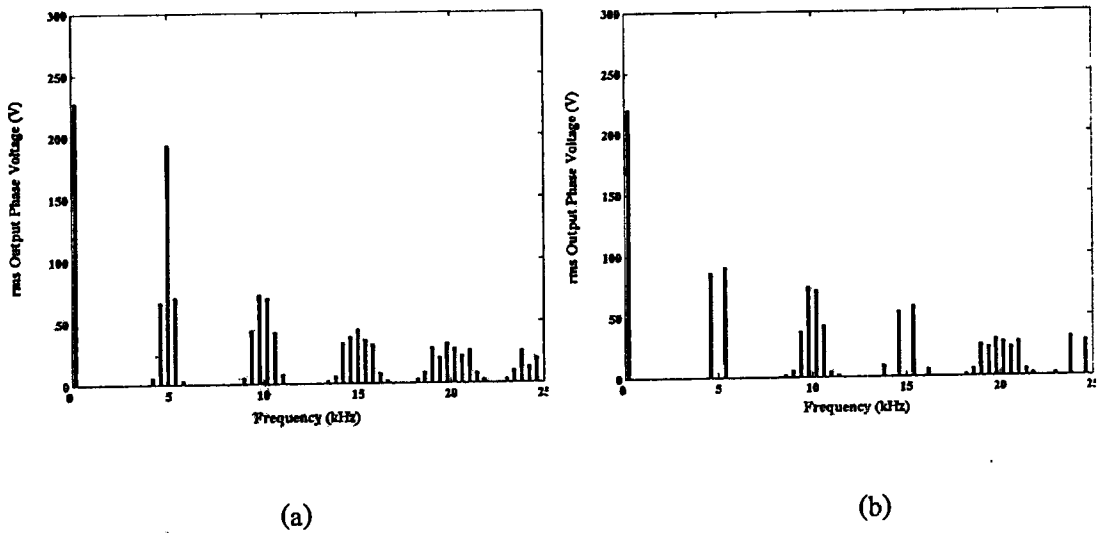


Figure 3.42 Measured harmonic voltage spectra for both windings
at inverter frequency of 50 Hz

- (a) the two-leg VSI
- (b) the three-leg VSI

CHAPTER 4

SIMULATION AND EXPERIMENTAL RESULTS

4.1 Unsymmetrical Two-phase Induction Motor Parameters

A permanent split capacitor motor (PSCM), 230 V, 2.66 A, 370 W, running capacitor $8 \mu\text{F}$ was tested. The motor parameters were measured at sinusoidal utility supply of 50 Hz. Prior to the investigation, the motor was operated at full load for approximately 3 hours to assure that all calculated results of equivalent circuit parameters were the actual information of the motor under traditionally operating conditions. Due to the fact that a PSCM comprises of many kinds of losses [84] and its windings also have unsymmetrical impedance, the determination methods of the motor parameters should be made in contemplation [85-89]. All circuit diagrams for equivalent circuit test and details of analysis are present in Appendix B. Five test methods can be briefly described as follows:

Firstly, the turn ratio test was conducted using the Vienott technique [96]. When the motor reached nearly synchronous frequency with no load, only the main winding was impressed the rated voltage (E_m). The induced voltage of the auxiliary winding (E'_a) was measured. Then the auxiliary winding voltage (E_a) was supplied at rated voltage. The induced voltage across the main winding (E'_m) was gauged. The winding turn ratio, a , of the tested motor was then calculated by using Equation (4.1). The computed turn ratio of the motor was found to be 1.7.

$$a = \sqrt{\frac{E'_a E_a}{E_m E'_m}} = \sqrt{\frac{285 \times 220}{220 \times 95.7}} \approx 1.7 \quad (4.1)$$

Secondly, the stator winding resistances were investigated. To measure the actual resistance values without the influence of skin effect as well as inductance values in conductor, a dc voltage source was provided to each stator winding. The dc voltage and dc current values were recorded step by step. The results were plotted as voltages versus currents using curve fitting technique as illustrated in Figure 4.1 and 4.2 for the main and the auxiliary windings, respectively. From these two figures, the measured main winding resistance R_{1m} and auxiliary winding resistance R_{1a} of the motor under test were found to be 9.0283Ω and 49.921Ω , respectively.

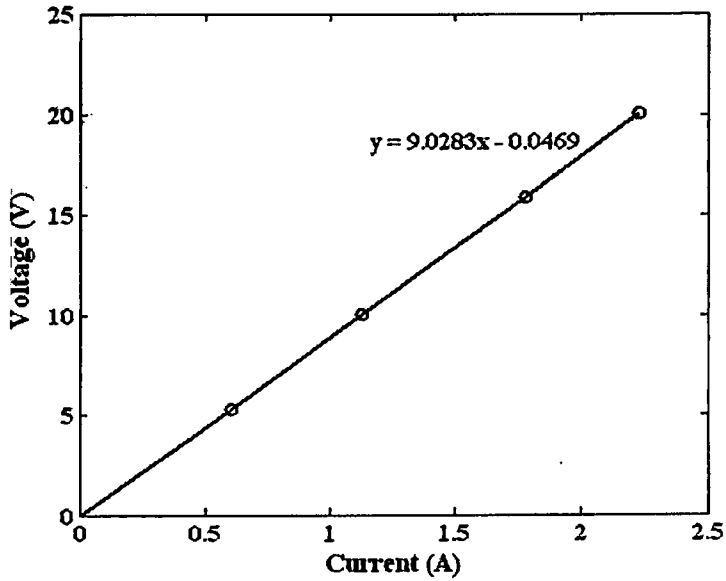


Figure 4.1 Voltage and current relationship of the main winding

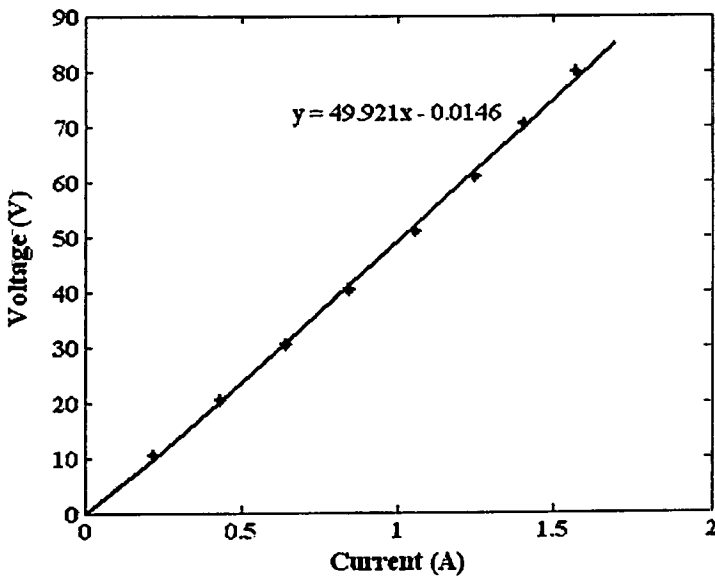


Figure 4.2 Voltage and current relationship of the auxiliary winding

Thirdly, the locked rotor test was conducted according to the conventional three-phase induction motor test [33, 96]. This test method is based on a general theory of induction motor that is the rotor voltage is proportional to the relative motion between the rotor and the stator magnetic fields. In the locked rotor test of PSCM, the main stator winding should be connected in parallel with the auxiliary one. The running capacitor in series with the auxiliary

This material is reserved for educational use only, not allowed for commercial use.

Forbidden to modify the content, and cite the document when use.

winding was removed. An ac sinusoidal voltage source was supplied to both of stator windings of the blocked motor shaft until the current reached the rated current. The approximate equivalent circuit parameters can be written as indicated in Figure 4.3 and can be briefly analyzed as described in Equation (4.2)- (4.7).

Where

P_{locked} = locked rotor real power

Q_{locked} = locked rotor imaginative power

I_{locked} = locked rotor current

V_{locked} = locked rotor voltage

Z_{locked} = locked rotor impedance

R_{locked} = locked rotor resistance

R_{1m} = stator winding resistance of the main winding

R_2 = rotor winding resistance

X_{locked} = locked rotor reactance

X_{1m} = stator leakage reactance of the main winding

X_2 = rotor winding leakage reactance

X_m = magnetizing reactance

L_{1m} = stator inductance of the main winding

L_2 = rotor inductance referred to the main winding

L_m = magnetizing inductance

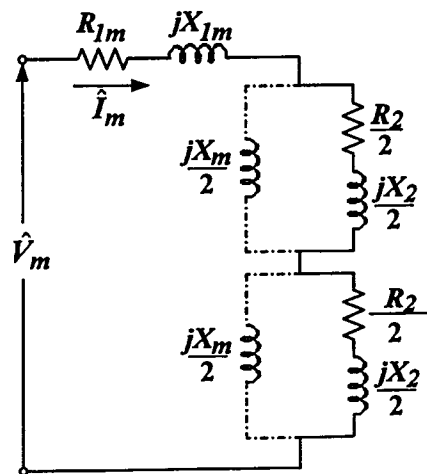


Figure 4.3 Approximate equivalent circuit for locked rotor test

This material is reserved for educational use only, not allowed for commercial use.

Forbidden to modify the content, and cite the document when use.

The induced voltage in a rotor contained both resistance and reactance. The stator and the rotor winding impedance can be calculated by the following equation:

$$R_{locked} = \frac{P_{locked}}{I_{locked}^2} = \frac{115.3}{(2.177)^2} \approx 24.328 \Omega \quad (4.2)$$

and

$$X_{locked} = \frac{Q_{locked}}{I_{locked}^2} = \frac{129.15}{(2.177)^2} \approx 27.25 \Omega \quad (4.3)$$

As previously mentioned, the stator resistance of the main winding was approximately 9.0283 Ω . The rotor winding resistance was given by:

$$R_2 = R_{locked} - R_1 = 24.328 - 9.0283 \approx 15.3 \Omega \quad (4.4)$$

Since the stator winding leakage reactance is equal to the rotor winding leakage reactance, hence,

$$X_{1m} = X_2 = \frac{X_{locked}}{2} \approx \frac{27.25}{2} \approx 13.625 \Omega \quad (4.5)$$

From $X_L = \omega L = 2\pi fL$, and frequency $f = 50$ Hz, the rotor and stator inductances in the motor parameter tests can be expressed by:

$$\begin{aligned} L_{1m} = L_2 &= \frac{X_{1m}}{2\pi f} \\ &\approx \frac{13.625}{2\pi \times 50} \approx 43.4 \text{ mH} \end{aligned} \quad (4.6)$$

and

$$\frac{L_2}{2} \approx \frac{43.4}{2} \approx 21.7 \text{ mH} \quad (4.7)$$

Fourthly, no-load test in which the motor was connected as conventional operation without load torque was made. The approximate equivalent circuit for the no load test is shown in Figure 4.4. From the figure, the no load impedance is equal to $R_{1m} + j(X_{1m} + X_m)$. Thus, the no-load reactance $X_{no\ load}$ can be expressed as:

$$\begin{aligned} X_{no\ load} &= \frac{Q_{no\ load}}{I_{no\ load}^2} \\ &= \frac{157}{(1.055)^2} = 141.05\ \Omega \end{aligned} \quad (4.8)$$

Where $X_{no\ load} = X_{1m} + X_m$ and the calculated stator leakage reactance of the main winding $X_{1m} \approx 13.625\ \Omega$, then magnetizing reactance X_m is defined by:

$$\begin{aligned} X_m &= X_{no\ load} - X_{1m} = 141.05 - 13.625 \\ &= 127.425\ \Omega \end{aligned} \quad (4.9)$$

Thus,

$$\begin{aligned} L_m &= \frac{X_m}{2\pi f} \approx \frac{127.425}{2\pi \times 50} \approx 405.6\ \text{mH} \\ \frac{L_m}{2} &\approx \frac{405.6}{2} \approx 202.83\ \text{mH} \end{aligned} \quad (4.10)$$

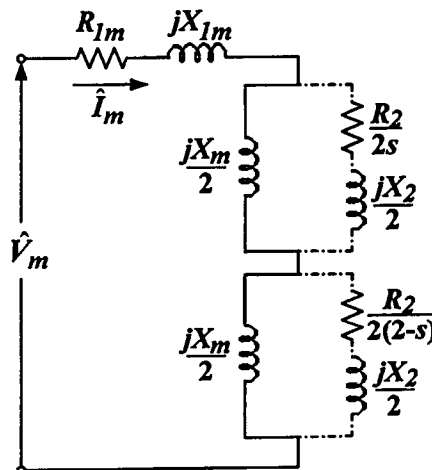


Figure 4.4 Approximate equivalent circuit for no load test

This material is reserved for educational use only, not allowed for commercial use.

Forbidden to modify the content, and cite the document when use.

Fifthly, friction & windage losses of the motor were investigated. The motor under test was connected with the voltage source as the no load test. In order to account for the effect of hysteresis losses, the ac voltage was initially applied to the rated voltage of the motor, then, the stator voltage was reduced step by step until the motor stops running. While decreasing the voltage, all input values such as the applied voltages, total input power, each winding currents were recorded.

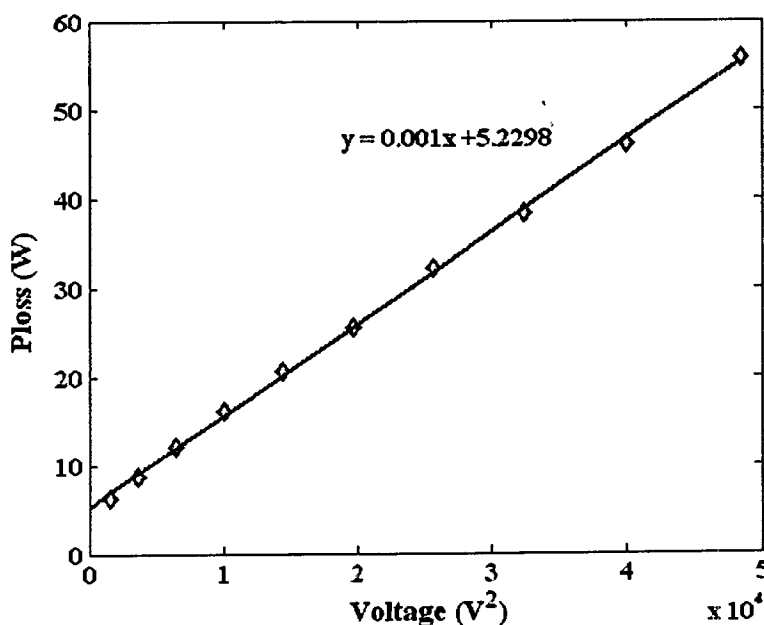


Figure 4.5 Friction and windage losses analysis

Power loss or rotational losses (P_{loss} : including both friction & windage and core losses) of the tested motor can be computed by $P_{loss} = P - I_m^2 R_{1m} - I_a^2 R_{1a}$. At rated voltage, rotational loss of the motor was equal to 55.645 W.

The correlation of P_{loss} versus V^2 is illustrated in Figure 4.5. To isolate friction & windage losses from core loss, at $V^2 = 0$, the loss in terms of core loss could be negligible. The remaining loss should then be the friction and windage losses known as the rotational loss. From the figure, the rotational loss was approximately 5.23 W. Core loss was calculated to be $55.645 - 5.23 = 50.415$ W.

4.2 Composition of Two-phase Induction Motor Model

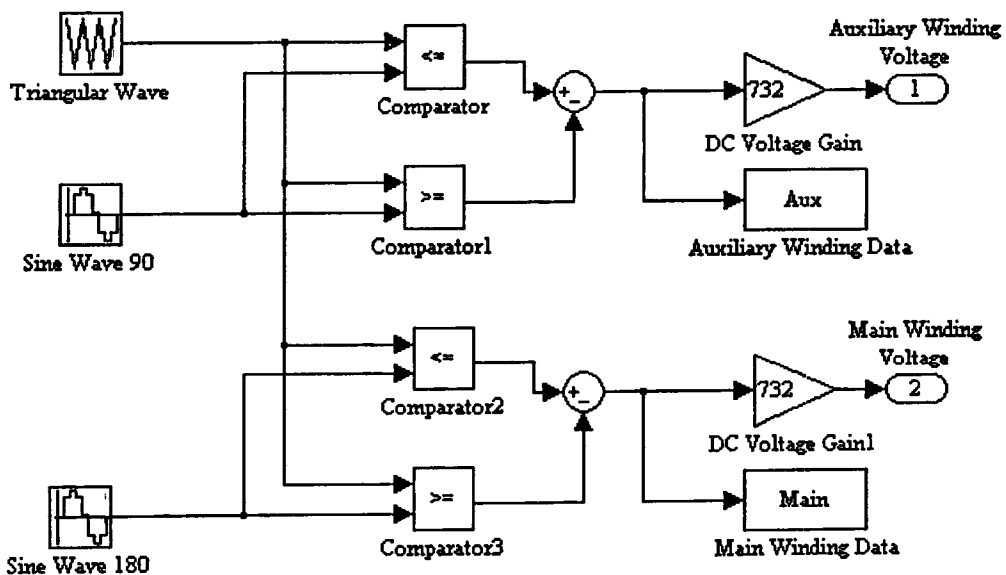
Due to the large majority of low-power applications that employ unsymmetrical type two-phase induction motors, the most appropriate control technique for small-power two-phase motor drive is an open loop control. This means that the steady state behavior model is more important than the dynamic one. However, when the influences of either harmonic voltage or magneto motive force with time variation on motor performance is an important consideration, the dynamic model is preferred.

As the PSCM has a rated voltage (V) and frequency (f) at 220 V and 50 Hz, respectively, therefore, $k = \frac{V_{rated}}{f_{rated}} = \frac{220}{50} = 4.4$. Along with the control methodology described in Section 2.3, the proportion of the main winding voltage to inverter frequency is strictly kept at a nominal value of 4.4 and the resultant turns ratio “ a ” of the tested motor is 1.7, as previously derived in Section 4.1.1. The amplitude voltage of the auxiliary winding has to be boosted over 1.7 times the main winding voltage. The frequency changing point, $\frac{f_{rated}}{a}$, of the auxiliary winding voltage is $\frac{f_{rated}}{a} = \frac{50}{1.7} = 29.41$ Hz. The diagram of voltage control for the PSCM is shown in Appendix B, Figure B.6. In the simulation, there are two induction motor models. A steady-state model as described in Appendix C is used to predict the average output torque of the motor. A dynamic model is utilized to forecast both input and output motor characteristics, such as harmonic voltage contents impacting on motor current configuration. Coupled models employ the same motor parameters from the analysis of the previous section.

Using the equations given in Chapter 2, the main block diagrams of the unsymmetrical two-phase motor model fed by the two-leg and the three-leg voltage source inverters are presented in Figures 4.6 and 4.7, respectively. It should be noted that the two-phase voltage source inverters applied to the tested motor are represented as an ideal sinusoidal pulse width modulation (SPWM) voltage source inverter (VSI).

Details of both the two-leg and the three-leg voltage source inverters are shown in Figures 4.8 and 4.9, respectively. In Figure 4.8, that is, the two-leg VSI, the single triangular wave is compared to two sinusoidal waveforms and both sinusoidal waveforms are in quadrature. Accordingly, the fundamental output voltages of the SPWM inverters for both the main and the auxiliary windings are also in quadrature. The amplitude voltages of each winding can be independently regulated by

Figure 4.9 shows the SPWM signal generator for the three-leg VSI. According to the generating SPWM pattern of the proposed technique, two sinusoidal reference voltages, with 180 and 45 degree phase shifts, were summed together and the output signal was compared to the carrier triangular wave. This SPWM output signal was the control signal of the third inverter leg (phase C). Two remaining sinusoidal voltages with 0 and 90 electrical degree phase difference were compared to the single triangular wave. The SPWM output signals were the control signals of the first and the second inverter leg (phase A and B). The fundamental output voltages of the SPWM inverters, for both the main and the auxiliary windings can be set by the relationship of the modulation index M and M_1 following Table 3.2. The DC link voltage gain for this drive was 518 V. Figure 4.10 shows the inside of the *ExtConn* block that produces the input voltages to the qs and ds circuits and the simulation for inserting the appropriate capacitor voltage and the winding turns ratio to the ds winding. The simulations of the qs and ds circuits in the *Qaxis* and *Daxis* blocks are presented in Figures 4.11 and 4.12. It can be seen that both circuits are similar, except for the unequal parameters of the qs and ds stator windings. The *Rotor* block in Figure 4.13 illustrates how the torque equation and the rotor's equation of motion are simulated. It should be noted that all motor parameters in the simulation were given using the standard test method with a sinusoidal voltage source at a frequency of 50 Hz. All simulation results, such as input voltages, input currents, and torque pulsation, were automatically saved as a new file in the form of a workspace database. To evaluate the fundamental, rms and THD values, these data were transferred to an analysis diagram as illustrated in Figure 4.14.



This material is copyrighted by the author. All rights reserved. No part of this material may be reproduced, stored in a retrieval system, or transmitted, in any form or by any means, electronic, mechanical, photocopying, recording, or by any information storage and retrieval system, without the prior written permission of the author. For commercial use, contact the author at: shahmoradian@shahmoradian.com

Figure 4.8 Two-phase voltage source diagram of the two-leg VSI

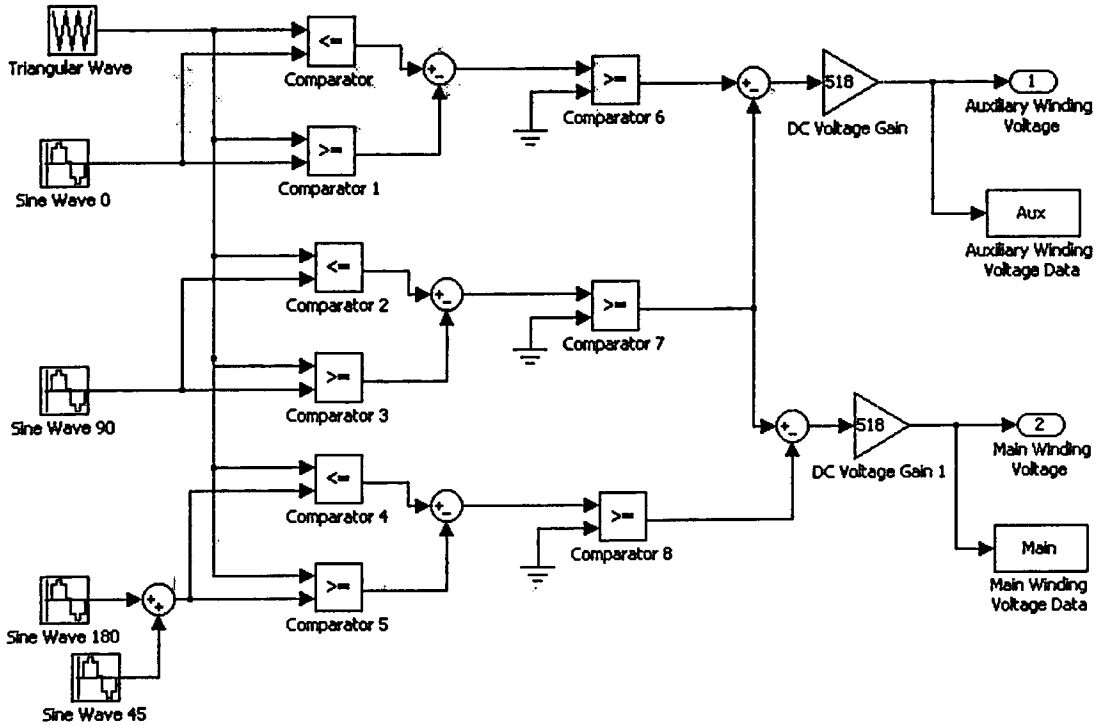


Figure 4.9 Two-phase voltage source diagram of the three-leg VSI

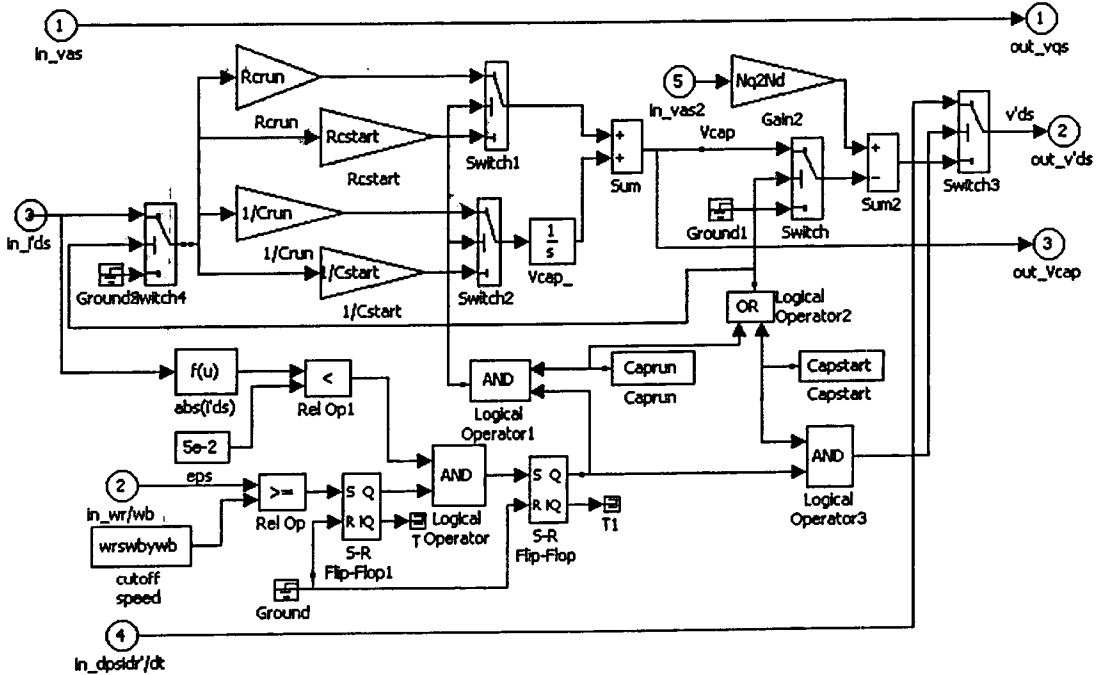


Figure 4.10 Details of Extconn block diagram

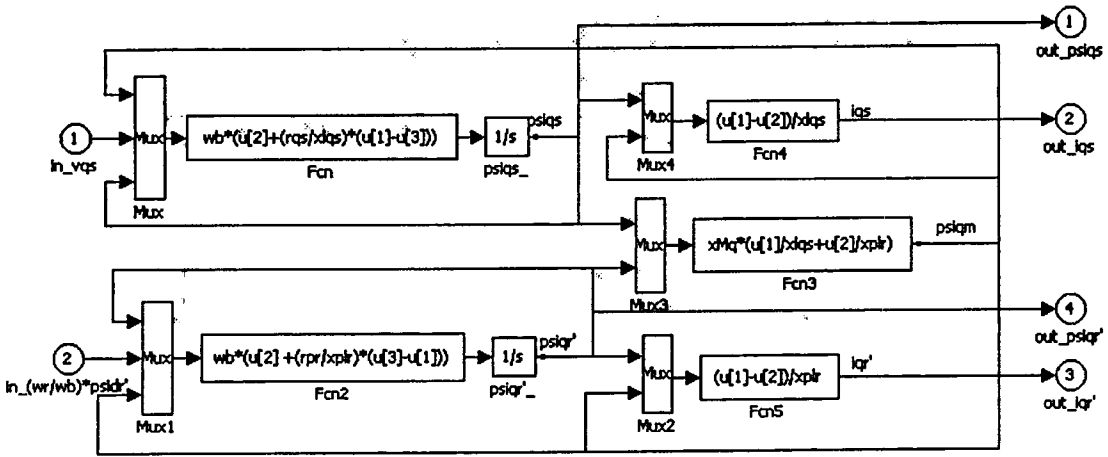


Figure 4.11 Details of *Qaxis* block diagram

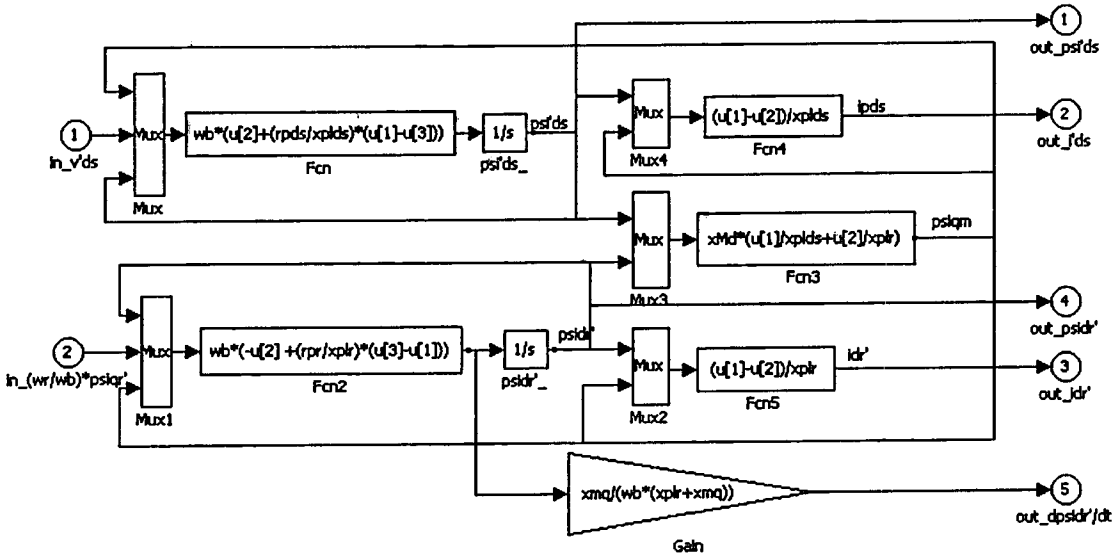
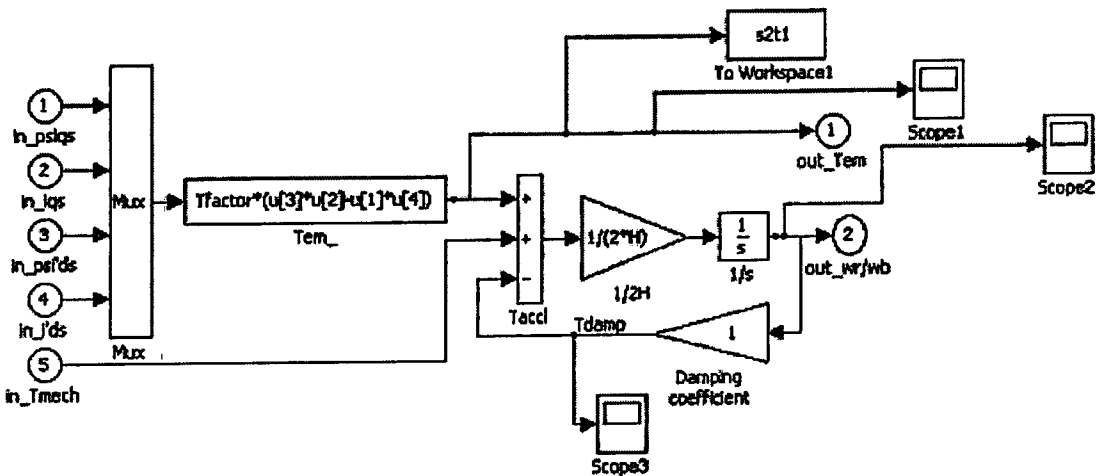


Figure 4.12 Details of *Daxis* block diagram



This material is reserved for commercial use. Figure 4.13 Details of *Rotor* block diagram

Forbidden to modify the content, and cite the document when use.

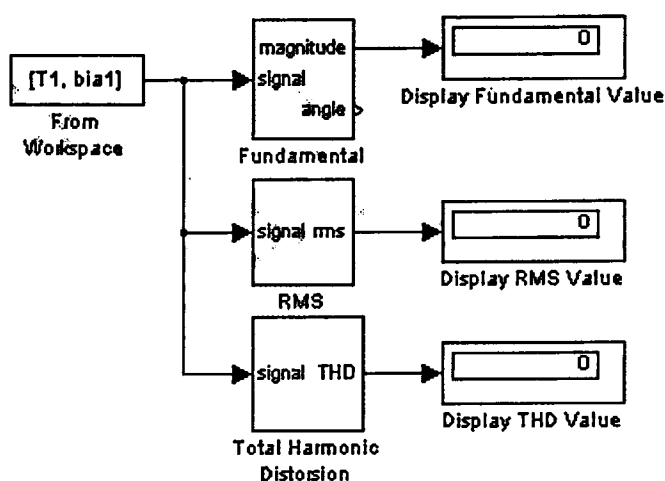


Figure 4.14 Analysis diagram of voltage and current characteristics

4.3 Experimental System

In order to verify the validity and the correctness of the proposed modulation technique, the effectiveness of PWM patterns in improving the quality of motor performance is demonstrated theoretically as well as experimentally. The experimental system setup is shown in Figure 4.15. Asynchronously natural-sampled PWM signals were generated by comparing a 5 kHz triangular carrier wave with a sinusoidal reference signal, created using a microcontroller. An IGBT IPM 25 A, 1200 V was used as the power switching devices in the power circuit. A 370-W 230-V 2.66-A 1375-rpm 50-Hz PSCM with turns ratio of 1.7 was used in the investigation. The ac source was a 0-260 V variable autotransformer with a rated frequency of 50 Hz.

Along with the control methodology, the running capacitor was removed. The motor was connected with a 1000 W servo motor, including its controller, to serve as a dynamic load and shaft torques and speeds were measured using a torque-speed sensor. In order to detect the acoustic noise signal, a microphone was installed at a distance of 3 cm from the motor. Experimental results of voltage, current and power were recorded using a Power Harmonics Analyzer, Yokogawa Model PZ4000. Practical verifications of the theoretical predictions derived from the mathematical model and the machine model was undertaken, recognizing that all measured motor parameters entered in the machine model were based on the sinusoidal utility supply at a frequency of 50 Hz. Furthermore, the converter operation was modeled as an ideal power electronic device.

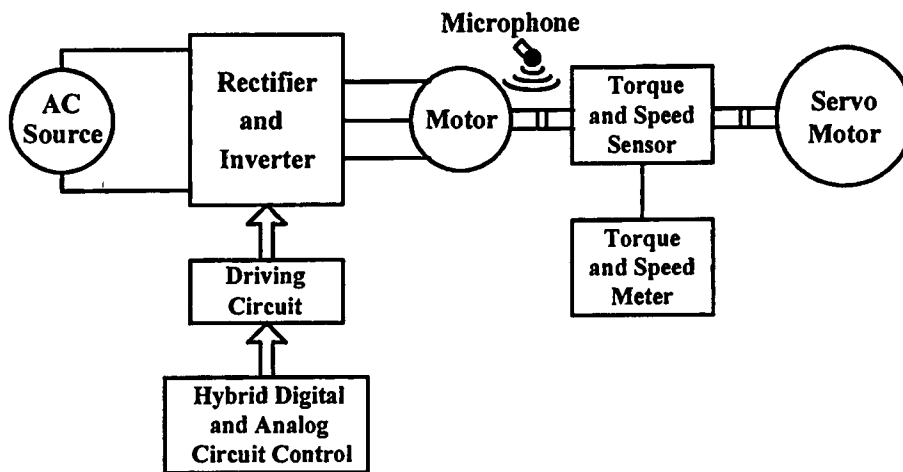


Figure 4.15 Block diagram of experimental system

4.4 Results and Discussion

4.4.1 Harmonic Voltage Stress

Additional magnetic noise created in the motor can be minimized by a reduction of the magnetic field in the motor's air gap and by taking care to avoid core resonance at the commutation frequency [67]. It is known that the more decreased harmonic voltage levels, the higher declined vibrations and magnetic noise volume [97-98]. Figures 4.16 - 4.22 show the profile of harmonic voltage stresses versus variable frequency range at each inverter frequency for the 2-leg and 3-leg VSI. It was found that, at the same inverter frequency, the proposed modulating strategy for the three-leg VSI provides lower harmonic voltage stresses than the two-leg VSI, especially at m_f .

In order to examine harmonic contents, the dominant harmonic voltages normalized by fundamental components as a function of modulation index are presented in Tables 4.1 and 4.2 for the main and the auxiliary windings, respectively. From these two tables, it can be seen that although harmonic sidebands of the unipolar PWM scheme of the 3-leg VSI are slightly greater than the bipolar PWM pattern of the 2-leg VSI, the harmonic at the carrier frequency m_f of the 3-leg VSI is dramatically lower than that of the 2-leg VSI. As a result, the proposed 3-leg VSI may markedly reduce the vibrations and acoustic noise of the induction motor.

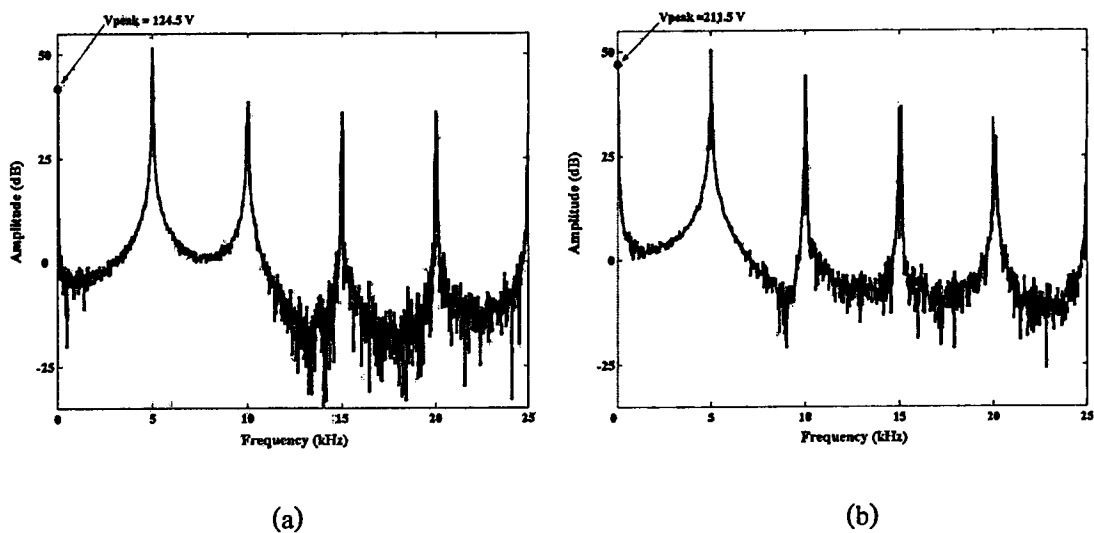


Figure 4.16 Measured results of voltage stress of the two-leg VSI at inverter frequency of 20 Hz

- (a) main winding
- (b) auxiliary winding

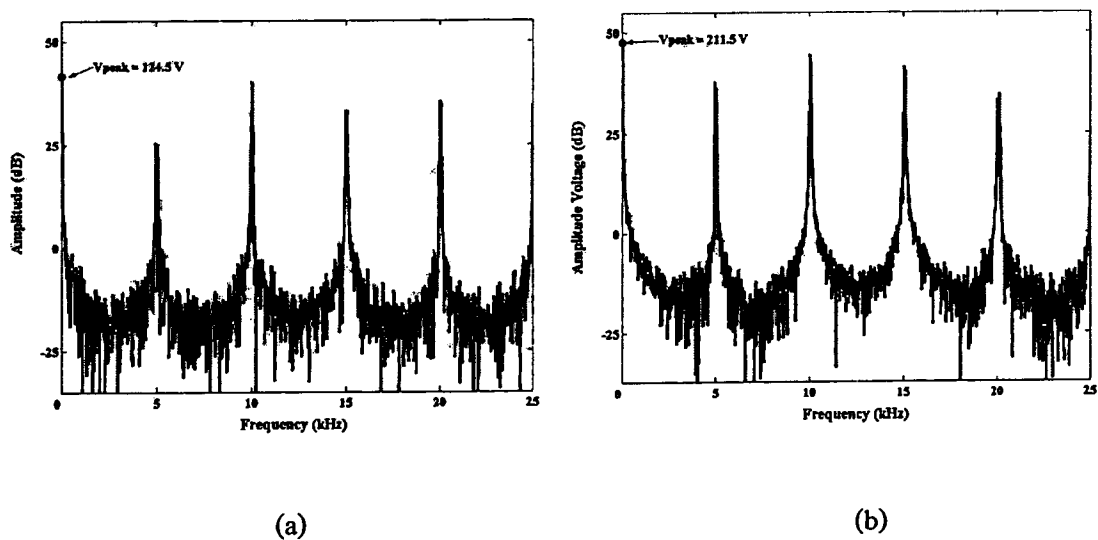
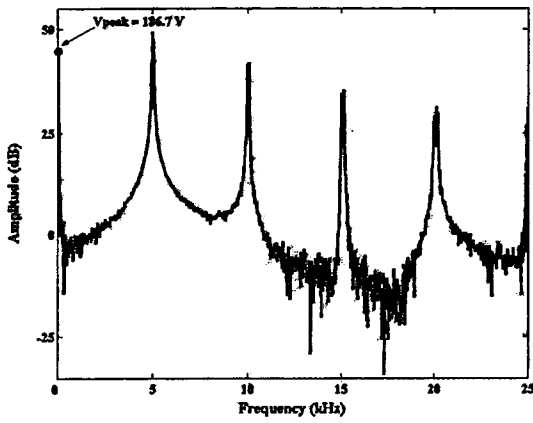
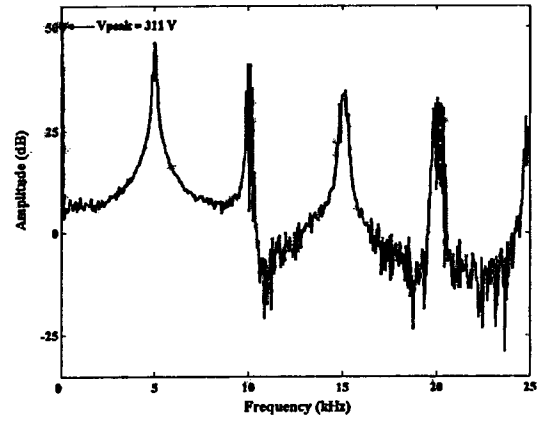


Figure 4.17 Measured results of voltage stress of the three-leg VSI at inverter frequency of 20 Hz

- (a) main winding
- (b) auxiliary winding



(a)

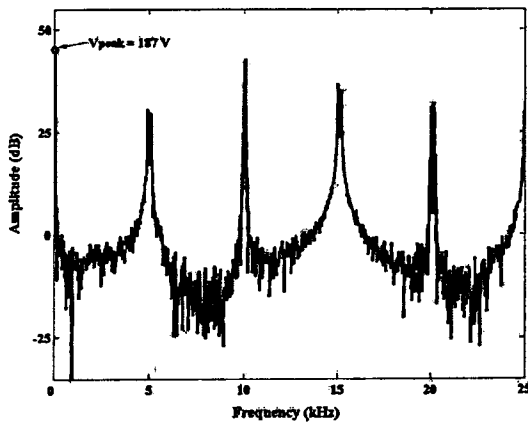


(b)

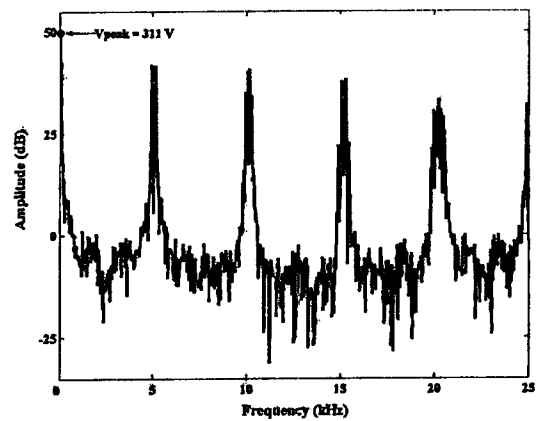
Figure 4.18 Measured results of voltage stress of the two-leg VSI at inverter frequency of 30 Hz

(a) main winding

(b) auxiliary winding



(a)



(b)

Figure 4.19 Measured results of voltage stress of the three-leg VSI at inverter frequency of 30 Hz

(a) main winding

(b) auxiliary winding

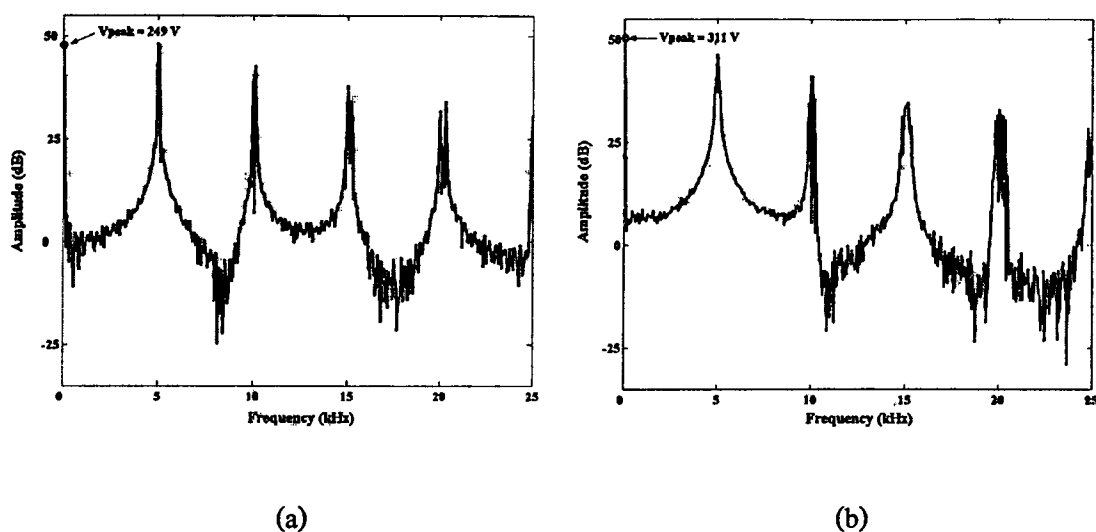


Figure 4.20 Measured results of voltage stress of the two-leg VSI at inverter frequency of 40 Hz

(a) main winding

(b) auxiliary winding

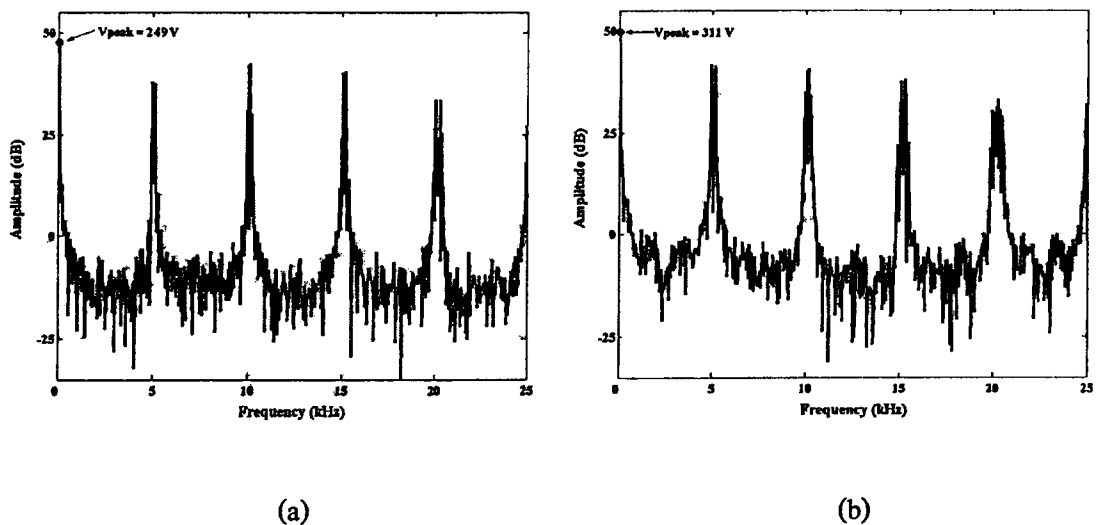


Figure 4.21 Measured results of voltage stress of the three-leg VSI at inverter frequency of 40 Hz

(a) main winding

(b) auxiliary winding

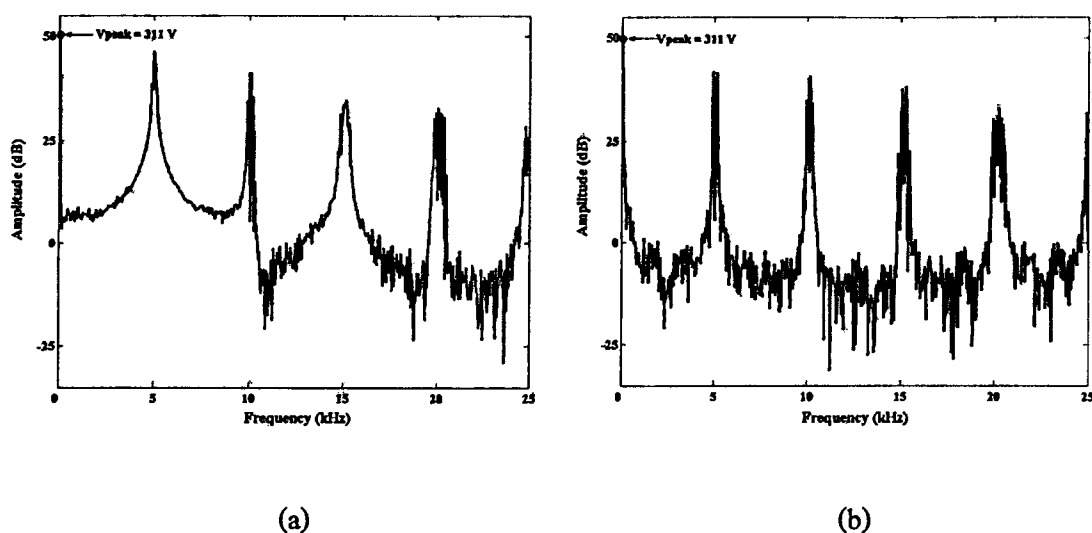


Figure 4.22 Measured results of both windings voltage stress at inverter frequency of 50 Hz

(a) the two-leg VSI

(b) the three-leg VSI

Table 4.1 Generalized harmonics of SPWM signals for the auxiliary winding

Inverter topology	2-leg				3-leg			
Frequency (Hz)	20	30	40	50	20	30	40	50
Fundamental (pu)	0.58	0.85	0.85	0.85	0.58	0.85	0.85	0.85
m_a	0.58	0.85	0.85	0.85	0.58	0.85	0.85	0.85
harmonic								
m_f	1.022	0.767	0.767	0.767	-	-	-	-
$m_f \pm 2$	0.124	0.244	0.244	0.244	0.175	0.345	0.345	0.345
$2m_f \pm 1$	0.371	0.287	0.287	0.287	0.371	0.287	0.287	0.287
$2m_f \pm 3$	0.066	0.158	0.158	0.158	0.066	0.157	0.157	0.157
$3m_f$	0.067	0.169	0.169	0.169	-	-	-	-
$3m_f \pm 2$	0.202	0.153	0.153	0.153	0.285	0.218	0.218	0.218
$3m_f \pm 4$	0.041	0.120	0.120	0.120	-	-	-	-

Table 4.2 Generalized harmonics of SPWM signals for the main winding

Inverter topology	2-leg				3-leg			
Frequency (Hz)	20	30	40	50	20	30	40	50
Fundamental (pu)	0.34	0.51	0.68	0.85	0.34	0.51	0.68	0.85
m_a	0.34	0.51	0.68	0.85	0.34	0.51	0.68	0.85
harmonic								
m_f	1.184	1.077	0.936	0.767	0.084	0.162	0.106	-
$m_f \pm 2$	0.045	0.097	0.165	0.244	0.112	0.228	0.287	0.345
$2m_f \pm 1$	0.294	0.363	0.359	0.287	0.230	0.225	0.281	0.287
$2m_f \pm 3$	0.014	0.046	0.096	0.158	0.064	0.164	0.169	0.157
$3m_f$	0.193	0.0003	0.136	0.169	0.121	0.053	0.016	-
$3m_f \pm 2$	0.109	0.183	0.206	0.153	0.202	0.213	0.245	0.218
$3m_f \pm 4$	0.005	0.026	0.068	0.120	0.036	0.112	0.071	-

4.4.2 Acoustic Noise

Acoustic noise or audible noise can be divided into two categories; radiated and conducted noise. In this research, the effect of harmonic voltage contents in SPWM voltage sources on the motor performance is the main area of interest and, hence, that conducted acoustic noise is of principal concern.

An acoustic noise test was initially conducted without machine operation and used as a reference acoustic noise signal. While the motor is operating, the noises with magnitudes that are greater than the reference signal are attributed as the additional noise generated by the tested motor. To confirm the precision of the obtained results, many factors of operating conditions were maintained. For example, at the same frequency, the fundamental amplitude voltages across the main and the auxiliary windings employed by both inverters were similar and the motor was connected with the same average load torque. The position of the installed microphone was fixed at a distance of 3 cm from the motor. The acoustic noise results from the installed microphone were recorded in form of filename.wav using the Audio program.

To separate the magnitude of noises in frequency variance, the raw data were analyzed by the program as described in Appendix D. Figures 4.23 - 4.26 show the profile of acoustic noise spectra characteristics versus frequency variation from 0-2000 Hz. These figures

This material is reserved for educational use only, not allowed for commercial use.

Forbidden to modify the content, and cite the document when use.

clearly show that, at the same inverter frequency, the noise components of three-leg VSI are mostly attenuated. These results confirm that the proposed technique can effectively diminish acoustic noise levels and proves that harmonics voltage stress on the motor are the main cause of acoustic noise generation [98].

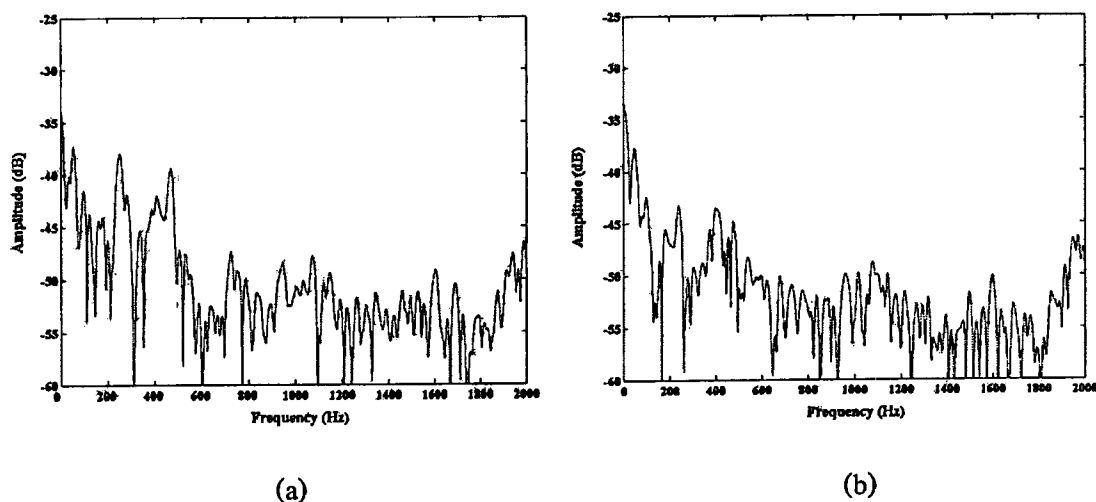


Figure 4.23 Measured spectra of acoustic noise with inverter fed induction motor at inverter frequency of 20 Hz

- (a) the two-leg VSI
- (b) the three-leg VSI

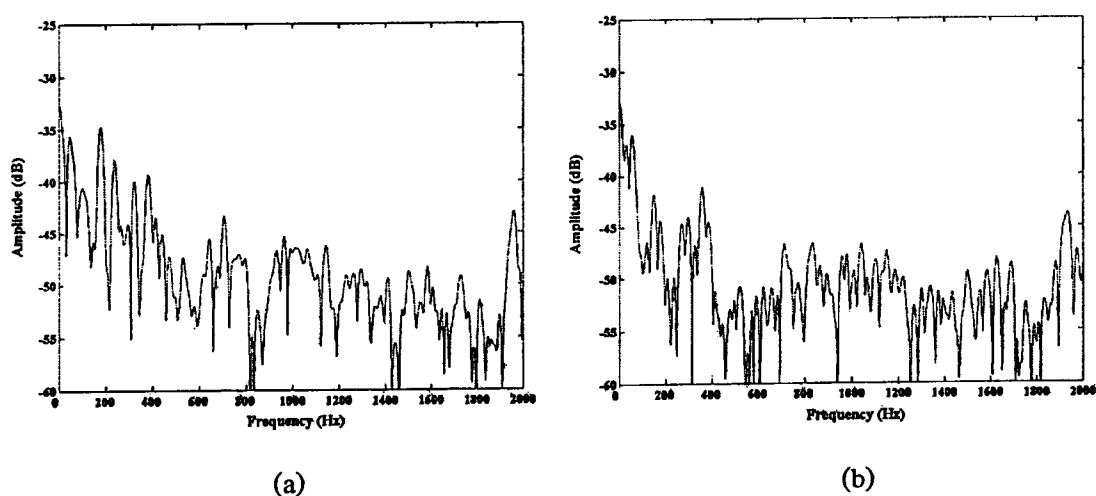
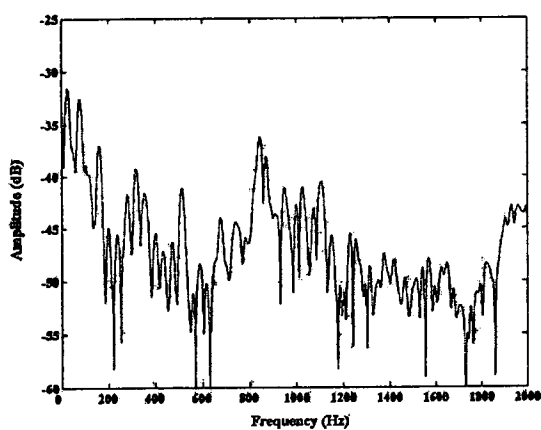
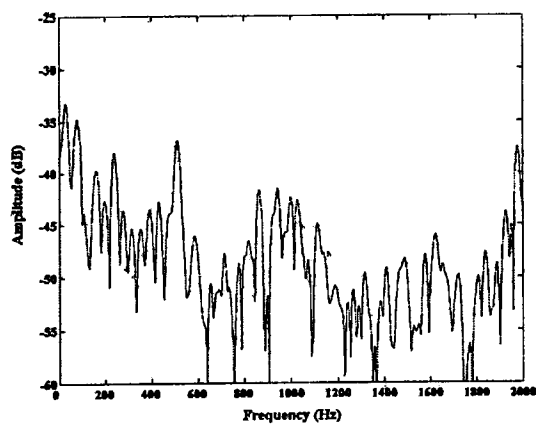


Figure 4.24 Measured spectra of acoustic noise with inverter fed induction motor at inverter frequency of 30 Hz

- (a) the two-leg VSI
- (b) the three-leg VSI



(a)

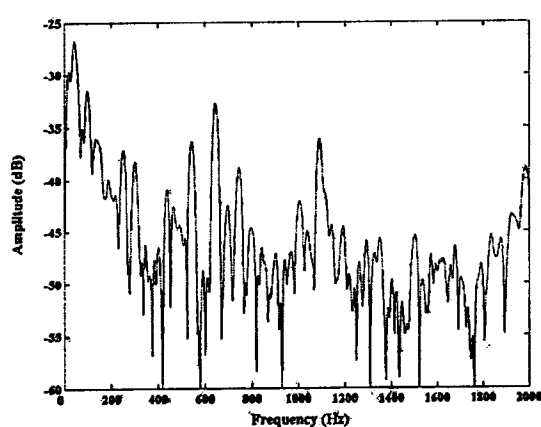


(b)

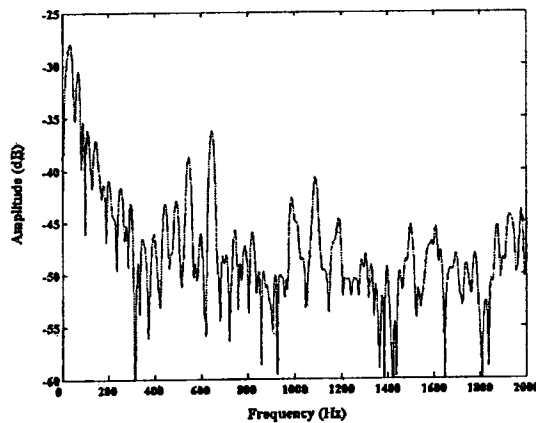
Figure 4.25 Measured spectra of acoustic noise with inverter fed induction motor
at inverter frequency of 40 Hz

(a) the two-leg VSI

(b) the three-leg VSI



(a)



(b)

Figure 4.26 Measured spectra of acoustic noise with inverter fed induction motor
at inverter frequency of 50 Hz

(a) the two-leg VSI

(b) the three-leg VSI

4.4.3 Harmonic Current and Total Harmonic Distortion of Current

In order to verify the simulated current results, and to investigate practical aspects related to two inverter topologies, the total harmonic distortion of current of each winding for both the 2-leg and the 3-leg drive systems, obtained from the unsymmetrical two-phase induction motor model over the same time domain and load torque (1.5 N-m), were compared to the measured values. Figures 4.27 - 4.34 show the simulated results using the two-phase motor model.

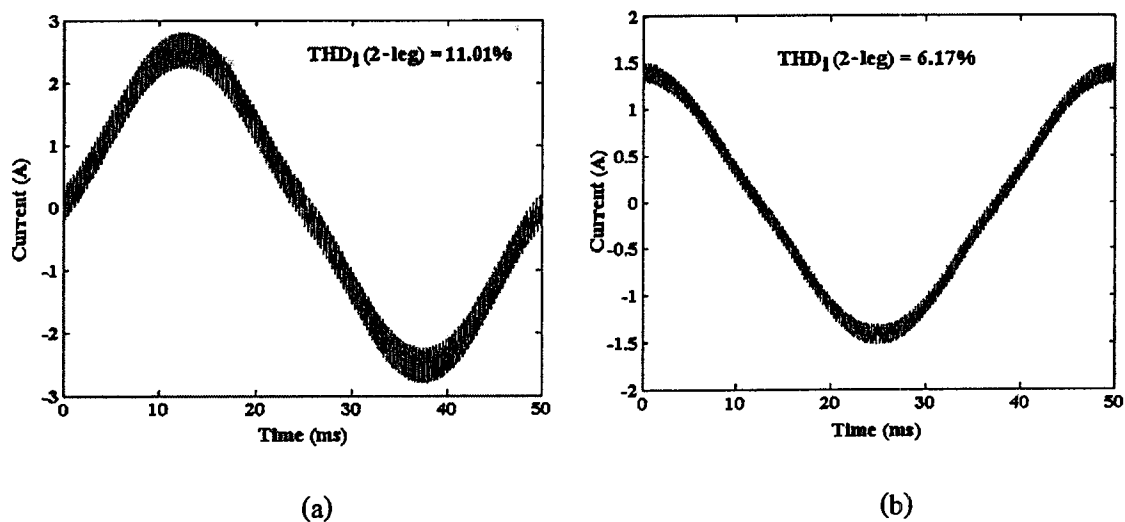


Figure 4.27 Simulated current waveform for two-leg VSI at inverter frequency of 20 Hz

(a) main winding

(b) auxiliary winding

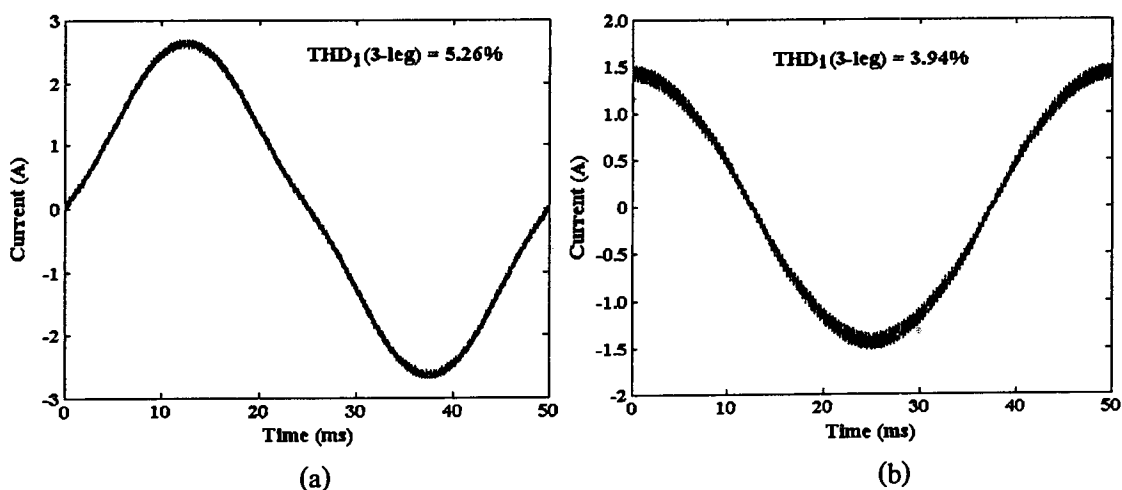


Figure 4.28 Simulated current waveform for three-leg VSI at inverter frequency of 20 Hz

(a) main winding

(b) auxiliary winding

This material is reserved for educational use only, not allowed for commercial use.

Forbidden to modify the content, and cite the document when use.

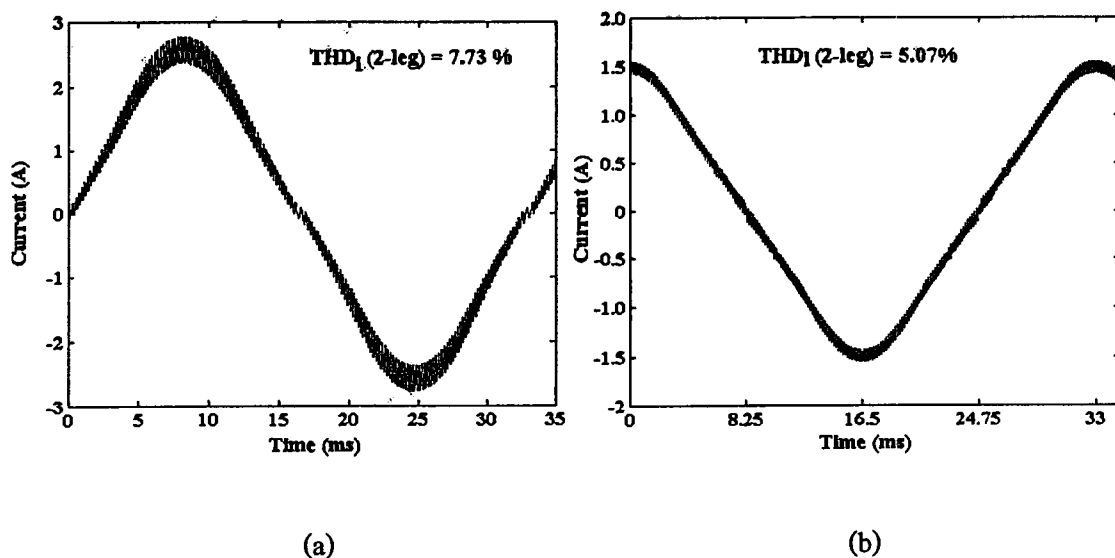


Figure 4.29 Simulated current waveform for two-leg VSI at inverter frequency of 30 Hz

- (a) main winding
- (b) auxiliary winding

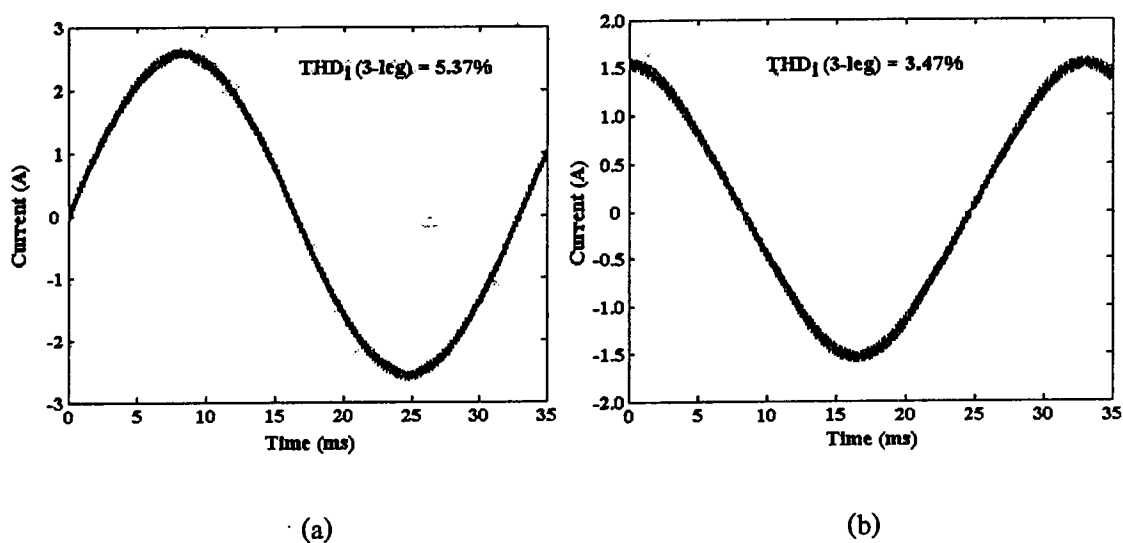


Figure 4.30 Simulated current waveform for three-leg VSI at inverter frequency of 30 Hz

- (a) main winding
- (b) auxiliary winding

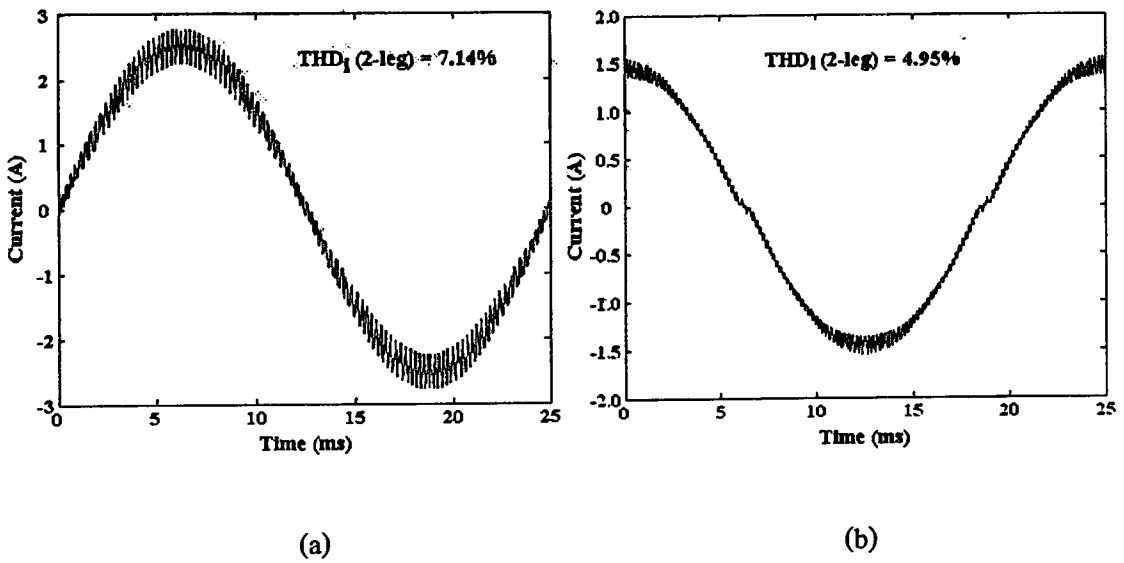


Figure 4.31 Simulated current waveform for two-leg VSI at inverter frequency of 40 Hz

- (a) main winding
- (b) auxiliary winding

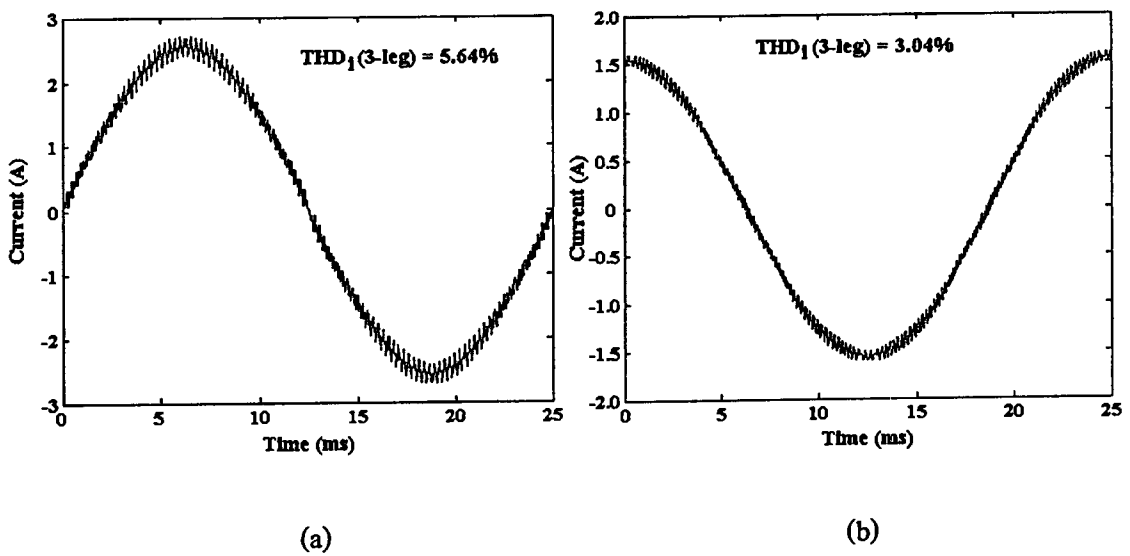


Figure 4.32 Simulated current waveform for three-leg VSI at inverter frequency of 40 Hz

- (a) main winding
- (b) auxiliary winding

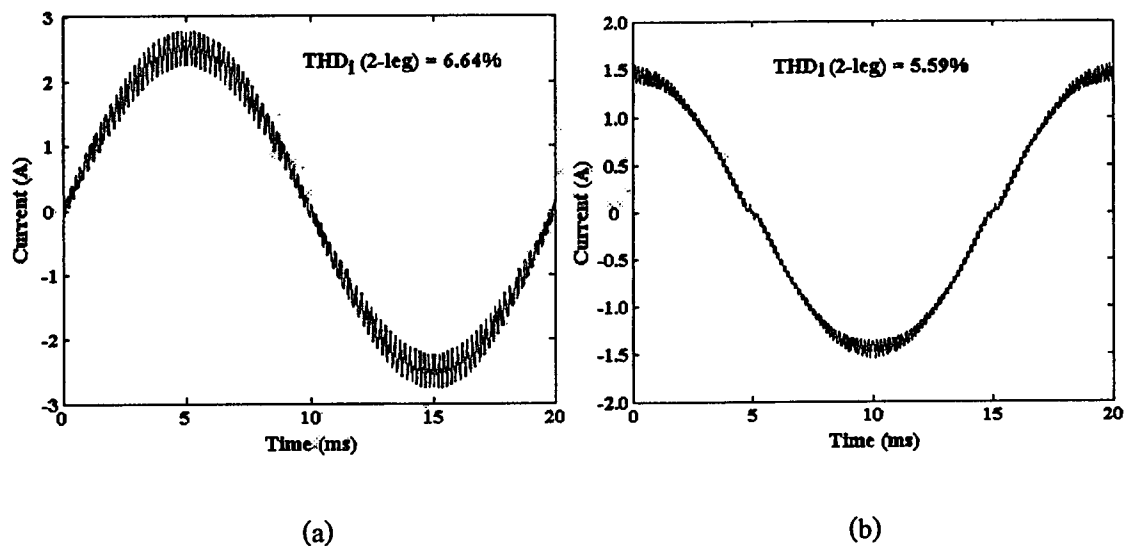


Figure 4.33 Simulated current waveform for two-leg VSI at inverter frequency of 50 Hz

- (a) main winding
- (b) auxiliary winding

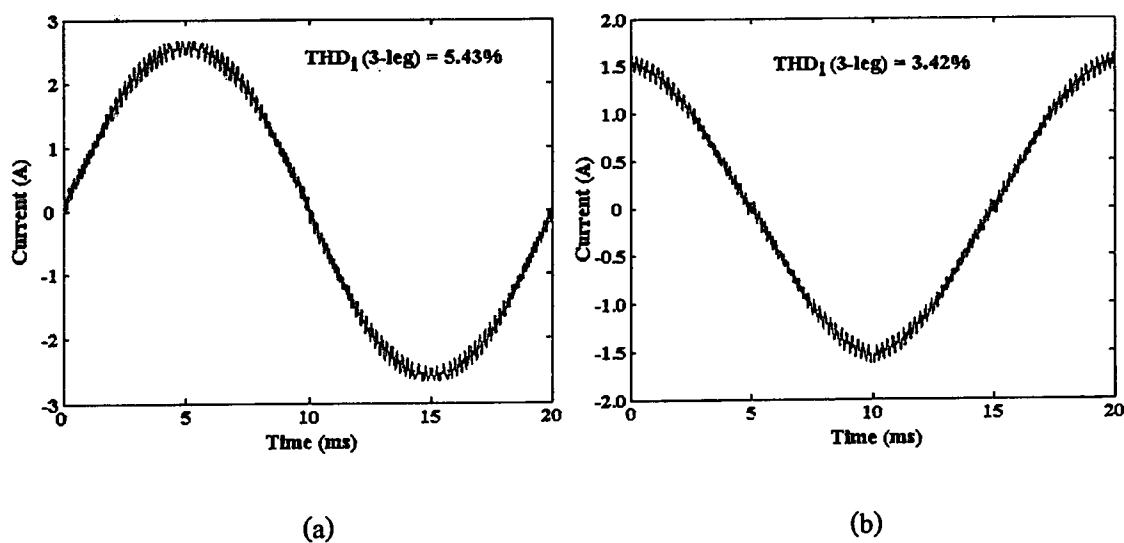


Figure 4.34 Simulated current waveform for three-leg VSI at inverter frequency of 50 Hz

- (a) main winding
- (b) auxiliary winding

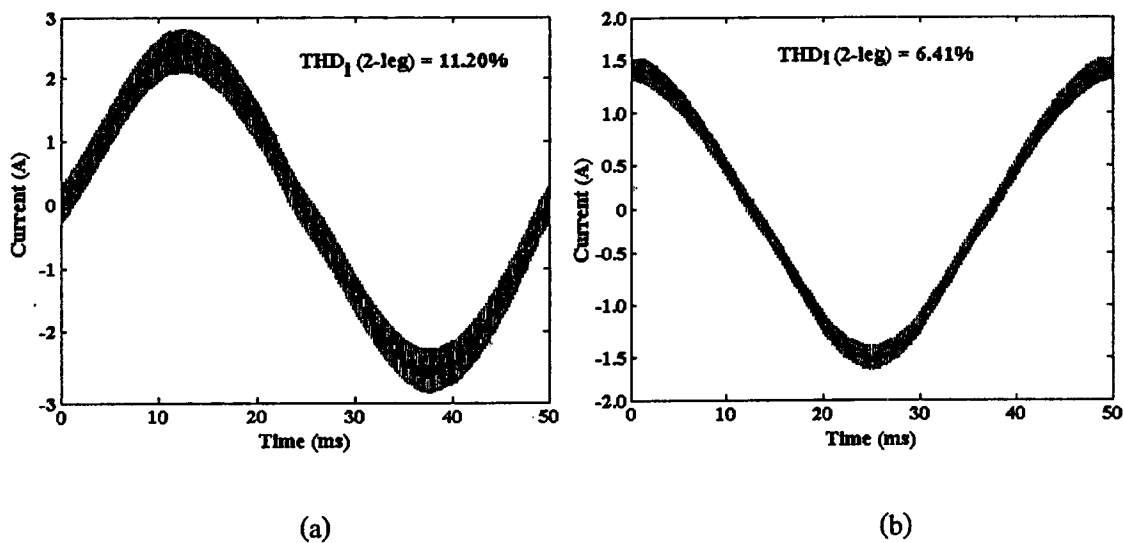


Figure 4.35 Measured current waveform for two-leg VSI at inverter frequency of 20 Hz

- (a) main winding
- (b) auxiliary winding

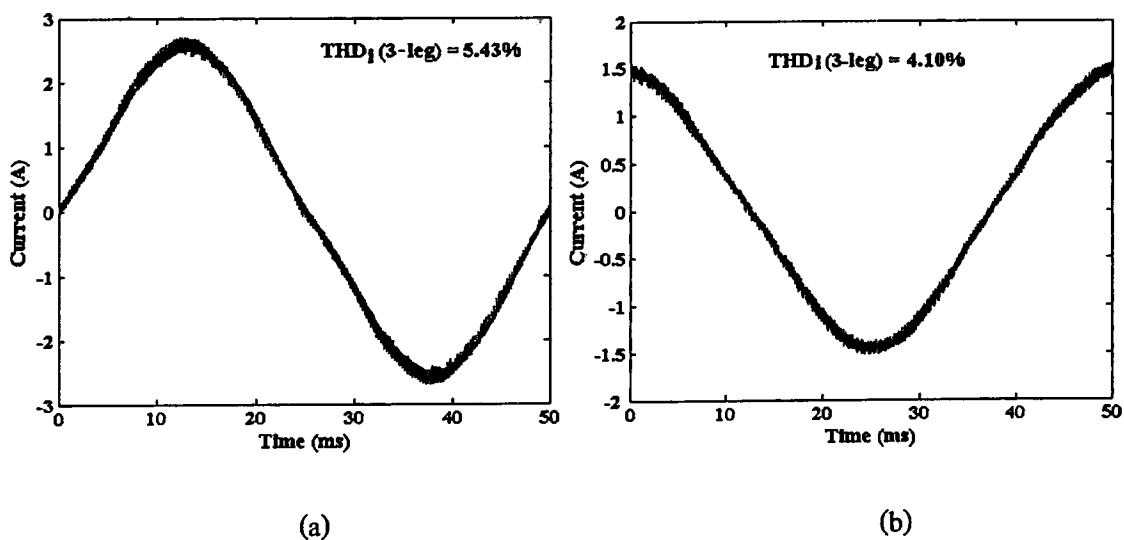


Figure 4.36 Measured current waveform for three-leg VSI at inverter frequency of 20 Hz

- (a) main winding
- (b) auxiliary winding

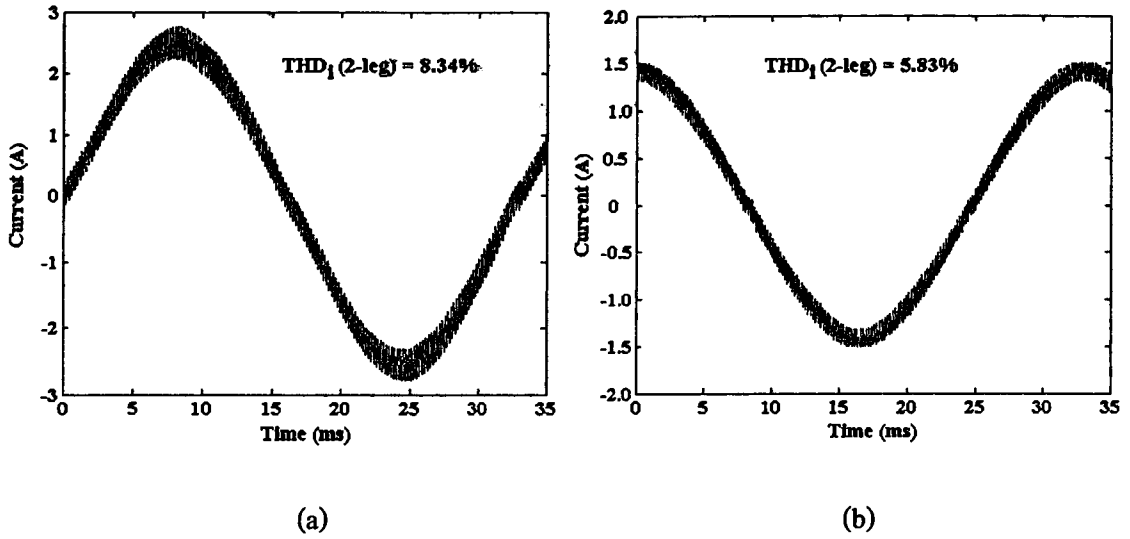


Figure 4.37 Measured current waveform for two-leg VSI at inverter frequency of 30 Hz

- (a) main winding
- (b) auxiliary winding

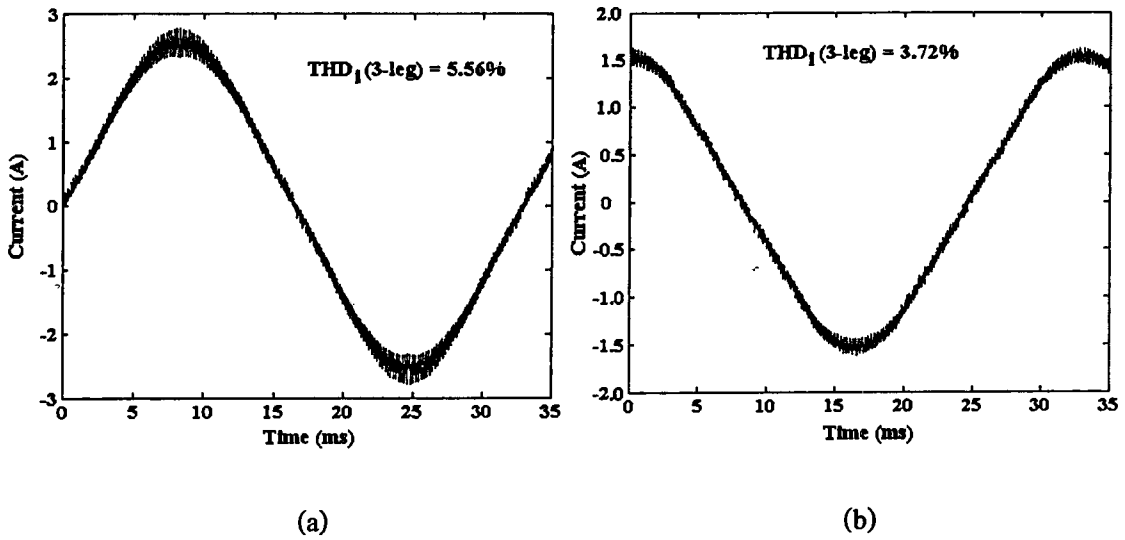


Figure 4.38 Measured current waveform for three-leg VSI at inverter frequency of 30 Hz

- (a) main winding
- (b) auxiliary winding

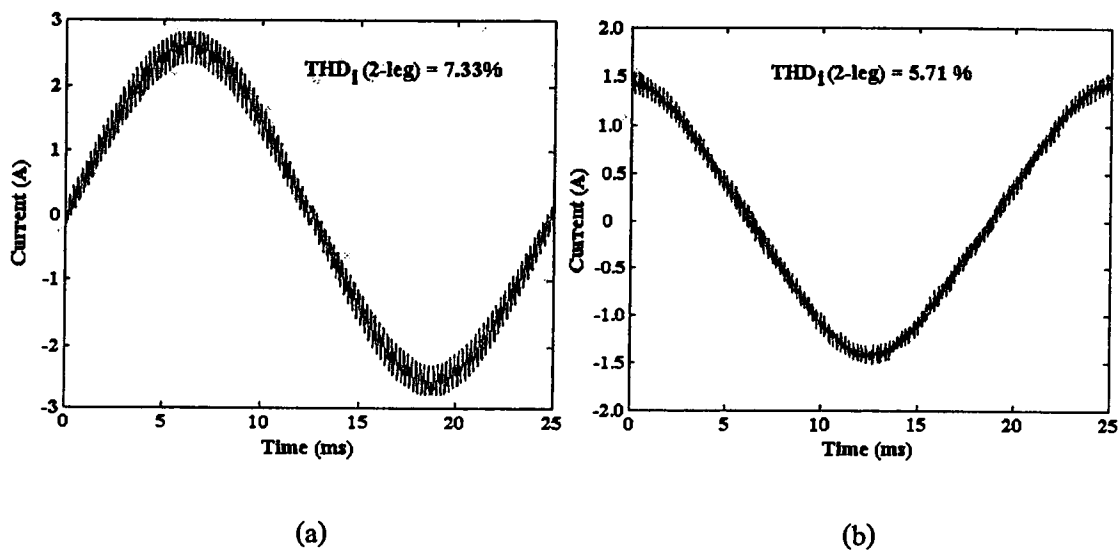


Figure 4.39 Measured current waveform for two-leg VSI at inverter frequency of 40 Hz

(a) main winding

(b) auxiliary winding

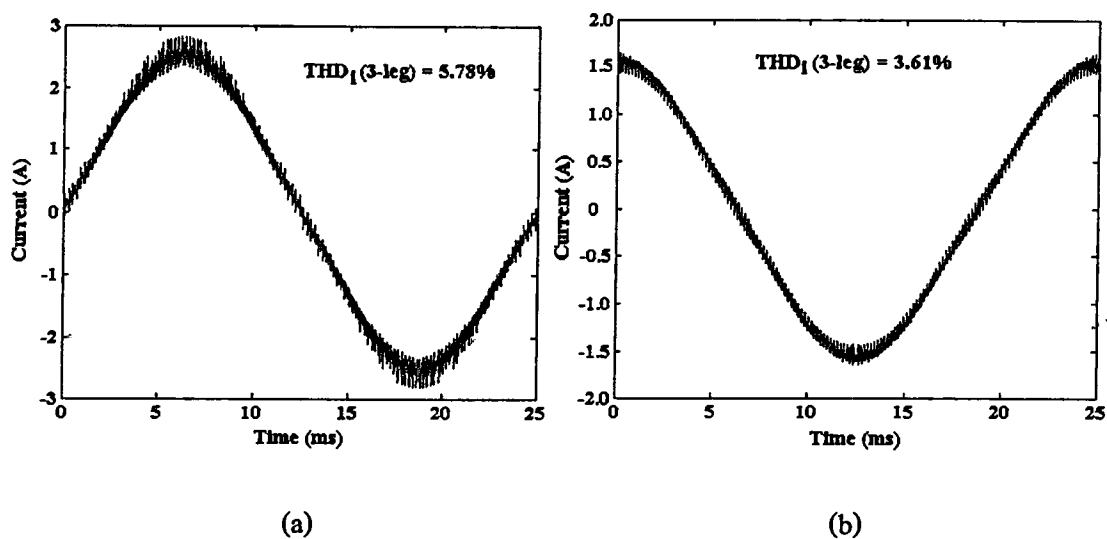


Figure 4.40 Measured current waveform for three-leg VSI at inverter frequency of 40 Hz

(a) main winding

(b) auxiliary winding

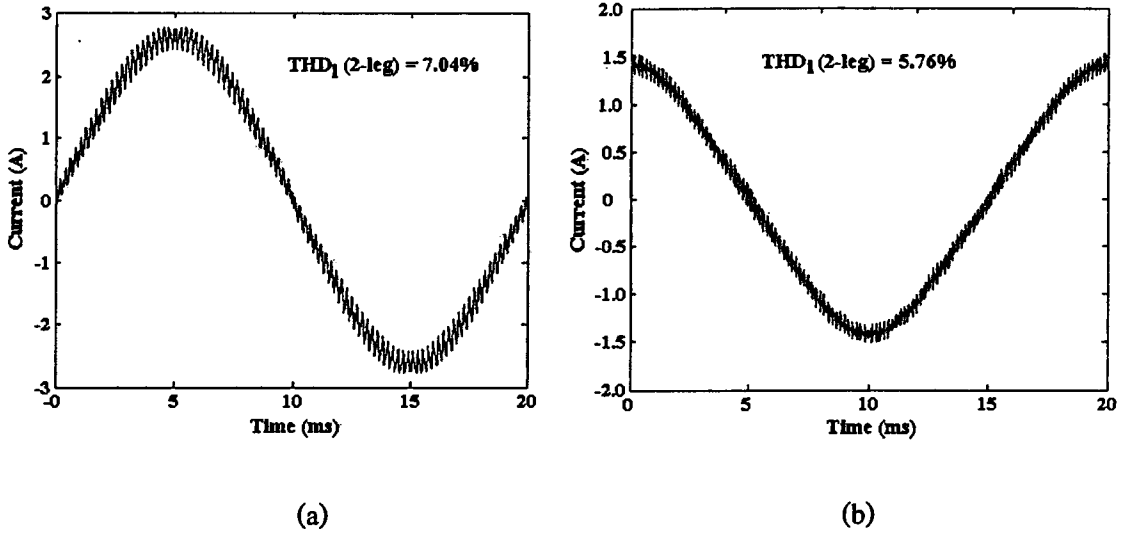


Figure 4.41 Measured current waveform for two-leg VSI at inverter frequency of 50 Hz

- (a) main winding
- (b) auxiliary winding

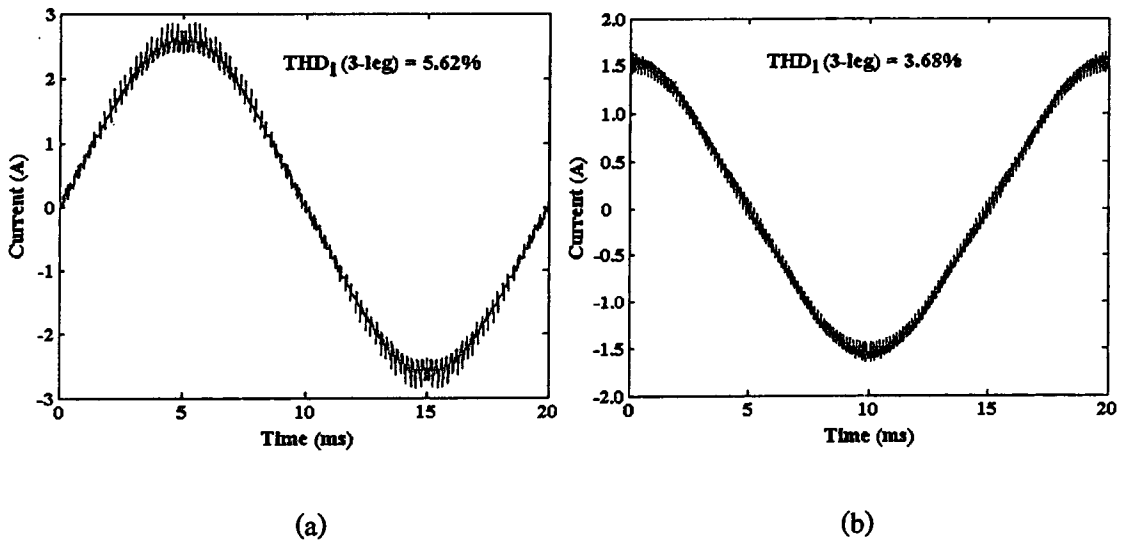


Figure 4.42 Measured current waveform for three-leg VSI at inverter frequency of 50 Hz

- (a) main winding
- (b) auxiliary winding

A power harmonic analyzer PZ4000 was used to measure the actual harmonic current data with high accuracy. Each experimental result was saved as a filename.csv in ASCII-file format. Matlab [®] was used to evaluate the total harmonic distortion of current and to plot the current configuration in one cycle at the same time domain.

To monitor the difference of the measured THDi for each drive system and for the simulation, all results are rewritten in terms of the THDi comparison and presented in Table 4.3. It is clear from the comparison that the three-leg configuration provides a better performance than the two-leg system in terms of THDi. This is consistent with the harmonic voltage spectra characteristics. It is observed that the simulated results yield total harmonic distortions of current that are slightly less than of the measured values, thereby proving the accuracy of the implemented circuits. The small discrepancy between the results may arise from various factors. For example, the simulation results were analyzed assuming ideal power electronic devices whereas the measured results incorporate many effects such as voltage ripple of the dc link voltage, blanking time in practical inverter legs, and voltage drop in devices.. However, it can be seen that the correlation is satisfactory.

Table 4.3 Comparison of the 2-leg and 3-leg inverter topologies in terms of THDi

Frequency (Hz)	Simulated THDi (%)				Measured THDi (%)			
	2-leg		3-leg		2-leg		3-leg	
	main	aux	main	aux	main	aux	main	aux
20	11.01	6.17	5.26	3.94	11.20	6.41	5.43	4.10
30	7.73	5.07	5.37	3.47	8.34	5.83	5.56	3.72
40	7.14	4.95	5.64	3.04	7.33	5.71	5.78	3.61
50	6.64	5.59	5.43	3.42	7.04	5.76	5.62	3.68

4.4.4 Current Characteristics and Loci Current

In order to validate the benefit of the proposed control technique, the main and the auxiliary winding current profiles were studied. The stator winding currents fed by the two-leg and the three-leg VSI are presented in Figures 4.43 and 4.44, respectively, when the motor is operated at rated current. These two figures confirm that the proposed modulation strategy

This material is reserved for educational use only, not allowed for commercial use.

Forbidden to modify the content, and cite the document when use.

significantly lowers the harmonic voltage, especially at low operating frequency, more so than the conventional system. Also, the output currents of the three-leg VSI under unbalanced output voltage are approximately a sinusoidal waveform and displaced by approximately 90 electrical degrees.

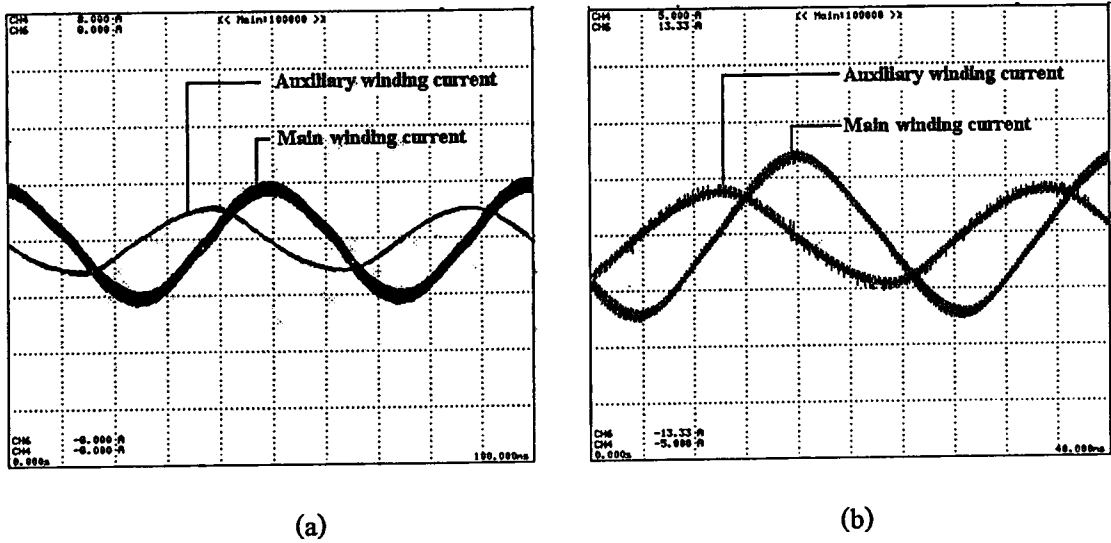


Figure 4.43 Experimental results of motor winding currents for the two-leg VSI

- (a) reference frequency at 20 Hz
- (b) reference frequency at 40 Hz

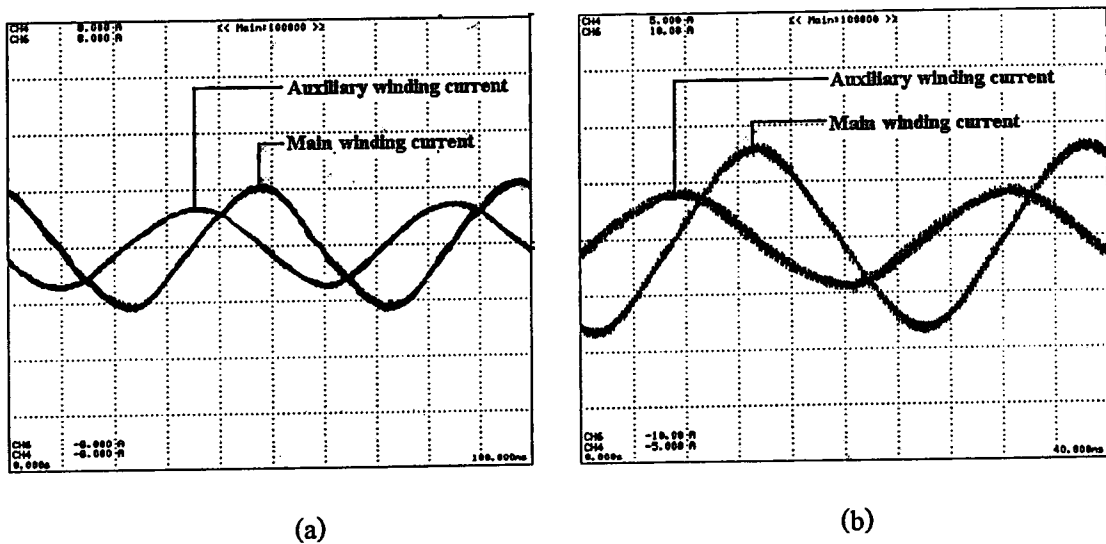


Figure 4.44 Experimental results of motor winding currents for the three-leg VSI

- (a) reference frequency at 20 Hz
- (b) reference frequency at 40 Hz

This material is restricted to personal use only, not allowed for commercial use.

Forbidden to modify the content, and cite the document when use.

The correlation of stator currents can be used to predict the stator magnetomotive force (MMF) and air gap flux features. The relationship between the measured auxiliary and main winding currents was plotted together as a locus of current. The stator current trajectory of the tested motor fed by the two-leg and the three-leg inverters are included in Figures 4.45 and 4.46, respectively.

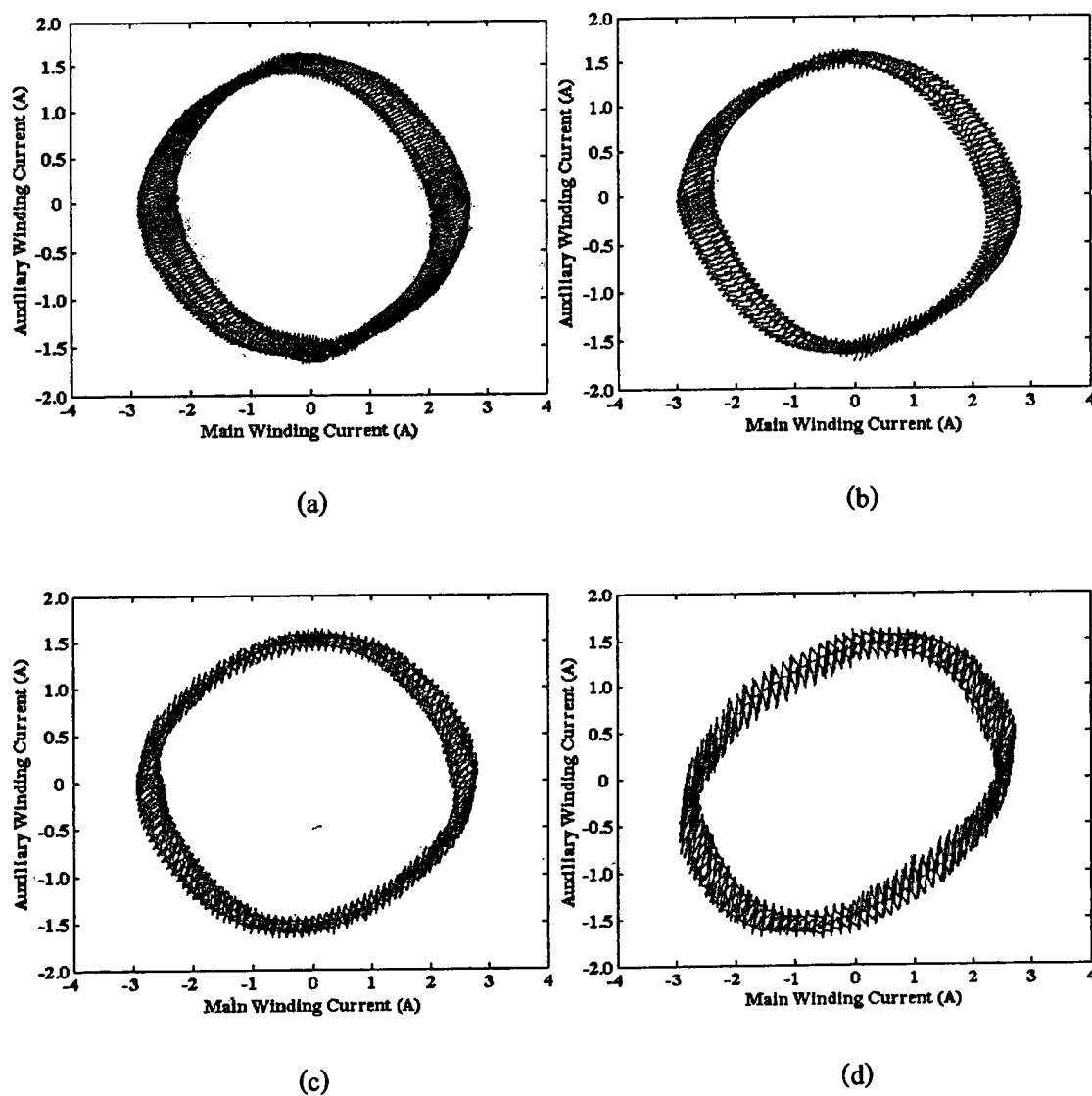


Figure 4.45 Experimental results of loci currents for the two-leg VSI

- (a) reference frequency at 20 Hz
- (b) reference frequency at 30 Hz
- (c) reference frequency at 40 Hz
- (d) reference frequency at 50 Hz

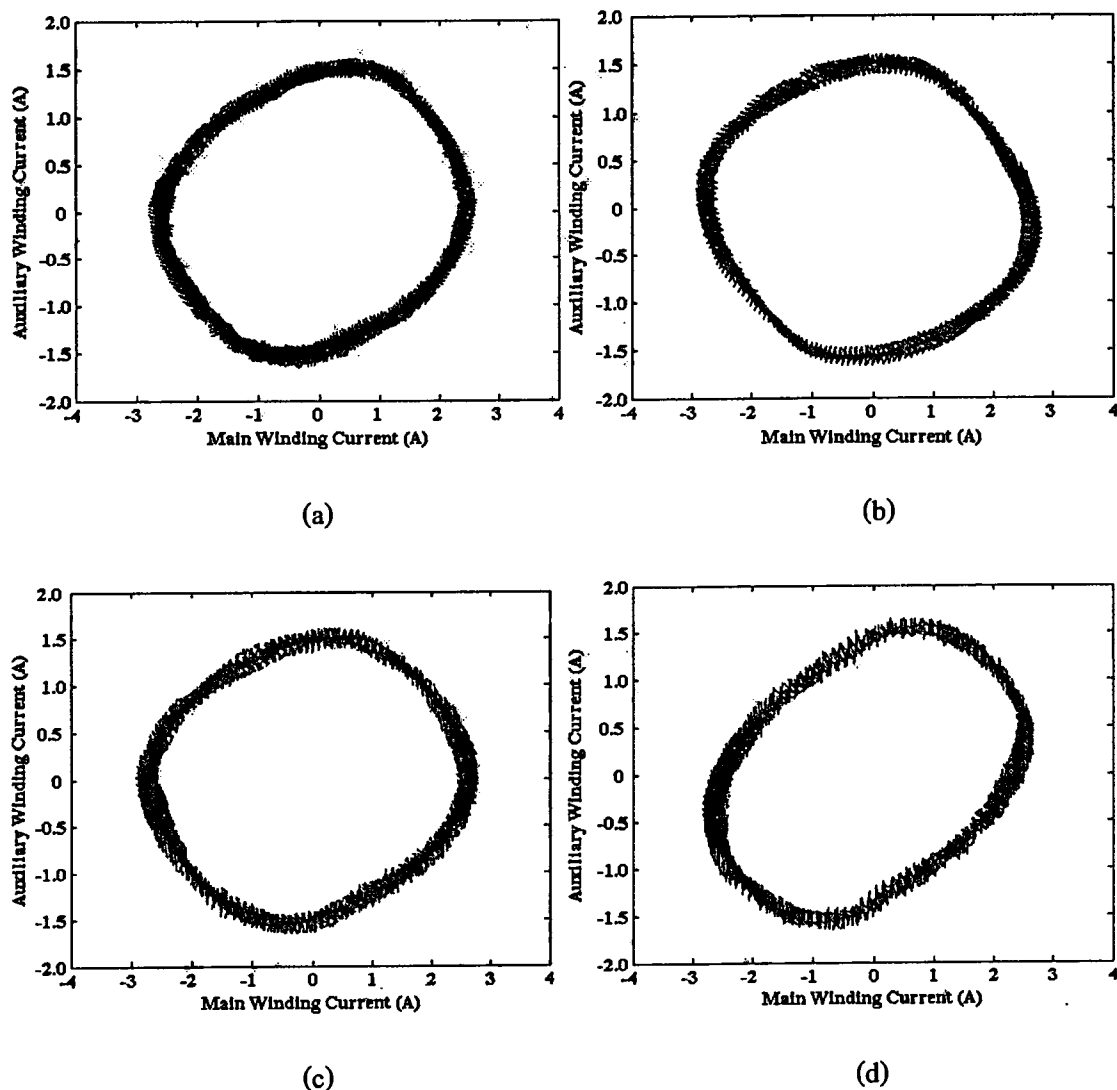


Figure 4.46 Experimental results of loci currents for the three-leg VSI

- (a) reference frequency at 20 Hz (b) reference frequency at 30 Hz
(c) reference frequency at 40 Hz (d) reference frequency at 50 Hz

Figures 4.45 and 4.46 prove that the current trajectory at the frequency of completed voltage boost of the auxiliary winding with turns ratio “ a ” times main winding voltage (i.e. 20 Hz) is fairly circle and symmetry. The loci currents at higher frequency are ellipse. This is expected because, at higher frequency of $\frac{f_{rated}}{a}$, the current compensation of the auxiliary winding with the voltage boost can be partially achieved. Figures 4.45 (a) and 4.46 (a) clearly show that the proposed control method can approach the less backward field in the motor. This means that the more circular loci current, the lower backward field, and the greater symmetry air gap flux.

This material is reserved for educational use only, not allowed for commercial use.

Forbidden to modify the content, and cite the document when use.

4.4.5 Motor Efficiency and Output Torque

To study the influence of the decreasing harmonic voltage component on motor performance, the motor efficiency and torque-speed characteristics were determined. The variation of motor efficiency as a function of load torque are presented in Figures 4.47 - 4.50 for the two-leg and the three-leg VSI, with typical V/F for both windings and the proposed control method, under the same fundamental voltage at a fundamental frequency of between 20 Hz and 50 Hz.

For the results presented in Figure 4.50 only, the motor under test was fed by the two drive systems and a sinusoidal supply at the rated frequency of 50 Hz. This operating frequency provides the same voltage level of both windings for both drive systems. When the motor is supplied by an ac sinusoidal source, a running capacitor of $8 \mu F$ was utilized in series with the auxiliary winding. The motor was connected as a conventional operation.

Figures 4.47 - 4.49 confirm that the proposed control method provides better efficiency than the conventional V/F control scheme for both windings. Furthermore, the three-leg VSI with the proposed technique gives the greatest motor efficiency over a wide range of speed, while the two-leg VSI with V/F control scheme for both windings provides the worst performance because of harmonic contents. Additionally, at low frequency, the motor efficiencies for both drive systems are significantly different since at low frequency (low modulation index) the two-leg VSI generates higher harmonic voltages, particularly at the order of m_f . The maximum efficiencies of each of the inverter topologies and of control methods with variable reference frequency are presented in Table 4.4.

It can be seen from Figure 4.50 that the operation ranges of the motor fed by the inverter are narrower than those of the sinusoidal supply. However, the three-leg VSI with the proposed scheme still obtains the best motor efficiency because the inverter structure can exactly control the quadrature of the two-winding voltages. Surprisingly, for the 50 Hz sinusoidal source, the efficiency is lower than both drive systems at a light load torque. This is because the running capacitor value is normally designed for heavy loads.

Figure 4.51 demonstrates torque-speed motor profiles with various fundamental frequencies under the proposed control method, while Figure 4.52 describes that relationship with constant V/F control scheme for both windings. When comparing these two figures, it is evident that unbalanced output voltage provides superior torque to the constant V/F scheme for

both windings and a wider range of operation. The measured and simulated results are reasonably close agreement and the measured results for the two-leg and the three-leg are also very similar. These results show that both drive systems provide the same average torque and, therefore, that harmonic voltages do not affect the average load torque. This is consistent with the the finding of other researchers [18-19, 35].

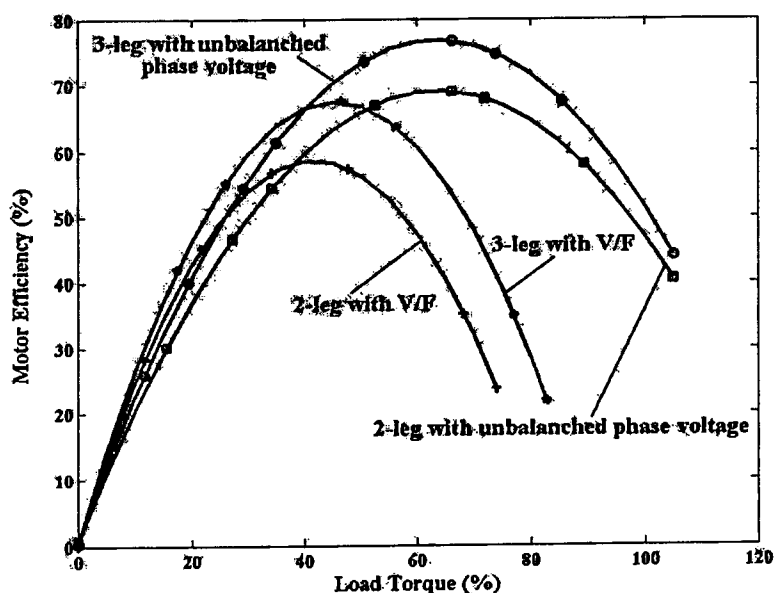


Figure 4.47 Experimental results of motor efficiency versus %load torque with reference frequency at 20 Hz

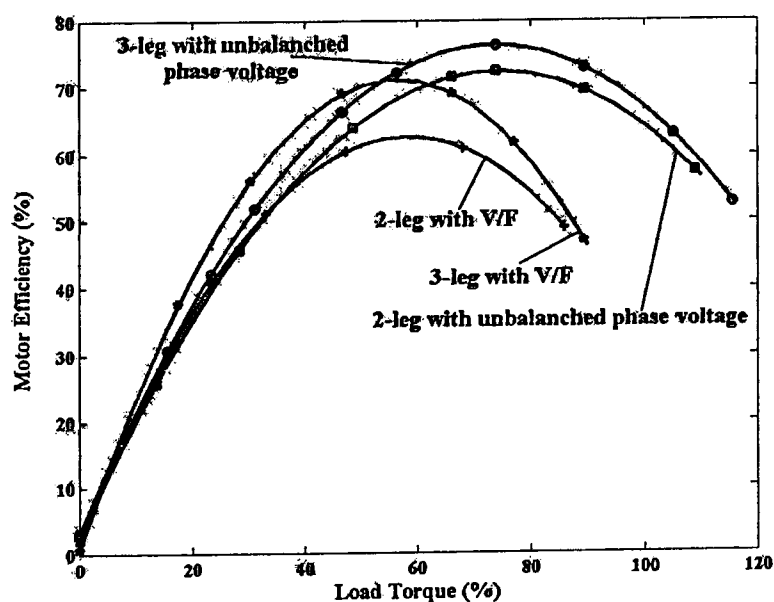


Figure 4.48 Experimental results of motor efficiency versus %load torque with reference frequency at 30 Hz

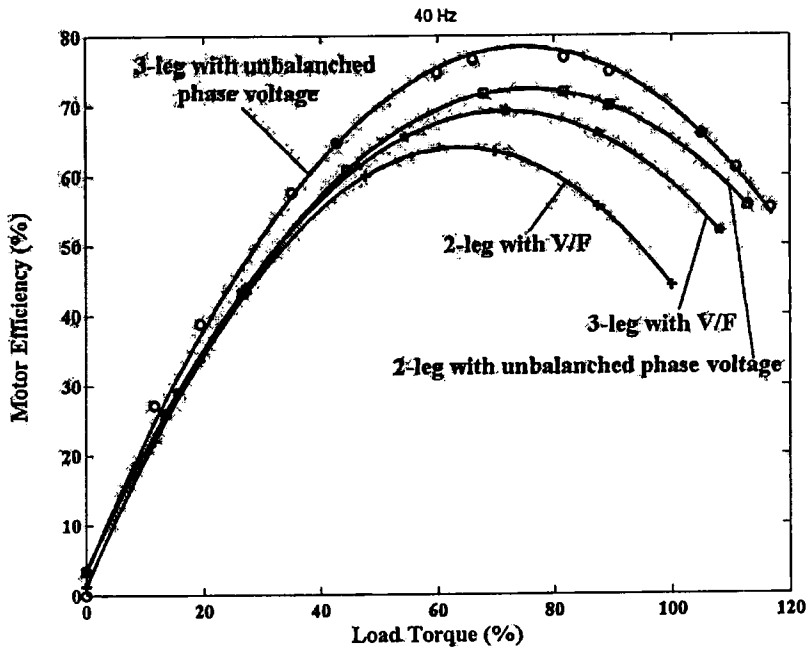


Figure 4.49 Experimental results of motor efficiency versus %load torque with reference frequency at 40 Hz

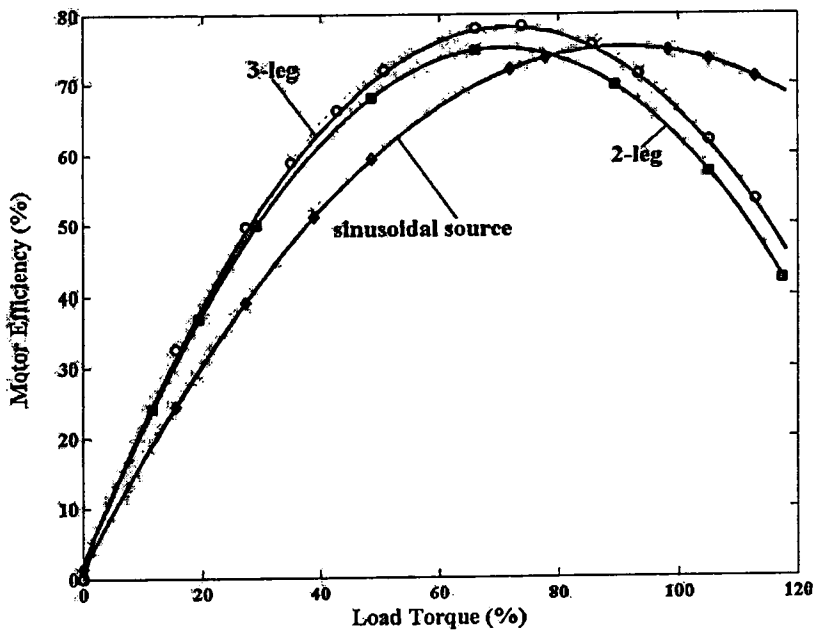


Figure 4.50 Experimental results of motor efficiency versus %load torque at rated frequency of 50 Hz

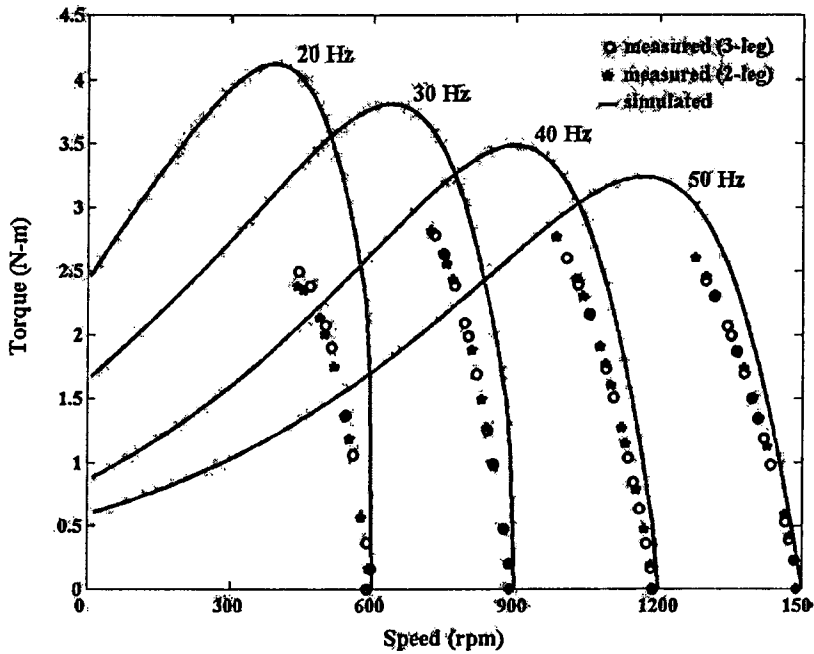


Figure 4.51 Torque as function of motor speed at various frequency for both simulation and experimental results with the unbalanced voltage control method

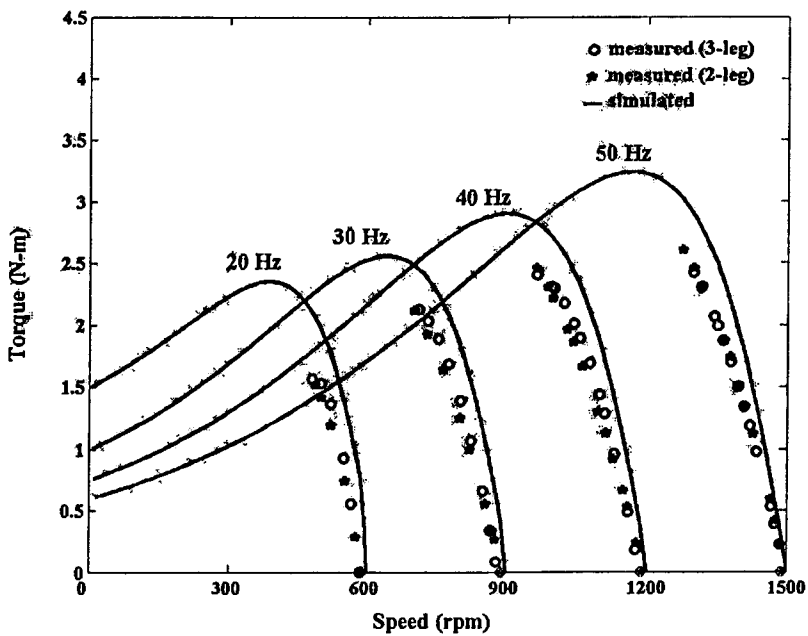


Figure 4.52 Torque as function of motor speed at various frequency for both simulation and experimental results with constant V/Hz control scheme for both windings

Table 4.4 Comparison of the 2-leg and 3-leg inverter topologies with different control method in terms of motor efficiency

Control method	V/F for both windings		Proposed method	
Inverter topology	2-leg	3-leg	2-leg	3-leg
Frequency (Hz)	Maximum motor efficiency (%)			
20	58.8	67.4	70.1	77.5
30	63.1	70.9	71.7	76.2
40	64.0	69.7	72.3	77.8
Supply type	Sinusoidal source		2-leg VSI	3-leg VSI
Frequency : 50 Hz	75.7		75.1	78.8

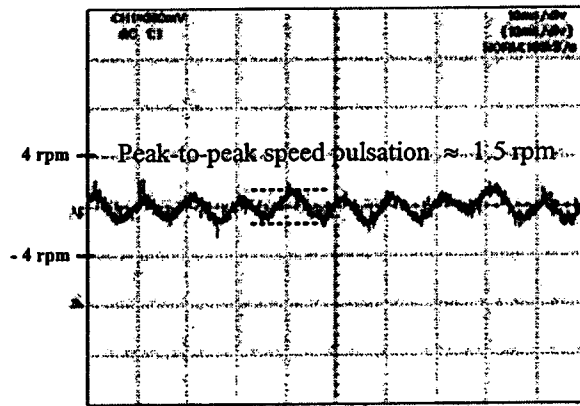
4.4.6 Speed and Torque Pulsations

If the average speed is defined as a dc component of speed response, the speed ripple would be identified as a difference between the highest and the lowest speeds of the steady state speed response. The speed responses for three cases (a sinusoidal supply, the 2-leg VSI, and the 3-leg VSI) at 50 Hz and full torque load are shown in Figure 4.53. All three cases exhibit double frequency (100 Hz) pulsating components. Of the three cases, the sinusoidal supply has smaller pulsating components than the other two and all three cases have the same dc component or average speed. Figures 4.53 (b) and 4.53 (c) verify that harmonic voltages do not significantly affect speed pulsation of the induction motor.

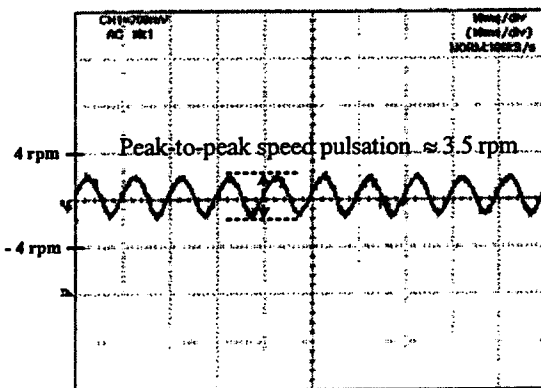
Torque pulsations can be defined in a manner similar to the aforementioned speed pulsations. The torque ripple is the difference between the peak and lowest torques of the steady state torque response and the average torque is an existing dc component of torque response. The load torque responses for three cases (a sinusoidal supply, the 2-leg VSI, and the 3-leg VSI) at 50 Hz with full load torque were considered.

Figure 4.54 highlights the obtainable double frequency (100 Hz) pulsating torque components. The amplitudes of average load torque and torque ripple of all three cases are almost identical. However, it is evident from Figures 4.54 (b) and 4.54 (c) that the harmonic torque components of the motor fed by the 3-leg VSI are lower than those of the motor fed by the

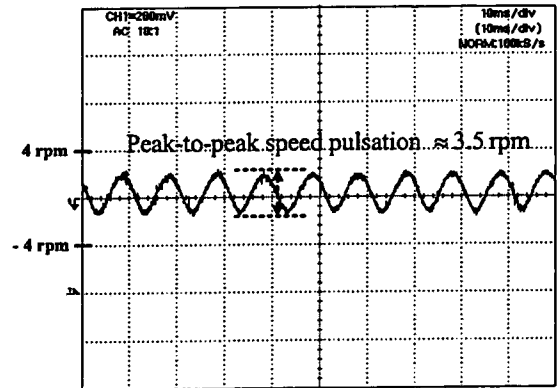
2-leg VSI. These figures prove that the fundamental voltage of PWM patterns mainly concern the dc torque component, while its harmonic voltages predominantly yield harmonic torque contents.



(a)



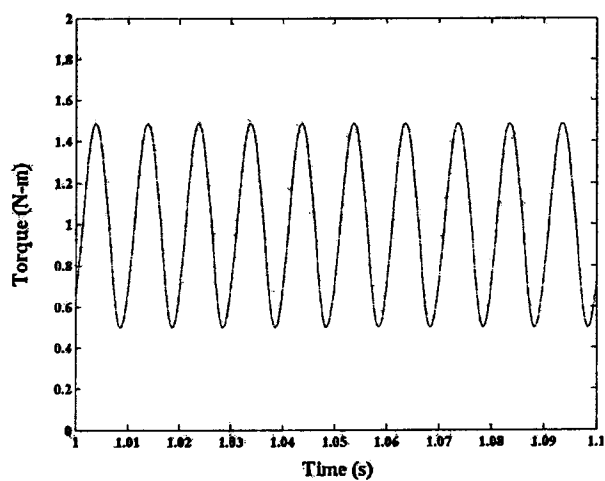
(b)



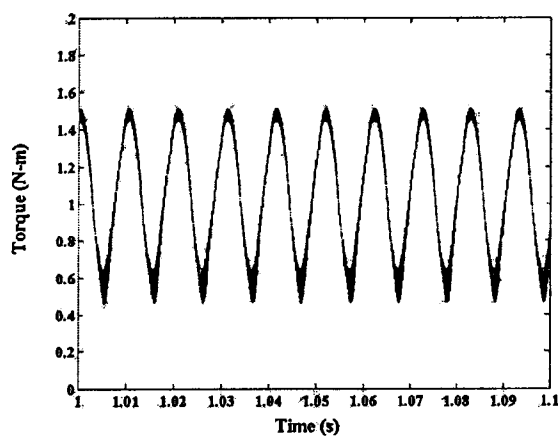
(c)

Figure 4.53 Speed pulsation of motor at the full load torque and the rated frequency

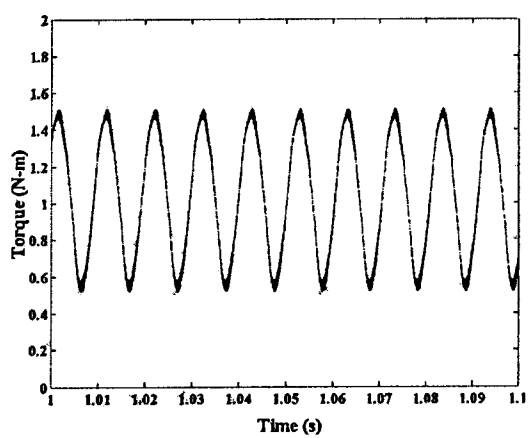
- (a) sinusoidal supply
- (b) the two-leg VSI
- (c) the three-leg VSI



(a)



(b)



(c)

Figure 4.54 Torque pulsation of motor at the full load torque and the rated frequency

- (a) sinusoidal supply
- (b) the two-leg VSI
- (c) the three-leg VSI

4.5 Advantages and Disadvantages

The advantages and disadvantages of the proposed 3-leg VSI in comparison with the conventional 2-leg VSI are evaluated in Table 4.5, including inverter features, cost of investment, and motor characteristics.

Table 4.5 The proposed 3-leg VSI evaluation

Descriptions	Advantages	Disadvantages
Inverter features	$\sqrt{2}$ times dc utilization	Two more power switching devices and two more anti-parallel diodes
	Markedly lower harmonic at carrier frequency and multiples of carrier frequency, especially at m_f	Slightly higher harmonic sidebands
		More complexity of the control method
Motor characteristics	Significantly lower acoustic noise level	
	1-6% THDi reduction	
	3-8% additional motor efficiency	
Cost		A little higher cost

CHAPTER 5

CONCLUSIONS AND FURTHER WORK

In accordance with the features of conventional PSCM, a smaller conductor size and a higher number of winding turns in the auxiliary winding yield greater impedance than that of the main winding. The starting torque for a single-phase PSCM is generally low because the specified parameters of the run capacitor are optimized for merely running conditions. As the capacitance of capacitors being optimized for running period, its magnitude is too small for starting. This results in the phase angle between the currents flowing in the main and the auxiliary windings to be less than 90 electrical degree phase shift, leading to the starting torque lower than a highest feasible starting torque. A solution for overcoming the above drawback of PSCM can be achieved by the proposed modulation strategy for two-phase induction motor drive using the three-leg voltage source inverter.

5.1 Conclusions

The investigations of a new modulation strategy for a three-phase voltage source inverter with unbalanced two-phase output voltages supplying an asymmetrical type two phase induction motor were conducted. A significant advantage of the proposed technique is found to be that this technique allows the unbalanced output voltage control for both main and auxiliary windings. The phase difference between the two voltages is also fixed at 90 electrical degrees. The amplitude of both voltages can be arbitrarily adjusted in accordance with the control technique. Harmonic voltage contents of the proposed drive system have been investigated and compared to those of the two-leg voltage source inverter. A superior PWM quality over the conventional technique can be achieved. The interpretation of the mathematical solution to harmonic voltage contents of SPWM waveform can also be accomplished.

The harmonic voltage spectra in form of dB with frequency variation can be used to predict the tendency of acoustic noise level. It was observed that the more harmonic voltage stress, the higher noise level. The harmonic currents inside the motor, induced by the harmonic voltage contents in voltage source inverter, can be reduced by the proposed modulation strategy.

At low frequency, the quadrature voltages applied to the two windings with the proposed control method can produce rated torques from the motor as expected. Moreover, this technique provides the performance close to that of the unsymmetrical type two-phase induction motor drives regarding cost, reliability, and harmonic effect on the system.

The main findings from the research work and the final conclusions are as follows:

- The proposed three-leg voltage source inverter exhibited less harmonic distortion than the two-leg voltage source inverter. Hence, the circulation of an ac current through the dc link bus can be avoided.

- With two quadrature voltages applied to the stator windings the unsymmetrical two-phase PSCM can be easily operated at the rated torque throughout a wide range of speeds. Also, the main and the auxiliary winding currents are almost 90 degree phase difference resulting in flux symmetry approach. This contributes to the high electromagnetic torque and the low torque pulsation.

- The proposed modulating strategy is found to be useful for the reduction of harmonic voltage stress affecting life span of the power electronic devices, as well as vibrations and magnetic noise levels.

- The results in terms of harmonic voltage components, current characteristics, total harmonic distortion of current and torque-speed relationship are in agreement with the accuracy of the software model.

- It is possible to design a high performance motor drive for an unsymmetrical two-phase machine employing a three-leg voltage source inverter. Although the 3-leg inverter composes of more devices than the 2-leg inverter, i.e. two more switching devices and two more diodes, the motor performance can be improved through dramatically decreasing harmonics voltages

- The simulation results have shown a very good agreement with the experimental results over a wide range of variable speed operation on different schemes. All results confirm that the performance of the proposed modulation strategy is superior to the conventional scheme.

5.2 Further Work And Suggestion

● The proposed drive system has several unsolved problems, for instance;

- Overmodulation region of generated PWM signal, and its PWM quality.
- Characteristics of either overall system or input performance such as system efficiency, inverter efficiency as well as input voltage, current and power factor.

● To eliminate circulating current and to improve power factor which have influences on system efficiency, two rectifying diodes may be added by anti-parallel switching devices to operate as a controlled rectifier or power factor correction circuit.

● The ripple current reduction method in the dc capacitor would improve the performance of the unbalanced two-phase drive system equipped with the three-leg VSI. Additionally, the dc link voltage across each capacitor in voltage-doubler circuit should be balanced.

● For investigation of the influence of control techniques and PWM strategies on the motor performances, the variable speed of single-phase permanent split capacitor induction motor with running capacitor in series with the auxiliary winding should be considered. The high reactance of running capacitor at low frequency can be partially compensated by two cases of the control technique. Those are:

- 1) keeping the auxiliary voltage amplitude at the rated value or at as much as possible and adjusting the main voltage amplitude in relation with frequency along with volt/frequency control scheme and
- 2) maintaining the voltage across the auxiliary winding with a factor equivalent to turns ratio times the voltage across the main winding while the voltage across the main winding is altered following volt/frequency profile.

● With the rapid progression in microelectronics technology, the proposed modulating function may be easily applied in practical use. For example, if a compact commercial drive is required, the proposed topology can be easily accomplished by using gate driver circuitry with the single chip such as digital signal processing (DSP).

REFERENCES

- [1] Thomas Kaporch. "Driving the future – use of electronically driven motors in appliances to grow." *Appliance Manufacturer Magazine*, September 2001, pp. 43-46.
- [2] Herbert N. Hickok. "Adjustable Speed – A Tool for Saving Energy Losses in Pumps, Fans, Blowers and Compressors." *IEEE Trans. on Industry Applications*, vol. IA-21, no. 1, January/February 1985, pp. 124-136.
- [3] Eduard Muljadi, Yifan Zhao, Tian-Hua Liu and Thomas A. Lipo. "Adjustable ac Capacitor for a Single-Phase Induction Motor." *IEEE Trans. on Industry Applications*, vol. 29, no. 3, May/June 1993, pp. 479-484.
- [4] Terrance A. Lettenmaier, Donald W. Novotny, and Thomas A. Lipo. "Single-Phase Induction Motor with an Electronically Controlled Capacitor." *IEEE Trans. on Industry Applications*, vol. 27, no.1, January/February 1991, pp. 38-43.
- [5] Edward Randolph Collins. "Torque and Slip Behavior of Single-Phase Induction Motors Driven From Variable Frequency Supplies." *IEEE Trans. on Industry Applications*, vol. 28, no. 3, 1992, pp. 710-715.
- [6] E.R. Collins Jr., R.E. Ashley. "Operating Characteristics of Single-Phase Capacitor Motors Driven From Variable Speed Supplies." *Proc. IEEE IAS-91, Detroit, 1991*, pp. 52-57.
- [7] Frede Blaabjerg, Florin Lungeanu, Kenneth Skaug, and Andreas Aupke. "Comparison of Variable Speed Drives for Single-Phase Induction Motors." *Proc. IEEE PCC-2002, 2002*, pp. 1328-1333.
- [8] Ali S. Ba-thunya, Rahul Khopkar, Kexin Wei, Hamid A. Toliyat. "Single Phase Induction Motor Drives-A Literature Survey." *Proc. IEMDC2001 (Electric Machines and Drives Conference), 2001*, pp. 911-916.
- [9] E.R. Collins Jr., H.B. Puttgen, W.E. Sayle II. "Single Phase Induction Motor Adjustable Speed Drive: Direct Phase Angle Control of The Auxiliary Winding Supply." *Proc. IEEE IAS-88, Pittsburgh, 1988*, pp. 246-251.
- [10] Alexander L. Julian, Richard S. Wallace, and Pradeep K. Sood. "Multi-Speed Control of Single-phase Induction Motors for Blower Applications." *IEEE Trans. on Power Electronics*, vol. 10, no.1, January 1995, pp. 72-77.

- [11] D. Jang and G. Choe. "Improvement of Input Power Factor in AC Choppers using Asymmetrical PWM Technique." *IEEE Trans. on Industrial Electronics*, vol. 42, no. 2, April 1995, pp. 179-185.
- [12] P. N. Enjeti and S. Choi. "An Approach to Realize Higher Power PWM AC Controller." *Proc. IEEE APEC'93*, 1993, pp. 323-327.
- [13] M. Bashir Uddin, M. Akhtar, M. Rezwana Khan, M.A. Choudhury and M.A. Rahman. "Phase Shifting by Static PWM Cycloconverters for Starting Single Phase Induction Motors." *Proc. PCC-Yokohama*, 1993, pp. 532-537.
- [14] A. Khoei and S. Yuvarjan. "Steady State Performance of a Single Phase Induction Motor Fed by a Direct ac-ac Converter." *Proceedings of IEEE Conference, Industry Applications Society Annual Meeting*. 1989, pp. 128-132.
- [15] Microslav Chomat and Thomas A. Lipo. "Two switch adjustable speed drive with single phase induction machines." *Proc. IEEE CPES Power Electronics Seminar*, September 2000, pp. 381-385.
- [16] M.F. Rahman and L. Zhong. "A Current-Forced Reversible Rectifier Fed Single-Phase Variable Speed Induction Motor Drive." *Proc. IEEE IAS'95*, vol. 1, 1995, pp. 584-590.
- [17] M.F. Rahman and L. Zhong. "A Single/Two Phase, Regenerative, Variable Speed, Induction Motor Drive with Sinusoidal Input Current." *Proc. IEEE IAS'95*, 1996, pp. 114-119.
- [18] C-M. Young, C-C. Liu, and C-h. Liu. "New Inverter Driven Design and Control Method for Two Phase Induction Motor Drives." *IEE Proceedings-Electric Power Applications*, vol. 143, no. 6, Nov.1996, pp. 458-466.
- [19] J. Sinthusonthichat, R. Areehamad, V. Kinnares. "Comparative Performance Evaluation of Two-Phase PWM Inverter Fed Induction Motor Drives with Various Topologies." *Proc. IEEE IPEC 2003*, 2003.
- [20] M.H. Rachid. **Power electronics: circuits, devices, and applications**. Pearson Prentice Hall, 2004.
- [21] J. Holtz. "Pulsewidth Modulation for Electronic Power Conversion." *Proceedings of the IEEE*, vol. 82, no. 8, August 1994, pp. 1194-1214.

- [22] M.F. Rahman and L. Zhong. "A Variable Speed Single-Phase Induction Motor Drive using a Smart Power Module." Proceedings of the 1996 IEE Power Electronics and Variable Speed Drives Conference, no. 429, 23-5 Sept. 1996, pp. 407-412.
- [23] Do-Hyun Jang, and Duck-Yong Yoon. "Space-Vector PWM Technique for Two-Phase Inverter-Fed Two-Phase Induction Motors." IEEE Trans. on Industry Applications, vol. 39, no. 2, March/April 2003, pp. 542-549.
- [24] D.G. Holmes, A. Kotsopoulos. "Variable Speed Control of Single and Two Phase Induction Motors Using a Three Phase Voltage Source Inverter." Proc. IEEE IAS-93, 1991, pp. 613-620.
- [25] Mauricio Beltrao de Rossiter Correa, Cursino Brandao Jacobina, Antonio Marcus Nogueira Lima, and Edison Roberto Cabral da Silva. "A Three-Leg Voltage Source Inverter for Two-Phase AC Motor Drive Systems." IEEE Trans. on Power Electronics, vol. 17, no. 4, July 2002, pp. 517-523.
- [26] P.N. Enjeti, and A. Rahman. "A New Single-Phase to Three-Phase Converter with Active Input Current Shaping for Low Cost ac Motor Drives." IEEE Trans. on Industry Applications, vol. 29, no. 4, July/August 1993, pp. 806-813.
- [27] C.B. Jacobina, M.B.R. Correa, E.R.C. da Silva, and A.M.N. Lima. "Induction motor drive system for low power applications." IEEE Trans. On Industry Applications, vol. 35, Jan./Feb. 1999, pp. 52-61.
- [28] S. Sinthusonthishat and V. Kinnares. "A New Modulation Strategy for Unbalanced Two Phase Induction Motor Drives Using a Three-Leg Voltage Source Inverter." IEE of Japan Trans. on Industry Applications, vol. 125-D, no. 5, 2005.
- [29] G. S. Brosan and J.T. Hayden. **Advanced Electrical Power and Machines**. London: Sir Isaac Pitman & Sons Ltd., 1966.
- [30] B. S. Guru and H. R. Hirziroglu. **Electric Machinery and Transformers**. Second Edition, Harcourt Brace College Publishers, 1995.
- [31] Cyril G. Veinott. **Theory and Design of Small Induction Motor**. Mc-Graw-Hill Book International Company, 1959.
- [32] W.J. Morrill. "The Revolving Theory of The Capacitor Motor." Proc. AIEE Winter Convention, New York, 1929, pp. 614-632.
- [33] A.E. Fitzgerald, Charles Kingsley, Jr., and Stephen D. Umans. **Electric Machinery**. Fifth Edition in SI Units, MaGraw-Hill, 1992.

- [34] Paul C. Krause, Oley Wasynczuk, and Scott D. Sudhoff. **Analysis of Electric Machinery and Drive Systems**. Second Edition, IEEE Press, 2002.
- [35] Frede Blaabjerg, Florin Lungeanu, Kenneth Skaug, and Michael Tonnes. "Evaluation of Low-Cost Topologies for Two Phase Induction Motor Drives, in Industrial Applications." Proc. IEEE PCC-2002, 2002, pp. 2358-2365.
- [36] E. R. Benedict and T. A. Lipo. "Improved PWM Modulation for a Permanent-Split Capacitor Motor." Proc. IEEE IAS Annual Meeting Conference, October 2000, pp. 2004-2010.
- [37] CHEE- MUN ON. **Dynamic Simulation of Electric Machinery using MATLAB/Simulink**. Prentice Hall PTR. 1998.
- [38] D. Grahame Holmes and Thomas A. Lipo. **Pulse Width Modulation for Power Converters: Principles and Practice**. IEEE Press Series on Power Engineering, 2003.
- [39] J. Sinthusonthichat, V. Kinnares. "Performance Evaluation of Variable Speed Two-Phase Induction Motors." Proc. IEEE PowerCon 2002, 2002, pp. 2565-2568.
- [40] John B. Buckman. "Single-Phase Induction Motor." US Patent no. 3940646 under A. O. Smith Corporation, Feb. 24, 1976.
- [41] E. Willis Frank, RII. H. Schnetzka, and R. D. Hoffer. "AC motor drive system." US patent no. 5146147 under York Int. Corp., 1992.
- [42] E. Willis Frank, RII. H. Schnetzka, and R. D. Hoffer. "AC motor drive system" US patent no. 5136216 under York Int. Corp., 1992.
- [43] E. Willis Frank, RII. H. Schnetzka, and R. D. Hoffer. "AC motor drive system with a two-phase power supply." US patent no. 5218283 under York Int. Corp., 1993.
- [44] E. Willis Frank, L. William Kopko. "Variable-speed drive for single phase motor." WO patent no. 0069061 under Work Smart Energy Enterprise Inc., 2000.
- [45] M.J. Gorman and M.E. Elbuluk. "A Simple Two-Swich Cycloconverter for Variable-Frequency Low-Speed Applications." IEEE Trans. on Power Electronics, vol. 6, no. 4, Oct. 1991, pp. 759-764.
- [46] C. Julio Moreira "Electric Motor Controller and Method." US patent no. 5883490, March 16, 1999.
- [47] T. Liu and P. Wand. "Implementation of a Single Phase Induction Motor Control on a DSP Based System." Proc. IEEE PESC'94, 1994, pp. 514-521.

This material is reserved for educational use only, not allowed for commercial use.

Forbidden to modify the content, and cite the document when use.

- [48] C.B. Rasmussen, E. Ritchie and A. Arkkio. "Variable Speed Induction Motor Drive for Household Refrigerator Compressor." Proc. IEEE-ISIE97, Guimaraes, Portugal, 1997, pp. 655-659.
- [49] D. Jang and J. Won. "Voltage, Frequency, and Phase-Difference Angle Control of PWM Inverters-Fed Two-Phase Induction Motors." IEEE Trans. on Power Electronics, vol. 9, no. 4, July 1994, pp. 377-383.
- [50] M.B.R. Correa, C.B. Jacobina, A.M.N. Lima, E.R.C. Lima and E.R.C. da Silva. "Rotor-Flux-oriented Control of a Single-Phase Induction Motor Drive." IEEE Trans. on Industrial Electronics, vol. 47, no. 4, August 2000, pp. 832-841.
- [51] P.N. Enjeti, A. Rahman, and R. Jakkli. "Economic Single-Phase to Three-Phase Converter Topologies for Fixed and Variable Frequency Output." IEEE Trans. on Power Electronics, vol. 8, no. 3, July 1993, pp. 329-335.
- [52] D. Jang, G. Choe, and M. Ehsani. "Asymmetrical PWM Technique with Harmonic Elimination and Power Factor Control in ac Choppers." IEEE Trans. on Power Electronics, vol. 10, no. 2, March 1995, pp. 175-184.
- [53] A-R. A.M. Makky, Gamal M. Abdel-Rahim, and Nabil Abd El-Latif. "A Novel DC Chopper Drive for a Single-Phase Induction Motor." IEEE Trans. on Industrial Electronics, vol.42, no.1, February 1995, pp. 33-39.
- [54] R.O. Carvvalho Jr., C.B. Jacobina, A.M.N. Lima, and E.R.C. da Silva. "Control of unbalanced three-phase power electronic systems." Proc. IEEE IAS, June 2000, pp. 1317-1324.
- [55] M.B. de R. Correa, C.B. Jacobina, A.M.N. Lima, and E.R.C. da Silva. "Adjustable-speed Single-phase Induction Motor Drives." Proc. IEEE APEC2002, 2002, pp. 770-776.
- [56] Tian-Hua Liu, Ming-Tsan Lin, and Hann-Chung Wu. "A Single Phase Induction Motor Drive with Efficiency And Torque Improvement." Proc. ISIE'97, Portugal, 1997, pp. 637-642.
- [57] M. Syed Jamil Asghar. "Smooth Speed Control of Single-Phase Induction Motors by Integral-Cycle Switching." IEEE Trans. on Energy Conversion, vol. 14, no.4, December 1999, pp. 1094-1099.
- [58] L.M.C. Mhango, and G.K. Creighton. "Novel Two-phase Inverter-fed Induction-motor drive." IEE Proceedings, vol.131, Pt.B., no.3, May 1984, pp. 99-104.

- [59] A.S. Zein El-Din, and A.E. El-Sabbe. "A Novel Speed Control Technique for Single-Phase Induction Motor." Proc. PEDS'99, Hong Kong, July 1999, pp. 276-280.
- [60] K.J. Lee, H.G. Kim, D.K. Lee, T.W. Chun, E.C. Nho. "High Performance Drive of Single-phase Induction Motor" Proc. ISIE-2001, Pusan, Korea, 2001, pp. 983-988.
- [61] D. Jang, G. Cja, D. Kim and J. Won. "Phase-Difference Control of 2-Phase Inverter-Fed." Proc. IEEE, 1989, pp. 571-578.
- [62] D. Jang and C. Yoon. "Space Vector PWM Technique for Two-Phase Inverter-Fed Single-Phase Induction Motors." Proc. IEEE 34th IAS'99, 1999, pp. 47-53.
- [63] Phillip L. Alger. **Induction Machines: Their Behavior and Use**. Second Edition, New York: Gordon and Breach, 1970.
- [64] Robert W. Smeaton. **Motor Application and Maintenance Handbook**. McGraw-Hill Book Company, 1987.
- [65] B.A.G. Churcher and A. J. King. "The Analysis and Measurement of the Noise Emitted by Machinery." IEE Proceedings, vol. 68, 1930, pp. 97-125.
- [66] W.R. Finley. "Noise in induction motors-causes and treatments." IEEE Trans. on Industry Applications, vol. 27, no. 6, November/December 1991, pp. 1204-1213.
- [67] W.J. Morrill. "Harmonics Theory of Noise in Induction Motors." AIEE Trans., vol. 59, 1940, pp. 474-480.
- [68] D.F. Muster and G.L. Wolfert. "Single-phase Induction Motor Noise due to Dissymmetry Harmonics." AIEE Trans. Vol. 74, Part III, 1955, pp. 1365-1372.
- [69] Bertrand Cassoret, Rodolphe Corton, Daniel Roger, and Jean-Francois Brudny. "Magnetic Noise Reduction of Induction Machines." IEEE Trans. on Power Electronics, vol. 18, no. 2, March 2003, pp. 570-579.
- [70] S. Watanabe, S. Kenjo, K. Ide, F. Sato, and M. Yamamoto. "Natural frequency and vibration behavior of motor stators." IEEE Trans. on PAS, vol. PAS-102, April 1983.
- [71] Ned Mohan, Tore M. Undeland, William P. Robbins. **Power Electronics: Converters Applications, and Design**. John Wiley & Sons, Inc., 1995.
- [72] Bimal K. Bose. **Modern Power Electronics and AC Drives**. Prentice Hall PTR, 2002.
- [73] Marian P. Kazmierkowski, R. Krishnan, and Frede Blaabjerg. **Control in Power Electronics: Selected Problems**. Academic Press, 2002.

- [74] S.R. Bowes, and B.M. Bird. "Novel Approach to the Analysis and Synthesis of Modulation Processes in Power Convertors." IEE Proceedings, vol.122, no.5, May 1975, pp. 507-513.
- [75] W.R. Bennett. "New Results in the Calculation of Modulation Products." The Bell System Technical Journal, vol. 12, April 1933, pp. 228-243.
- [76] Harold S. Black. **Modulation Theory**. Van Nostrand Reinhold Company, 1953.
- [77] John Hamman and Frederik S. van der Merwe. "Voltage Harmonics Generated by Voltage-Fed Inverters Using PWM Natural Sampling." IEEE Trans. on Power Electronics, vol. 3, no.3, July 1988, pp. 377-383
- [78] E.O. Brigham. **The Fast Fourier Transform**. Prentice-Hall, Englewood Cliffs, NJ, 1974.
- [79] G.N. Watson. **Theory of Bessel Functions**. New York: MacMillan, 1994.
- [80] Aldo Boglietti, Paolo Ferraris, Mario Lazzari, and Michele Pastorelli. "About the Possibility of Defining a Standard Method for Iron Loss Measurement in Soft Magnetic Materials with Inverter Supply." IEEE Trans. On Industry Applications, vol. 33, no. 5, September/October 1997, pp. 1283-1288.
- [81] A. Boglietti, P. Ferraris, M. Lazzari, and F. Profumo. "Iron Losses in Magnetic Materials with Six-Step and PWM Inverter Supply." IEEE Trans. On Magnetics, vol. 27, no. 6, November 1991, pp. 5334-5336.
- [82] A. Boglietti, P. Ferraris, M. Lazzari, and F. Profumo. "Effects of Different Modulation Index on the Iron Losses in Soft Magnetic Material Supplied by PWM Inverter." IEEE Trans. On Magnetics, vol. 29, no. 6, November 1993, pp. 3234-3236.
- [83] A. Boglietti, P. Ferraris, M. Lazzari, and M.Pastorelli. "Change of the Iron Losses with the Switching Frequency in Soft Magnetic Materials Supplied by PWM Inverter." IEEE Trans. On Magnetics, vol. 31, no. 6, November 1995, pp. 4250-4252.
- [84] C. G. Veinott. "Segregation of losses in single-phase induction motors." AIEE Transaction, vol. 54, December 1935, pp. 1302-1306.
- [85] C. van der Merwe and F.S. van der Merwe. "Determination of Single-phase Induction Motor Parameters through Two-phase Measurements." The Transaction of The S.A Institute of Electrical Engineers, June 1991, pp. 152-155.
- [86] C.van der Merwe; F.S. van der Merwe. "A Study of Methods to Measure the Parameters of Single-phase Induction Motors." IEEE Trans. on Energy Conversion, vol. 10, no. 2, June 1995, pp. 248-253.

- [87] Eleazar F. Bustmante. "Evaluating the parameters of the Equivalent Circuit of Single-phase Induction Motors." *Electric Machines and Power System*, Hemisphere Publishing Corporation, 1987, 13:173-184.
- [88] S. D. Umans. "Steady-state, lumped-parameter model for capacitor-run, single-phase induction motors." *IEEE Trans. on Industry Applications*, vol. 32, no. 1, January/February 1996, pp. 169-179.
- [89] M. Popescu, and V. Navrapescu. "Modelling in stationary frame reference of single and two-phase induction machines including the effect of iron loss and magnetising flux saturation." *Proc. IEEE-ICEM 2000*, August 2000, pp. 407-411.
- [90] L. Lorenz, and K. Kanelis. "Design criteria for low cost drive systems." *IEE Proceedings of Drives and Controls 2001*, London, March 2001, pp. 23-31.
- [91] L. Xu. "Dynamical model of and Integral-cycle controlled single-phase induction machine." *IEEE Trans. on Industry Applications*, vol. 7, no. 4, December 2001, pp. 761-767.
- [92] J.T.Boys, S.J. Walton. "Scalar Control: an Alternative AC Drive Philosophy." *IEE Proceedings*, vol.135, Pt.B., no.3, May 1988, pp. 151-158.
- [93] B. K. Bose and H. A. Sutherland. "A high performance pulse-width modulator for an inverter-fed drive system using a microcomputer." *IEEE Trans. on Industry Applications*, vol. 19, March/April 1983, pp. 235-243.
- [94] Thomas L. Harman, James Dabney, Norman Richert. **Advanced Engineering Mathematics with MATLAB**.-Second Edition, Brooks/Cole, 2000.
- [95] A.L. Kimball, Jr., and P.L. Alger. "Single-Phase Motor Torque Pulsations." *AIEE Trans.*, vol. 43, 1924, pp. 730-739.
- [96] Cyril G. Veinott and Joseph E. Martin. **Fractional and Subfractional Horsepower Electric Motors**. Fourth Edition, Mc-Graw-Hill Book International Company, 1987.
- [97] C.M. Liaw, and Y.M. Lin. "Random Slope PWM Inverter Using Existing System Background Noise: Analysis, Design and Implementation." *IEE Proc.-Electr. Power Appl.*, vol. 147, no.1, January 2000, pp. 45-54.
- [98] Bertrand Cassoret, Rodolphe Corton, Daniel Roger, and Jean-Francois Brudny. "Magnetic Noise Reduction of Induction Machines." *IEEE Trans. On Power Electronics*, vol. 18, no. 2, March 2003.

- [99] Eugene Jahnke and Fritz Emde **Table of Functions Translation**. New York: Dover Press, 1945, pp. 149.
- [100] S.R. Bowes. "New sinusoidal pulse-width modulated inverter." IEE Proceedings, vol. 122, no. 11, Nov. 1975, pp. 1279-1285.
- [101] รศ. ดร. มนัส สัจจวิเศษ, วรรณิ์ กัทรอมรกุล. คู่มือการใช้งาน MATLAB ฉบับสมบูรณ์. สำนักพิมพ์อินโฟเพรส, 2543.

APPENDIX A

JACOBI-ANGER AND BESSEL FUNCTION RELATIONSHIPS

The Bessel function is the solution of the Bessel differential equation defined as:

$$x^2 y'' + xy' + (x^2 - n^2)y = 0 \quad (\text{B.1})$$

where $n \geq 0$ or is a non-negative real number. The functions are found for systems with cylindrical symmetry. The solutions of this equation are called the Bessel function with order n . Since Bessel's differential equation is a second order ordinary differential equation, two sets Bessel function of the first kind $J_n(x)$ and the Bessel function of the second kind $Y_n(x)$ are needed to form the general solution:

$$y(x) = c_1 J_n(x) + c_2 Y_n(x) \quad (\text{B.2})$$

However, $Y_n(x)$ is divergent at $x=0$. The associated coefficient c_2 is forced to be zero physically meaningful result when there is no source or sink at $x=0$. The Bessel function of the first kind of order n can be expressed as a functions:

$$\begin{aligned}
 J_n(x) &= \frac{x^n}{2^n \Gamma(n+1)} \left\{ 1 - \frac{x^2}{2(2n+2)} + \frac{x^4}{2.4(2n+2)(2n+4)} - \dots \right. \\
 &= \sum_{k=0}^{\infty} \frac{(-1)^k \left(\frac{x}{2}\right)^{n+2k}}{k! \Gamma(n+k+1)}
 \end{aligned} \quad (\text{B.3})$$

A.1 Jacobi-Anger Expansions

A common expression that appears in the development of the analytical Fourier solution of a PWM waveform under various modulation strategies is $e^{\pm j\xi \cos\theta}$, i.e. a sinusoid which has as its argument another sinusoid. In the enhancement of the analytical solutions for PWM, this

expression must be multiplied by the term $\cos n\theta$ and integrated over some fraction of 2π , and this is facilitated by expanding the $e^{\pm j\xi \cos\theta}$ expression into a Bessel series form using the Jacobi-Anger expansion [28] of

$$e^{\pm j\xi \cos\theta} = J_0(\xi) + 2 \sum_{k=1}^{\infty} j^{\pm k} J_k(\xi) \cos k\theta \quad (\text{B.4})$$

Equation (B.1) can be restated from its complex form as

$$\begin{aligned} \cos(\xi \cos\theta) &= J_0(\xi) + 2 \sum_{k=1}^{\infty} \cos k \frac{\pi}{2} J_k(\xi) \cos k\theta \\ &= J_0(\xi) + 2 \sum_{k=1}^{\infty} \cos k\pi J_{2k}(\xi) \cos 2k\theta \end{aligned} \quad (\text{B.5})$$

and

$$\begin{aligned} \sin(\xi \cos\theta) &= 2 \sum_{k=1}^{\infty} \sin k \frac{\pi}{2} J_k(\xi) \cos k\theta \\ &= 2 \sum_{k=1}^{\infty} \cos k\pi J_{2k+1}(\xi) \cos[(2k+1)\theta] \end{aligned} \quad (\text{B.6})$$

Additionally, using the substitution of $\theta = \theta' - \frac{\pi}{2}$, Equations (B.2) and (B.3) lead to the following relationship of

$$\cos(\xi \sin\theta') = J_0(\xi) + 2 \sum_{k=1}^{\infty} J_{2k}(\xi) \cos(2k\theta') \quad (\text{B.7})$$

and

$$\sin(\xi \sin\theta') = 2 \sum_{k=1}^{\infty} J_{2k+1}(\xi) \sin[(2k+1)\theta'] \quad (\text{B.8})$$

A further useful result is the expansion of the expression $\cos(\delta + \xi \sin\theta)$, which proceeds as follows:

$$\cos(\delta + \xi \sin\theta) = \cos\delta \cos(\xi \sin\theta) - \sin\delta \sin(\xi \sin\theta) \quad (\text{B.9})$$

Substituting from Equations (B.4) and (B.5) into Equation (B.6) gives

$$\begin{aligned}
\cos(\delta + \xi \sin \theta) &= \cos \delta \left[J_0(\xi) + 2 \sum_{k=1}^{\infty} J_{2k}(\xi) \cos(2k\theta) \right] \\
&\quad - \sin \delta \left[2 \sum_{k=0}^{\infty} J_{2k+1}(\xi) \sin([2k+1]\theta) \right] \\
&= J_0(\xi) \cos \delta + \sum_{k=1}^{\infty} J_{2k}(\xi) [\cos(\delta + 2k\theta) + \cos(\delta - 2k\theta)] \\
&\quad + \sum_{k=0}^{\infty} J_{2k+1}(\xi) [\cos(\delta + [2k+1]\theta) - \cos(\delta - [2k+1]\theta)]
\end{aligned} \tag{B.10}$$

Grouping similar to sinusoids and after some manipulation and simplification gives the final form of

$$\cos(\delta + \xi \sin \theta) = \sum_{k=-\infty}^{\infty} J_k(\xi) \cos(\delta + k\theta) \tag{B.11}$$

A.2 Bessel Function Integral Relationships

The product of $e^{j\xi \cos \theta}$ and $\cos(n\theta)$ integrated over a 2π interval is

$$\int_{-\pi}^{\pi} e^{\pm j\xi \cos \theta} \cos n\theta \, d\theta = \int_{-\pi}^{\pi} \left[J_0(\xi) + 2 \sum_{k=1}^{\infty} j^{\pm k} J_k(\xi) \cos k\theta \right] \cos n\theta \, d\theta \tag{B.12}$$

which becomes

$$\int_{-\pi}^{\pi} e^{\pm j\xi \cos \theta} \cos n\theta \, d\theta = \int_{-\pi}^{\pi} J_0(\xi) \cos n\theta \, d\theta + \int_{-\pi}^{\pi} 2 \sum_{k=1}^{\infty} j^{\pm k} J_k(\xi) \cos k\theta \cos n\theta \, d\theta \tag{B.13}$$

The only term of the right hand side of Equation (B.10) which does not integrate to zero over 2π is when $k = n$, thus Equation (B.10) turns into

$$\int_{-\pi}^{\pi} e^{\pm j\xi \cos \theta} \cos n\theta \, d\theta = \int_{-\pi}^{\pi} 2 j^{\pm n} J_n(\xi) \cos n\theta \, d\theta \tag{B.14}$$

which simplifies to

$$\int_{-\pi}^{\pi} e^{\pm j\xi \cos \theta} \cos n\theta \, d\theta = 2\pi j^{\pm n} J_n(\xi) \tag{B.15}$$

Using the similar development, $e^{\pm j\xi \cos\theta}$ multiplied by $\sin(n\theta)$ and integrated over 2π gives

$$\int_{-\pi}^{\pi} e^{\pm j\xi \cos\theta} \sin n\theta \, d\theta = 0 \quad (\text{B.16})$$

Hence from Equation (B.12), for any positive value of n and positive exponential of the natural logarithm,

$$\int_{-\pi}^{\pi} e^{j\xi \cos\theta} e^{jn\theta} \, d\theta = 2\pi j^n J_n(\xi) \quad (\text{B.17})$$

In particular, when $n = 0$,

$$\int_{-\pi}^{\pi} e^{j\xi \cos\theta} \, d\theta = 2\pi J_0(\xi) \quad (\text{B.18})$$

For a negative value of n , an additional useful identity can be developed. As previous described in Equation (B.10), the only nonzero term on the right hand side of the integration over 2π will take place when $k = |n|$, irrespective of the sign of n . Therefore, for n negative, the Equation (B.12) becomes

$$\begin{aligned} \int_{-\pi}^{\pi} e^{j\xi \cos\theta} \cos(-n\theta) \, d\theta &= 2\pi j^{|n|} J_{|n|}(\xi) = 2\pi j^{-n} J_{-n}(\xi) \\ \int_{-\pi}^{\pi} e^{j\xi \sin\theta} \sin(-n\theta) \, d\theta &= 2\pi J_{|n|}(\xi) = 2\pi J_n(\xi) \end{aligned} \quad (\text{B.19})$$

From Equation (B.16), the following identity can be stated:

$$\begin{aligned} J_{-n}(\xi) &= (-1)^n J_n(\xi) \\ J_n(-\xi) &= (-1)^n J_n(\xi) \end{aligned} \quad (\text{B.20})$$

Another important identity can be derived for the case where the exponent of the natural logarithm is negative. That is the case of a negative exponent of the natural logarithm from Equation (B.12)

$$\int_{-\pi}^{\pi} e^{-j\xi \cos \theta} \cos n\theta \, d\theta = 2\pi j^{-n} J_n(\xi) \quad (\text{B.21})$$

Equation (B.18) can be alternatively written as

$$\int_{-\pi}^{\pi} e^{-j\xi \cos \theta} \cos n\theta \, d\theta = 2\pi j^n J_n(-\xi) = 2\pi j^{-n} J_n(\xi) \quad (\text{B.22})$$

From Equation (B.19), the following identity can be declared:

$$J_n(-\xi) = (-1)^n J_n(\xi) \quad (\text{B.23})$$

Particularly when $n = 0$,

$$J_0(-\xi) = J_0(\xi) \quad (\text{B.24})$$

The shape of the first seven Bessel Functions for argument up to 10 [99] is demonstrated in Figure B.1. It is noticed that only the first Bessel Function $J_0(\xi)$ has a nonzero value for an argument of zero.

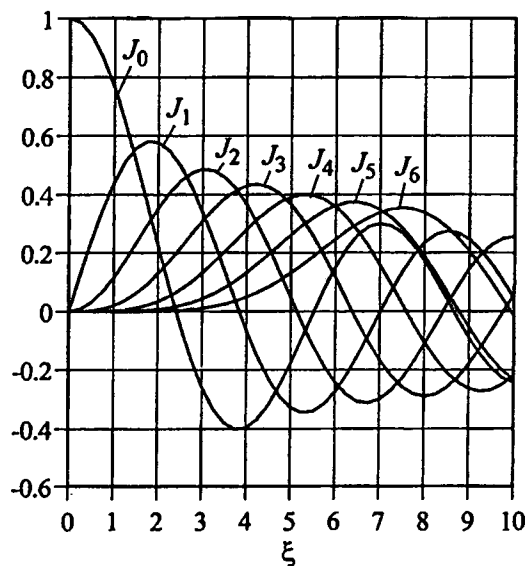


Figure A.1 Bessel functions $J_n(\xi)$ for $n = 0, 1, 2, \dots, 6$

APPENDIX B

UNSYMMETRICAL TWO-PHASE INDUCTION MOTOR TEST

B.1 Turns Ratio Test

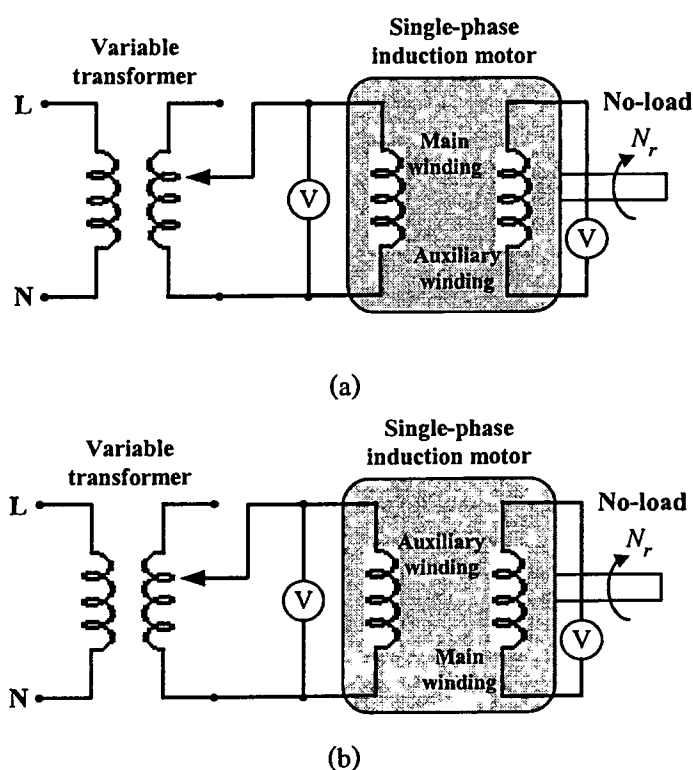


Figure B.1 Circuit diagram for turn ratio test

- (a) impressed voltage on main winding
- (b) impressed voltage on auxiliary winding

Turns ratio test is made following Vienott technique [96]. The motor runs with the rated voltage (E_m) which is impressed on the main winding only, and measures the induced voltage of the auxiliary winding (E'_a) as the diagram in Figure B.1 (a). The motor has to have no load on the shaft. After that, impress the auxiliary winding voltage (E_a) should approximately be 118 percent of E'_a to operate the motor at normal flux. Due to the 118 percent of E'_a is more than the rated voltage, thus, the selected value of E_a under the test is 220 V. Let the motor run at no load

This material is reserved for educational use only, not allowed for commercial use.

Forbidden to modify the content, and cite the document when use.

like the previous case. Then, measure the induced voltage across the main winding (E'_m) as the diagram in Figure B.1 (b). Where

$$a = \frac{\text{effective conductors in the auxiliary winding}}{\text{effective conductors in the main winding}} \quad (\text{B.1})$$

$$= \sqrt{\frac{E'_a E_a}{E_m E'_m}}$$

Table B.1 The impressed and induced voltages of each winding

E_m (V)	E'_a (V)	E_a (V)	E'_m (V)
220	285	220	95.7

B.2 DC Test

A circuit diagram for dc test is demonstrated in Figure B.2. DC voltage is firstly applied to the main winding. The given results are presented in Table B.2 and B.3.

Table B.2 The relationship of DC voltage and current of the main winding

V (V)	5.31	10.02	15.92	20.03
I (A)	0.601	1.129	1.785	2.23

Table B.3 The relationship of DC voltage and current of the auxiliary winding

V (V)	10.29	20.29	30.3	40.4	51	61	70.3	80
I (A)	0.22	0.433	0.641	0.847	1.057	1.25	1.406	1.572

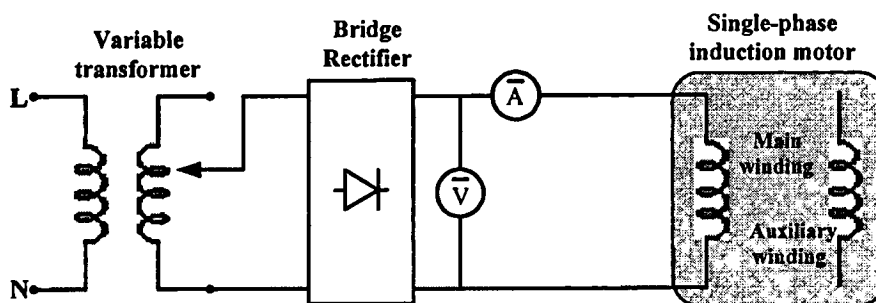


Figure B.2 Circuit diagram for DC test

B.3 Locked Rotor Test

The locked rotor test has been made following the standard test method. The circuit diagram of locked rotor test has been made following Figure B.3. Current is applied until as same as the rated current value. The obtained results are indicated in Table B.4.

Table B.4 Locked rotor test information

Main winding				Auxiliary winding			
V (V)	I (A)	P (W)	Q (VAR)	V (V)	I (A)	P (W)	Q (VAR)
79.86	2.177	115.3	129.15	79.86	0.524	27.9	29.7

B.4 No Load Test

The no load test has been made following the standard test method. The motor is connected as conventional operation without load torque as illustrated in Figure B.4. The results of the no load test is shown in Table B.5.

Table B.5 No load test information

V (V)	I (A)	P (W)	Q (VAR)
220.02	1.055	171	157

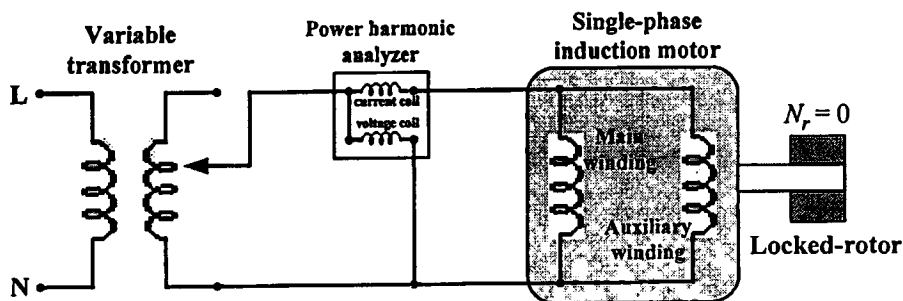


Figure B.3 Circuit diagram for locked rotor test

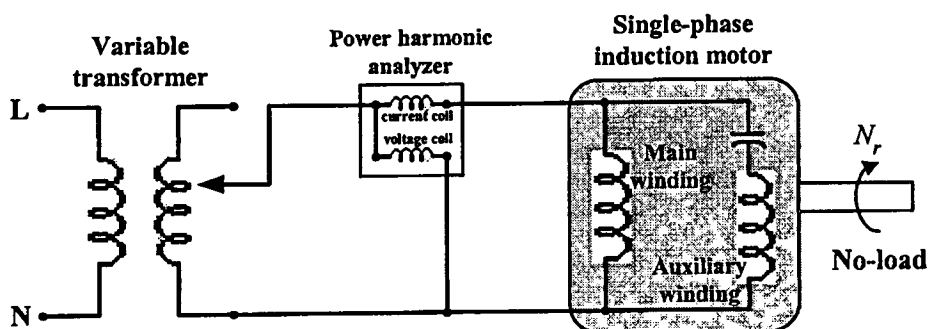


Figure B.4 Circuit diagram for no load test

B.5 Friction And Windage Losses Test

In order to find out friction & windage losses of the motor, the motor under test has to be connected with the voltage source as the no load test. The motor is applied the voltage from rated value until the motor stops running. All recorded data are utilized to separate power loss of the motor (P_{loss}) where the power loss can be reckoned by $P_{loss} = P - I_m^2 R_{1m} - I_a^2 R_{1a}$. The measured and calculated results are demonstrated in Table B.6.

Table B.6 Friction and windage losses test information

V (V)	220	200	180	160	140	120	100	80	60	40
I (A)	1.30	0.96	0.72	0.56	0.45	0.36	0.3	0.25	0.22	0.20
P (W)	100.5	78.2	62.8	50.2	39.4	30.2	22.7	16.25	11.08	7.30
I_m (A)	1.30	0.96	0.72	0.56	0.45	0.36	0.30	0.25	0.22	0.20
I_a (A)	0.77	0.69	0.63	0.55	0.49	0.41	0.34	0.27	0.20	0.12
P_{loss} (W)	55.645	46.112	38.306	32.268	25.586	20.638	16.117	12.05	8.646	6.22
V^2 (V^2)	48400	40000	32400	25600	19600	14400	10000	6400	3600	1600

From the equivalent circuit tests, an unsymmetrical two-phase equivalent circuit of the tested motor can be written as indicated in Figure B.5. Also, the relationship of each fundamental output voltage versus fundamental invert frequency utilized in this research can be described and illustrated in Figure B.6.

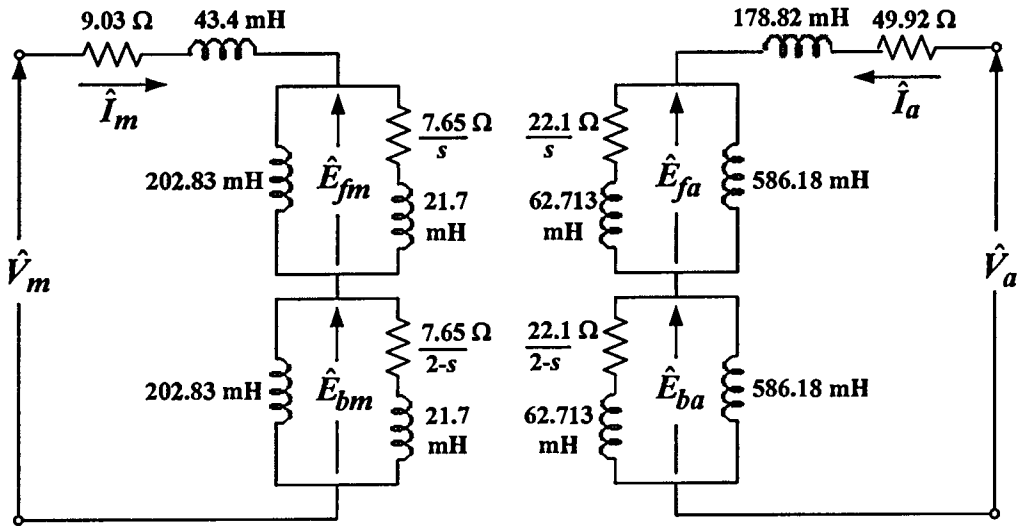


Figure B.5 Unsymmetrical two-phase equivalent circuit of the tested motor

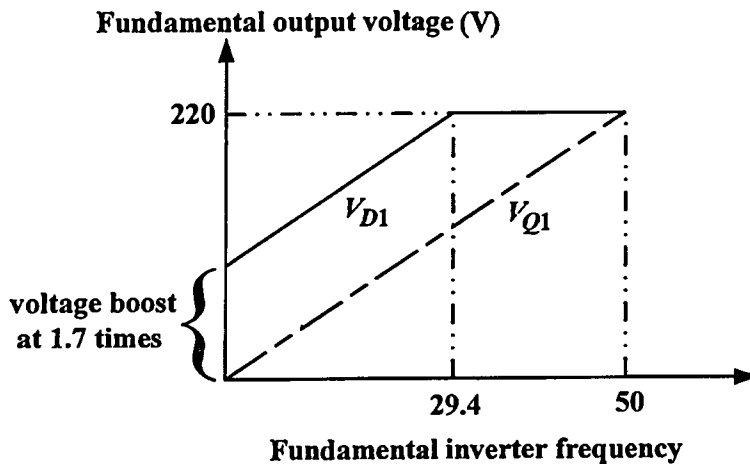


Figure B.6 Relationship of each fundamental output voltage versus fundamental invert frequency

APPENDIX C

MOTOR PERFORMANCE EVALUATION

To calculate electromagnetic torques of twice control method, V/F control and voltage boost method, at each inverter frequency, the program in m-file type using the MatLab[®] is written as follows:

```
%% Calculation the averagely electromagnetic torque using the tested motor parameters %%

%% Motor Parameter %%

Vm=input('Main Winding Voltage = ');
Va=input('Auxiliary Winding Voltage= ');
f=input('Inverter frequency = ');
p=input('Pole Number = ');
ws=[4*pi*f/p];
w=[2*pi*f];
a=[1.7];
R1m=[9.028];
R1a=[49.921];
R2m=[15.283];
R2a=a*R2m;
L1m=L2m=[43.398e-03];
L1a=L2a=a*L1m;
Lmm=[202.915e-03];
Lam=a*Lmm;
rot=[55.645]; %%Rotatioal and Core Losses%%
s=1e-08:0.01:0.99999;

%% Impedance Calculation in Each Part of Equivalent Circuit %%

%% Auxiliary winding impedance %%

Xam=[w*Lam*i];
X2a=[w*L2a*i];
Z1a=[R1a+(w*L1a*i);
```

This material is reserved for educational use only, not allowed for commercial use.

Forbidden to modify the content, and cite the document when use.

```

Z2fa=[(R2a./(2*s))+(X2a/2)];
Zfa=[(Xam*Z2fa)/(Xam+Z2fa)];
Z2ba=[(R2a./(2*(2-s)))+(X2a/2)];
Zfa=[(Xam*Z2ba)/(Xam+Z2ba)];
%% Main winding impedance %%
Xmm=[w*Lmm*i];
X2m=[w*L2m*i];
Z1m=[R1m+(w*L1m*i)];
Z2fm=[(R2m./(2*s))+(X2m/2)];
Zfm=[(Xmm*Z2fm)/(Xmm+Z2fm)];
Z2bm=[(R2m./(2*(2-s)))+(X2m/2)];
Zfm=[(Xmm*Z2bm)/(Xmm+Z2bm)];
%% Current Calculation %%
K=[(2.*Zf.*Zba)+(2.*Zb.*Zfa)+(Z1a*Z1m)+(Z1a.*Zf)+(Z1a.*Zb)+(Zfa.*Z1m)+(Zba.*Z1m)];
Im=[((Vm*a*Z1a)+(Vm*a*Zfa)+(Vm*a*Zba)+(i*Zfa*Va)-(i*Zba*Va))/(a*K)];
Ia=[(i*((-Zf*Vm*a)+(Zb*Vm*a)-(i*Va*Z1m)-(i*Va*Zf)-(i*Va*Zb)))/K];
aseta=angle(Ia)*180/pi;
mseta=angle(Im)*180/pi;
%% Power and Torque Calculation %%
Efm=Zf.*Im;
Ebm=Zb.*Im;
Efa=Zfa.*Ia;
Eba=Zba.*Ia;
Sgm=((Efm-Ebm).*conj(Im))+((-Efa.*i./a)-(Eba.*i./a)).*conj(Im));
Sga=((Efa-Eba).*conj(Ia))+((Efm.*a.*i)+(Ebm.*a.*i)).*conj(Ia));
Pg=real(Sgm)+real(Sga);
Pout=((1-s).*Pg)-rot;
Tout=Pout./((1-s).*ws);
figure (1); plot (s,Pout);
figure (2); plot (s,Tout);
%%%%%%%%%%

```

APPENDIX D

ACOUSTIC NOISE CALCULATION

Noise waveforms from a microphone are recorded by Audio program and are saved as a filename.wav. This data is analyzed and plotted for acoustic noises spectra using the Matlab®.

D.1 Acoustic Noise Frequency Separation

```
[y,fs]=wavread('400'); %% Load the file from database
d=0.05; w=0.08; %% Limit length and window of operation
N=32768; % N must be greater than fs*w
W=round(w*fs);
D=round(d*fs);
dt=D/fs; tc=0.5*w;
hw=hamming(W);
HN=N*0.5;
L=length(y);
J=1:W;
t=[]; f=(0:HN-1)*(fs/N); Ms=[];
while J(W)<=L,
    t=[t tc];
    s=y(J).*hw;
    S=fft(s,N);
    M=abs(S(1:HN))/fs;
    Ms=[Ms M];
    %subplot(211); plot(s); subplot(212); plot(M); pause
    tc=tc+dt;
    J=J+D;
end
save 400 t f Ms HN; %% Save the analysed information for next evaluation called spg-file
```

This material is reserved for educational use only, not allowed for commercial use.

Forbidden to modify the content, and cite the document when use.

D.2 Time And Frequency Limitation

```

load 400; %%Load file from the spg-file
t1=0.8; t2=0.8; f1=0; f2=20000; %% Set time and frequency
Lt=length(t); Lf=length(f);
    if t1==t2,
        for i=1:Lt,
            if t(i)>=t1, I=i; break; end
        end
    for j=1:Lf,
        if f(j)>=f1, J=j; break; end
    end
    for j=(J+1):Lf,
        if f(j)>=f2, J=J;j; break; end
    end
figure;
plot(f(J),Ms(J,I));
xlabel('frequency (Hz)');
ylabel('magnitude');
axis([min(f(J)) max(f(J)) 0 1.1*max(Ms(J,I))]);
t(I)
end
    if f1==f2,
        for i=1:Lt,
            if t(i)>=t1, I=i; break; end
        end
    for i=(I+1):Lt,
        if t(i)>=t2, I=I;i; break; end
    end
    for j=1:Lf,
        if f(j)>=f1, J=j; break; end
    end
end

```

This material is reserved for educational use only, not allowed for commercial use.

Forbidden to modify the content, and cite the document when use.

```

figure;
plot(t(I),Ms(J,I));
xlabel('time (second)');
ylabel('magnitude');
axis([min(t(I)) max(t(I)) 0 1.1*max(Ms(J,I))]);
f(J)
end
if (t1~=t2)&(f1~=f2),
    for i=1:Lt,
        if t(i)>=t1, I=i; break; end
    end
    for i=(I+1):Lt,
        if t(i)>=t2, I=i; break; end
    end
    for j=1:Lf,
        if f(j)>=f1, J=j; break; end
    end
    for j=(J+1):Lf,
        if f(j)>=f2, J=j; break; end
    end
figure;
surf(t(I),f(J),Ms(J,I));
xlabel('time (second)');
ylabel('frequency (Hz)');
zlabel('magnitude');
view(0,90); % top view
end
noise=10*log(Ms(J))
figure;
plot(f(J),noise);
xlabel('Frequency (Hz)');
ylabel('Acoustic Noise (db)');

```

This material is reserved for educational use only, not allowed for commercial use.

Forbidden to modify the content, and cite the document when use.

APPENDIX E

IMPLEMENTED CIRCUITS AND TEST RIG

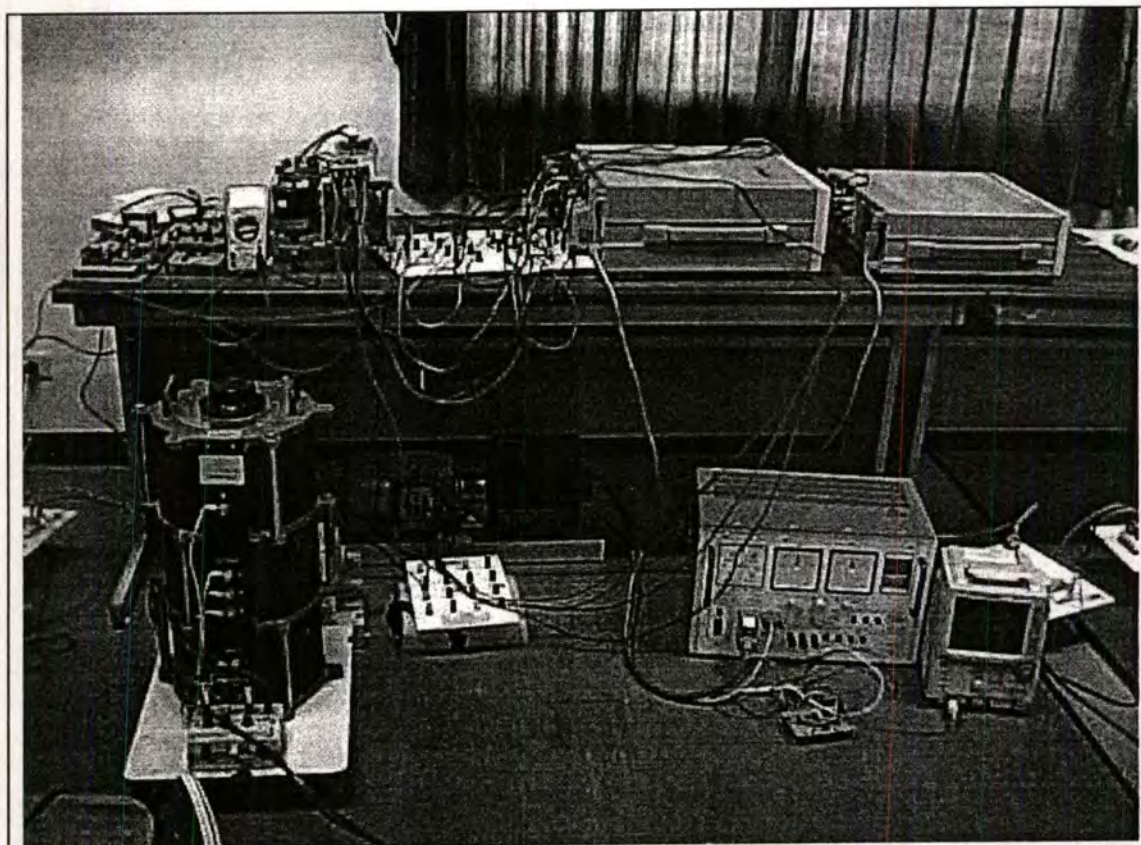


Figure E.1 Overall experimental set up

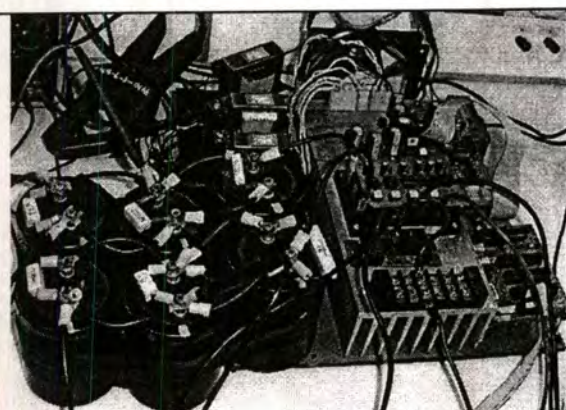


Figure E.2 Power circuit

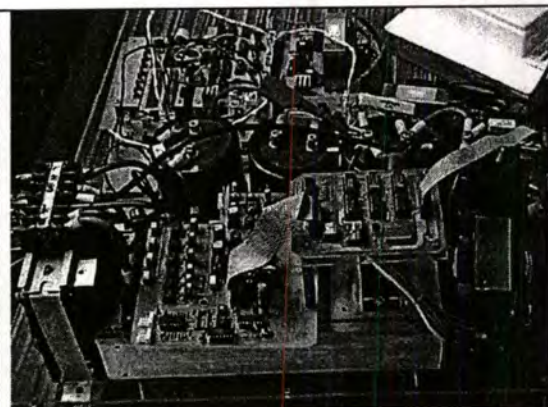


Figure E.3 Inverter configuration

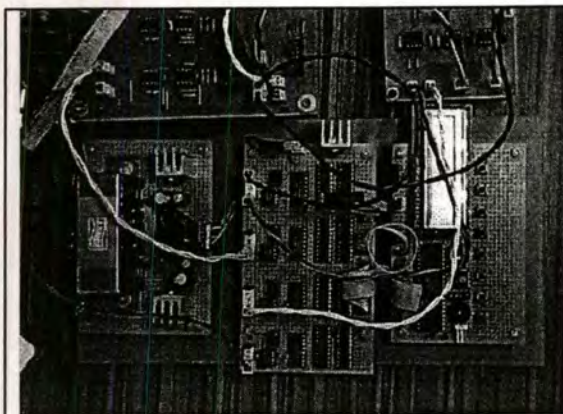


Figure E.4 Sinusoidal signal generator circuit

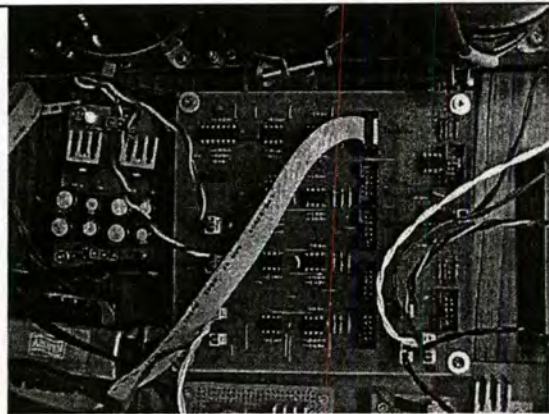


Figure E.5 SPWM signal generator circuit

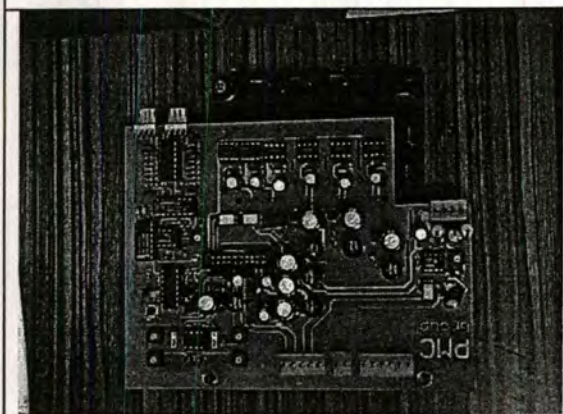


Figure E.6 Isolated ground and protection circuits

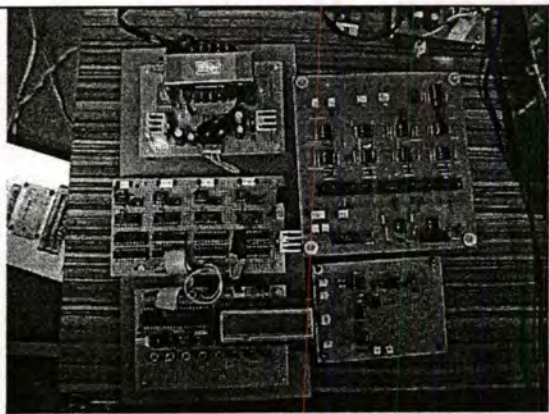


Figure E.7 Gate drive circuit

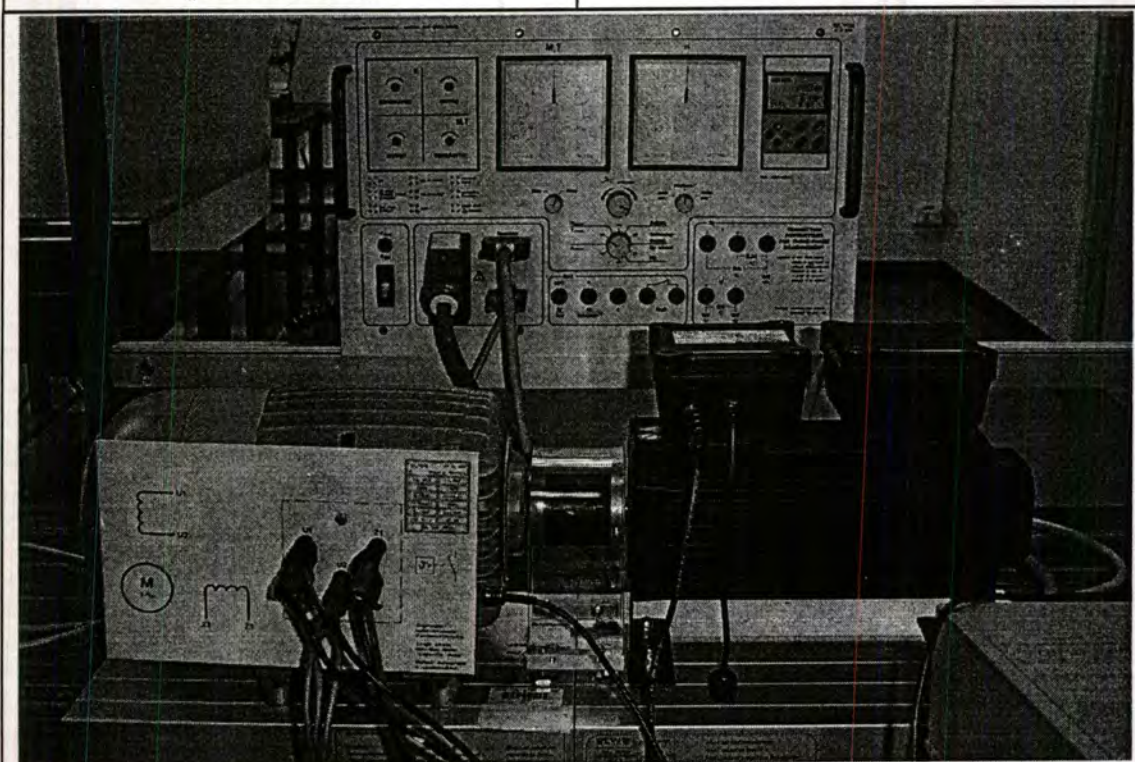


Figure E.8 Overall test rig for normal operation

This material is reserved for educational use only, not allowed for commercial use.

Forbidden to modify the content, and cite the document when use.

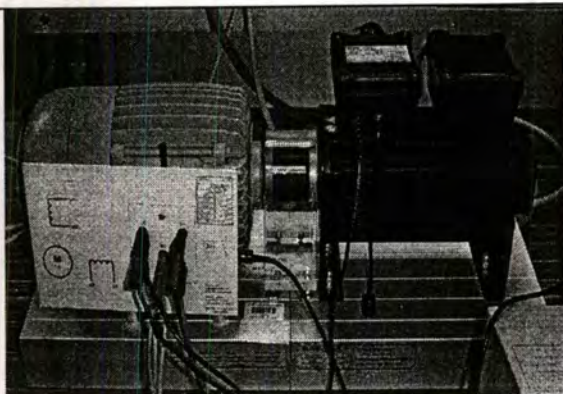


Figure E.9 The tested motor with load coupling

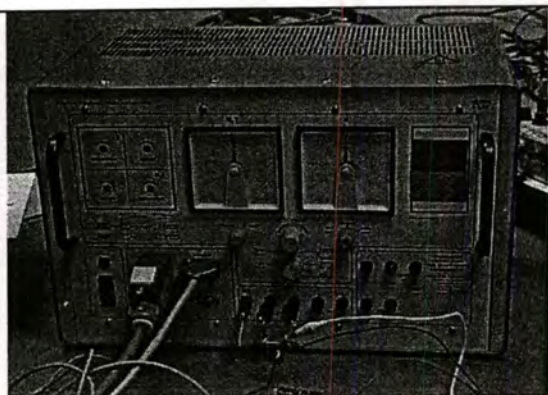


Figure E.10 Control unit

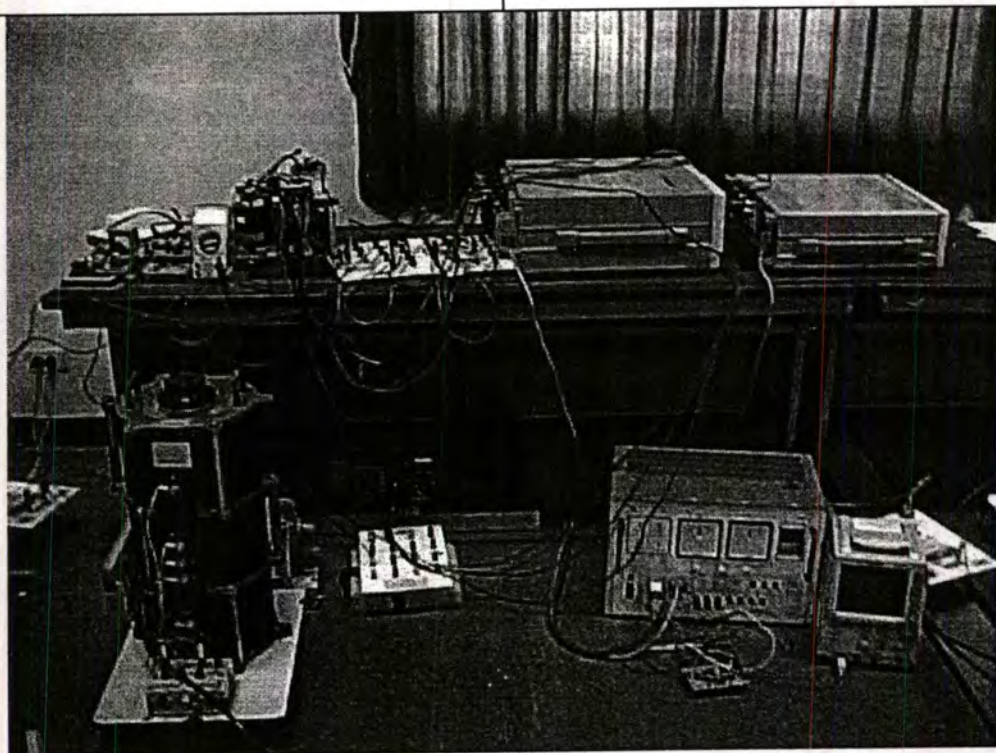


Figure E.11 Overall test rig in case of acoustic noise test

APPENDIX F

THE AUTHOR'S PUBLICATIONS

PowerCon 2002

IEEE Catalog Number: 02EX572C
ISBN: 0-7803-7459-6



2002 INTERNATIONAL CONFERENCE ON POWER SYSTEM TECHNOLOGY



Kunming, China October 13-17, 2002

Copyright © 2002 by IEEE

CHINA ELECTRIC POWER RESEARCH INSTITUTE

Performance Evaluation of Variable Speed Control of Two-Phase Induction Motors

J. Sinthusonthichat, and V. Kinnarees

Abstract—In this paper, various control methods for two-phase winding capacitor induction motor drives are proposed. Comparative performance evaluation of three different control techniques with the same fundamental voltage is given. For the first condition, the motor is fed by a sinusoidal power supply provided from a synchronous generator for both main and auxiliary windings without phase shifting of the supply voltage (conventional method). For the second condition, the motor is fed by the designed half-bridge inverter with 90 degree current phase difference for each winding. The voltage sources of both windings are regulated by V/f control scheme. Like the second case, the last condition provides constant maximum current of the auxiliary winding and variable current depending load torque of the main winding. All experimental results are compared and discussed.

Index Terms—Two-phase induction motor, SPWM Inverter, Motor Performance, Variable Speed Drive of single phase motor.

I. INTRODUCTION

Single-phase induction motors are one of the most widely used motors in the world, especially for domestic appliances. However, there is little work that has been done in the applications of drives to achieve variable speed operation. In [1] the authors introduced a single-phase inverter to regulate the phase angle of the voltage applied to the auxiliary winding of the non-capacitor motor, whilst the main winding was connected to the ac supply. Few papers have revealed the characteristics of a standard motor when driven from a single-phase variable frequency supply under each condition [2]-[3]. Other works proposed the optimum control strategy to operate an unbalanced two-phase motor under variable speed control with maintaining the winding currents in quadrature [4]. Symmetrical and unsymmetrical-type two-phase induction motor fed by inverter-driven two-phase induction motor drive are presented in [7].

This paper has focused on performance evaluation between conventional method and two-phase SPWM inverter fed induction motor topology. Three conditions of supply voltage are studied. Condition I is conventional method that the two-phase winding is simultaneously energized by sinusoidal voltage source from a generator. The motor in condition II is supplied by the proposed inverter which treats phase shifting between auxiliary and main current in quadrature. Finally, in condition III, both amplitude and frequency of the main winding can be varied depending on mechanical load. Phase shifting of both windings is 90 degrees like the second condition.

J. Sinthusonthichat, and V. Kinnarees is with the Department of Electrical Engineering, Faculty of Engineering, King Mongkut's Institute of Technology Ladkrabang KMITL, Bangkok 10520, Thailand (e-mail: jsinrat@rmut.ac.th).

In addition, the auxiliary winding current has to be kept at a maximum constant current. Amplitude current detector should have faster response and more accuracy than conventional detector.

II. SYSTEM CONFIGURATION

A. Sinusoidal Supply

Sinusoidally variable frequency, adjustable voltage source from the generator is applied to the motor as single phase capacitor run motor (i.e. conventional case). Obviously displays in Fig. 1. Test rig set up for investigation in condition I is drawn in Fig. 2. Frequency of the generator can be adjusted by speed regulation of prime mover which is directly motivated by the conventional drive while the amplitude voltage can be controlled by traditionally exciting field current. Ono sokki torque detector and meter model SS-501 and TS-200, respectively is used.

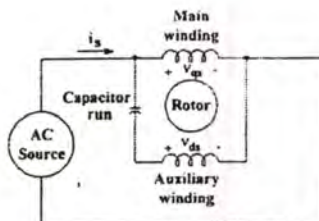


Figure 1: Schematic diagram of conventional supply (condition I)

B. SPWM Supply

SPWM is generated for switching of IGBTs in the main power circuit Module (IPM of IGBTs Module 6 PCs). The control block diagram of the implemented inverter designed for condition II and III testing is shown in Fig. 3. The phase shifter is included in order to keep the phase difference between the auxiliary and main winding currents 90 degrees. Inverter frequency and fundamental output voltage can be independently adjusted. As shown in Fig. 4, voltage doubler rectifier is utilized as front-end converter in order to increase dc link voltage for the half-bridge inverter. Each leg of the inverter is supplied to the main and auxiliary with capacitor run windings with the common node return to center tap of dc filter capacitor, C_1 and C_2 . To verify the inverter-driven control strategies for two-phase induction motor drive, the test rig is set up as block diagram illustrated in Fig. 5.

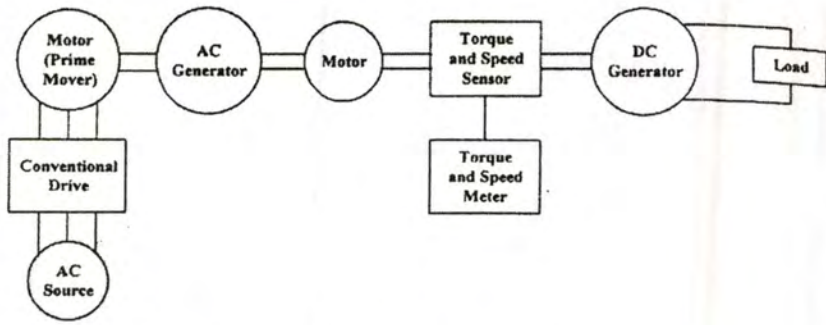


Figure 2: Test rig for sinusoidal investigation

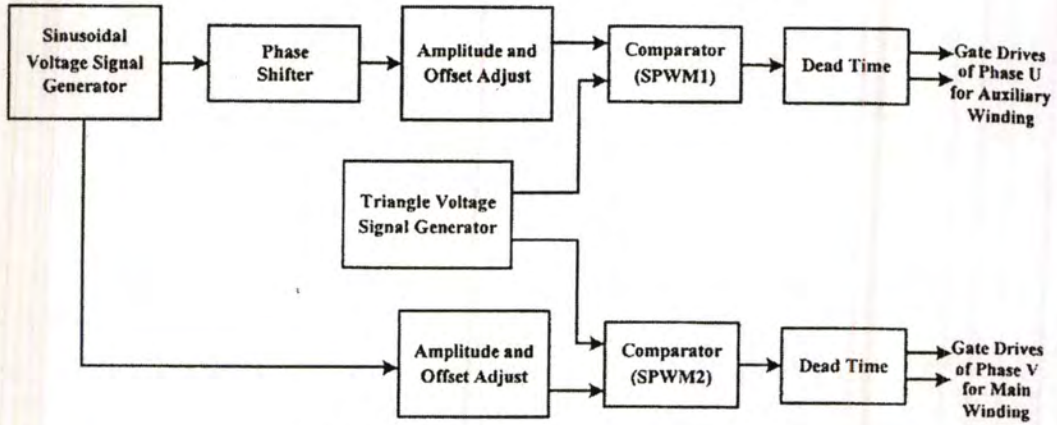


Figure 3: The control diagram of IGBT's gate drive

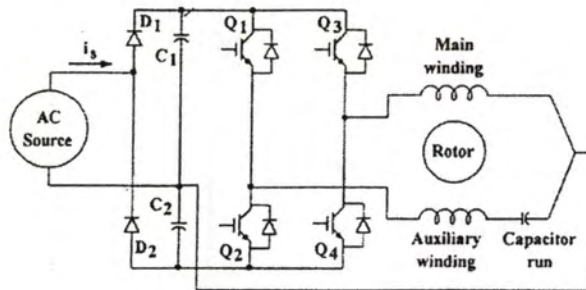


Figure 4: Schematic diagram of half bridge inverter with voltage doubler rectifier (condition II and III)

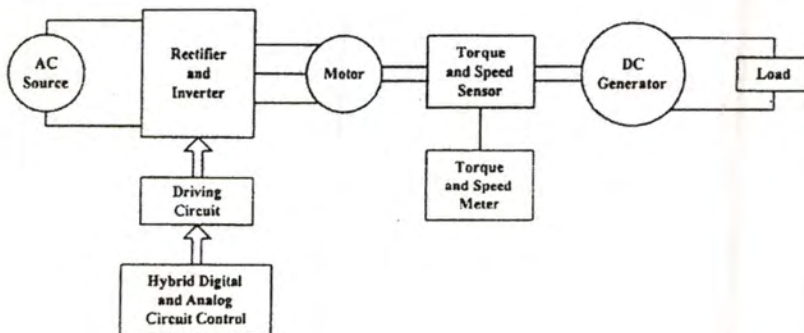


Figure 5: Test rig for SPWM investigation

III. EXPERIMENTAL RESULTS

In the case of condition I, the motor is fed by the synchronous generator which can be varied amplitude voltage by conventionally exciting current of field winding and can be changed the supplied frequency by speed control of prime mover as shown in Fig 2. During taking more load torque by adding electrical load, the main winding has the higher current while the auxiliary one has lower current. When the motor is supplied at rated voltage of 220 V and rated frequency of 50 Hz with no load condition; the auxiliary winding current is 1.32 A. This current value is considered as maximum value for the condition III. The auxiliary current at frequency of 50 Hz is the highest value. From the test results, the lower frequency of power source, the less auxiliary winding current.

Under condition II and III, the auxiliary winding current is in quadrature as presented in Fig. 6. Those are difference in that both main and auxiliary winding in condition II are obtained V/F control scheme. In condition III, the auxiliary winding is kept at maximum constant current of 1.32 A as described above, while only the main winding voltage is maintained with V/f control. The main winding current, therefore, depends on mechanical load. Carrier frequency (i.e. frequency of triangular waveform) is 5 kHz. The 5 kHz carrier frequency is normally used for compromised switching losses, acoustic noise, and low core losses. Fundamental frequency (i.e. frequency of sinusoidal waveform) is varied between 35 and 50 Hz. While operating at condition I, the more increased load torque (more input current demand), the lower auxiliary winding current. This might give obtained lower flux value resulting in lower load torque value. The experimental results of torque-speed curve are shown in Fig. 7. Figs. 8 – 11 illustrate the system efficiency for both sinusoidal and SPWM wave shapes. Tendency of motor performance from Fig. 7 is drastically good agreement with Figs. 8 – 11. The control strategy of condition III provides the highest system efficiency and best torque capability over a wide range of speed. The reason is that compensating current (keeping auxiliary winding current maximum) might compensate magnetizing flux and other additional losses which is confirmed by [2]. This implies that this condition provides the lowest losses of variable speed drive compared to the other conditions. The condition II provides the worst operation even though the phase difference of both winding current is kept in quadrature. The reason is that the manufacturer is likely to design permanent capacitor motor to obtain maximum torque above 80% of rated load torque for sinusoidal supply.

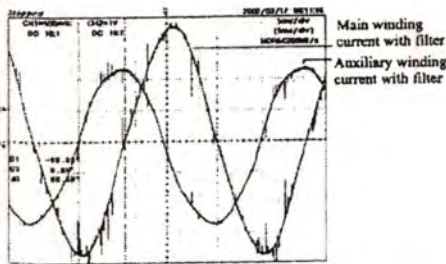


Figure 6: Waveform of main and auxiliary winding current with filter in quadrature

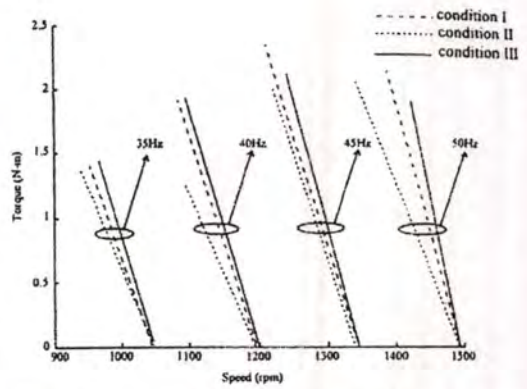


Figure 7: Torque-speed curve of three conditions at variable frequency

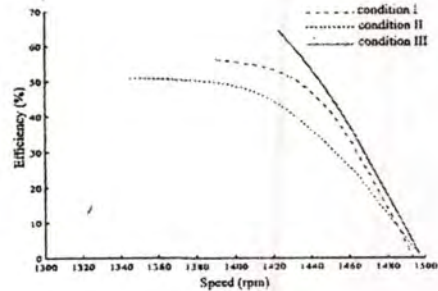


Figure 8: Efficiency comparison at frequency 50 Hz

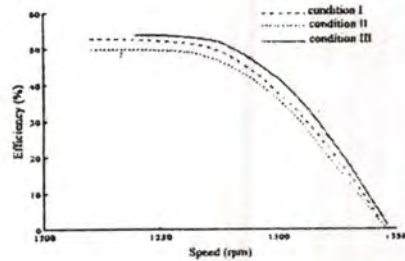


Figure 9: Efficiency comparison at frequency 45 Hz

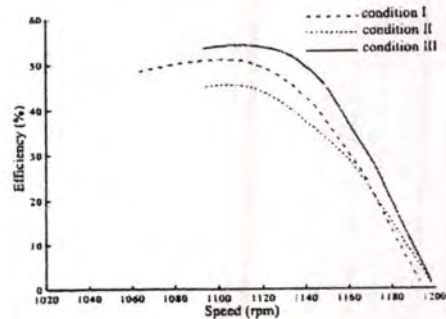


Figure 10: Efficiency comparison at frequency 40 Hz

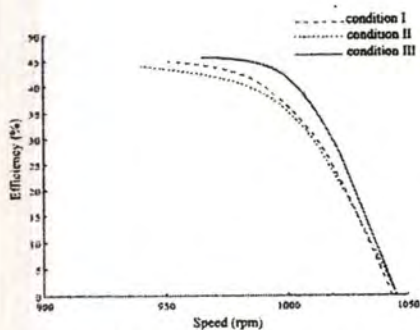


Figure 11: Efficiency comparison frequency 35 Hz

IV. CONCLUSION

The experimental results are clearly shown that the condition III is the best way to improve performance of two-phase capacitor motors. The main finding of this research work are as follows:

- Current control is better than voltage control but more difficult and complicated circuit. Furthermore, in practical for industrial applications, current sensor utilized for current detection is not preferred for low cost applications.
- To improve performance of variable speed induction motor, two-phase winding of the motor should be supplied their power sources independently.
- 90 degree voltage phase difference for each winding might provide the lower performance than 90 degree current phase difference.
- The best strategy is the control of maximum constant current of auxiliary winding similar to maximum voltage of auxiliary winding over a wide range operating conditions.

However, this scalar control is complicated function to maintain real time response. In the further work, the simulation and experiment of two-phase PWM inverter with various topologies will be compared to carry out the effectiveness and system efficiency of the inverter-driven motor in achieving higher performance. The further designed inverter will take into account not only performance of wide range of operation but also low cost of the drive.

V. APPENDIX

Motor name plate: permanent-split capacitor motor

4 poles, single phase, 50 Hz., 220 V, 2.5 A,
1440 rpm, capacitor 15 μ F, 350 V_{AC},
Insulation class E

VI. ACKNOWLEDGEMENT

The authors gratefully acknowledge the contribution of S. Nahuanil, S. Jai-ay, T. Komchaipoom, R. Areehamad, and B. Pooldech for their assistance in obtaining the experimental results.

VII. REFERENCES

- [1] E.R. Collins Jr., H.B. Puttgen, W.E. Sayle II, "Single Phase Induction Motor Adjustable Speed Drive: Direct Phase Angle Control of The Auxiliary Winding Supply", in *Proc. 1988 IEEE IAS-88 Conf.*, Pittsburgh, pp. 246-252.
- [2] E.R. Collins Jr., "Torque And Slip Behavior of Single-Phase Induction Motors Driven From Variable Speed Supplies". in *Proc. 1990 IEEE IAS-90 Conf.*, Seattle, 1990, pp. 61-66.
- [3] E.R. Collins Jr., R.E. Ashley, "Operating Characteristics of Single-Phase Capacitor Motors Driven From Variable Speed Supplies". in *Proc. IEEE IAS-91 Conf.*, Detroit, 1991, pp. 52-57.
- [4] D.G. Holmes, A. Kotsopoulos, "Variable Speed Control of Single and Two Phase Induction Motors Using a Three Phase Voltage Source Inverter". in *Proc. IEEE IAS-93 Conf.*, 1991, pp. 613-620.
- [5] W.J. Morrill, "The Revolving Theory of The Capacitor Motor", in *Proc. AIEE Winter Convention*, New York, 1929, pp. 614-633.
- [6] P. C. Krause, G. Wasyzcuk, and S. D. Sudhoff, *Analysis of electric machinery*, IEEE Press, Piscataway, NJ, 1996, ISBN 0-7803-1101-9
- [7] C-M. Young, C-C. Liu, and C-h. Liu, "New Inverter Driven Design and Control Method for Two Phase Induction Motor Drives". *Electric Power Applications*, IEE Proceedings, Nov. 1996, vol. 143, pp 458-466, issue 6
- [8] Frede Blaabjerg, Florin Lungeanu, Kenneth Skaug, and Andreas Aupke "Comparison of Variable Speed Drives for Single-Phase Induction Motors". in *Proc. IEEE PCC-2002 Conf.*, 2002, pp. 1328-1333.

VIII. BIOGRAPHIES



J. Sinthusonthichai received her B.Eng. and M.Eng. degrees from King Mongkut's Institute of Technology Ladkrabang, Bangkok, Thailand in 1993 and 1997, respectively. Her research interests are in energy conversion, electrical machines and variable speed drives.



V. Kinnares received the B.Eng. and M.Eng. degrees from King Mongkut's Institute of Technology Ladkrabang, Bangkok, Thailand, and received the Ph.D. Degree from University of Northingham, UK. Currently, he is an Assit. Professor at King Mongkut's Institute of Technology Ladkrabang. His research interests are in power electronics and

IPEC2003

The 6th International
Power Engineering Conference

ISBN: 981-04-8705-3

This material is reserved for educational use only, not allowed for commercial use.

Forbidden to modify the content, and cite the document when use.

COMPARATIVE PERFORMANCE EVALUATION OF TWO-PHASE PWM INVERTER FED INDUCTION MOTOR DRIVES WITH VARIOUS TOPOLOGIES

J. Sinthusonthichat R. Areehamad V. Kinnares

Dept. of Electrical Engineering, Faculty of Engineering,
King Mongkut's Institute of Technology Ladkrabang, Thailand

Abstract

In order to compare the performance and to achieve a wide range of variable speed control of two-phase induction motor, various types of SPWM inverter topologies focused on high system efficiency and low torque pulsation are designed and implemented. By those topologies, two-phase unsymmetrical induction motor has been tested under the same conditions. The voltages supplied for main and auxiliary windings are independent with displaced 90 electrical degrees phase shift. The energised voltage of main winding is varied by V/F control scheme while that of auxiliary winding is kept at maximum level as nominal voltage. All experimental results are compared to validate the drive capability and motor performance.

Keywords

Two-phase induction motor, SPWM Inverter, Motor Performance, Variable Speed Drives.

1 INTRODUCTION

Even though the single phase induction motor holds such a dominant position, there are a few works on a wide speed range of operation. Induction motors are usually used in fixed speed applications. In situation where variable speed is required, various mechanical and electrical techniques such as gears, tapped winding or pole switching are needed. These methods normally do not achieve for continuous control of motor speed. Moreover, inefficient and complicated either mechanical or electrical techniques may make overall system efficiency lower. In [1] the method was proposed for the variable speed control of single phase induction motor. The main winding is supplied from the utility and the auxiliary winding is energized by a fixed-frequency variable voltage and variable phase-angle voltage source. The resultant operating speed range is quite limited. In [2] the torque and slip behavior of a single phase induction motor driven from a variable frequency supply were studied. However, variable frequency voltage applied to the motor is supplied by a synchronous generator but not by an inverter. A conventional three

phase inverter in [3] was proposed for driving two-phase unsymmetrical induction motors. The inverter consists of six power transistor formed as three legs configuration. Two phase variable speed induction motor drive with regenerative mode utilizing only six power semiconductor switches is presented in [5 6]. Symmetrical and unsymmetrical-type two-phase induction motor fed by inverter-driven two-phase induction motor drive are presented in [7]. However, there is no paper taking into account on various types of PWM topologies.

This paper focuses on the performance evaluation of two-phase induction motor fed by various sinusoidal pulse-width-modulation (SPWM) inverter topologies. Case 1 is a half bridge SPWM inverter with bipolar voltage switching technique. Case 2 and 3 is a full bridge SPWM inverter with bipolar and unipolar voltage switching techniques, respectively. Those three case inverters are supplied to two-phase induction motor with unbalance motor parameters to study motor characteristics. All experimental results from three inverter topologies such as system efficiency, motor efficiency, machine input and motor characteristics at the same load torque are compared together to show the effectiveness of the induction motor drives.

2 SYSTEM CONFIGURATION

There are three PWM inverter topologies proposed in this paper. The first PWM inverter (Case 1) consists of a single phase voltage-doubler rectifier, two filter capacitors in series, two pairs of power transistors, and a source inductor. The center points of the two pairs of IGBTs are connected to each one of terminals of main and auxiliary windings, respectively. The rest two terminals of the main and auxiliary windings are connected together to the center-tap of the series capacitor as shown in Fig 1. The second and the third strategies utilize a full wave bridge rectifier as full-bridge inverter which have two more diodes than the two previous topology. The common terminals of both main and auxiliary windings are connected directly to the source as illustrated in Fig. 2. The pulse-width-modulated switching scheme in Case 2 is bipolar while

Case 3 is unipolar voltage switching. To verify the system performance for two-phase induction motor drives, the experimental set up has been implemented as shown in Fig. 3. In the block of hybrid digital and analog circuit control for PWM generator, two sinusoidal waveforms with 90 degree difference are digitally implemented by MCS51 as drawn in Fig. 4. Consequently, the PWM control signals for both windings of single phase induction motor are generated as illustrated in Fig 5.

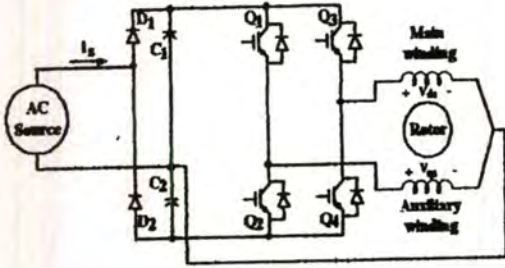


Figure 1: Schematic diagram of half bridge inverter with voltage-doubler rectifier (Case 1)

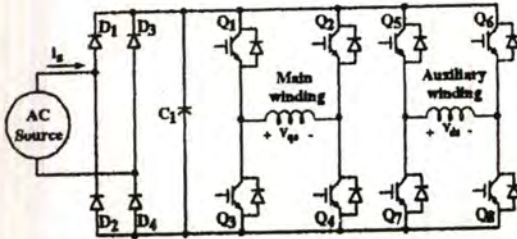


Figure 2: Schematic diagram of full bridge inverter (Case 2 and 3; different PWM strategies)

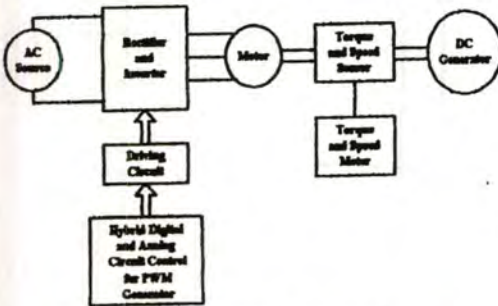


Figure 3: Block diagram of experimental system

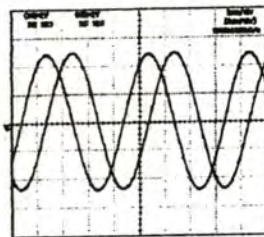


Figure 4: Two sinusoidal reference waveforms with 90 degree electrical angle difference

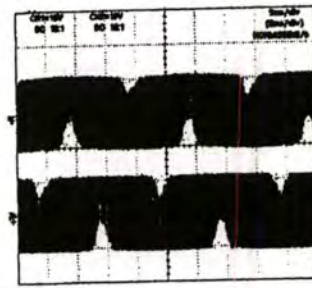


Fig 5: Generated PWM control signals

3 SIMULATION MODEL

Since the axes of the main and auxiliary stator windings are orthogonal, the stationary qd axes may be aligned with the orthogonal axes of the physical windings. Using the coupled circuit approach and motor notation, the voltage equations of the magnetically coupled stator and rotor circuits can be written as follows [4], [9]:

$$v_{qs} = i_{qs} r_{qs} + \frac{d\lambda_{qs}}{dt} \tag{1}$$

$$v_{ds} = i_{ds} r_{ds} + \frac{d\lambda_{ds}}{dt} \tag{2}$$

$$v_{qr} = i_{qr} r_{qr} + \frac{d\lambda_{qr}}{dt} \tag{3}$$

$$v_{dr} = i_{dr} r_{dr} + \frac{d\lambda_{dr}}{dt} \tag{4}$$

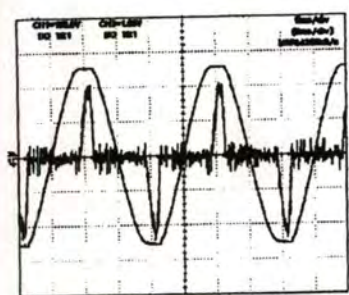
Torque and rotor motion equations is:

$$T_{em} = \frac{P}{200_b} (\Psi'_{ds} i'_{qr} - \Psi'_{qs} i'_{dr}) \tag{5}$$

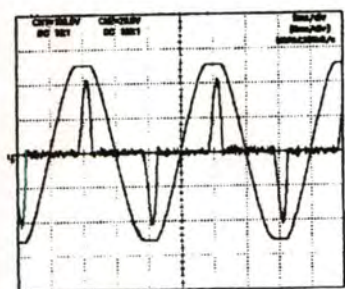
4 RESULTS AND DISCUSSION

Under the test, while variable frequencies, either dc link voltage at 691.4 V for case1 as well as 345.5 V for case 2 and 3 or modulation index of 0.9 of PWM waveform for auxiliary winding supply are kept constant to obtain rated fundamental voltage at 220 V. Only modulation index of main winding is varied depending on V/F control scheme. The proposed control technique is approached to a wide range of speed operation [8].

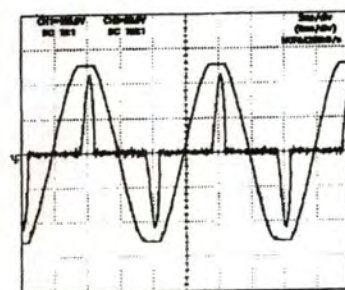
From experimental results, input waveforms in Fig 6 (a) - 6 (c) are shown that case 1 made up of unsymmetrical current waveshape in each half electrical cycle as well as higher harmonic current providing lower power factor than case 2 and 3. Therefore, input current characteristic should be improved by adding power factor controller circuit. However, this will make high cost and complicated controller of inverter.



(a) case 1



(b) case 2



(c) case 3

Fig 6: Input voltage and current waveforms

Torque-speed behavior of two-phase induction motor drive in Fig. 7 indicates that unipolar full bridge inverter contributes the better torque property than bipolar inverter both half and full bridge configurations. The experimental results well agree with the simulation ones as illustrated in Fig. 8 and 9. The figure reveals that bipolar control scheme either voltage doubler circuit in case 1 or full bridge circuit in case 2 is composed of more torque ripple than that of unipolar control scheme in case 3. Using Fourier transform and mathematical analysis in Matlab, at the same mechanical torque known as average torque or dc torque component, fundamental and second order harmonic torque in case 1 and 2 are approximately 0.468 and 0.08 N-m, sequentially. Those of case 3 are only around 0.442 and 0.05 N-m, respectively. Moreover, these correspond to motor and

efficiency characteristics as depicted in Fig 10. Figure 11 indicates that, at the same fundamental voltage control with discrepancy PWM topologies, full bridge inverter topology with unipolar control strategy makes two-phase unsymmetrical induction motor had the best not only motor characteristics but also system effectiveness. Although full bridge PWM inverter utilizes four legs and bridge rectifier comprising of high conduction and switching losses, according to the first side band harmonics is at $2m_t$, and full bridge rectifier makes up of lower harmonic current, the case 3 provides either lower torque ripple than two previous cases which energize the first side band harmonics at m_t or higher input efficiency than that of case 1. Due to case 2 comprises of both bipolar PWM scheme generating high torque pulsation, as well as more four switching devices than case 1, the motor performance and system efficiency is the worst condition.

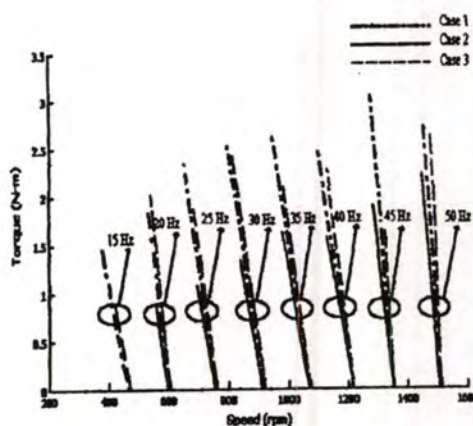
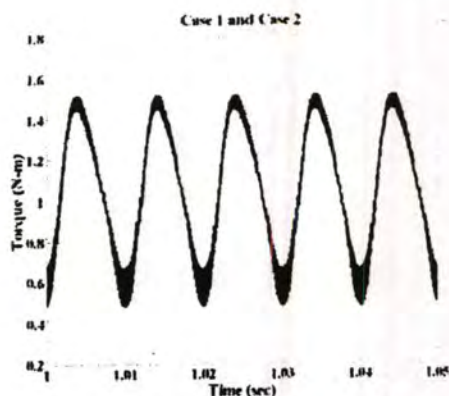


Fig 7: Torque-speed curve for a wide range of speed



(a)

advantage for constant voltage of auxiliary winding as a rated voltage and merely adjusts voltage of main winding.

However, unipolar full bridge inverter utilising four legs of IGBTs is high cost, high conduction losses and inconvenient for industrial utilisation. In the further work, the three branches IGBTs in IPM module with unipolar control scheme of two-phase PWM inverter which may decrease torque pulsation because of no dominant harmonics at m_f will be compared to carry out the effectiveness and system efficiency of the inverter-driven motor in achieving high efficiency and motor performance, low cost as well as wide range of speed drives. The further designed inverter will take into account not only performance of a wide range of operation but also reasonable cost of the drive. Furthermore, both motor and system characteristics under included and excluded series capacitor of auxiliary winding will be investigated.

APPENDIX

Motor name plate: permanent-split capacitor motor, 4 poles, single phase, 50 Hz., 220 V, 2.5 A, 1440 rpm, capacitor 15 μ F, 350 V_{AC}, Insulation class E

REFERENCES

- [1] E. R. Collins Jr., H.B. Puttgen, and W. E. Sayle II, "Single Phase Induction Motor Drive: Direct Phase Control of The Auxiliary Winding Supply", Proceeding of Industry Applications Society Annual Meeting, 1988, pp. 246-252.
- [2] E. R. Collins Jr., "Torque and Slip Behavior of Single-Phase Induction Motor Driven from Variable-Frequency Supply", IEEE Transaction on Industry Applications, Vol. 28, No. 3, 1992, pp. 710-715.
- [3] D.G. Holmes, and A.Kotsopoulos, "Variable Speed Control of Single and Two Phase Induction Motors Using A Three Phase Voltage Source Inverter", Proc. Of Industry Applications Society Annual Meeting, 1993, pp. 613-620.
- [4] P. C. Krause, O. Wasyczuk, and S. D. Sudhoff, *Analysis of electric machinery*, IEEE Press, Piscataway, N.J, 1996, ISBN 0-7803-1101-9.
- [5] M.F Rahman, and L.Zhong, "A Single/two Phase, Regenerative, Variable Speed, Induction Motor Drive with Sinusoidal Input Current", Thirtieth IAS Annual Meeting, IAS' '95 Proceeding, 1995, pp. 584-590, vol. 1.
- [6] BOYS, J.T. and GREEN, A. W., "Current-forced Single-phase Reversible Rectifier", IEE Proceedings, B 1989, Vol 136, pp. 205-211.
- [7] C-M. Young, C-C. Liu, and C-h. Liu, "New Inverter Driven Design and Control Method for Two Phase Induction Motor Drives", Electric Power Applications, IEE Proceedings, Nov.1996, pp 458-466, vol. 143, issue 6.
- [8] Frede Blaabjerg, Florin Lugeanu, Kenneth Skaug, and Andreas Aupke, "Comparison of Variable Speed Drives for Single-phase Induction Motors", PCC-OSAKA Conference, 2002, pp1328-1333.
- [9] CHEE- MUN ONG, *Dynamic Simulation of Electric Machinery using MATLAB/Simulink*, Prentice Hall PTR. 1998, ISBN 0-13-723785-5.



The Institute of Electrical Engineers of Japan

Homat Horizon Bldg. 8F. 6-2, Go-bancho Chiyoda-ku, Tokyo 102, Japan

December 13, 2004

Ms S. Sinthusonthishat
13/94 Chahornvil Village, Nong-jok.
P. O. Box 10, Nong-jok, Thailand, 10530

Paper No. : 16-0566
Paper Title: A New Modulation Strategy for Unbalanced Two Phase Induction
Motor Drives Using a Three-Leg Voltage Source Inverter

Dear Ms S. Sinthusonthishat

We are pleased to inform you that the above titled paper is acceptable for publication in the Transactions of The Institute of Electrical Engineers of Japan (IEE of Japan), Industry Applications Society (Section D).

Please send the following materials to us by February 18, 2005.

1. Type-written final manuscript complied with "Author's Guide of Paper for Society Transactions of The IEE Japan".
2. Please put in and send the data created by Ms-Word to FD or MO.

Your paper will be published on vol. 125-D, No. 5, 2005, which will be issued on May 1, 2005. If you have any questions, please contact us together with above indicated your Paper No. 16-566.

Sincerely yours,

for

Akihiro Ametani

Akihiro Ametani
Chairman
The Editorial Board
The Institute of Electrical
Engineers of Japan

A New Modulation Strategy for Unbalanced Two Phase Induction Motor Drives Using a Three-Leg Voltage Source Inverter

S. Sinthusonthishat* and V. Kinnarees*

This paper proposes a new modulation scheme providing unbalanced output terminal voltages of a standard three-leg voltage source inverter (VSI) for unsymmetrical type two-phase induction motors. This strategy allows a control method of the output voltages with typically constant V/Hz for a main winding and with voltage boost to compensate magnitude of current for an auxiliary winding. Harmonic voltage characteristics and the motor performance are investigated under a wide range of operating conditions. Practical verification is presented to confirm correctness and capabilities of the proposed technique. All results are compared to those of a conventional two-leg half bridge topology. The results show that the simulation results well agree with the experimental ones, and also the proposed scheme is superior to the conventional drive.

Key words: Unsymmetrical two phase induction motor, Harmonic voltages, Unbalanced output terminal voltage, PWM voltage source inverter

List of Symbols

\hat{V}_m	= main winding voltage
\hat{V}_a	= auxiliary winding voltage
\hat{i}_m	= main winding current
\hat{i}_a	= auxiliary winding current
\hat{E}_{fm}	= forward induced voltage of main winding
\hat{E}_{fa}	= forward induced voltage of auxiliary winding
\hat{E}_{bm}	= backward induced voltage of main winding
\hat{E}_{ba}	= backward induced voltage of auxiliary winding
a	= turns ratio of auxiliary to main windings
s	= slip
ω_s	= synchronous angular frequency (rad/sec)
ϕ	= phase angle between the main and the auxiliary winding currents
T_e	= average electromagnetic torque
T_{puls}	= amplitude of pulsating torque
R_{1m}, X_{1m}	= main winding resistance and leakage reactance
R_{1a}, X_{1a}	= auxiliary winding resistance and leakage reactance
X_m	= main winding magnetizing reactance
R_2, X_2	= rotor resistance and leakage reactance referred to main winding
$\frac{R_2}{a^2}, \frac{X_2}{a^2}$	= rotor resistance and leakage reactance referred to auxiliary winding
Z_f	= forward impedance of main winding
Z_b	= backward impedance of main winding
R_f, X_f	= forward resistance and leakage reactance of main winding
R_b, X_b	= backward resistance and leakage reactance of main winding
$\frac{R_f}{a^2}, \frac{X_f}{a^2}$	= forward resistance and leakage reactance referred to auxiliary winding
$\frac{R_b}{a^2}, \frac{X_b}{a^2}$	= backward resistance and leakage reactance referred to auxiliary winding

v_a, v_b, v_c	= reference modulating function of control signal phase $a, b,$ and $c,$ respectively
V_{Q1}	= fundamental main winding voltage
V_{D1}	= fundamental auxiliary winding voltage
V_m	= amplitude of modulating function
V_{dc}	= dc link voltage
V_x	= amplitude of additional modulating function
V_c	= amplitude of carrier signal
M_1	= modulation index of additional modulating function
M	= modulation index
ω_r	= reference angular frequency (rad/s)
ω_c	= carrier angular frequency (rad/s)
m_f	= modulation frequency ratio

1. Introduction

Single phase induction motors have been widely used in residential and industrial applications. The most encountered single phase motor is actually a two-phase machine known as the permanent split capacitor motor (PSCM). The motors are normally used in single speed drive applications. In case of desirably variable speed, the mechanical or electrical techniques are needed. These methods do not accomplish continuous speed control and energy saving viewpoint because of constant voltage and constant frequency sources. The reduction in the cost of the power electronic circuitry and importance of energy saving issue has made the use of a variable single phase motor drive system possible. The single phase induction motor has serious problems, when operating at low frequencies such as overheating, reduced pull-down torque and higher pulsating torque amplitude [1]. Several publications [3-6] have proved that, by varying frequencies and magnitude of the two-phase stator voltage, the torque ripple and audible noise can be reduced. Also, a 2-leg VSI provides the lower motor performance than a 4-leg VSI because of the quality of PWM scheme as well as dc link voltage utilization. Some publications [2, 7, 11] have reported the 3-leg VSI drives with their own modulation strategies. A conclusion of almost the same performance between 3-leg and 4-leg topologies can be found in [11]. However, the 4-leg VSI has main drawbacks in switching device counts. Additionally, the 3-leg topology is now available in a commercially compact Intelligent Power Module (IPM). To optimize between cost and performance of the drive system, 3-leg VSI is a good trade. Since each motor winding voltage of the 3-leg VSI has the same common node at an inverter branch, the normal regulating function cannot be succeeded for the unbalanced two-phase voltage control methodology. A specially modulating PWM strategy to accomplish wide range variable speed operation of commonly existing machines for the three-leg drive is needed.

* Department of Electrical Engineering, Faculty of Engineering, King Mongkut's Institute of Technology Ladkrabang Bangkok 10250 Thailand

This paper describes the principle of generating PWM patterns for driving inverter fed two-phase squirrel cage induction motors using a 3-leg inverter system. This structure is less expensive than the 4-leg VSI and provides better performance in terms of harmonic distortion when compared with that of the 2-leg VSI. To maintain the 90 electrical degree difference of unbalanced type two-winding voltages with variable-voltage variable-frequency 3-leg VSI, the additional modulating function is required. To achieve a wide range of operation, the fundamental amplitude of the main winding voltage is kept constant at rated volt/hertz while that of auxiliary winding voltage is proportional to inverter frequency with constant boost voltage at "a" (turns ratio) times. The proposed PWM technique and the two-phase motor model are simulated to predict the harmonic voltage characteristics and the machine performance. To verify the validity of the proposed strategy, both simulation and experimental results of 3-leg VSI are compared with those of the conventional 2-leg VSI while the 4-leg VSI is not interested here because of more cost and switching devices. The results obviously show the performance improvement of the proposed method. The proposed modulation technique is appropriate for the drive of the ordinarily asymmetrical two-phase induction machine.

2. Unsymmetrical two-phase motor model

A two unsymmetrical stator windings motor formed in space quadrature can be illustrated as a similar single equivalent circuit for each winding including the induced voltage in the winding from the other winding's flux as shown in Fig. 1 [12]. Since the main and auxiliary windings are typically quite different, with a different number of turns, wire size and turns distribution, the turns ratio test should be made following Veinott technique [13]. Both stator resistances, R_{1m} and R_{1a} , can be derived from DC test. The remaining parameters can be obtained by a standard test method. In the equivalent circuit, no attempt has been made to include the core losses resistance into the model. However, the core loss is summed with friction and windage losses called as rotational losses, and is utilized for calculating the precisely mechanical output power. The motor parameter values used in this work are given in Appendix. The forward and backward impedances drawn in Fig. 1 are:

$$Z_f = R_f + jX_f = \frac{jX_m}{2} // \left(\frac{R_2}{2s} + \frac{jX_2}{2} \right) \quad (1)$$

$$Z_b = R_b + jX_b = \frac{jX_m}{2} // \left(\frac{R_2}{2(2-s)} + \frac{jX_2}{2} \right) \quad (2)$$

$$\hat{V}_D = \hat{I}_m (R_{1m} + jX_{1m}) + \hat{E}_{fm} - \frac{j\hat{E}_{fb}}{a} + \hat{E}_{bm} + \frac{j\hat{E}_{ba}}{a} \quad (3)$$

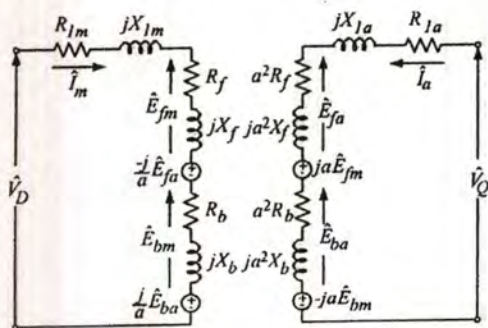


Fig. 1. Equivalent circuit of unsymmetrical two-phase induction motor

$$\hat{V}_Q = \hat{I}_a (R_{1a} + jX_{1a}) + \hat{E}_{fa} + ja\hat{E}_{fm} + \hat{E}_{ba} - ja\hat{E}_{bm} \quad (4)$$

As indicated in [12], the developed average electromagnetic torque using this model is given by:

$$T_e = \frac{1}{\omega_s} \left\{ \left[(I_m^2 + (aI_a)^2) (R_f - R_b) \right] + \left[2aI_m I_a (R_f + R_b) \sin \phi \right] \right\} \quad (5)$$

and a pulsating torque:

$$T_{puls} = \frac{1}{\omega_s} \left\{ \left[I_m^4 + (aI_a)^4 + 2(aI_m I_a)^2 \cos 2\phi \right]^{\frac{1}{2}} \left[(R_f - R_b)^2 + (X_f - X_b)^2 \right]^{\frac{1}{2}} \right\} \quad (6)$$

From Equation (5), it can be seen that the maximum average torque will be present when $\phi = 90^\circ$. When considering Equation (6), at $\phi = 90^\circ$, undesirable pulsating torque can also be eliminated at any motor slips if;

$$I_m^4 + (aI_a)^4 - 2(aI_m I_a)^2 = 0 \quad (7)$$

thus:

$$\left(\frac{I_m}{aI_a} \right)^2 + \left(\frac{aI_a}{I_m} \right)^2 = 2 \quad (8)$$

giving:

$$I_m = aI_a \quad (9)$$

Equation (9) is demonstrated that the relative amplitude of the winding currents should be the inverse of the winding turns ratio. In order to achieve the relationship between both currents, the voltage ratio is approximately equal to

$$V_D = aV_Q \quad (10)$$

Equations (5)-(10) are expressed that the optimum control method to operate an unsymmetrical two-phase motor under variable frequency control is to maintain the winding currents in quadrature with a ratio between the main and the auxiliary winding currents equal to the turns ratio. Many papers [4-8] have proved better performance of this method. The relationship between inverter frequency and fundamental output voltage V_{D1} and V_{Q1} can be seen in Fig. 2 as solid and dashed lines, respectively. While the fundamental frequency varies up to rated value, volt/hertz of the main winding is kept constant at nominal value. The fundamental amplitude of the auxiliary winding voltage is proportional to inverter frequencies with a boost voltage level at "a" times V/Hz of the main winding in the frequency range of $0 < f < \frac{f_{rated}}{a}$. When

inverter frequency reaches at $\frac{f_{rated}}{a}$, the auxiliary winding voltage will be maintained constant at a rated value for the reason of preventing machine saturation in the frequency range of $\frac{f_{rated}}{a} \leq f \leq f_{rated}$.

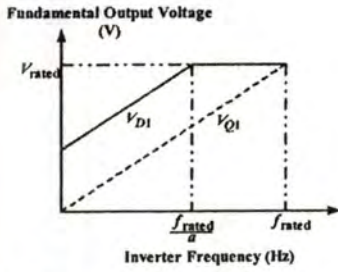


Fig. 2. The relationship between inverter frequency and fundamental output voltage for each winding

3. Converter modulation strategy

The conventional two-leg half bridge inverter supplying a two-phase induction motor as shown in Fig. 3 consists of a single phase voltage doubler rectifier, two filter capacitors in series, and two legs of an IGBT pair. The one end of the main and auxiliary windings are connected to the two-leg inverter. The other ends are connected together with the center-tap of the filter capacitors. Their fundamental components of output voltage are shifted with 90 electrical degree differences. The principle of generating balanced two-phase PWM output voltages is based on a comparison between balanced two-phase modulating sinusoidal signals with 90 electrical degree phase shift compared to a common triangular wave, known as a sinusoidal pulsewidth modulation (SPWM) is shown in Fig. 4. PWM output voltages are classified as bipolar PWM.

Two modulating function signals with balanced output voltages for a two-leg system are:

$$\begin{aligned} v_a &= V_m \sin(\omega, t) \\ v_b &= V_m \sin(\omega, t - 90^\circ) \end{aligned} \tag{11}$$

The amplitude and frequency of the output phase voltages can be controlled independently by varying a sinusoidal reference amplitude and a frequency of each modulating signal whilst the carrier signal is fixed with a constant frequency and amplitude. More details of PWM parameters such as modulation index, modulation frequency ratio can be found in [16]. Note that an unbalanced case in accordance with the control method as mentioned in Fig. 2 can also be easily obtained due to independent control for each modulating signal.

Fig. 5 indicates the proposed three-leg VSI so-called semi-fullbridge PWM inverter for a two-phase motor drive system. When compared to the conventional two-leg half bridge inverter, the third modulating function for the third leg is needed as given in Equation (12). With these modulating functions for balanced output voltages, the both winding voltages are always in quadrature.

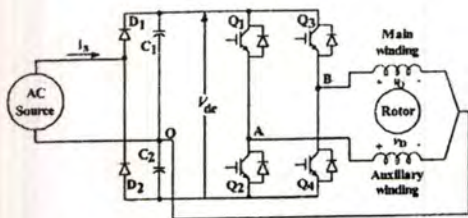


Fig. 3. Main power circuit of the typical two-leg half bridge inverter for comparing with Fig. 5

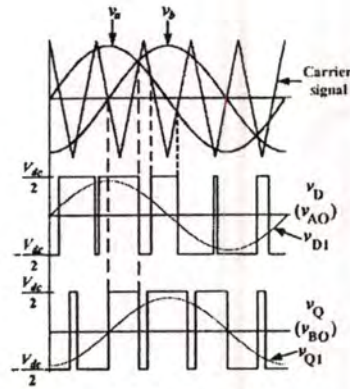


Fig. 4. Principle of generating PWM patterns for the typical two-leg VSI corresponding to Fig. 3

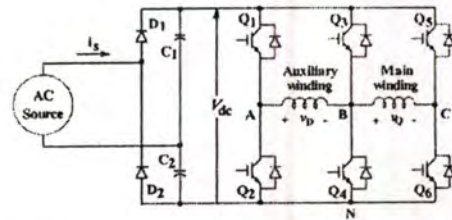


Fig. 5. Main power circuit of the proposed three-leg VSI supplying a two-phase induction motor

$$\begin{aligned} v_a &= V_m \sin(\omega, t) \\ v_b &= V_m \sin(\omega, t - 90^\circ) \\ v_c &= V_m \sin(\omega, t - 180^\circ) \end{aligned} \tag{12}$$

Unfortunately, unbalanced output voltages having 90 electrical degree phase differences cannot occur with independent control of those modulating function signals. In order to overcome this problem, the additional modulating function is required as follows: Let

$$v_{c1} = V_m \sin(\omega, t - 180^\circ)$$

and additional modulating function

$$v_{c2} = V_s \sin(\omega, t - 45^\circ)$$

and let

$$v_r = v_{c1} + v_{c2}$$

The modulating function for the third leg can be rewritten as:

$$v_c = \frac{\sqrt{2}}{2} V_s (\sin \omega, t - \cos \omega, t) - V_m \sin \omega, t \tag{13}$$

Thus

$$\begin{aligned} v_{ab} &= v_a - v_b = \sqrt{2} V_s \sin(\omega, t + 45^\circ) \\ v_{br} &= v_b - v_c = (\sqrt{2} V_s - V_s) \sin(\omega, t - 45^\circ) \end{aligned} \tag{14}$$

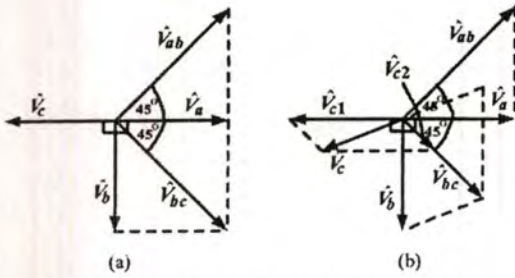


Fig. 6. Phasor diagram of modulating functions for the two-phase drive system of 3-leg VSI
(a) balanced output voltage case
(b) unbalanced output voltage case

As can be seen in Equation (14), the two voltages, v_{ab} and v_{bc} equivalent to the fundamental auxiliary and main winding voltages, respectively, are in quadrature. The amplitude of both is 1.414 times the amplitude of each modulating function. This implies that this technique gives an advantage in terms of dc voltage utilization over the two-leg half bridge VSI. In order to better understand the principle of the proposed modulating functions, the phasor diagrams in Fig. 6 (a) for the balanced and 6 (b) for the unbalanced two-phase terminal voltage are illustrated. It is clear from the figure that with the additional modulating functions v_{c2} , the unbalanced output terminal voltage with different magnitude and fixed 90° phase shift at any operating conditions can be obtained. The principle of generating unbalanced PWM output voltages based on the proposed modulation scheme for three-leg VSI is described in Fig. 7.

PWM output voltages are classified as unipolar PWM. The fundamental output voltage of the auxiliary winding can be expressed as

$$v_{o1} = \frac{\sqrt{2}M V_{dc}}{2} \sin(\omega t + 45^\circ) \tag{15}$$

Also the fundamental output voltage of the main winding can be expressed as

$$v_{o2} = \frac{(\sqrt{2}M - M_1) V_{dc}}{2} \sin(\omega t - 45^\circ) \tag{16}$$

where $M = \frac{V_n}{V_i}$ and $M_1 = \frac{V_x}{V_i}$

As can be seen in Equations (15) and (16), the fundamental of PWM output voltages for both windings are in quadrature and can be set by M and M_1 in accordance with the control method as mentioned in Fig. 2.

4. Simulation and experimental results

To verify correctness and features of the proposed modulation strategy, the experimental system is setup as demonstrated in Fig. 8. Asynchronously natural-sampled PWM signals are generated by comparing a triangular carrier with a sinusoidal reference modulating function generated from a microcontroller. 25 A, 1200 V IGBT IPM is used for the main power circuit. A 370-W 230-V 2.66-A 1375-rpm 50-Hz PSCM with turns ratio of 1.7 is used in the investigation. Along with the control methodology, the running capacitor is removed. The motor is connected with a 400 W DC generator to serve as a dynamic load. Shaft torques and speeds are

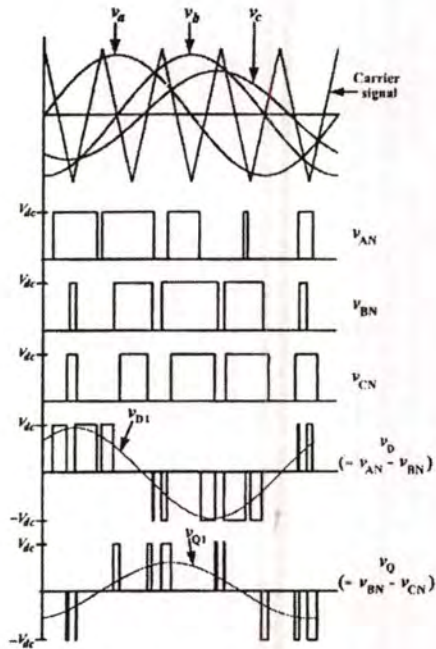


Fig. 7. Principle of generating unbalanced PWM output voltages based on the proposed modulating functions for three-leg VSI corresponding to Fig. 5

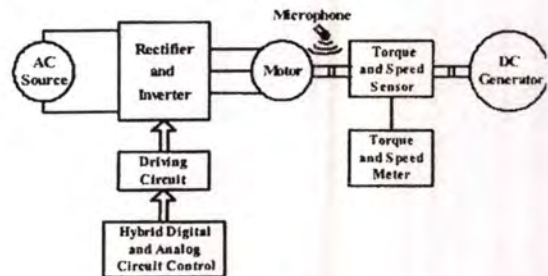


Fig. 8. Block diagram of experimental system

measured using torque-speed sensor. In order to detect the acoustic noise signal, a microphone is installed at a distance of 3 cm from the motor. Experimental results of voltage, current and power are recorded using a Power Harmonics Analyzer, Yokogawa Model PZ4000. Practical verification of the theoretical predictions derived from the mathematical and the machine model is corroborated. The motor parameters in the machine model are measured at 50 Hz utility supply as given in Appendix.

The effectiveness of PWM patterns in improving the quality of motor performance is demonstrated theoretically as well as experimentally. The motor is supplied by both 2-leg and 3-leg VSI at the same conditions. To inspect the harmonic voltage contents, the reference frequency of 20 Hz, and the triangular carrier frequency of 5 kHz are selected. The reason is that the inverter frequency is somewhat low (worst case) and in the voltage boost region, and the switching frequency is in the range of commercial drives available

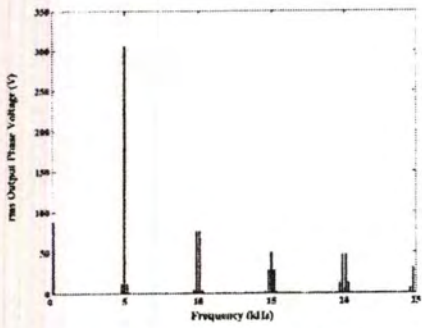


Fig. 9. Calculated main winding harmonic voltage spectra of 2-leg VSI at inverter frequency of 20 Hz

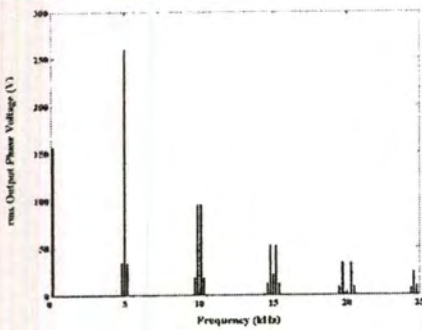


Fig. 10. Calculated auxiliary winding harmonic voltage spectra of 2-leg VSI at inverter frequency of 20 Hz

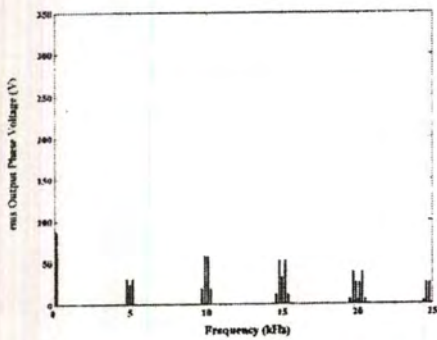


Fig. 11. Calculated main winding harmonic voltage spectra of 3-leg VSI at inverter frequency of 20 Hz

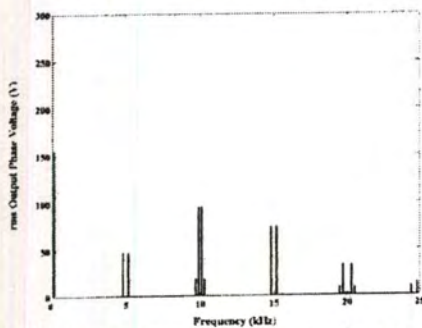


Fig. 12. Calculated auxiliary winding harmonic voltage spectra of 3-leg VSI at inverter frequency of 20 Hz

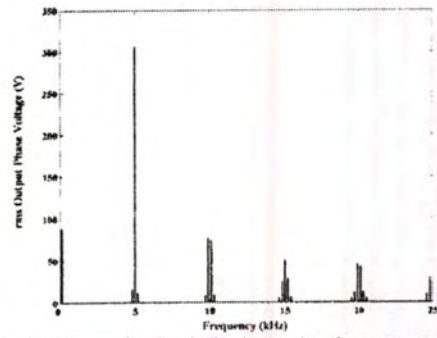


Fig. 13. Measured main winding harmonic voltage spectra of 2-leg VSI at inverter frequency of 20 Hz

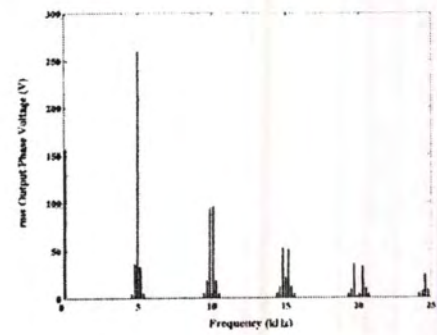


Fig. 14. Measured auxiliary winding harmonic voltage spectra of 2-leg VSI at inverter frequency of 20 Hz

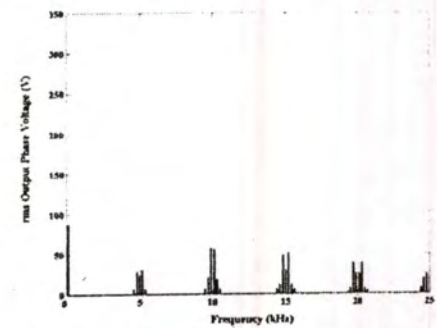


Fig. 15. Measured main winding harmonic voltage spectra of 3-leg VSI at inverter frequency of 20 Hz

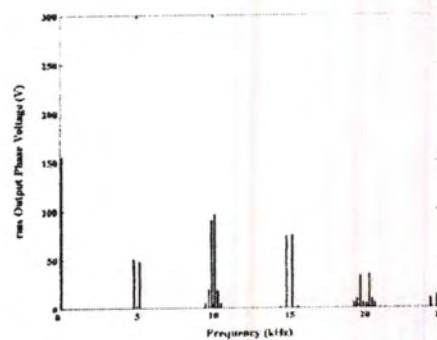


Fig. 16. Measured auxiliary winding harmonic voltage spectra of 3-leg VSI at inverter frequency of 20 Hz

The fundamental peak voltage of the main winding is approximately 124.5 V. The fundamental peak voltage of the auxiliary winding is about 211.6 V. The load torque is fixed on 2.5 N-m. The calculated and measured rms output voltages versus functions of frequency are illustrated in Figs. 9-12 and Figs. 13-16, respectively. These figures confirm the precision of not only numerical analysis but also the drive implementation. A comparison of Figs. 13-14 and Figs. 15-16 also verify that although the sidebands voltage of 2-leg VSI are slightly less than those of 3-leg VSI, the harmonic magnitude at carrier frequency of 2-leg is remarkably higher than those of 3-leg, thus resulting in more motor losses.

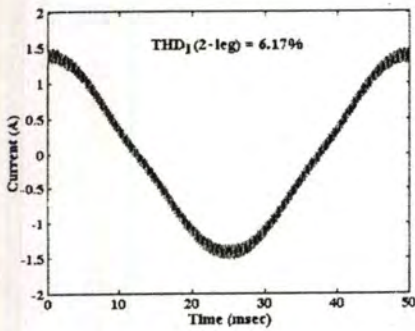


Fig. 17. Simulated auxiliary winding current waveform for 2-leg VSI at inverter frequency of 20 Hz

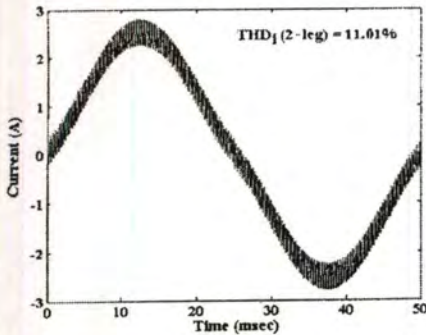


Fig. 18. Simulated main winding current waveform for 2-leg VSI at inverter frequency of 20 Hz

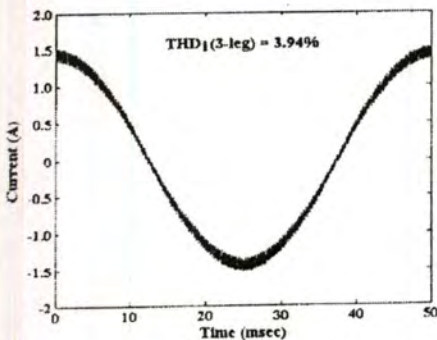


Fig. 19. Simulated auxiliary winding current waveform for 3-leg VSI at inverter frequency of 20 Hz

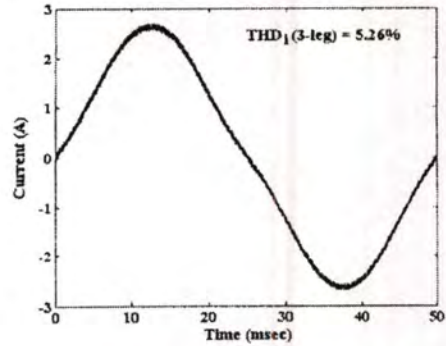


Fig. 20. Simulated main winding current waveform for 3-leg VSI at inverter frequency of 20 Hz

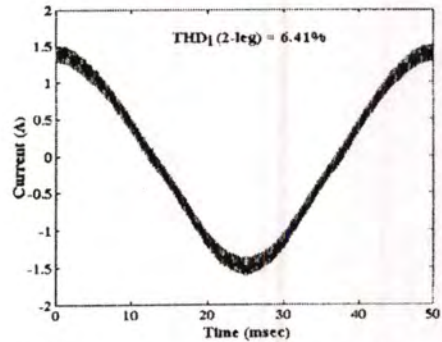


Fig. 21. Measured auxiliary winding current for 2-leg VSI at inverter frequency of 20 Hz

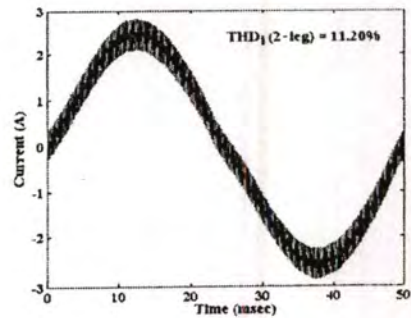


Fig. 22. Measured main winding current for 2-leg VSI at inverter frequency of 20 Hz

The calculated amplitude of each harmonic voltage from the fundamental up to 25 kHz harmonic frequency is considered. This range covers the significant harmonic contents. The calculated harmonic voltages are applied to the equivalent circuit in Fig. 1. The calculated currents of each winding at the same time domain, then, are summed by the superposition technique as shown in Figs. 17-18 for 2-leg VSI and also Figs. 19-20 for 3-leg VSI. The actual current results as illustrated in Figs. 21-24 are obtained from the power harmonic analyzer. It is clear from the comparison that the 3-leg presents a better performance than the 2-leg in terms of THD. This keeps in touch with harmonic voltage spectra characteristics.

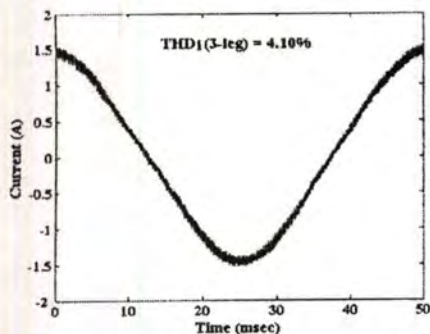


Fig. 23. Measured auxiliary winding current for 3-leg VSI at inverter frequency of 20 Hz

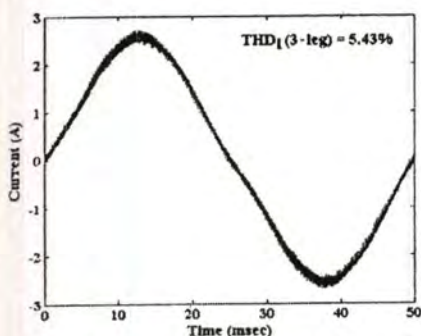


Fig. 24. Measured main winding current for 3-leg VSI at inverter frequency of 20 Hz

It is observed from the results that the simulated results give total harmonic distortion of current component slightly less than those of measured ones. This has proved the accuracy of the implemented circuits. The small error may be arisen from various factors. For example, the given simulation results have been analyzed from the ideal power electronic devices while the actual results have taken many effects such as voltage ripple of dc link voltage, blanking time in practical inverter legs, and voltage drop in devices, etc. into account. However, those are seen that the correlation is acceptable. The tested configuration of both winding motor currents with 2-leg and also 3-leg VSI are indicated in Figs. 25 and 26, respectively. These two figures confirm that the proposed modulation strategy dramatically provides the lower harmonic voltage than the conventional system, especially at low operating frequency. Also, the output currents of 3-leg VSI under unbalanced output voltage are approximately a sinusoidal waveform and nearly 90 degree differences.

To study the influence of the decreasing harmonic voltage component on motor performance, the motor efficiency, torque-speed characteristics and acoustic noise are carried out. The variation of motor efficiency of 2-leg and 3-leg VSI with typical V/F for both windings and the proposed control method under the same fundamental voltage at fundamental frequency between 20 Hz and 50 Hz as a function of load torque are illustrated in Figs. 27-29. Only in Fig. 29, the motor under test fed by the two drive systems and sinusoidal supply at rated frequency of 50 Hz. This operating frequency provides the same voltage level of both windings for both drive systems. In case of sinusoidal source, the motor is utilized with a running capacitor of $8 \mu F$ in series with the auxiliary winding. It is clear from the figures that the proposed control method provides better efficiency than the conventional

V/F control scheme for both windings. Also, the 3-leg VSI with the proposed technique gives the greatest motor efficiency at a wide range of speed, while the 2-leg VSI with V/F control scheme for both windings provides the worst performance because of harmonic contents. It is monitored from the figures that the operation ranges of motor fed by inverter are narrower than those of sinusoidal supply. The 3-leg VSI with the proposed scheme, however, still obtains the best motor efficiency because the inverter structure can exactly control the quadrature two-winding voltages. Surprisingly, for the 50 Hz sinusoidal source, the efficiency is lower than both drive system at light load torque. This is because the running capacitor value is normally designed suitable for heavy load.

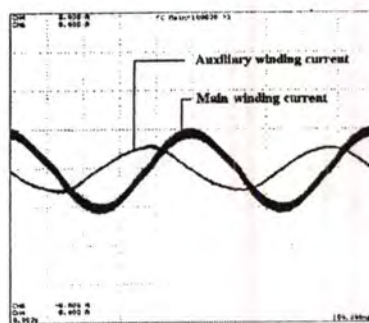


Fig. 25. Experimental results of motor winding currents for 2-leg VSI at inverter frequency of 20 Hz

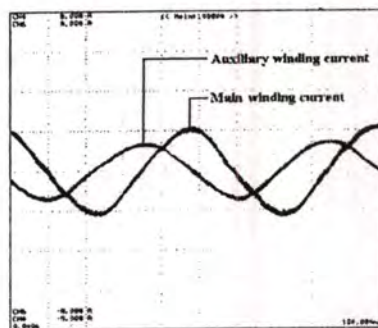


Fig. 26. Experimental results of motor winding currents for 3-leg VSI at inverter frequency of 20 Hz

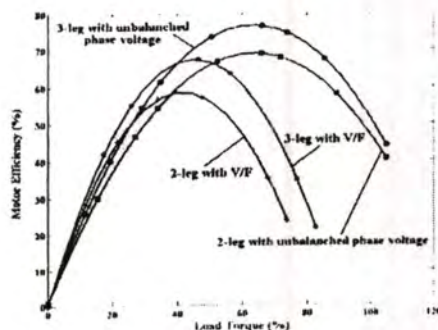


Fig. 27. Experimental results of motor efficiency versus %load torque with reference frequency at 20 Hz

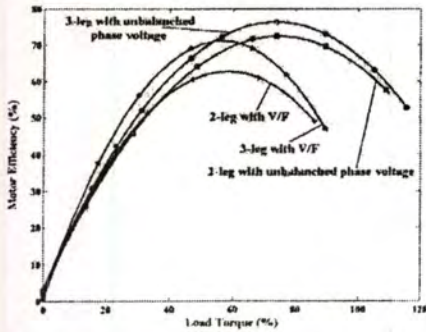


Fig. 28. Experimental results of motor efficiency versus %load torque with reference frequency at 30 Hz

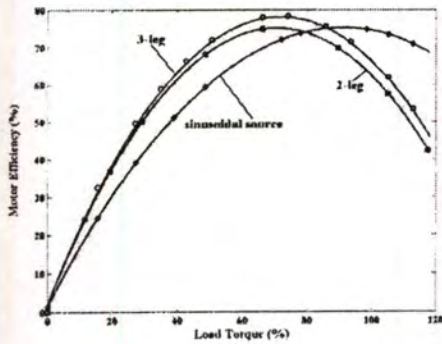


Fig. 29. Experimental results of motor efficiency versus %load torque at rated frequency of 50 Hz

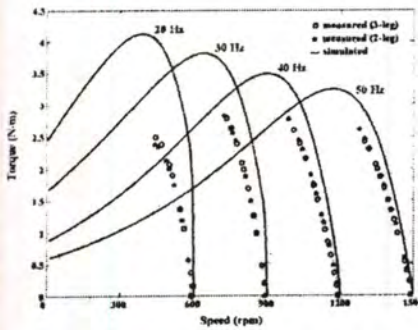


Fig. 30. Torque as function of motor speed at various frequency for both simulation and experimental results with the unbalanced voltage control method

Additionally, at low frequency, the motor efficiencies for both drive systems are significantly different since at low frequency (low modulation index) the 2-leg VSI generates higher harmonic voltages, particularly, at order of m_f . Fig. 30 demonstrates torque-speed motor profiles with various fundamental frequencies under the proposed control method, while Fig. 31 describes that relationship with constant V/F control scheme for both windings. When comparing these two figures, it can be evidently seen that unbalanced output voltage remarkably provides superior torque to

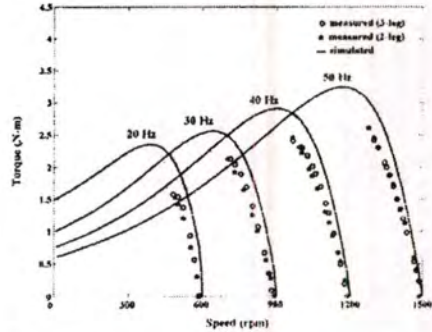


Fig. 31. Torque as function of motor speed at various frequency for both simulation and experimental results with constant V/F control scheme for both windings

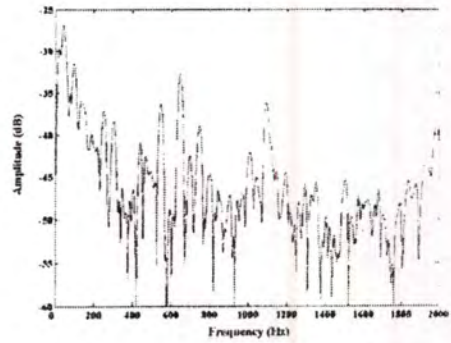


Fig. 32. Measured spectra of acoustic noise with 2-leg VSI fed induction motor at rated frequency of 50 Hz

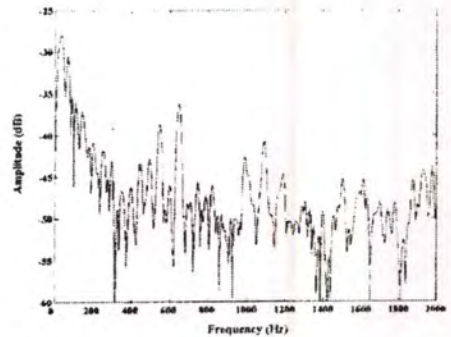


Fig. 33. Measured spectra of acoustic noise with 3-leg VSI fed induction motor at rated frequency of 50 Hz

constant V/F scheme for both windings and a wider range of operation. Measured and simulated results are in fairly agreement. The measured results for 2-leg and 3-leg are very close. These show that both drive systems provide the same average torque. This means that harmonic voltages do not affect average torque. This agrees with the publications [4, 8]. The acoustic noise spectra are illustrated in Figs. 32-33. These have clearly shown that at the same frequency the noise components of 3-leg VSI are mostly

attenuated. Consequently, the proposed technique can effectively diminish acoustic noise levels. This strongly confirms that harmonics voltages stress on motor mainly generate acoustic noise [15].

5. Conclusions

This paper has dealt with the analysis of a new modulation strategy for a three-phase voltage source inverter with unbalanced two-phase output voltages supplying an asymmetrical type two-phase induction motor. This technique allows in unbalanced output voltage control for both main and auxiliary windings with 90° electrical phase shift. Harmonic voltage contents have been investigated and compared to those of the two-leg voltage source inverter. A superior PWM quality over the conventional technique is achieved. The different schemes for obtaining a wide range of variable speed operation have been simulated and experimentally verified. The simulation results have shown very good agreement with the experimental results. All results confirm that the performance of the proposed modulation strategy is superior to the conventional scheme.

Appendix

Parameters of motor used in experiments:

$$R_{1m} = 9.028 \Omega, R_{2a} = 49.921 \Omega, R_2 = 15.283 \Omega,$$

$$L_{1m} = L_2 = 43.4 \text{ mH}, L_{2a} = 178.82 \text{ mH}, L_m = 202.92 \text{ mH},$$

$$\frac{N_a}{N_m} = a = 1.7$$

Acknowledgement

The authors wish to thank the Director of Minburi Technical College, Bangkok, Thailand, the staff of Elwe (Thailand) Co., Ltd., and Mr. Wattana Dewaje for providing all kinds of support and more importantly, allowing us to utilize equipments and devices needed for this research. The authors also appreciate useful suggestion and comments of Assoc. Prof. Dr. Pichetjamroen Viriya and Assist. Prof. Dr. A. Kunakorn, Department of Electrical Engineering, King Mongkut's Institute of Technology Ladkrabang, Thailand.

References

- 1 E.R. Collins Jr., H.B. Puttgen, W.E. Sayle II, "Single Phase Induction Motor Adjustable Speed Drive: Direct Phase Angle Control of The Auxiliary Winding Supply", in *Proc. IEEE IAS-88 Conf.*, Pittsburgh, 1988, pp. 246-251.
- 2 D.G. Holmes, A. Kotsopoulos, "Variable Speed Control of Single and Two Phase Induction Motors Using a Three Phase Voltage Source Inverter", in *Proc. IEEE IAS-93 Conf.*, 1991, pp. 613-620.
- 3 J. Sinthusonthichat, V. Kinnares "Performance Evaluation of Variable Speed Two-Phase Induction Motors", in *Proc. IEEE PowerCon 2002 Conf.*, 2002, pp. 2565-2568.
- 4 C-M. Young, C-C. Liu, and C-h. Liu, "New Inverter Driven Design and Control Method for Two Phase Induction Motor Drives", *Electric Power Applications*, IEE Proceedings, vol. 143, issue 6, Nov.1996, pp. 458-466.
- 5 Frede Blaabjerg, Florin Lugeanu, Kenneth Skaug, and Andreas Aupke, "Comparison of Variable Speed Drives for Single-Phase Induction Motors", in *Proc. IEEE PCC-2002 Conf.*, 2002, pp. 1328-1333.
- 6 Frede Blaabjerg, Florin Lugeanu, Kenneth Skaug, and Michael Tonnes, "Evaluation of Low-Cost Topologies for Two Phase Induction Motor Drives, in Industrial Applications", in *Proc. IEEE PCC-2002 Conf.*, 2002, pp. 2358-2365.
- 7 E. R. Benedict and T. A. Lipo, "Improved PWM Modulation for a Permanent-Split Capacitor Motor", *Proceedings of IEEE IAS Annual Meeting Conference*, October 2000, pp. 2004-2010.
- 8 J. Sinthusonthichat, R. Areehamad, V. Kinnares "Comparative Performance Evaluation of Two-Phase PWM Inverter Fed Induction Motor Drives With Various Topologies", in *Proc. IEEE IPEC 2003 Conf.*, 2003.
- 9 P.N. Enjeti, and A. Rahman, "A New Single-Phase to Three-Phase Converter with Active Input Current Shaping for Low Cost ac Motor Drives", *IEEE Trans. on Industry Applications*, Vol. 29, No. 4, July/August 1993, pp. 806-813.
- 10 P.N. Enjeti, A. Rahman, and R. Jakkji, "Economic Single-Phase to Three-Phase Converter Topologies for Fixed and Variable Frequency Output", *IEEE Trans. on Power Electronics*, Vol. 8, No. 3, July 1993, pp. 329-335.
- 11 Mauricio Beltrao de Rossiter Correa, Cursimo Brandao Jacobina, Antonio Marcus Nogueira Lima, and Edison Roberto Cabral da Silva, "A Three-Leg Voltage Source Inverter for Two-Phase AC Motor Drive Systems" *IEEE Trans. on Power Electronics*, Vol. 17, No. 4, July 2002, pp. 517-523.
- 12 W.J. Morrill, "The Revolving Field Theory of The Capacitor Motor", in *Proc. AIEE Winter Convention*, New York, 1929, pp. 614-633.
- 13 Cyril G. Veinott and Joseph E. Martin, *Fractional and Subfractional Horsepower Electric Motors*, Forth Edition, Mc-Graw-Hill International Company, 1987, pp. 390.
- 14 S.R. Bowes, and B.M. Bird, "Novel Approach to the Analysis and Synthesis of Modulation Processes in Power Convertors", *IEE Proceedings*, Vol.122, No.5, May 1975, pp. 507-513.
- 15 Bertrand Cassoret, Rodolphe Corton, Daniel Roger, and Jean-Francois Brudny, "Magnetic Noise Reduction of Induction Machines", *IEEE Trans. On Power Electronics*, Vol. 18, No. 2, March 2003.
- 16 Ned Mohan, Tore M. Undeland, and William P. Robbins, "Power Electronics: Converters, Applications, and Design", John Wiley & Sons, Inc., 1995.

S. Sinthusonthichat



was born in Bangkok, Thailand, in 1972. She received the B. Eng. and M. Eng. Degrees from King Mongkut's Institute of Technology Ladkrabang, Thailand. She is pursuing the D. Eng. Degree at King Mongkut's Institute of Technology Ladkrabang. Currently, she is with Electrical Engineering Department of Mahanakorn University of Technology. Her research interest includes Electrical Machines and Electric Drives.

V. Kinnares



was born in Sagolnakhon, Thailand, in 1962. He received the B. Eng. and M. Eng. Degrees from King Mongkut's Institute of Technology Ladkrabang, Thailand. He received the Ph.D. Degree from the University of Nottingham, U.K. in 1997. He has been an associate professor with King Mongkut's Institute of Technology Ladkrabang since 2003. His research interest includes Energy Conversion, Power Electronics and Electric Drives.

BIOGRAPHY

Family Name: Sinthusonthishat
First Name: Saliltip
Date of Birth: January 15, 1972
Home Address: 13/94 Moo 6 Chakornvil Village, Kog-phad,
Nong-jok, Bangkok, 10530, THAILAND.
Home Phone: +66 2 9881076
Mobile Phone: +66 9 9941083
e-mail: saliltips@yahoo.com

Education Qualifications:

1994 - 1997 M. Eng in Electrical Engineering,
King Mongkut's Institute of Technology Ladkrabang (KMIT'L), Thailand.
1990 - 1993 B. Eng in Electrical Engineering,
King Mongkut's Institute of Technology Ladkrabang (KMIT'L), Thailand.

Work Experience:

July 1993 – Till Date : A lecturer in the Department of Power Electrical Engineering at
Mahanakorn University of Technology,
March 1993 – June 1993: A electrical engineer in the department of maintenance of Heng Seng
Power Plant,
October 1992 – February 1993: A part-time laboratory demonstrator (while a forth year student)
in the department of power electrical engineering at Mahanakorn Institute.

Research Interest: Energy Conversion, and Electric Drives.